ScuDo
Scuola di Dottorato ~ Doctoral School
WHAT YOU ARE, TAKES YOU FAR

Doctoral Dissertation
Doctoral Program in Aerospace Engineering (29^{th}cycle)

Vibrations Prediction and Measurement of Multi-Stage Bladed Disks with non Linear Behavior due to Friction Contacts

By

Giuseppe Battiato

******

Supervisor(s):
Prof. Teresa M. Berruti, Supervisor
Eng. Paolo Calza, Co-Supervisor

Doctoral Examination Committee:
Prof. Paolo Tiso , Referee, ETH Zurich
Prof. Dario Di Maio , Referee, University of Bristol

Politecnico di Torino
2017

Declaration

I hereby declare that, the contents and organization of this dissertation constitute my own original work and does not compromise in any way the rights of third parties, including those relating to the security of personal data.

Giuseppe Battiato
2017

* This dissertation is presented in partial fulfillment of the requirements for **Ph.D. degree** in the Graduate School of Politecnico di Torino (ScuDo).

This thesis is dedicated to Azzurra, my wife, who has been a constant source of support and encouragement during the challenges of my life. It is also dedicated to my parents, who have always loved me unconditionally and whose good examples have taught me to work hard for the things that I aspire to achieve.

Acknowledgements

Over the last three years I had the opportunity to perform my Ph.D. research project in cooperation with *GE Avio Aero*, investigating methods to predict and measure vibrations in bladed disk assemblies. This made these years very exciting, with a formidable combination of scientific basis and practical application in the world of aircraft turbine engineering. Now the thesis is completed and the time to reflect and express my appreciation to those who supported this work along the way has finally come.

Firstly, I would like to express my sincere gratitude to my advisor Prof. Teresa M. Berruti, for the continuous support of my Ph.D. studies and related research, for her patience and motivation. Her guidance helped me in all the time of research and writing of this thesis. I could not have imagined having a better advisor.

Secondly, I would like to thank *GE Avio Aero* for the *Ugo Buffa* fellowship, which financial supported me for a fruitful research activity on extremely interesting topics. In particular I am thankful to Paolo Calza, who has been a great supporter of all the Ph.D. activities, always asking the right questions and safeguarding the balance between scientific content and practical applicability.

Special thanks must go out to Prof. Christian M. Firrone, who introduced me in the field of turbomachinery dynamics and convinced me to apply for the Ph.D. program in aerospace engineering at the Politecnico di Torino. Christian, you have been a source of inspiration throughout the my studies, I admire your passion for teaching, your professional knowledge and positive spirit.

I am deeply indebted to Prof. Bogdan I. Epureanu from the University of Michigan, who made my long stay in Ann Arbor pleasant and rich of new knowledge. I gratefully acknowledge his technical and strategic expertise, as well as its immense patience, leading to the successful completion of my doctorate.

Furthermore I want to thank all the members of the *LAQ AerMec Laboratory* for the pleasant working environment and the great time we had every day spent together. Thanks!

Last but certainly not least I would like to thank my family. Mum and Dad, if it weren't for your continuous support and all the opportunities you gave me, I could have never gotten this and other important milestones of my life. Finally I have to thank Azzurra for her loving and understanding, but most of all for simply always being there and making life pleasant.

Abstract

The architecture of current aircraft turbofan engines consists of multi-stage assemblies resulting from the coupling of bladed disks by means of bolted flange joints. The efficiency of such systems in real working condition is strictly related to the dynamic properties of blades and disks constituting them. According to the current design practices, blades and disks are designed so that their weights are reduced and their slenderness increased. Therefore, latest generation turbofan engine thus result much more sensible to mechanical vibrations that may cause failure by high cycle fatigue phenomena. For these reasons robust computational techniques and innovative measurement systems have become necessary tools for the design and validation of multi-stage bladed disks assemblies, in order to preserve their structural integrity while operating in real working conditions. The topics developed in this Ph.D. thesis concern aspects of linear and non-linear dynamics in the turbomachinery field and give a series of important guidelines for the study of multi-stage bladed disks systems from both a numerical and experimental point of view.

The research activity has been mainly focused on the following two topics:

1. *Development of reduced order model techniques for the prediction of forced response of multi-stage bladed disk assemblies*. The main challenge associated with modeling multi-stage assemblies is strictly related to the possible different cyclic symmetry characterizing the coupled stages. In such case a sector representative of the whole multi-stage system does not exist in general and typical dynamic calculations based on cyclic constraints can not be performed as in the case of single bladed disks. Therefore, two novel reduced order model techniques for multi-stage systems have been developed in order to overcome the mentioned drawback while guaranteeing high fidelity in modeling the system dynamics. Furthermore, for the first time the bolted flange joint coupling two bladed disks is considered as a possible source of damping

due to friction phenomena. Understanding the effects of such non-linearities in damping blade vibrations could be crucial in design of bolted flange joint. The proposed reduction techniques then also allow the prediction of the forced response of a multi-stage system when friction contacts are present at the flange joint interface while maintaining low computational costs.

2. *Validation of the Blade Tip-Timing measurement technique*, for the identification of the modal properties of two laboratory dummy disks. In this frame an experimental procedure to validate the Blade Tip-Timing system against the strain gauges measurement has been proposed. Furthermore, a novel methodology for the identification of the *operative deflection shape* of a vibrating bladed disks in presence of small mistuning has been developed.

Contents

List of Figures

List of Tables

Nomenclature

Roman Symbols

$\boldsymbol{a}$	Real Fourier coefficient
$\boldsymbol{C}$	Compatibility matrix
$\boldsymbol{D}$	Collocation or interpolation matrix
$\boldsymbol{D}^f$	Dinamic Stiffness matrix of order f
$\boldsymbol{E}$	Fourier matrix
$\boldsymbol{e}$	Complex Fourier coefficient
$\boldsymbol{F}$	Real valued Fourier matrix
$\boldsymbol{f}$	Vector of nodal forces
$\boldsymbol{H}^f$	Receptance matrix of order f
$\boldsymbol{K}$	Stiffness matrix
$\boldsymbol{M}$	Mass matrix
$\boldsymbol{R}$	Reduction matrix
$\boldsymbol{T}$	Transformation matrix
$\boldsymbol{u}_i$	i^{th} eigenvector of a full cyclic symmetric structure
$\boldsymbol{x}$	Vector of nodal displacements
z_i	i^{th} complex eigenvector of a cyclic symmetric structure

$\tilde{h}$	Maximum number of nodal diameters
EO	Engine Order
f_0	Normal preload
f_c	Contact force
f_n	Normal contact force
f_t	Tangential contact force
h	Number of nodal diameters
k	Extra harmonic index
k_n	Normal contact stiffness
k_t	Tangential contact stiffness
N	Number of sectors
n_s	Number of DoFs for each sector
W	Number of wavelengths
Z	Number of radial line segments per sector

Greek Symbols

α_n	Sector's angle
$\imath$	unit imaginary number $\sqrt{-1}$
η	Modal coordinate
Γ_d	Matrix reducing the dominant cyclic interface DoFs
$\varphi_{b,j}$	j^{th} CC mode
Φ_{bb}	CC modal matrix
Ψ_{Nn_b}	Constraint-mode matrix
μ	Friction coefficient

ω	Excitation frequency
ω_i	i^{th} eigenfrequency
$\phi_{e,j}$	j^{th} fixed-interface normal mode
π	$\simeq 3.14\ldots$
θ	Generic angle on a cyclic symmetric structure
Ω	Angular velocity
φ_h	Inter-Sector Phase Angle or Inter-Blade Phase Angle
φ_k	Inter-Node Phase Angle of Inter-Line Phase Angle
Φ_{ee}	Fixed-interface modal matrix
φ_{h_r}	Dominant inter-line phase angle
φ_{k_m}	Extra inter-line phase angle

Superscripts

A	Assembled
h	Cyclic reduction for the harmonic index h
rel	Relative coordinate

Subscripts

a	Active degrees of freedom
b	Boundary degrees of freedom
c	Cosine component
CB	Craig-Bampton reduction
CC	Characteristic Constraint modal reduction
cs	Cyclic symmetry reduction
e	Exceeding degrees of freedom

G Guyan reduction

GS Gram-Schmidt Interface modal reduction

i Interface degrees of freedom

i Internal

l Left frontier

M Mead reduced matrix

r r^{th} radial line segment

r Right frontier

s Sectors quantity

s Sine component

T Thomas reduced matrix

Other Symbols

$\bar{}$ Row echelon form

$\hat{}$ Gram-Schmidt orthonormalization

Acronyms / Abbreviations

CB-CMS Craig-Bampton component mode synthesis

CC modes Characteristic Constraint modes

GSI modes Gram-Schmidt Interface modes

AFT Alternating Frequency Time

CMS Component mode synthesis

HBM Harmonic Balance Method

HFT Hybrid Frequency Time

IBPA Inter-Blade Phase Angle

INPA Inter-Node Phase Angle

ISPA Inter-Sector Phase Angle

MAC Modal Assurance Criterion

MHBM Multi Harmonic Balance Method

ODS Operative Deflection Shape

ROM Reduced order model

SHBM Single Harmonic Balance Method

WLs Wavelengths

Chapter 1

Introduction

1.1 The Jet Engine

A *jet engine* is a reaction engine discharging a fast-moving stream of fluid, or simply a jet, that generates thrust by *jet propulsion*. In general, jet engines are combustion engines that can be either *airbreathing* or *non-airbreating*.

Jet propulsion is a practical application of Newton's third law of motion, stating that, "*for every force acting on a body there is an opposite and equal reaction*". For aircraft propulsion, the "body" is atmospheric air that is forced to accelerate as it passes through the engine. The force required to give this acceleration has an equal effect in the opposite direction acting on the system producing the acceleration. A jet engine produces thrust by propelling a large weight of air backwards in the form of a very high speed jet of gas. The resultant thrust acting on the engine is given by the *general thrust equation*:

$$F = \dot{m}_e v_e - \dot{m}_0 v_0 + (p_e - p_0) A_e \tag{1.1}$$

where $\dot{m}$ is the the mass rate, v the air flow velocity, p the pressure, the subscripts e and 0 refers to the exhausted and the entering quantities respectively and A_e is the exit area (Figure 1.1). From Eqn. 1.1 it can be noted how the same thrust can be obtained either by giving a small velocity to a large mass of air, or vice-versa, a large velocity to a small mass of air. In practice the former is preferred, since by lowering the jet velocity relative to the atmosphere a higher propulsive efficiency

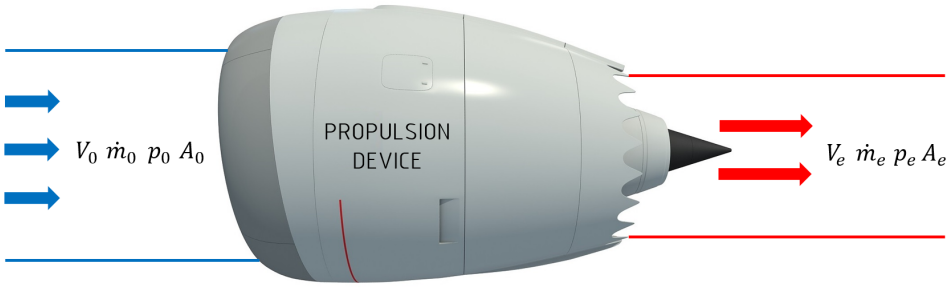

Fig. 1.1 Propulsion device working scheme: the resultant thrust acting on the engine depends on the entering (0) and exhausted (e) quantities according to Eqn 1.1

is obtained. The different type of jet engine, whether gas turbine, ram jet, rocket, turbo/ram jet or turbo-rocket, differ only in the way how the "propulsion provider", or engine, converts and supplies the energy into thrust.

Most passenger and military aircraft are powered by gas turbine engines that fall in the class of airbreathing jet engines. The latest version of the basic gas turbine engine is the so called *turbofan*, which basically represents the combination of the earlier turbojet engine with a ducted *fan*.

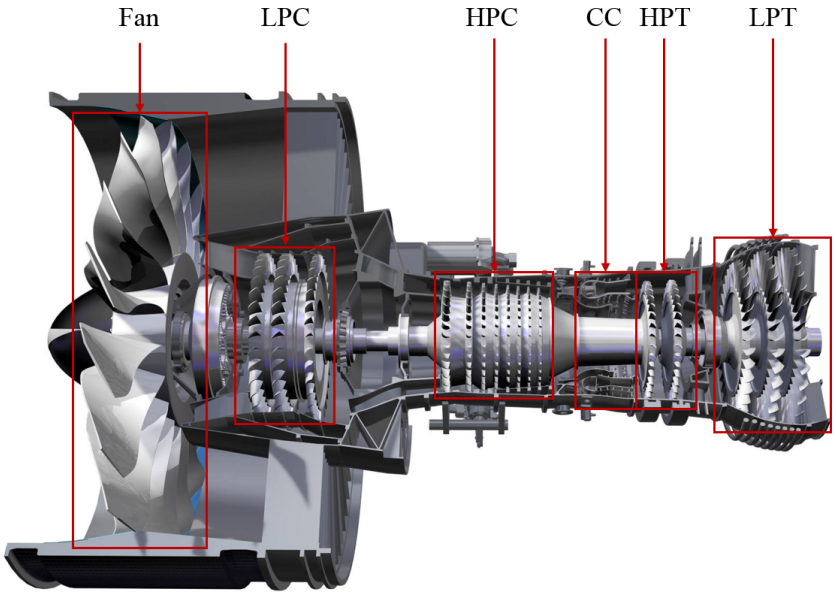

Fig. 1.2 Turbofan cross-section and list of its basic components.

The architecture a of turbofan engine is quite simple. For instance, on Figure 1.2 the cross-section of a typical dual-shaft engine is shown; it is possible to single out some basic components:

- *Air Intake*: all turbine engines have an *air intake*, or simply an *inlet* to bring free stream air into the engine. The inlet sits upstream of the low pressure compressor and generally has a divergent shape in order to decelerate the air flow. Especially for supersonic aircrafts the inlet must slow the flow down to subsonic speeds before the air reaches the compressor.

- *Fan and Low pressure compressor (LPC)*: LPC consists of one or two stages, each one compound by a row of rotating blades mounted on a disk followed by a stator vane. In the two-spool engine arrangement the LPC and Fan are connected to a *low pressure shaft*, which is driven by the low pressure turbine. While the LPC has the important role to perform an initial compression of the air flow, the Fan contributes to the engine's thrust by accelerating the cold air flow rearwards. The stator vanes, fixed on the engine case, are necessary to straighten the air flow back to the axial direction, but they can be also useful to perform a secondary flow compression by means of an opportunely design of the air ducts between airfoils of adjacent blades.

- *High pressure compressor (HPC)*: is the first part of the core engine, and consists of several stages (10-12 or more) connected with a *high pressure shaft*. Here the hot flow undergoes a high compression (compression rate equal to 30 or higher) and consequently warming, up to about 900 K temperature. From the front to the rear of the compressor, i.e. from the low to the high pressure end, there is a gradual reduction of the air annulus area between the rotor shaft and the stator casing. This is necessary to maintain a near constant air axial velocity as the density increases through the length of the compressor.

- *Combustion chamber (CC)*: has the task of burning large quantities of fuel, supplied through several fuel spray nozzles, with extensive volumes of air, supplied by the compressor, in order to release the heat in such a manner that the air is expanded and accelerated to give a smooth stream of uniformly heated gas at all conditions required by the turbine. The amount of fuel added to the air will depend upon the temperature rise required. However, the maximum temperature is limited within the range of 1100 K to 1900 K by the material from which the turbine blades and nozzles are made.

- *High pressure turbine (HPT)*: the turbine has the task to provide the power to drive the compressor and the accessories. It consists of few stages, typically

2-3, each one formed by a rotor following the stator: the former is connected to the high pressure shaft (in order to supply power to the high pressure compressor), the latter is fixed to the casing. Here, rotor and stator airfoils are usually both designed to provide an expansion of the flow. The pressure drop across a single turbine stage can be much greater than the pressure increase across a corresponding compressor stage. A single turbine stage can thus be used to drive multiple compressor stages.

- *Low pressure turbine (LPT)*: connected to the low pressure shaft, supplies the power to the LPC and Fan.

- *Exhaust system*: aero gas turbine engines have an exhaust system that passes the turbine discharge gasses to atmosphere at a velocity, and in the required direction, in order to provide thrust. The design of the exhaust system therefore, exerts a considerable influence on the performance of the whole engine. The areas of the jet pipe and propelling nozzle affect the turbine entry temperature, the mass air flow and the and pressure of the exhaust jet.

Turbofan uses two separate air flows in working conditions. The first, the *hot flow*, traverses the core of the engine from the inlet to the propelling nozzle, through the fan, compressor, combustion chamber and turbine. The second flow, called *cold flow*, bypasses the core going from the fan directly to the nozzle. According to this description a turbofan can be thought of as a turbojet being used to drive the fan, with both contributing to the resultant thrust. The ratio of the mass-flow of air bypassing the engine core compared to the mass-flow of air passing through the core is referred to as the *bypass ratio*. Engines that exploit more jet thrust relative to fan thrust are known as low-bypass turbofans, conversely those that have considerably more fan thrust than jet thrust are known as high-bypass. Due to their high fuel efficiency high-bypass ratio turbofans are employed for civil aviation, while low-bypass ratio turbofans equipped with afterburns are used on modern military fighters.

The thermodynamic cycle upon which the gas turbine engine works is, in its simplest form, the *Brayton's* cycle shown in Figure (1.3).

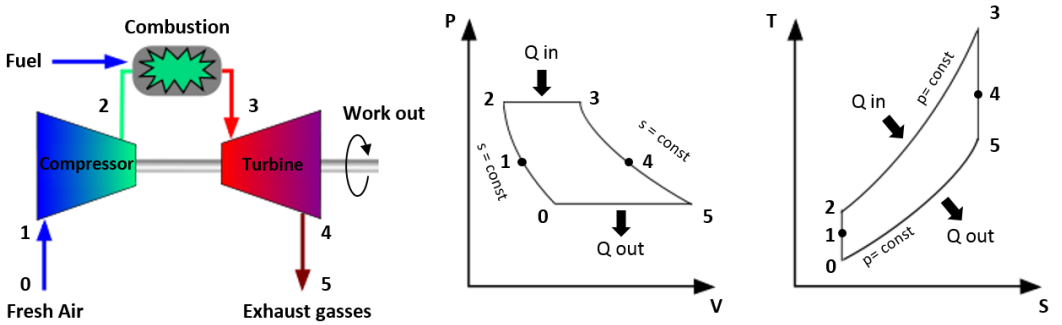

Fig. 1.3 Idealized Brayton's cycle: airflow path over the engines' main components, P-V and T-S diagrams.

Using the turbine engine station numbering system, the cycle begins with free stream conditions at station 0. In cruising flight, the inlet slows the air stream as it is brought to the compressor face at station 1. As the flow slows, some of the energy associated with the aircraft velocity increases the static pressure of the air and the flow is compressed. Ideally, the compression is isentropic and the static temperature is also increased as shown on the plot. The compressor does work on the gas and increases the pressure and temperature isentropically to station 2 the compressor exit. Since the compression is ideally isentropic, a vertical line on the T-s diagram describes the process. In reality, the compression is not isentropic and the compression process line leans to the right because of the increase in entropy of the flow. The combustion process in the burner occurs at constant pressure from station 2 to station 3. The temperature increase depends on the type of fuel used and the fuel-air ratio. The hot exhaust is then passed through the power turbine in which work is done by the flow from station 3 to station 4. Because the turbine and compressor are on the same shaft, the work done on the turbine is exactly equal to the work done by the compressor and, ideally, the temperature change is the same. The nozzle then brings the flow isentropically back to free stream pressure from station 4 to station 5. Externally, the flow conditions return to free stream conditions, which completes the cycle. The area under the T-s diagram is proportional to the useful work and thrust generated by the engine.

1.2 Turbine

The general arrangement and working principle of a modern turbofan engine were briefly described in the previous sections. This section is mainly focused on the general design of turbines, representing the most critical rotating components of a jet engine. Although common geometrical and structural characteristics can be found between turbine and compressor stages, it is known that the former work in a much more hostile environment than the latter. In fact, sitting just downstream of the burner, the turbine blades experience flow temperatures higher than the those typical of the compressor air flow (see section 1.1).

As already mentioned the main task of a turbine is to transform the gas potential energy into mechanical energy, in order to provide the power needed by the compressor stages. This energy conversion is possible through two rows of blades, a *stator* followed by a *rotor* (Figure 1.4).

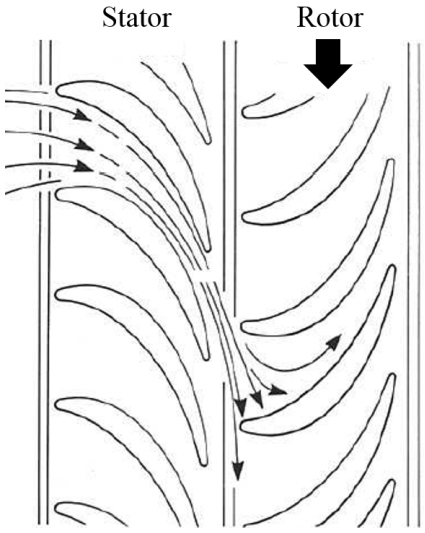

Fig. 1.4 Turbine driven by the impulse of the gas flow and its subsequent reaction as it accelerates through the converging blade passage.

Each pair of stator blades realizes a convergent duct with the scope to deviate and accelerate the axial gas flow. The flow deviation causes tangential forces acting on rotor blades in the same sense of rotation, and consequently power transmitted to the shaft. Further flow acceleration and deviation (flow expansion) are then performed by the convergent ducts in between adjacent rotor blades, before the flow encounters the following stator.

1.2.1 Turbine Design

The design of a turbine is an iterative procedure aimed at achieving the best compromise between aerodynamic and structural requirements. The aerodynamic aspects of the design have to be carefully faced first by defining the turbine *flowpath*. For a certain working condition known as *design point* the flowpath denotes the channel traveled by the air flow while expanding. From a geometric point of view it is simply a 2-D sketch defined by a collection of *corner points* representing the projection on the engine cross-section of the maximum size of stator and rotor aerodynamic blade profiles (Figure 1.5).

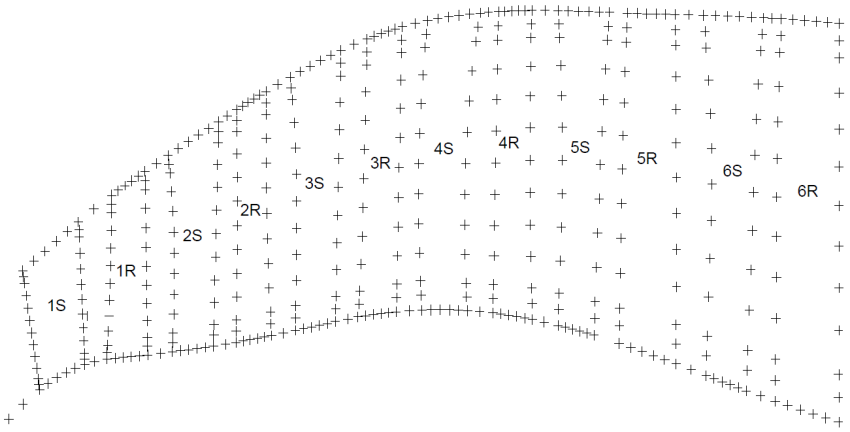

Fig. 1.5 2-D flowpath of a 6 stages LPT: the sketch defined by the corner points (+) identifies the position and maximum size of both stator (S) and rotor (R) blade profiles in hot conditions.

The definition of the flow path is followed by the blade design in working condition (*hot condition*). Firstly, the bi-dimensional profiles corresponding to the blade cross-sections from the root to the tip needed to realize the optima velocity triangles have to be defined. The tri-dimensional geometry of the blade *airfoil* is then obtained by interpolating the bi-dimensional profiles in the radial direction. Due to the different values of the *stagger angle*, larger at the tip than at the root (Figure 1.6), the turbine blades result "twisted", which ensure equal work done by the gas flow at all locations along the length of the blade.

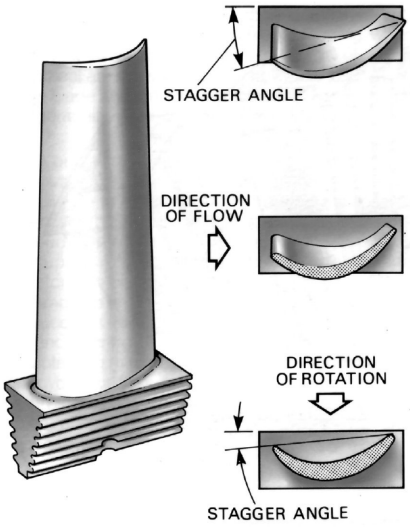

Fig. 1.6 Typical turbine blade showing twisted contour. The variation of the stagger angle from the root to the tip ensures equal work done by the gas flow at all locations along the length of the blade.

One of the most important aspects in the design of either rotating or non-rotating elements of a turbine is the *hot to cold scaling*. As already mentioned the flowpath and the blade profiles are determined in hot condition. Conversely, the turbine is assembled in *cold condition*, but it has to guarantee the correct positioning of the blade profiles such that in working condition designed flowpath can be realized. For both rotor and stator blades the operations needed for scaling the profiles from hot to cold condition are briefly listed below.

- *Scaling*: represents the scale reduction of the blade profiles from the designed geometry by removing the material dilatation due to the high temperatures.
- *Twisting*: the blade cross-sections in hot condition have to be "twisted" around their radial direction if the blade in cold condition is required. The effects of such twisting disappear in working condition when the blades are loaded by the hot gasses.
- *Positioning*: defines the position of the *platforms* needed to keep fixed the blade profiles; the *outer bands* connected to the engine casing for the stator, the *platforms* and *shrouds* for the rotor.

The "cold" blade profiles have to be structurally verified since they suffer several types of mechanical stress, which can be collected in four main categories: thermal, centrifugal, bending and vibration.

Thermal Stress

The high temperature of the exhaust gas flowing through the first HPT stage causes thermal expansion on all the components involved. Referring to the relationship between the extensional strain and the change in temperature of a generic body, the engine's components experience a *thermal strain* ε_T that is generally proportional to the difference between the hot gasses and the entering air flow temperature ΔT:

$$\varepsilon_T = \alpha \Delta T \tag{1.2}$$

where the parameter α is the coefficient of thermal expansion. Although the temperature change does not lead to mechanical stresses in a component that is free to expand, thermal stresses occur in components that are either restrained (i.e. not completely free to expand) or featuring a non-uniform coefficient of thermal expansion. For instance, shrouded turbine blades during operation nearly behave as clamped-clamped structures due to the centrifugal twist-back moment enabling a tight contact between adjacent shrouds (Figure 1.9). Such condition clearly avoid the natural extension of the blade involving a stress distribution in their structure.

Besides the thermal expansion the other phenomenon correlated with the high working temperature typical of turbine blades is the *creep*. Creep generally occurs as a result of long term exposure to levels of stress that are below the yield strength of the material, and especially for turbine blades, which are permanently loaded in working conditions by high centrifugal stress and bending stress, it results accelerated by the high temperature.

Two are the possible solutions to limit the thermal stresses: the first is the correct material choice, the second is to provide a cooling system for the blade. The second solution is extensively employed and requires to spill out from the compressor a certain amount of air that is forced to pass through a series of ducts realized inside the airfoil (Figure 1.7).

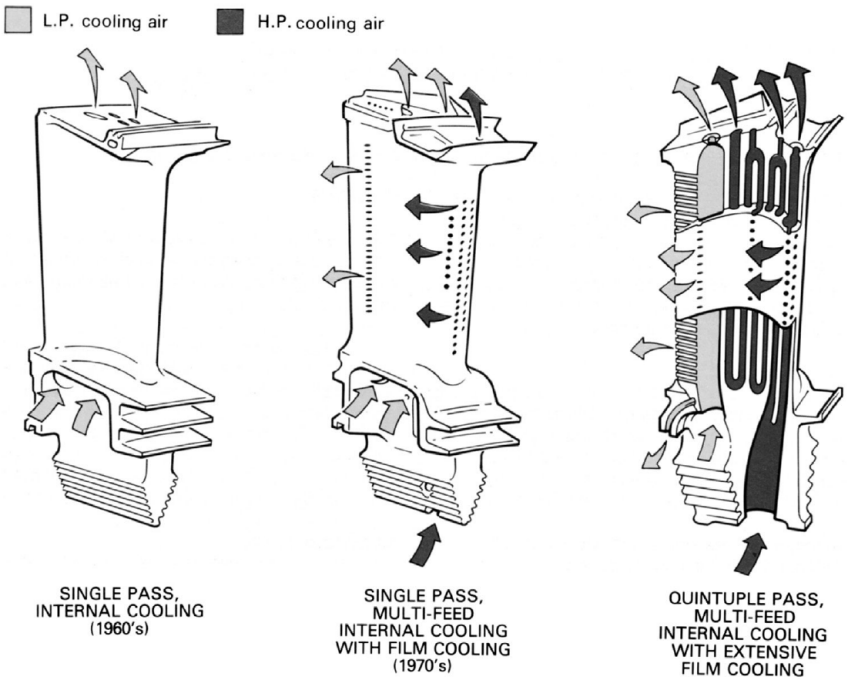

Fig. 1.7 Developement of HPT blade cooling systems. Turbine blade life depends not only on their shape but also on the method of cooling. Generally, single pass internal (convection) cooling was of great practical benefit, but further developments have lead to multipass internal cooling with external air film cooling.

Centrifugal Stress

Due to the high rotation speed characterizing the bladed disks in working conditions, i.e. ≈ 7000 rpm for the LP shaft and 1200 rpm for the HP shaft, centrifugal loads have to be considered in the structural validation of a rotor blade. If r denotes the generic radial coordinate of a blade cross-section from the blade root and R is the maximum blade radius, the centrifugal force acting on the selected cross-section is given by:

$$F_c = \int_r^R dF_c = \rho\omega^2 \int_r^R r \cdot dV = \rho\omega^2 \int_r^R rA(r) \cdot dr \tag{1.3}$$

where ρ is the material density, ω the rotation speed and $A(r)$ the blade cross section a t radius r.

The blade section most suffering centrifugal stress is intuitively the root. In order to prevent the blade root failure, a possible solution would consist on a suitable design

of the *shank* between the root and the platform in order to opportunely undertake centrifugal stresses.

Bending Stress

Besides centrifugal loads the blade root is also subjected to the bending moment due to the pressure exerted by the hot gasses over the pressure side of the blade (Figure 1.8 a)). The effects of the bending moment M_{FLOW}, involving bending stresses at the blade root, are attenuated by skewing the blade in the flow direction. This practice, which is called *camber*, requires to tilt the blade airfoil of 1 or 2 degrees with respect its center of gravity, such that a new moment M_C, generated by the centrifugal force F_C and opposite to M_{FLOW}, can be obtained (Figure 1.8 b)).

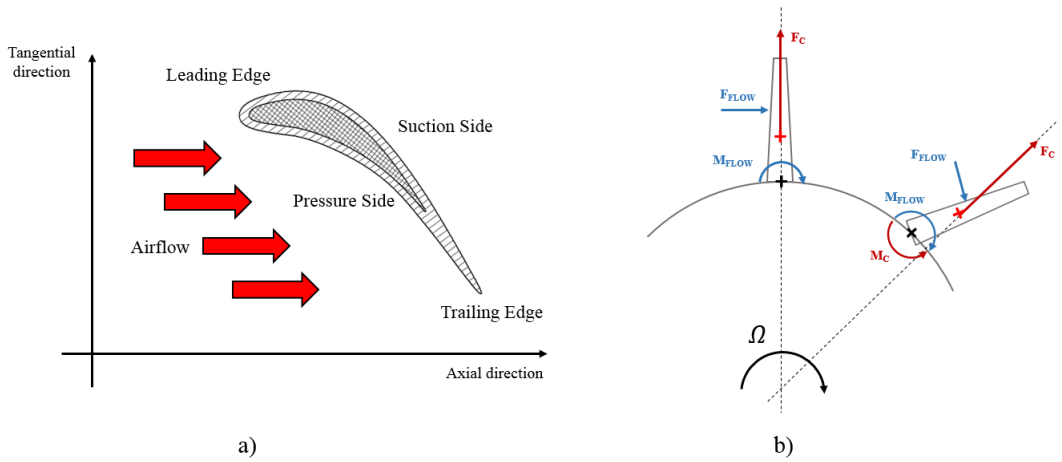

Fig. 1.8 a) Radial cross section of a turbine blade and airflow action over the blade's pressure side. The pressure distribution acting on the blade's pressure side involves a bending moment at the blade's root as happens at the clamped end of a clamped-free beam under the action of a distributed load. b) The camber moment M_C generated by the centrifugal force F_C acting on a tilted blade compensates for the bending moment M_{FLOW} at the blade's root.

The mechanical equilibrium between the two moments is achieved only at a certain rotation speed and a value of centrifugal force. For all the other working conditions the bending stresses will be considerably decreased but not completely eliminated.

Vibration Stress

Vibration stresses in turbine bladed disks result from dynamic excitations. These can be grouped in two main classes depending on the nature of the source generating them:

- *Mechanical excitations*: ascribable to the wrong rotor balance (*whirl*), blade tip - casing contacts and possible impacts between either rotating or non-rotating components with items sucked into the engine while working.
- *Aerodynamic excitations*: while bending stresses are caused by the stationary component of the gas flow pressure (mean value), vibration stresses are induced by its non-stationary components. These are attributable to the gas flow - structure interaction concerning the non-uniform circumferentially distributed pressure, stator - rotor interactions and self-excited aeroelastic phenomena (*flutter*).

In bladed disks both mechanical and aerodynamic excitations are the main responsible for *High Cycle Fatigue* (HCF), which is considered the "major cost, safety and reliability issue for gas turbine engine" [1]. Therefore blades and disks require special attention and a very careful design due to the crucial role they play during the operation of gas turbine engines. As so much is dependent on the reliability of these components, the tendency of manufacturers would be to over-design them in order to largely cope the safety specifications. On the other hand, limited weights are necessary to achieve the high efficiency characterizing the latest generation gas turbine engines. This aspect unavoidably leads to design much slender blades and thinner disks, making them more sensible to mechanical vibrations.

Due to the large operative speed range, bladed disks cannot work outside of all resonant zones. In fact, since their configuration is obtained from preliminary aerodynamic and efficiency calculations, it cannot be easily modified. In this regard, some critical resonances cannot be avoided and a way to provide additional damping to the system is necessary. One of the most used practices to reduce vibration stresses consists in exploiting the *dry friction* occurring at the interfaces of joints employed in the bladed disk assemblies. Nowadays the mechanical arrangements used to perform this energy dissipation are mainly three:

1. *Blade root joint*: the method of attaching the blades to the turbine disk is of considerable importance, due to the high stress concentration at disk rim around the fixing slot or at the blade root. Blades are connected to the disk rim by means of *firtree* or *dovetail* roots, inserted in the corresponding disk slots. These configurations enable friction damping at the contact interfaces between the blade root and the disk slot during the vibration of the assembly.

2. *Blade shrouds*: As shown on Figure 1.9, the *shroud* is a sort of roof placed at the tip of each blade. The key idea behind the shrouds design is to damp the blade vibration amplitudes through dry friction. Typically the shrouds have an "S" shape which guarantees an optimal blade-to-blade interface for efficient damping. Moreover, to further increase the damping level, the blades can be pre-twisted during the rotor assembly.

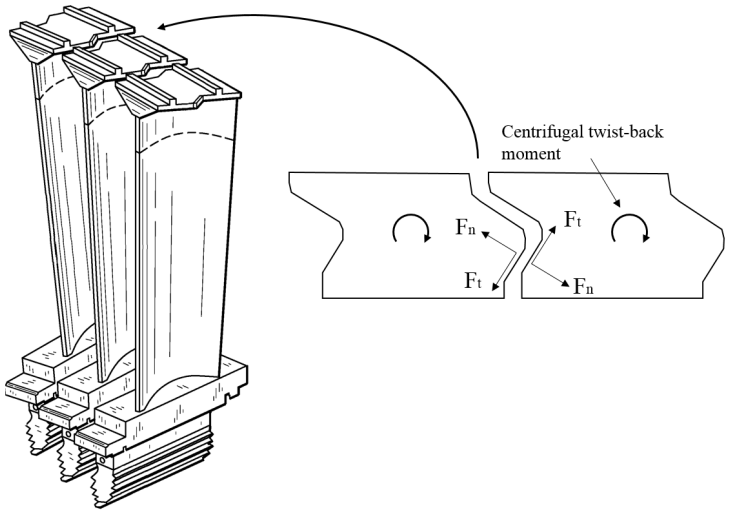

Fig. 1.9 Contact between adjacent shrouded blades: the centrifugal load acting on the blades during operation causes a twisting moment around the blade axis that brings the shrouds into contact.

3. *Underplatform dampers*: Blade shrouds can considerably influence the aerodynamic configuration of the rotor, increasing, for instance, the level of low turbulence or disturbing the air-cooling flow exiting from the blades internal duct, especially in HPT stages. An alternative damping device able to damp vibrations by dry friction is the *underplatform damper*. This is basically a piece of metal with a suitable shape that is pressed against the blade platforms during rotation by the centrifugal force (Figure 1.10). Underplatform dampers

are particularly effective when the adjacent blades vibrate with a phase lag of π.

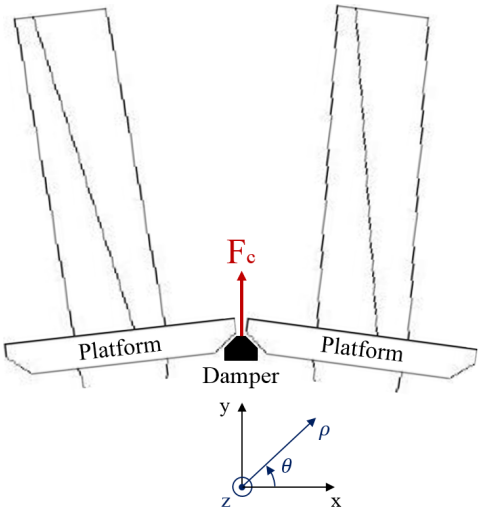

Fig. 1.10 Simplified scheme of under-platform damper placements: during rotation the damper (black body) is pressed against the blades' platforms by the centrifugal force F_c.

1.3 Dynamics Prediction and Testing of a Bladed Disk

Although established, the mentioned arrangements exploit as sources of friction damping specific blade locations, being focused on the attenuation of the dynamic response of a single-stage bladed disk. Recently, the interest of the scientific community is moving towards other types of joints whose nonlinear behavior may affect the dynamic response of the aircraft engine at a system level. This is the case of the bolted flange joint connecting two bladed disks, where the contact phenomena at the inter-stage boundary may lead to further sources of friction damping (see Chapter 5).

In order to optimize the design of bladed disks, all the mentioned sources of stress have to be carefully taken into account, but nonetheless, due to the complexity of the dynamic phenomena involved in a turbomachinery, time-varying excitations play the most important role. In fact, much research has addressed the design optimization process towards the *dynamical investigation* of single components first and partial assemblies recently, according to the following three steps: *design*, *analysis* and *testing* (Figure 1.11).

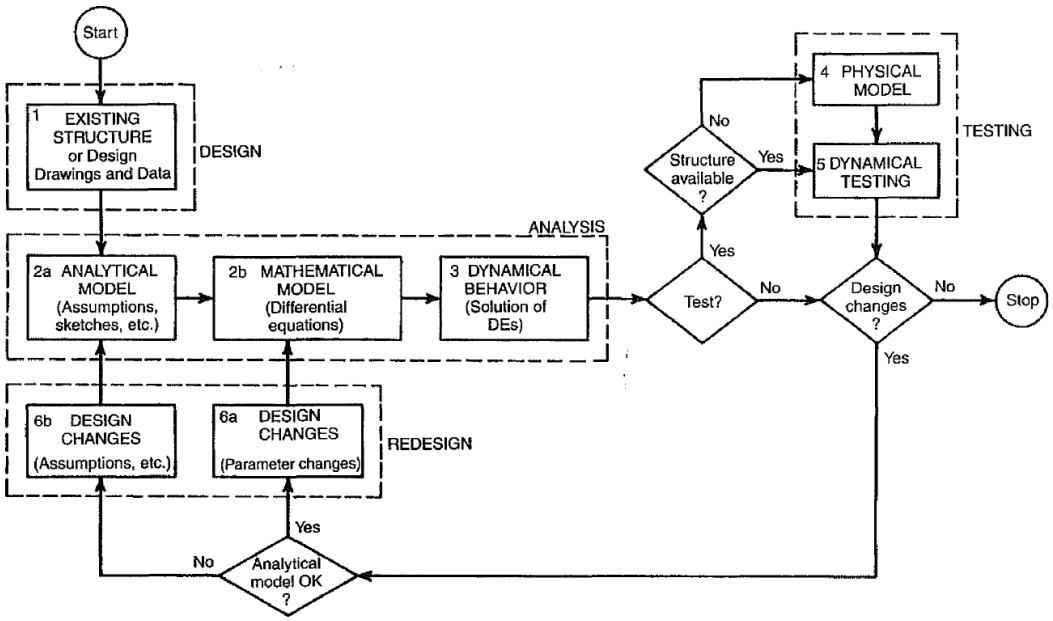

Fig. 1.11 Steps in a dynamical investigation [1].

The most demanding step of this complex procedure is the creation of accurate *mathematical models* capturing the structure dynamics. In this frame, modeling the non-linearities due to friction contacts in turbomachinery and their effects on the bladed disks dynamics is not a trivial task. It has been, and still it is, the main objective of several studies carried out by the *LAQ AerMec* group of the Politecnico di Torino and few other research groups around the world. As a result of this vigorous research, several Finite Element based computer codes have been developed in order to predict either the linear or non-linear forced response of bladed disk assemblies, facilitating the design process. The development of such codes, being thought mainly for industrial applications, requires the capability of modeling contacts and high expertise in *model order reduction*. This last feature makes more efficient the design process since allows reducing the number of degrees of freedom involved in the simulation and then a faster evaluation of the effects that small modifications of the design parameters have on the system's dynamics.

In order to guarantee accuracy and predictability, a numerical tool has to be validated against real structures preferably in realistic working conditions. Otherwise, the lack of experimental validations makes the manufacturers reluctant to use such codes in their design practices. An extensive experimental validation would avoid

possible sources of mismatch between the real and simulated data and guide the codes through corrections to produce acceptable and reliable outputs.

Generally, discrepancies between computer model predictions and actual system responses are due either to the inaccurate modeling of the system dynamics or to the lack of modeling them at all. Therefore, the only way to ensure whether the numerical models are efficient or not is to check their predictions against measurements. However, the experimental validation of a model simulating vibration responses of real gas turbines is an extremely difficult task for different reasons:

- Measurements should be performed on the most critical components as the blades in a turbofan engine are. Due to the complexity of the global engine architecture, the presence of several other components inevitably affects the blades response, with obvious difficulties in modeling the resulting dynamic coupling mathematically;
- The high temperature characterizing the engine in working condition prevents the employment of well-established measurement systems which need to be in contact with the blades (e.g. the strain gauges);
- From a practical point of view there is no enough room to install measurement systems able to monitor the blades response in real-time during operation.

For all these motivations it is a common practice to carefully design experimental setups which exhibit only the dynamic phenomena under investigation. Once the numerical model are demonstrated to be accurate representation of the experimental data, they can be used can be used as optimization tool for real bladed disks design.

1.4 Thesis Objectives & Outline

The present work gives an insight into how the forced response of multi-stage bladed disk assemblies can be efficiently predicted by using tailor-made reduction techniques. Such models can be widely employed for industrial applications concerning the dynamic study of complex multi-stage systems usually analyzed as a whole by finite element commercial codes. Due to the large number of degrees of freedom involved the simulation, also the simple evaluation of eigenfrequencies and mode

shape may become prohibitive for the large computational costs. Consequently, a model simplification is usually requested without any loss of accuracy.

Three novel reduction approaches are developed throughout this thesis. All of them take their basis on the well-know *Craig-Bampton* technique and go further by exploiting ad-hoc interface reduction methods. The first reduction technique, presented at the ISMA 2016 [4], is here named as *CC*-CMS method and represents the extension of the classic modal interface reduction method based on the *Characteristic Constraint Modes* formulation proposed by Castanier et al. [5]. The *CC*-CMS method is here developed to perform two different tasks, i.e. dynamic coupling of two component having non compatible meshes at the interface and the reduction of the independent frontier of a bladed disk sector treated in cyclic symmetry conditions. The other two techniques are developed for application concerning multi-stage structures. In a different fashion these allow the single-stages' reduction and their subsequent coupling by exploiting the spatial harmonic periodicity of the mode shapes of cyclic symmetric structures [6, 7]. The mentioned reductions allow a substantial simplification of the forced response prediction of multi-stage bladed disks featuring friction contacts at the inter-stage boundary. In this regard for the first time it will be possible to consider the bolted flange joint linking two bladed disks as a source of friction damping useful to mitigate the blades vibration amplitudes.

In the last part of this work the capabilities of the *Blade Tip-Timing* measurement system are explored in order to understand whether it can be used as a valid tool for the modal identification of real bladed disk assemblies. In this frame and extensive experimental campaign was performed on two dummy bladed disks having different geometric, structural and dynamical properties and a novel method to experimentally identify the *operative deflection shape* of bladed disk is presented [8].

The present thesis is organized as following:

Chapter 2 introduces to the dynamics of *cyclic symmetric structures*. Here the theory developed in literature is reviewed and its application on bladed disks is discussed. Furthermore, a new important feature of the mode shapes of cyclic symmetric structures is presented: the *extra harmonics* pattern. These small wavelenght vibratory phenomena characterizing the motion of cyclic symmetric structures at the interface, where the continuity of the material is guaranteed in the circumferential direction, are useful when the bladed disk's dynamics has to be precisely approximated at the flange joint.

Chapter 3 reviews the commonest *dynamic substructuring* methods in the class of *component mode synthesis*. Here the most used fixed-interface methods, i.e. the *Guyan* and *Craig-Bampton* methods, are reviewed. Interface reduction techniques are later introduced and the novel *Gram-Schmidt Interface* reduction method is developed from the pre-existing *Characteristic Constraint Mode* formulation.

Chapter 4 introduces the existing state of the art on multi-stage reduction techniques and proposes two novel reduction methods for the dynamic response prediction of multi-stage bladed disk assemblies. The first approach starts from the Craig-Bampton reduced order models of the full-wheel stages and goes further by reducing the physical displacements at the inter-stage boundaries by few harmonic basis functions [6, 7]. The second approach starts from the two fundamental sectors that are reduced by using a modified version of the *cyclic symmetry Craig-Bampton* method [9]. In both cases the multi-stage dynamics is studied in the reduced order space only.

Chapter 5 concerns the study of the bolted flange joint between two bladed disks as a possible source of friction damping capable to mitigate the blades' vibration amplitudes. This aspect, which is not yet present in the current state of the art, is carried out by combining the multi-stage reduction techniques developed in Chapter 4 with the macroslip contact model involving the classic spring-slider contact element. The validity of the mentioned practice is checked on a multi-stage system under simplified hypotheses.

Chapter 6 evaluates the accuracy of a latest generation Blade Tip-Timing system by means of an extensive experimental campaign on two dummy blisks. Here, a new sensor arrangement named *beam shutter* configuration is proposed in order to detect the vibrations of shrouded bladed disks. Furthermore an original method used to identify the operative deflection shape of a bladed disk through the experimental determination of its nodal diameters is presented.

Chapter 2

Dynamics of Cyclic Symmetric Structures

Among the possible sources of stress affecting the bladed disks particular emphasis has been given to time-varying excitations, being the major responsible of failure due to HFC. Understanding the bladed disks dynamics is thus essential to accurately predict their natural frequencies and mode shapes, so that the effects of unavoidable strong resonances can be limited.

Bladed disks fall in the class of structures exhibiting *rotational periodicity* or *cyclic symmetry*, meaning that they consist of a finite number of identical substructures or *sectors* forming a closed geometry (Figure 2.1).

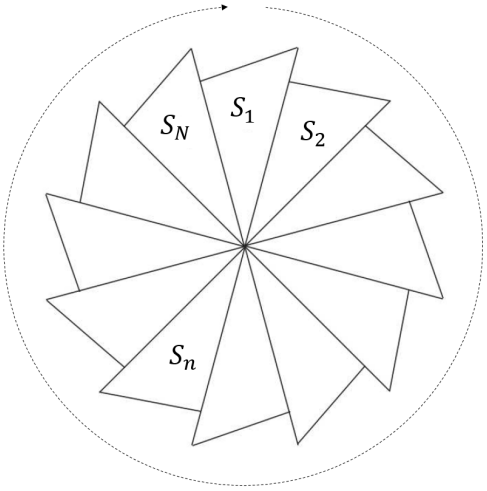

Fig. 2.1 Cyclic symmetric structure.

In the simplest case the substructure consists of one disk sector and one attached blade, but several other types of bladed disk assemblies showing different geometric and structural features exist. Examples of bladed disks featuring cyclic symmetry are those characterized by:

- Unshrouded identical blades on a disk (Figure 2.2 a));
- Continuously tip-shrouded blades on a disk (Figure 2.2 b));
- Mid-height shrouded blades on a disk (Figure 2.2 c));
- Blades that are integral parts with the disk; in this case the bladed disk is simply referred to as *blisk* (Figure 2.2 d)).

Fig. 2.2 Examples of cyclic symmetric structures.

Mathematically, the disk geometry for any radial and axial position at a certain angle θ is identical to itself at the angular position $(\theta + n\alpha_n)$, where $\alpha_n = 2\pi/N$ represents the so called *sector angle*. Both N and n are integers: the first denotes the number of disk's sectors, the second is defined as $n = 1, \ldots, N$. A satisfactory description of the cyclic symmetric structures dynamics has been given by Thomas in [10, 11]. The mode shape classification made in his work will be briefly reviewed in the following sections, since they are essential for subsequent developments on reduced order model techniques for multi-stage bladed disks.

2.1 Mode Shapes of Cyclic Symmetric Structures

The evaluation of natural frequencies and mode shapes of complex structures is commonly carried out by means of *Finite Element* (FE) dynamic calculations, which involve to discretize the structure in *elements*. This procedure, also known as *meshing*, allows to turn a continuous structure in a discrete mathematical model from which the real *mass* and *stiffness* matrices, $\boldsymbol{M}$ and $\boldsymbol{K}$ respectively, can be set up. The dynamic study of a bladed disk has no exceptions. After the aforementioned discretization, the bladed disk can be studied as a multi-degrees of freedom system, whose linear and conservative equation of motion (EQM) can be expressed according to the following general form:

$$\boldsymbol{M}\ddot{\boldsymbol{x}}(t)+\boldsymbol{K}\boldsymbol{x}(t)=\boldsymbol{f}(t) \tag{2.1}$$

where $\boldsymbol{x}(t)$ is the vector of degrees of freedom (DoFs) listing the nodal displacements, while $\boldsymbol{f}(t)$ represents the corresponding vector of external forces. If n_n is the total number of nodes resulting from the structure discretization, for the matrices and vectors of Eqn. 2.1 the following statements hold:

$$\begin{aligned} \boldsymbol{M} &\in \mathbb{R}^{3n_n\times 3n_n} \qquad \boldsymbol{K} \in \mathbb{R}^{3n_n\times 3n_n} \\ \boldsymbol{x}(t) &\in \mathbb{R}^{3n_n\times 1} \qquad \boldsymbol{f}(t) \in \mathbb{R}^{3n_n\times 1} \end{aligned} \tag{2.2}$$

$\boldsymbol{M}$ is positive definite since non-vanishing mass is associated to all DoFs, while $\boldsymbol{K}$ is at least semi-positive definite. $\boldsymbol{K}$ becomes positive definite for *well-constrained* structures, i.e. no rigid body modes are allowed.

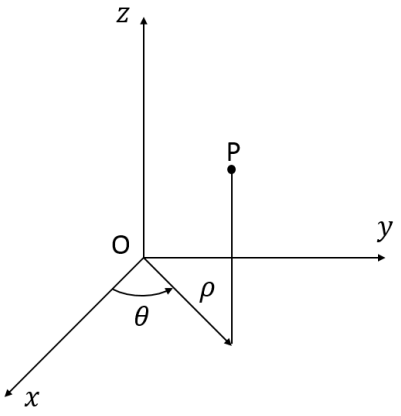

Fig. 2.3 Cylindrical reference frame.

For cyclic symmetric structures it is convenient to write Eqn. 2.1 in a cylindrical coordinate system with the z-axis coinciding with the structure's revolution one (Figure 2.3) and to rearrange the matrices and vectors such that the n_s DoFs of the first sector are followed by n_s DoFs of the second sector and so on. Under these hypotheses the matrices $\boldsymbol{M}$ and $\boldsymbol{K}$ and the vectors $\boldsymbol{x}$ and $\boldsymbol{f}$ can be written as follows:

$$\boldsymbol{M} = \begin{bmatrix} \boldsymbol{M}_0 & \boldsymbol{M}_1 & \boldsymbol{M}_2 & \dots & \boldsymbol{M}_2 & \boldsymbol{M}_1 \\ \boldsymbol{M}_1 & \boldsymbol{M}_0 & \boldsymbol{M}_1 & \dots & \boldsymbol{M}_3 & \boldsymbol{M}_2 \\ \boldsymbol{M}_2 & \boldsymbol{M}_1 & \boldsymbol{M}_0 & \dots & \boldsymbol{M}_4 & \boldsymbol{M}_3 \\ \vdots & \vdots & \vdots & \ddots & \vdots & \vdots \\ \boldsymbol{M}_2 & \boldsymbol{M}_3 & \boldsymbol{M}_4 & \dots & \boldsymbol{M}_0 & \boldsymbol{M}_1 \\ \boldsymbol{M}_1 & \boldsymbol{M}_2 & \boldsymbol{M}_3 & \dots & \boldsymbol{M}_1 & \boldsymbol{M}_0 \end{bmatrix} \qquad \boldsymbol{K} = \begin{bmatrix} \boldsymbol{K}_0 & \boldsymbol{K}_1 & \boldsymbol{K}_2 & \dots & \boldsymbol{K}_2 & \boldsymbol{K}_1 \\ \boldsymbol{K}_1 & \boldsymbol{K}_0 & \boldsymbol{K}_1 & \dots & \boldsymbol{K}_3 & \boldsymbol{K}_2 \\ \boldsymbol{K}_2 & \boldsymbol{K}_1 & \boldsymbol{K}_0 & \dots & \boldsymbol{K}_4 & \boldsymbol{K}_3 \\ \vdots & \vdots & \vdots & \ddots & \vdots & \vdots \\ \boldsymbol{K}_2 & \boldsymbol{K}_3 & \boldsymbol{K}_4 & \dots & \boldsymbol{K}_0 & \boldsymbol{K}_1 \\ \boldsymbol{K}_1 & \boldsymbol{K}_2 & \boldsymbol{K}_3 & \dots & \boldsymbol{K}_1 & \boldsymbol{K}_0 \end{bmatrix}$$

$$\boldsymbol{x} = \begin{Bmatrix} \boldsymbol{x}_1 \\ \boldsymbol{x}_2 \\ \boldsymbol{x}_3 \\ \vdots \\ \boldsymbol{x}_{N\text{-}1} \\ \boldsymbol{x}_N \end{Bmatrix} \qquad \boldsymbol{f} = \begin{Bmatrix} \boldsymbol{f}_1 \\ \boldsymbol{f}_2 \\ \boldsymbol{f}_3 \\ \vdots \\ \boldsymbol{f}_{N\text{-}1} \\ \boldsymbol{f}_N \end{Bmatrix} \tag{2.3}$$

$\boldsymbol{M}$ and $\boldsymbol{K}$ have a *block circulant symmetric* structure, where the blocks $\boldsymbol{M}_h$ and $\boldsymbol{K}_h$ ($h = 0,\dots,\text{int}(N/2)$ if N is even or $h = 0,\dots,\text{int}\big((N-1)/2\big)$ if N is odd) are symmetric matrices whose dimension equals the number n_s of each sector's DoFs [12, 8]. It must be remarked that the fashion assumed by $\boldsymbol{M}$ and $\boldsymbol{K}$ in Eqn. 2.3 only occurs if the DoFs are collected sector by sector, by placing the homologous ones in the same positions within the subvectors $\boldsymbol{x}_n$ ($n = 1,\dots,N$). Note that a cyclic symmetric structure can always be considered as an entire wheel whose sectors are physically constrained to each other. From a mathematical point of view this condition is guaranteed by the non-null off-diagonal entries of $\boldsymbol{K}$, while the matrix $\boldsymbol{M}$ still remains diagonal. An example on how the matrices $\boldsymbol{M}$ and $\boldsymbol{K}$ are obtained from a lumped parameters cyclic symmetric structure is shown in Appendix A.

When the mass and stiffness matrices are derived from the FE model, mode shapes and corresponding natural frequencies can be found by solving he following eigenproblem:

$$(\boldsymbol{K} - \omega_i^2 \boldsymbol{M})\boldsymbol{u}_i = \boldsymbol{0} \qquad i = 1, \ldots, Nn_s \tag{2.4}$$

where ω_i^2 and $\boldsymbol{u}_i$ are the real i^{th} eigenvalue and eigenvector respectively. Assuming the DoFs partition of Eqn. 2.3, the i^{th} eigenvector can be written as follows:

$$\boldsymbol{u}_i = \left[(\boldsymbol{u}_{1_i})^T \; (\boldsymbol{u}_{2_i})^T \; \ldots \; (\boldsymbol{u}_{N_i})^T \right]^T \tag{2.5}$$

where $\boldsymbol{u}_{n_i}$ $(n = 1, \ldots, N)$ is a vector of size n_s containing the modal displacements of n^{th} substructure when the i^{th} mode shape occurs.

As happens for axisymmetric structures, for the cyclic symmetric ones it is found that most vibration modes occur in orthogonal pairs. In fact, for axisymmetric strutures it is clear that if a mode shape shows the maximum deflection at some point on the structure, a rotation of the same mode through an arbitrary angle does not change the corresponding frequency of vibration. The same effect holds for cyclic symmetric structures, where the rotation that leaves the mode identical to itself is an integer multiple of the sector's angle α_n. As a consequence, the possible mode shapes of a cyclic symmetric structure $\boldsymbol{u}_i$ fall into three classes, depending on the relative motion between the individual sectors:

(a) Each sector has the same mode shape as its neighbors and vibrates in-phase with them:

$$\boldsymbol{u}_{n_i} = \boldsymbol{u}_{(n+1)_i} \qquad \forall\, n \tag{2.6}$$

Since the mode shape of the complete structure can be expressed as $\boldsymbol{u}_i = \left[(\boldsymbol{u}_{1_i})^T \; (\boldsymbol{u}_{1_i})^T \; \ldots \; (\boldsymbol{u}_{1_i})^T \right]^T$, it is obvious that rotating the mode shape through any arbitrary number of sectors leaves the mode unchanged. This is a *standing wave* mode shape that is described by a single eigenvalue and eigenvector (Figure 2.4).

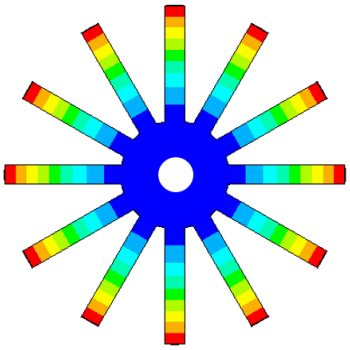

Fig. 2.4 Example of an out-of-plane standing wave mode shape on a dummy disk with 12 blades: all the blades have the same mode shape and vibrate in-phase to each other. The modal displacement shows its minimum at the disk's center (blue zone) and reaches its maximum at the blades' tips (red zone) at a time instant that is the same for all the blades.

(b) Each sector has the same mode shape as its neighbors, but vibrates in anti-phase with them:

$$\boldsymbol{u}_{n_i} = -\boldsymbol{u}_{(n+1)_i} \qquad \forall\, n \tag{2.7}$$

For this second class the mode shape of the whole structure can be written as $\boldsymbol{u}_i = \left[(\boldsymbol{u}_{1_i})^T \; -(\boldsymbol{u}_{1_i})^T \; (\boldsymbol{u}_{1_i})^T \; \ldots \; (\boldsymbol{u}_{1_i})^T \; -(\boldsymbol{u}_{1_i})^T\right]^T$. It can be noted that rotating the mode shape through an even number of sectors leaves the mode unchanged, while the rotation through an odd number of sectors makes the modes equal to $-\boldsymbol{u}_i$. This however does not represents a new mode shape, but just a change in phase of π in the vibration. As in the previous case the mode is standing and a single eigenvector and eigenvalue are necessary for its complete description (Figure 2.5).

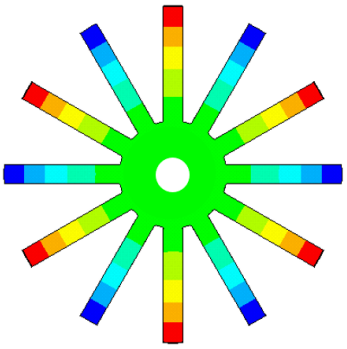

Fig. 2.5 Example of an out-of-plane standing wave mode shape on a dummy disk with 12 blades: all the blades have the same mode shape and vibrate in anti-phase to each other. The mode shape exhibits the alternation in sign of the maximum blades' vibration amplitude, negative for the blue zones and positive for the red ones.

(c) All other possible mode shapes, meaning that:

$$\boldsymbol{u}_{n_i} \neq \boldsymbol{u}_{(n+1)_i} \qquad \boldsymbol{u}_{n_i} \neq -\boldsymbol{u}_{(n+1)_i} \qquad \forall\, n \tag{2.8}$$

These modes occur in orthogonal pairs of standing waves corresponding to the same eigenvalue. Their combination results in a *rotating* mode shape.

The third class of mode shapes requires further considerations. Since all the sectors are identical, when the mode shape $\boldsymbol{u}_i$ is shifted of one sector's angle α_n, a new mode shape $\boldsymbol{u}_i'$ with the same eigenvalue is found. The set of all the possible eigenvectors obtained by subsequent shifts of $\boldsymbol{u}_i$, each one of α_n, is spanned by the following basis:

$$\boldsymbol{U}_i = [\boldsymbol{u}_i \;\; \bar{\boldsymbol{u}}_i] \tag{2.9}$$

where $\bar{\boldsymbol{u}}_i$ is an eigenvector orthogonal to $\boldsymbol{u}_i$ with the same eigenvalue ω_i^2:

$$\boldsymbol{u}_i^T \bar{\boldsymbol{u}}_i = 0 \tag{2.10}$$

The eigenvector $\boldsymbol{u}_i'$ can thus be expressed as a linear combination of $\boldsymbol{u}_i$ and $\bar{\boldsymbol{u}}_i$ as follows:

$$\boldsymbol{u}_i' = c\boldsymbol{u}_i + s\bar{\boldsymbol{u}}_i \qquad c, s \in \mathbb{R} \tag{2.11}$$

Assuming the eigenvectors $\boldsymbol{u}_i$, $\bar{\boldsymbol{u}}_i$ and $\boldsymbol{u}_i'$ normalized so that:

$$\boldsymbol{u}_i^T \boldsymbol{u}_i = 1, \quad \bar{\boldsymbol{u}}_i^T \bar{\boldsymbol{u}}_i = 1, \quad (\boldsymbol{u}_i')^T \boldsymbol{u}_i' = 1 \tag{2.12}$$

it can be demonstrated that c and s can be written respectively as $\cos(\varphi_h)$ and $-\sin(\varphi_h)$, where φ_h would be the generic rotation angle of which the eigenvector $\boldsymbol{u}_i$ should be rotated in order to give $\boldsymbol{u}_i'$. However, since $\boldsymbol{u}_i'$ has been already defined as resulting from one sector's angle rotation of $\boldsymbol{u}_i$, and considering that the application of Eqn. 2.11 N times leaves $\boldsymbol{u}_i$ unchanged, the angle φ_h must take one of the following values:

$$\varphi_h = \pm \frac{2\pi}{N} h \tag{2.13}$$

where h is an integer that measures the periodicity of the mode shape over the structure (Figure 2.6).

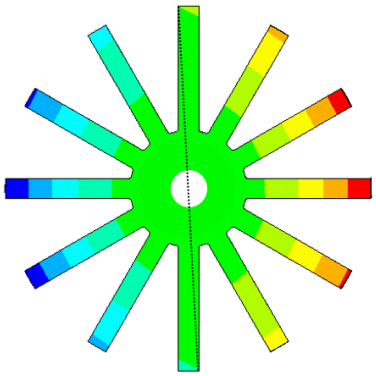

Fig. 2.6 The periodicity of the mode shape over the structure can be expressed in terms of *number of nodal diameters*. This Figure shows a mode shape having $h = 1$ nodal diameter, denoting a nodal line (dashed line) along which the modal quantities are equal to zero.

Similarly, the eigenvector $\bar{\boldsymbol{u}}_i'$ orthogonal to $\boldsymbol{u}_i'$, defined by shifting the eigenvector $\bar{\boldsymbol{u}}_i$ by α_n, can also be expressed as a linear combination of $\boldsymbol{u}_i$ and $\bar{\boldsymbol{u}}_i$:

$$\bar{\boldsymbol{u}}_i' = -s\boldsymbol{u}_i + c\bar{\boldsymbol{u}}_i \qquad c,s \in \mathbb{R} \tag{2.14}$$

The transformation that rotates both $\boldsymbol{u}_i$ and $\boldsymbol{u}_i'$ round one substructure is obtained rewriting the Eqns. 2.11 and 2.14 in matrix form:

$$\begin{Bmatrix} \boldsymbol{u}_i' \\ \bar{\boldsymbol{u}}_i' \end{Bmatrix} = \begin{bmatrix} c\boldsymbol{I}_{Nn_s} & s\boldsymbol{I}_{Nn_s} \\ -s\boldsymbol{I}_{Nn_s} & c\boldsymbol{I}_{Nn_s} \end{bmatrix} \begin{Bmatrix} \boldsymbol{u}_i \\ \bar{\boldsymbol{u}}_i \end{Bmatrix} = \boldsymbol{R} \begin{Bmatrix} \boldsymbol{u}_i \\ \bar{\boldsymbol{u}}_i \end{Bmatrix} \tag{2.15}$$

where $\boldsymbol{I}_{Nn_s}$ is the identity matrix of order Nn_s. The result of Eqn. 2.15 can be finally exploited to the write the mode shape of one sector in terms of mode shape of any other sector as follows:

$$\begin{Bmatrix} \boldsymbol{u}_{(n-1)_i} \\ \bar{\boldsymbol{u}}_{(n-1)_i} \end{Bmatrix} = \begin{bmatrix} c\boldsymbol{I}_{n_s} & s\boldsymbol{I}_{n_s} \\ -s\boldsymbol{I}_{n_s} & c\boldsymbol{I}_{n_s} \end{bmatrix} \begin{Bmatrix} \boldsymbol{u}_{n_i} \\ \bar{\boldsymbol{u}}_{n_i} \end{Bmatrix} \qquad \forall\, n \tag{2.16}$$

where $\boldsymbol{I}_{n_s}$ is the identity matrix of order n_s.

According to Eqns. 2.11 and 2.14, every linear combination of standing modes falling in the class (c) is a new real eigenvector still satisfying the eigenproblem of Eqn. 2.4. However, also the complex vectors $\boldsymbol{z}_i$ and $\bar{\boldsymbol{z}}_i$, defined as:

$$\boldsymbol{z}_i = \boldsymbol{u}_i + \imath\bar{\boldsymbol{u}}_i \qquad \bar{\boldsymbol{z}}_i = \boldsymbol{u}_i - \imath\bar{\boldsymbol{u}}_i \tag{2.17}$$

are valid solution of Eqn. 2.4, being eigenvectors with the same eigenvalue ω_i^2 of $\boldsymbol{u}_i$ and $\bar{\boldsymbol{u}}_i$. The physical meaning of real and complex eigenvectors of a cyclic symmetric structure is strictly related to their time evolution over the structure itself. In particular, it has been already stated that the classes of modes (a) and (b) collect real eigenvectors denoting standing wave mode shapes. The spatial configuration or *operative deflection shape* (ODS) of a standing mode shape $\boldsymbol{u}_i$ at a certain time instant t is given by the real part of the complex quantity $\boldsymbol{u}_i e^{\imath\omega t}$:

$$\Re[\boldsymbol{u}_i e^{\imath\omega t}] = \Re[\boldsymbol{u}_i \cos(\omega t) + \imath \boldsymbol{u}_i \sin(\omega t)] = \boldsymbol{u}_i \cos(\omega t) \tag{2.18}$$

The result of Eqn. 2.18 shows that all the DoFs pulsate without any relative time delay between them. In fact, assuming at $t = 0$ a non null ODS such that $\|\boldsymbol{u}_i\| \neq 0$, at $t = \pi/(2\omega)$ all the DoFs cross the zero value simultaneously (Figure 2.7)

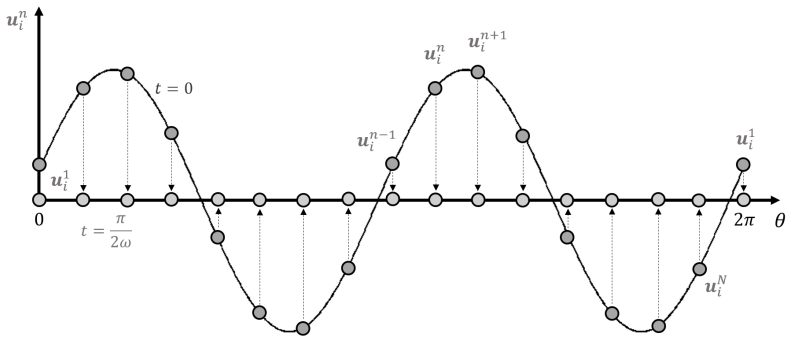

Fig. 2.7 Schematic representation of a standing mode shape of a cyclic symmetric structure: assuming a certain configuration of the mode shape at $t = 0$ such that $\|\boldsymbol{u}_i\| \neq 0$, at $t = \pi/(2\omega)$ the modal displacement of each DoF is equal to zero.

The same does not happen for the complex eigenvector z_i. In this case the instantaneous ODS can be found as the real part of $z_i e^{i\omega t}$:

$$\Re\left[z_i e^{\imath\omega t}\right] = \Re\left[\left(\boldsymbol{u}_i + \imath\bar{\boldsymbol{u}}_i\right)\left[\cos(\omega t) + \imath\sin(\omega t)\right]\right] = \\ = \boldsymbol{u}_i \cos(\omega t) - \bar{\boldsymbol{u}}_i \sin(\omega t) \tag{2.19}$$

By looking at the time evolution of the mode shape it can be noted that at $t = 0$ Eqn. 2.19 gives exactly the ODS $\boldsymbol{u}_i$, while at $t = \varphi_h/\omega$ it gives:

$$\Re\left[z_i e^{\imath\varphi}\right] = \boldsymbol{u}_i \cos(\varphi_h) - \bar{\boldsymbol{u}}_i \sin(\varphi_h) \tag{2.20}$$

which is exactly $\boldsymbol{u}_i'$ (Eqn. 2.11). Therefore, the complex eigenvector $\boldsymbol{z}_i$ describes a rotating vibration mode, where the same instantaneous ODS appears after successive time intervals $t = \varphi_h/\omega$, rotated round an additional substructure each time (Figure 2.8).

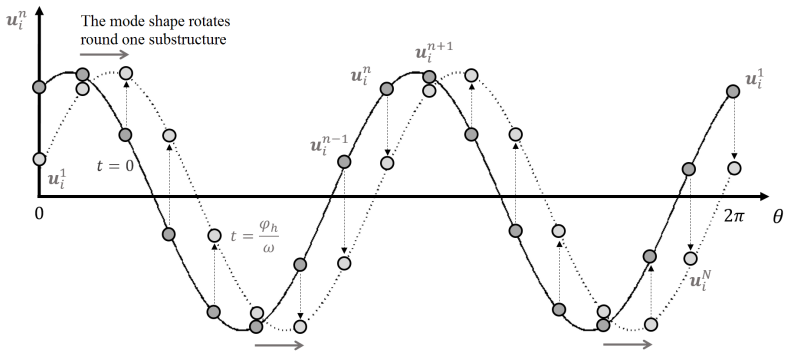

Fig. 2.8 Schematic representation of a rotating mode shape of a cyclic symmetric structure: after successive time intervals $t = \varphi_h/\omega$ the mode shape rotates round an additional sector.

It must be pointed out that $\boldsymbol{z}_i$ contains information of both standing modes $\boldsymbol{u}_i$ and $\bar{\boldsymbol{u}}_i$. According to Eqn. 2.19, the complex eigenvectors $\boldsymbol{z}_i$ appears as rotating since their components are in quadrature in space (Eqn. 2.10) but also in time. If $\boldsymbol{z}_i$ corresponds to a clockwise rotating eigenvector, the complex eigenvector $\bar{\boldsymbol{z}}_i$, orthogonal to $\boldsymbol{z}_i$ ($\bar{\boldsymbol{z}}_i^* \boldsymbol{z}_i = 0$)[1], rotates in a counter-clockwise direction.

The direction characterizing the rotation of a complex mode shape can be better defined by looking at the relationship between the deflections of neighboring substructures. This can be derived by rewriting Eqn. 2.15 in terms of $\boldsymbol{z}_i$:

$$\boldsymbol{z}_i' = \boldsymbol{z}_i e^{\imath \varphi_h} \tag{2.21}$$

and isolating the DoFs of the generic n^{th} substructure the following relationship can be found:

$$\boldsymbol{z}_{(n-1)_i} = \boldsymbol{z}_{n_i} e^{\imath \varphi_h} \tag{2.22}$$

It can be easily proved that Eqn. 2.22 corresponds to Eqn. 2.16 if the real and imaginary part are written separately. Eqn. 2.22 is of practical importance for a complete understanding of cyclic symmetric structures dynamics: the angle φ_h already introduced in Eqn. 2.13 will be hereafter identified as *Inter-Sector Phase Angle*[2] (ISPA)

[1] The * superscript stands for conjugate transpose.

[2] In the case of bladed disks φ_h is called *Inter-Blade Phase Angle* (IBPA).

and represent the phase lag between adjacent vibrating sectors. Conventionally, if a clockwise increasing number of sectors is adopted (Figure 2.1), negative values of φ_h refer to clockwise propagating waves over the structure, since the $(n-1)^{th}$ sector vibrates with a phase lag of φ_h with respect the n^{th}. Conversely, positive values of φ_h are associated to counter-clockwise rotations.

Eqn. 2.22 has been deducted for the mode shape of the class (c), but can be easily extended for those of the classes (a) and (b). In fact, since the mode shapes belonging to those classes do not have their orthogonal counterparts, z_i coincides to $\boldsymbol{u}_i$ and Eqn. 2.22 becomes:

$$\boldsymbol{u}_{(n-1)_i} = \boldsymbol{u}_{n_i} e^{\imath \varphi_h} \tag{2.23}$$

Regardless of the class, the instantaneous ODS of a mode shape is always modulated by harmonic functions like $\cos(h\theta)$ and $\sin(h\theta)$. The angle θ identifies the circumferential coordinate over the cyclic symmetric structure, while h gives information about the periodicity of the mode. From a physical point of view h represents the *number of nodal diameters* of a mode shape, i.e. the number of nodal lines crossing the center of the structure along which the modal quantities (displacements, strains, stresses, ect.) are equal to zero (Figure 2.9).

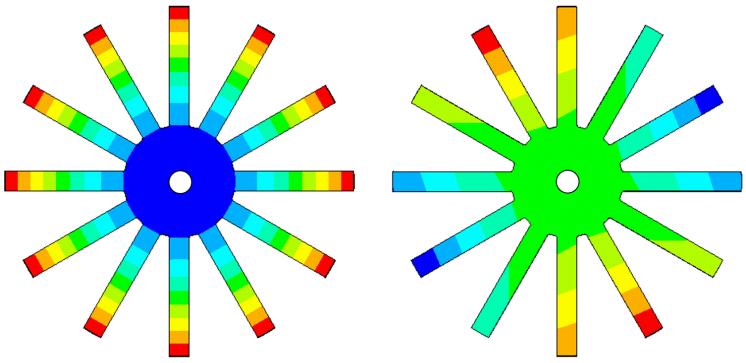

Fig. 2.9 Nodal diameters of a cyclic symmetric structure: a) Mode shape with $h = 0$ nodal diameters, b) Mode shape with $h = 2$ nodal diameters.

Although h has been simply introduced as an "integer", the set of its possible values depends on the number of sectors N. In fact, not all the possible modes with a cosine or sine shape can be correctly represented by a finite number of sectors. In particular, for structure with N equally spaced sectors h can assume integer values such that

$0 \leq h \leq \tilde{h}$, where $\tilde{h}$ is defined as:

$$\tilde{h} = \begin{cases} \dfrac{N}{2} & \text{if } N \text{ is even} \\ \\ \dfrac{N-1}{2} & \text{if } N \text{ is odd} \end{cases} \tag{2.24}$$

Once the number of nodal diameter h is given, the ISPA φ_h between sectors can be found according to Eqn. 2.13. The definitions given about the three classes of modes at the beginning of this section can be completed by associating them the corresponding values of h and φ_h:

- The mode shapes of the class (a) exist for every possible cyclic symmetric structure. These have all the sectors vibrating in-phase to each other, which leads to have $\varphi_h = 0$ in Eqn. 2.23 and then real eigenvectors ($e^{\imath\varphi_h} = 1$). The modes falling in this class are characterized by a number of nodal diameters $h = 0$ (Eqn. 2.13).

- The mode shape of the second class are those for which adjacent sectors vibrate in anti-phase to each other ($\varphi_h = \pm\pi$). This condition is clearly possible if and only if the number of sectors N is even. In that case the number of nodal diameters h corresponding to $\varphi_h = \pm\pi$ is necessary $\tilde{h} = N/2$. Furthermore the quantity $e^{\imath\varphi_h}$ is in this case equal to -1, which ensure again real eigenvectors (Eqn. 2.13). The class (b) of mode shapes does not exist if N is odd.

- The modes of the third and last class are those such that $0 < h < \tilde{h}$ if N is even, or $0 < h \leq \tilde{h}$ if N is odd.

Finally, although h is always a positive integer, the values assumed by φ_h for all the classes of modes together are:

$$\varphi_h \in \left[-\pi, -\frac{2\pi(\frac{N}{2}-1)}{N}, \ldots, -\frac{4\pi}{N}, -\frac{2\pi}{N}, 0, \frac{2\pi}{N}, \frac{4\pi}{N}, \ldots, \frac{2\pi(\frac{N}{2}-1)}{N}, \pi\right]$$

if N is even, and:

$$\varphi_h \in \left[-\frac{2\pi(N-1)}{2N}, \ldots, -\frac{4\pi}{N}, -\frac{2\pi}{N}, 0, \frac{2\pi}{N}, \frac{4\pi}{N}, \ldots, \frac{2\pi(N-1)}{2N}, \pi\right]$$

if N is odd.

2.2 Modal Analysis of Cyclic Symmetric Structures

In the previous section the mode shapes of a cyclic symmetric structure have been classified and the kinematic relationship between the vibrating sectors has been found. This section presents three different mathematical approaches used to efficiently perform the *modal analysis* of a cyclic symmetric structure for a prescribed value of the ISPA.

2.2.1 Thomas' Approach

The kinematic relationship expressed by Eqn. 2.22 is also valid when applied to the physical DoFs of adjacent sectors. In particular, if the mode shape corresponding to φ_h is searched, the following coordinate transformation holds:

$$\begin{Bmatrix} \boldsymbol{x}_1 \\ \boldsymbol{x}_2 \\ \vdots \\ \boldsymbol{x}_N \end{Bmatrix} = \begin{bmatrix} \boldsymbol{I}_{n_s} \\ \boldsymbol{I}_{n_s} e^{i\varphi_h} \\ \vdots \\ \boldsymbol{I}_{n_s} e^{i(N-1)\varphi_h} \end{bmatrix} \boldsymbol{x}_1^h = \boldsymbol{T}_T^h \boldsymbol{x}_1^h \tag{2.25}$$

where $\boldsymbol{T}_T^h$ is the Thomas' transformation matrix and $\boldsymbol{x}_1^h$ is the reduced vector of physical DoFs for the coordinates transformation involving the harmonic index h. Eqn. 2.25 results from the recursive application of Eqn. 2.22, where the DoFs of the generic n^{th} sector are expressed in terms of those of the first one. By applying the former transformation to Eqn. 2.1, a reduced set of EQM is obtained:

$$\boldsymbol{M}_T^h \ddot{\boldsymbol{x}}_1^h + \boldsymbol{K}_T^h \boldsymbol{x}_1^h = \boldsymbol{f}_T^h; \tag{2.26}$$

where

$$\boldsymbol{M}_T^h = (\boldsymbol{T}_T^h)^* \boldsymbol{M} \boldsymbol{T}_T^h \in \mathbb{R}^{n_s \times n_s} \qquad \boldsymbol{K}_T^h = (\boldsymbol{T}_T^h)^* \boldsymbol{K} \boldsymbol{T}_T^h \in \mathbb{C}^{n_s \times n_s}$$
$$\boldsymbol{f}_T^h = (\boldsymbol{T}_T^h)^* \boldsymbol{f} \in \mathbb{C}^{n_s \times 1} \tag{2.27}$$

are the reduced mass and stiffness matrices and the reduced vector of external forces. The dynamic behavior of the cyclic symmetric structure for a certain φ_h can thus be evaluated by solving the following reduced eigenproblem:

$$\left(\boldsymbol{K}_T^h - \omega_i^2 \boldsymbol{M}_T^h\right) \boldsymbol{z}_1^h = \boldsymbol{0} \tag{2.28}$$

whose solution gives the *cyclic eigenvector* $\boldsymbol{z}_1^h$, i.e. the modal displacement of the 1^{st} sector, and the corresponding eigenfrequencies ω_i. Despite the complexity of $\boldsymbol{K}_T^h$ the eigenvalues ω_i^2 are real, while the eigenvectors $\boldsymbol{z}_1^h$ are complex in general. Therefore, the j^{th} component of $\boldsymbol{z}_1^h$ can be expressed as:

$$z_{1_j}^h = Z_{1_j} e^{\iota \phi_j} \qquad \forall\ j = 1, \ldots, n_s \tag{2.29}$$

where $Z_{1_j}^h$ and ϕ_j can be physically interpreted as the amplitude and phase of the h^{th} order harmonic function that modulates the mode shape over the cyclic symmetric structure (Figure 2.10).

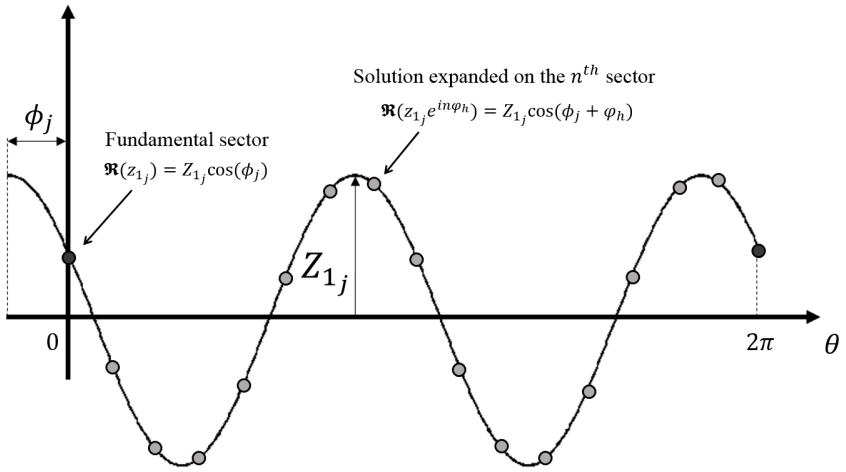

Fig. 2.10 Harmonic function modulating the mode shape over the cyclic symmetric structure.

The solution obtained for the 1^{st} sector can be finally expanded on the other sectors by using the Thomas' transformation matrix defined in Eqn. 2.25.

2.2.2 Mead's Approach

The same results can be obtained by setting the modal analysis from the mass and stiffness matrices $\boldsymbol{M}_s$ and $\boldsymbol{K}_s$ of the generic isolated sector. As well described by D. J. Mead [13, 14], the vector $\boldsymbol{x}_s$ of the sector's DoFs can be partitioned as:

$$\boldsymbol{x}_s = \begin{Bmatrix} \boldsymbol{x}_l \\ \boldsymbol{x}_i \\ \boldsymbol{x}_r \end{Bmatrix} \tag{2.30}$$

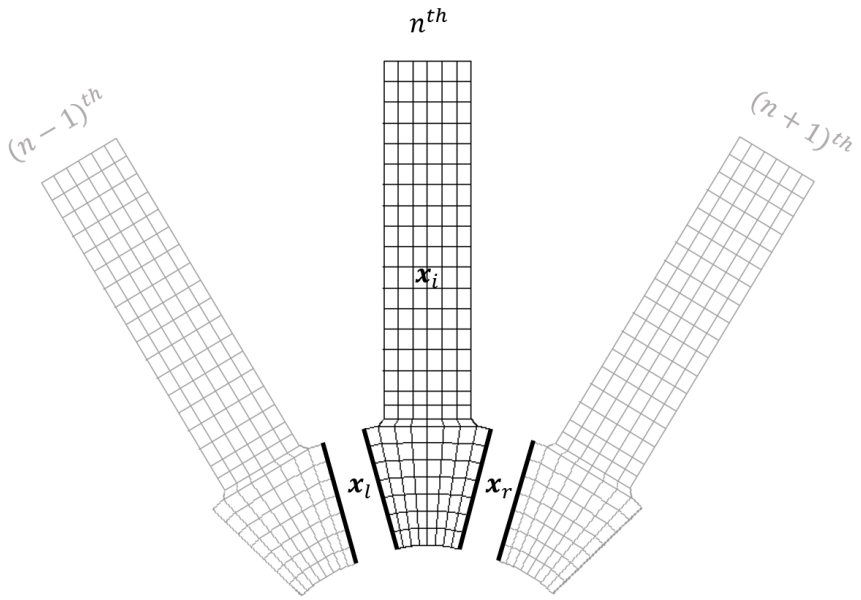

Fig. 2.11 DoFs partitions for the n^{th} fundamental sector.

where:

- $\boldsymbol{x}_l$ are the DoFs at the *left* frontier of the fundamental sector, i.e. those at the boundary with the $(n-1)^{th}$ sector (Figure 2.10). The number of DoFs in $\boldsymbol{x}_l$ is denoted by n_l.
- $\boldsymbol{x}_i$ are the *internal* DoFs of the fundamental sector, i.e. those not shared with the neighboring sectors. The number of DoFs in $\boldsymbol{x}_i$ is denoted by n_i.
- $\boldsymbol{x}_r$ are the DoFs at the *right* frontier of the fundamental sector, i.e. those at the boundary with the $(n+1)^{th}$ sector (Figure 2.10). The number of DoFs in $\boldsymbol{x}_r$ is denoted by n_r.

Note that the number of DoFs at the left and right frontier is the same ($n_l = n_r$). Moreover, if the whole cyclic symmetric structure is taken as reference, the number of DoFs per sector n_s is equal to $n_l + n_i$ ($n_i + n_r$), since the DoFs at the right (left) frontier of one sector shall be considered as belonging to the left (right) frontier of the following (previous) sector. The Mead's approach starts from the model of an isolated sector consisting of $n_l + n_i + n_r$ DoFs, leading to a reduced model with $n_l + n_i$ DoFs.

According to Eqn. 2.30 it is possible to coherently partition the vector of external force, the mass and the stiffness matrices of the isolated sector:

$$\boldsymbol{M}_s = \begin{bmatrix} \boldsymbol{M}_{ll} & \boldsymbol{M}_{li} & \boldsymbol{M}_{lr} \\ \boldsymbol{M}_{il} & \boldsymbol{M}_{ii} & \boldsymbol{M}_{ir} \\ \boldsymbol{M}_{rl} & \boldsymbol{M}_{ri} & \boldsymbol{M}_{rr} \end{bmatrix} \qquad \boldsymbol{K}_s = \begin{bmatrix} \boldsymbol{K}_{ll} & \boldsymbol{K}_{li} & \boldsymbol{K}_{lr} \\ \boldsymbol{K}_{il} & \boldsymbol{K}_{ii} & \boldsymbol{K}_{ir} \\ \boldsymbol{K}_{rl} & \boldsymbol{K}_{ri} & \boldsymbol{K}_{rr} \end{bmatrix}$$

$$\boldsymbol{f}_s = \begin{Bmatrix} \boldsymbol{f}_l \\ \boldsymbol{f}_i \\ \boldsymbol{f}_r \end{Bmatrix} \tag{2.31}$$

By expressing right frontier DoFs in terms of left's one (Eqn. 2.22), $\boldsymbol{x}_s$ can be reduced as:

$$\boldsymbol{x}_s = \begin{Bmatrix} \boldsymbol{x}_l \\ \boldsymbol{x}_i \\ \boldsymbol{x}_r \end{Bmatrix} = \begin{bmatrix} \boldsymbol{I} & \boldsymbol{0} \\ \boldsymbol{0} & \boldsymbol{I} \\ \boldsymbol{I}e^{\iota\varphi_h} & \boldsymbol{0} \end{bmatrix} \begin{Bmatrix} \boldsymbol{x}_l^h \\ \boldsymbol{x}_i^h \end{Bmatrix} = \boldsymbol{T}_M^h \begin{Bmatrix} \boldsymbol{x}_l^h \\ \boldsymbol{x}_i^h \end{Bmatrix} \tag{2.32}$$

where $\boldsymbol{T}_M^h$ is the Mead's transformation matrix and $\left\{(\boldsymbol{x}_l^h)^T \ (\boldsymbol{x}_i^h)^T\right\}^T$ is the reduced vector of DoFs for the coordinate transformation involving the harmonic index h. When transformation of Eqn. 2.32 is applied to the mass and stiffness matrices $\boldsymbol{M}_s$ and $\boldsymbol{K}_s$, the new eigenproblem corresponding to φ_h is found:

$$\left(\boldsymbol{K}_M^h - \omega_i^2 \boldsymbol{M}_M^h\right) \boldsymbol{z}_i^h = \boldsymbol{0} \tag{2.33}$$

where:

$$\boldsymbol{M}_M^h = (\boldsymbol{T}_T^h)^* \boldsymbol{M}_s \boldsymbol{T}_T^h =$$

$$= \begin{bmatrix} \boldsymbol{M}_{ll} + \boldsymbol{M}_{rr} + \boldsymbol{M}_{lr}e^{i\varphi_h} + \boldsymbol{M}_{rl}e^{-i\varphi_h} & \boldsymbol{M}_{li} + \boldsymbol{M}_{ri}e^{-i\varphi_h} \\ \boldsymbol{M}_{il} + \boldsymbol{M}_{ir}e^{i\varphi_h} & \boldsymbol{M}_{ii} \end{bmatrix} =$$

$$= \begin{bmatrix} \boldsymbol{M}_{ll} + \boldsymbol{M}_{rr} & \boldsymbol{0} \\ \boldsymbol{0} & \boldsymbol{M}_{ii} \end{bmatrix} \in \mathbb{R}^{(n_l+n_i+n_r)\times(n_l+n_i)} \tag{2.34}$$

is a real matrix since the blocks of $\boldsymbol{M}_s$ out of the main diagonal are zero matrices, while the matrix $\boldsymbol{K}_M^h$ is defined as:

$$\boldsymbol{K}_M^h = (\boldsymbol{T}_T^h)^* \boldsymbol{K}_s \boldsymbol{T}_T^h =$$

$$= \begin{bmatrix} \boldsymbol{K}_{ll} + \boldsymbol{K}_{rr} + \boldsymbol{K}_{lr}e^{i\varphi_h} + \boldsymbol{K}_{rl}e^{-i\varphi_h} & \boldsymbol{K}_{li} + \boldsymbol{K}_{ri}e^{-i\varphi_h} \\ \boldsymbol{K}_{il} + \boldsymbol{K}_{ir}e^{i\varphi_h} & \boldsymbol{K}_{ii} \end{bmatrix} =$$

$$= \begin{bmatrix} \boldsymbol{K}_{ll} + \boldsymbol{K}_{rr} & \boldsymbol{K}_{li} + \boldsymbol{K}_{ri} e^{-i\varphi_h} \\ \boldsymbol{K}_{il} + \boldsymbol{K}_{ir} e^{i\varphi_h} & \boldsymbol{K}_{ii} \end{bmatrix} \in \mathbb{C}^{(n_l+n_i+n_r)\times(n_l+n_i)} \tag{2.35}$$

The main effect of the reduction is that the number of equations has been decreased from $(n_l + n_i + n_r)$ to n_s. The importance of this approach is quite evident: *by varying the value of φ_h it is possible to evaluate the dynamic behavior of the whole structure starting from the matrices of isolated sectors.*

Although the eigenproblems of Eqns. 2.28 and 2.33 have the same dimension, the size of the mass and stiffness matrices required by the Thomas and Mead's approach at the beginning of the corresponding reduction process is different. In the first case the matrices of the whole cyclic symmetric structure have to be apriori set up and then reduced by employing the transformation matrix of Eqn. 2.25. Differently, the Mead's transformation (Eqn. 2.32) is less costly from a computational point of view, since it just operates on the sector's matrices.

All the considerations carried out for the cyclic eigenvector obtained by the Thomas' approach still remain valid for the eigenvectors of Eqn. 2.33.

2.2.3 Fourier Matrix's Approach

Another possible formulation used for the analysis cyclic symmetric structures was proposed by Óttarson [15, 12]. In his work the properties of the mass and stiffness matrices of cyclic symmetric structures were exploited in order to isolate the dynamic behavior of the system for a certain φ_h.

As already introduced in section 2.1 the mass and stiffness matrices of any linear cyclic symmetric system have a block-circulant symmetric form (Eqn. 2.3). The general form of a square block-circulant matrix is:

$$\boldsymbol{C} = \mathrm{Bcirc}\Big(\boldsymbol{C}_1, \boldsymbol{C}_2, \ldots, \boldsymbol{C}_N\Big) = \begin{bmatrix} \boldsymbol{C}_1 & \boldsymbol{C}_2 & \boldsymbol{C}_3 & \ldots & \boldsymbol{C}_{N\text{-}1} & \boldsymbol{C}_N \\ \boldsymbol{C}_N & \boldsymbol{C}_1 & \boldsymbol{C}_2 & \ldots & \boldsymbol{C}_{N\text{-}2} & \boldsymbol{C}_{N\text{-}1} \\ \vdots & \vdots & \vdots & \ddots & \vdots & \vdots \\ \boldsymbol{C}_3 & \boldsymbol{C}_4 & \boldsymbol{C}_5 & \ldots & \boldsymbol{C}_1 & \boldsymbol{C}_2 \\ \boldsymbol{C}_2 & \boldsymbol{C}_3 & \boldsymbol{C}_4 & \ldots & \boldsymbol{C}_N & \boldsymbol{C}_1 \end{bmatrix} \tag{2.36}$$

All circulant matrices of order N share the same set of eigenvectors that are arranged as the columns of the *Fourier matrix* $\boldsymbol{E}$:

$$\boldsymbol{E} = \begin{bmatrix} 1 & 1 & 1 & \cdots & 1 \\ 1 & e^{\imath\frac{2\pi}{N}} & e^{\imath 2\frac{2\pi}{N}} & \cdots & e^{\imath(N-1)\frac{2\pi}{N}} \\ 1 & e^{\imath 2\frac{2\pi}{N}} & e^{\imath 4\frac{2\pi}{N}} & \cdots & e^{\imath 2(N-1)\frac{2\pi}{N}} \\ \vdots & \vdots & \vdots & \ddots & \vdots \\ 1 & e^{\imath(N-1)\frac{2\pi}{N}} & e^{\imath 2(N-1)\frac{2\pi}{N}} & \cdots & e^{\imath(N-1)(N-1)\frac{2\pi}{N}} \end{bmatrix} \tag{2.37}$$

which in compact form becomes:

$$\boldsymbol{E} = e_{sh} = e^{\imath\frac{2\pi}{N}(h-1)(s-1)} \qquad s,h = 1,\ldots,N$$

$\boldsymbol{E}$ is a symmetric matrix ($\boldsymbol{E} = \boldsymbol{E}^T$), it is not Hermitian ($\boldsymbol{E} \neq \boldsymbol{E}^*$) and its main diagonal is not real. Starting from $\boldsymbol{E}$, the *unitary Fourier matrix* $\boldsymbol{E}_u$ can be defined as:

$$\boldsymbol{E}_u = \frac{1}{\sqrt{N}}\boldsymbol{E} \tag{2.38}$$

which the following property holds:

$$\boldsymbol{E}_u^*\boldsymbol{E}_u = \left(\frac{1}{\sqrt{N}}\boldsymbol{E}^*\right)\left(\frac{1}{\sqrt{N}}\boldsymbol{E}\right) = \boldsymbol{I} \tag{2.39}$$

According to the definition of Fourier matrix, $\boldsymbol{E}_u$ diagonalizes any block-circulant matrix $\boldsymbol{C}$:

$$\left(\boldsymbol{E}_u^* \otimes \boldsymbol{I}_{n_s}\right)\cdot\boldsymbol{C}\cdot\left(\boldsymbol{E}_u \otimes \boldsymbol{I}_{n_s}\right) = \mathrm{Bdiag}\left(\tilde{\boldsymbol{C}}_1, \tilde{\boldsymbol{C}}_2, \ldots, \tilde{\boldsymbol{C}}_N\right), \tag{2.40}$$

where $\otimes$ denotes the Kronecher product.

The Fourier matrix arises from the numerical calculation of the *inverse Fast Fourier Transform* (iFFT) [16]. In particular, the relationship between the generic discrete signal $\boldsymbol{g}$ and the complex set of Fourier coefficients $\boldsymbol{f}$ denoting the importance of the its harmonic components is:

$$\boldsymbol{g} = \boldsymbol{E}_u\boldsymbol{f} \qquad \boldsymbol{g} \in \mathbb{R}^{N\times 1}, \quad \boldsymbol{f} \in \mathbb{C}^{N\times 1} \tag{2.41}$$

Similarly, the generic physical configuration $\boldsymbol{x}$ of a cyclic symmetric structure results from the weighted sum of its harmonic mode shapes. In particular, adopting the DoFs partition of Eqn. 2.3, $\boldsymbol{x}$ can be written as:

$$\boldsymbol{x} = \begin{Bmatrix} \boldsymbol{x}_1 \\ \boldsymbol{x}_2 \\ \boldsymbol{x}_3 \\ \vdots \\ \boldsymbol{x}_{N\text{-}1} \\ \boldsymbol{x}_N \end{Bmatrix} = \left(\boldsymbol{E}_u \otimes \boldsymbol{I}_{n_s}\right) \begin{Bmatrix} \boldsymbol{c}_0 \\ \boldsymbol{c}_1 \\ \boldsymbol{c}_2 \\ \vdots \\ \boldsymbol{c}_2^* \\ \boldsymbol{c}_1^* \end{Bmatrix} \tag{2.42}$$

where $\boldsymbol{c}_h$ and $\boldsymbol{c}_h^*$ $(0 \leq h \leq \tilde{h})$ are the h^{th} order complex and conjugate Fourier coefficients. For cyclic symmetric structure the columns of $\boldsymbol{E}_u$ assume an important physical meaning: they are the eigenvectors of the classes (a), (b) and (c) described in section 2.1. In fact, the modal matrix resulting from the eigenproblem Eqn. 2.3 diagonalizes the block-circulant matrix $\boldsymbol{M}$ and $\boldsymbol{K}$ exactly as $\boldsymbol{E}_u$ does. The real columns of $\boldsymbol{E}_u$ corresponds to the eigenvectors of the class (a) and (b), while the complex ones are those of the class (c).

The complex coefficients $\boldsymbol{c}_n$ can be turned into real quantities if the *real valued Fourier matrix* is used instead of $\boldsymbol{E}_u$. For N cyclic symmetric components the real valued Fourier matrix is defined as [12]:

$$\boldsymbol{F}_{NN} = f_{sh} = \begin{cases} \dfrac{1}{\sqrt{N}} & \text{if } h = 1 \\ \sqrt{\dfrac{2}{N}} \cos\left[\dfrac{2\pi(h-1)(s-1)}{N}\right] & \text{if } 1 < h < \dfrac{N+2}{2} \\ \dfrac{(-1)^{s-1}}{\sqrt{N}} & \text{if } h = \dfrac{N+2}{2} \\ \sqrt{\dfrac{2}{N}} \sin\left[\dfrac{2\pi(h-1)(s-1)}{N}\right] & \text{if } \dfrac{N+2}{2} < h \leq N \end{cases} \tag{2.43}$$

which is an orthogonal matrix, i.e. $\boldsymbol{F}_{N,N}^T \boldsymbol{F}_{N,N} = \boldsymbol{I}_N$. The coordinate transformation expressed by Eqn. 2.42 can thus be rewritten employing $\boldsymbol{F}_{N,N}$:

$$\boldsymbol{x} = \Big(\boldsymbol{F}_{N,N} \otimes \boldsymbol{I}_N\Big)\boldsymbol{a} \tag{2.44}$$

where

$$\boldsymbol{a} = \left[\boldsymbol{a}_0^T \; (\boldsymbol{a}_1^c)^T \; \ldots \; (\boldsymbol{a}_{\tilde{h}-1}^c)^T \; \boldsymbol{a}_{\tilde{h}}^T \; (\boldsymbol{a}_{\tilde{h}-1}^s)^T \; \ldots \; (\boldsymbol{a}_1^s)^T\right]^T \tag{2.45}$$

denotes the vector of real Fourier coefficients with superscript c and s identifying the cosine and sine components respectively. When the coordinate transformation of Eqn. 2.45 is applied to the matrices of Eqn. 2.4, the following block-diagonal eigenproblem is obtained:

$$\begin{bmatrix} \tilde{\boldsymbol{K}}_0 & \boldsymbol{0} & \boldsymbol{0} & \ldots & \boldsymbol{0} & \boldsymbol{0} \\ \boldsymbol{0} & \tilde{\boldsymbol{K}}_1^c & \boldsymbol{0} & \ldots & \boldsymbol{0} & \boldsymbol{0} \\ \boldsymbol{0} & \boldsymbol{0} & \tilde{\boldsymbol{K}}_2^c & \ldots & \boldsymbol{0} & \boldsymbol{0} \\ \vdots & \vdots & \vdots & \ddots & \vdots & \vdots \\ \boldsymbol{0} & \boldsymbol{0} & \boldsymbol{0} & \ldots & \tilde{\boldsymbol{K}}_2^s & \boldsymbol{0} \\ \boldsymbol{0} & \boldsymbol{0} & \boldsymbol{0} & \ldots & \boldsymbol{0} & \tilde{\boldsymbol{K}}_1^s \end{bmatrix} \begin{Bmatrix} \boldsymbol{a}_0 \\ \boldsymbol{a}_1^c \\ \boldsymbol{a}_2^c \\ \vdots \\ \boldsymbol{a}_2^s \\ \boldsymbol{a}_1^s \end{Bmatrix} =$$

$$= \omega_i^2 \begin{bmatrix} \tilde{\boldsymbol{M}}_0 & \boldsymbol{0} & \boldsymbol{0} & \ldots & \boldsymbol{0} & \boldsymbol{0} \\ \boldsymbol{0} & \tilde{\boldsymbol{M}}_1^c & \boldsymbol{0} & \ldots & \boldsymbol{0} & \boldsymbol{0} \\ \boldsymbol{0} & \boldsymbol{0} & \tilde{\boldsymbol{M}}_2^c & \ldots & \boldsymbol{0} & \boldsymbol{0} \\ \vdots & \vdots & \vdots & \ddots & \vdots & \vdots \\ \boldsymbol{0} & \boldsymbol{0} & \boldsymbol{0} & \ldots & \tilde{\boldsymbol{M}}_2^s & \boldsymbol{0} \\ \boldsymbol{0} & \boldsymbol{0} & \boldsymbol{0} & \ldots & \boldsymbol{0} & \tilde{\boldsymbol{M}}_1^s \end{bmatrix} \begin{Bmatrix} \boldsymbol{a}_0 \\ \boldsymbol{a}_1^c \\ \boldsymbol{a}_2^c \\ \vdots \\ \boldsymbol{a}_2^s \\ \boldsymbol{a}_1^s \end{Bmatrix} = \boldsymbol{0} \tag{2.46}$$

In this way the modal analysis of a cyclic symmetric structure can be performed for each harmonic component separately. For instance, the sine mode shapes corresponding to the harmonic index 2 (i.e. the imaginary part of the mode shapes with $h = 2$ nodal diameters) can be found by solving the reduced eigenproblem:

$$\Big(\tilde{\boldsymbol{K}}_2^s - \omega_i^2 \tilde{\boldsymbol{M}}_2^s\Big)\boldsymbol{a}_2^s = \boldsymbol{0} \tag{2.47}$$

which effectively reduces the size of the problem to that of only one sector.

When the modal analysis is performed after having performed the coordinate transformation of Eqn. 2.42, the mode shapes are found in terms of complex harmonic coordinates for each harmonic index h. The corresponding pair of counter-rotating physical mode shape expanded over the entire structure can be generated by using the Kronecker product:

$$z_h = \boldsymbol{e}_h \otimes \boldsymbol{c}_h, \qquad z_h^* = \boldsymbol{e}_h^* \otimes \boldsymbol{c}_h^* \tag{2.48}$$

where $\boldsymbol{e}_h$ is the h^{th} column of the unitary Fourier matrix $\mathbf{E}_u$. Being $\boldsymbol{e}_h$ complex, it can be written in terms of its real and imaginary components. This, applied to Eqns. 2.48 yields:

$$\begin{aligned} z_h, z_h^* = [\Re(\boldsymbol{e}_h) \otimes \Re(\boldsymbol{c}_h) - \Im(\boldsymbol{e}_h) \otimes \Im(\boldsymbol{c}_h)] \pm \\ \pm i[\Im(\boldsymbol{e}_h) \otimes \Re(\boldsymbol{c}_h) + \Re(\boldsymbol{e}_h) \otimes \Im(\boldsymbol{c}_h)] \end{aligned} \tag{2.49}$$

which can be also expressed by resorting to the columns of the real valued Fourier matrix $\boldsymbol{F}$:

$$\begin{aligned} z_h, z_h^* = \frac{1}{\sqrt{2}}[\boldsymbol{f}_h^c \otimes \Re(\boldsymbol{c}_h) - \boldsymbol{f}_h^s \otimes \Im(\boldsymbol{c}_h)] \pm \\ \pm i\frac{1}{\sqrt{2}}[\boldsymbol{f}_h^s \otimes \Re(\boldsymbol{c}_h) + \boldsymbol{f}_h^c \otimes \Im(\boldsymbol{c}_h)] \end{aligned} \tag{2.50}$$

where $\boldsymbol{f}_h^c$ and $\boldsymbol{f}_h^s$ denote the h^{th} harmonic cosine and sine vector columns of $\boldsymbol{F}$.

2.3 Extra Harmonics

The mode shapes introduced in the previous sections were described by looking at the structure as composed by a discrete number of identical sectors. According to this point of view, the mode shapes discretization by N homologous locations[3] would lead to see them exactly as they were classified in section 2.1 (Figure 2.12).

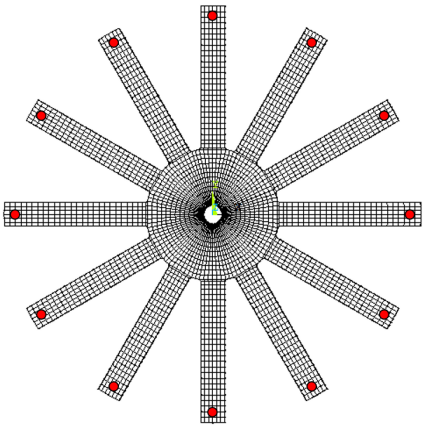

Fig. 2.12 Homologous locations on a cyclic symmetric structure's FE model: the red circles at the same radial coordinate are equally spaced along the circumferential direction.

For example, the discretization of the mode shape having $h = 1$ nodal diameters by N homologous locations results, as expected, in a sinusoidal wave like $\cos(\theta)$ or $\sin(\theta)$. This happens because the N equally spaced nodes are able to correctly discretize the mode's kinematic for $0 \leq h \leq \tilde{h}$ avoiding the *aliasing phenomenon*.

Consider now as a cyclic symmetric structure a simple blisk (Figure 2.13). By "observing" its modes over a circumference where the continuity of the geometry is guaranteed, not only the $\cos(h\theta)$ or $\sin(h\theta)$ shapes can be detected. Small wavelength spatial harmonics can also be visible. These are referred to as *extra harmonics* and were described for the first time in a recent paper concerning a reduced order model technique for multi-stage bladed disks [6].

The extra harmonic existence can be empirically proved by analyzing the eigenvectors resulting from the FE modal analysis of the blisk. It is required that the fundamental sector's mesh is realized so that at least one arc of n_{arc} equally spaced

[3] If a cylindrical coordinate system with the z-axis coincident to that of the cyclic symmetric structure is considered, the homologous locations are those having the same ρ and z coordinates with an angular distance between them equal to the sector's angle α_n.

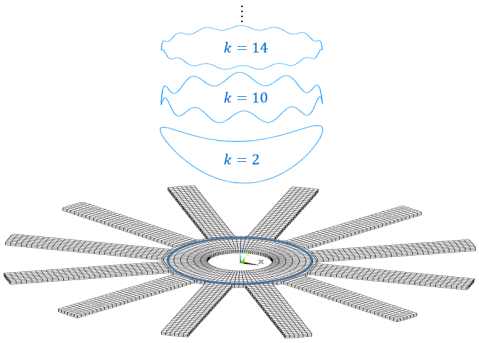

Fig. 2.13 Mode shape with $h = 2$ nodal diameters. The mode shape at the blue circumference can be decomposed into a series of harmonics featuring increasing order.

nodes can be identified (Figure 2.14). By repeating the FE model of the fundamental sector N times until a closed structure is obtained, the arc is expanded giving a discrete circumference with $n_c = N(n_{arc} - 1)$ nodes .

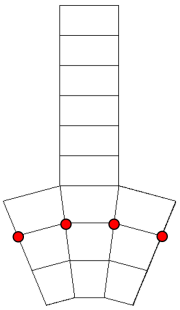

Fig. 2.14 Arc of n_{arc} equally spaced nodes on the fundamental sector's FE model.

Although the relationship between the modal quantities of adjacent sectors has been derived (Eqn. 2.22), no information are available on the shape of the modes within a sector. In general, the modal quantities' trend along the previously defined circumference cannot be described only by a pure $\cos(h\theta)$ or $\sin(h\theta)$, although these functions still remain dominant over the global structure dynamics. Given these considerations, the harmonic content of a mode shape can be calculated by performing the Fourier transform of a certain modal quantity along the previously defined circumference of nodes (e.g. the modal displacement in one direction). Being this sampled at the n_c finite locations, the generic mode shape can thus show at most a number of spatial harmonics equal to $n_c/2$. In particular, for a mode shape of order h, it can be verified that the complete set harmonics indexes k denoting the non-null harmonics along the

circumference is given by:

$$k = z \cdot N \pm h \qquad z = 0, \ldots, \left(\frac{n_c}{2} + \tilde{h}\right)\frac{1}{N} \tag{2.51}$$

The *extra harmonics* are those corresponding to the set of harmonic indexes $k \neq h$. For example, if a blisk with $N = 12$ sectors is considered, the complete set of harmonics detectable when a mode shape of order $h = 2$ occurs is:

$$\begin{cases} k = 0 \cdot 12 \pm 2 & \rightarrow \quad k^- = \cancel{-2}, \; k^+ = 2 \\ k = 1 \cdot 12 \pm 2 & \rightarrow \quad k^- = 11, \; k^+ = 13 \\ k = 2 \cdot 12 \pm 2 & \rightarrow \quad k^- = 23, \; k^+ = 25 \\ \vdots & \\ k = n_s \cdot 12 \pm 2 & \end{cases} \tag{2.52}$$

Negative harmonic indexes are neglected since they do not have physical meaning.

Different order harmonics do not have the same importance. For cyclic symmetric structures exhibiting a well-defined cyclic symmetry the amplitude of the dominant harmonic is larger than the extra ones. In general it is found that the larger the harmonic index k, the smaller the extra harmonic amplitude (Figure 2.15).

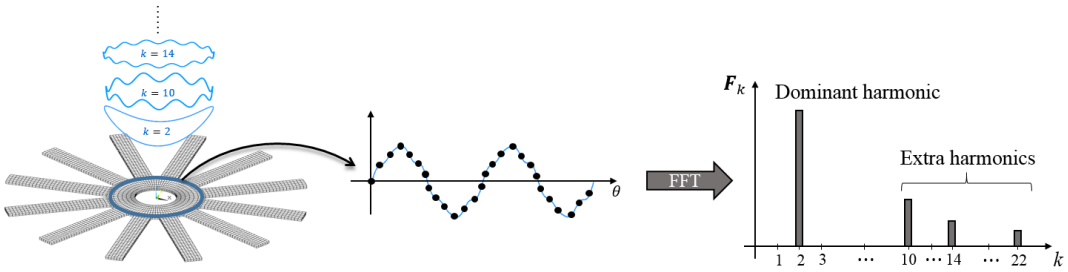

Fig. 2.15 Fourier transform of a mode shape detected along region denoted by the blue circumference. The mode shape does not appear as a pure sinusoidal wave, but shows a multi-harmonics content.

Note that the amplitude of each harmonics, either dominant or extra, only depends on the geometric characteristics of the cyclic symmetric structure and on the nature of mode shapes. However, although the mesh roughness is strictly related to the maximum order of the detectable extra harmonics (Eqn. 2.51), it might affect the harmonics' amplitude if the number of location n_c is not so large. Intuitively, the larger the harmonics' order, the larger the approximation on the harmonics' amplitude

with respect the actual ones. Although in most of the cases such approximation is negligible, the detection of the harmonics amplitude with high accuracy in general requires a very refined mesh.

As it will be shown in Chapter 4 the extra harmonics pattern is found useful when the model order reduction on a single-stage bladed disk is performed.

2.3.1 Extra Harmonics: Analitycal Proof

Besides their empirical observation, the extra harmonic existence can be analytically proved. As already stated in section 2.1, the modes of the three classes were defined assuming identical shape for each vibrating sector with a phase shift between them that depends on h. Let us consider the case of a mode with zero nodal diameters ($\varphi_h = 0$). In this case each mode repeats the same shape sector by sector, meaning that the mode shape is spatially periodic with a period that is equal to the sector angle α_n. Therefore, the distribution of the modal quantities within a single sector can be expressed by employing the Fourier series in complex notation:

$$f(\vartheta) = \sum_{s=0}^{+\infty} A_s e^{is\vartheta} \qquad 0 \leq \vartheta \leq \alpha_n \tag{2.53}$$

The number of harmonics of Eqn. 2.53 is theoretically infinite, but in the case n_{arc} equally spaced locations (Figure 2.14) Eqn 2.53 becomes:

$$f(\vartheta) = \sum_{s=0}^{n_{arc}-1} A_s e^{is\vartheta} \qquad 0 \leq \vartheta \leq \alpha_n \tag{2.54}$$

Then, the function $f(\vartheta)$ can be expanded from the single sector to the whole disk (Fig. 2.16):

$$f(\theta) = \sum_{s=0}^{n_{arc}-1} A_s e^{isN\theta} \qquad 0 \leq \theta \leq 2\pi \tag{2.55}$$

However, Eqn. 2.55 does not yet take into account any phase between the vibrating sectors. In order to enforce the phase shift, $f(\theta)$ has to be modulated by the dominant mode corresponding to h. Finally, the function representing the mode shape at the

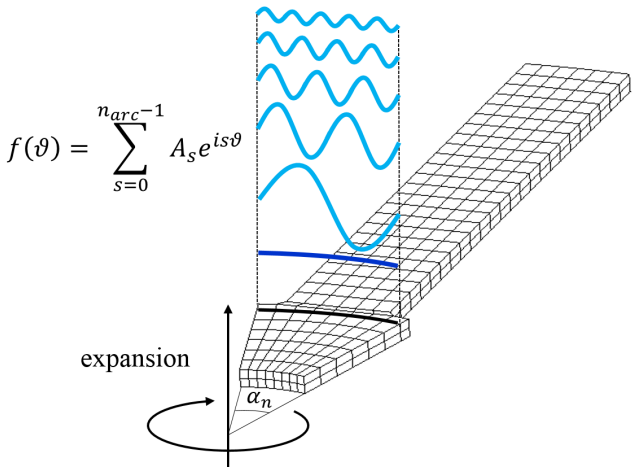

Fig. 2.16 The Fourier series of Eqn 2.54 is expanded from the single sector to the whole cyclic symmetric structure.

interface is given by:

$$F(\theta) = \left(\sum_{s=0}^{n_{arc}-1} A_s e^{isN\theta} \right) e^{\pm ih\theta} \qquad 0 \leq \theta \leq 2\pi \tag{2.56}$$

where $e^{\pm ih\theta}$ refers to either the clockwise (+) or anticlockwise (-) rotating mode shape if $1 \leq h < \tilde{h}$.

The Fourier coefficients $F_k \in \mathbb{C}$ corresponding to the harmonic functions constituting $F(\theta)$ are computed as:

$$F_k = \frac{1}{\Theta} \int_0^{2\pi} F(\theta) e^{-ik\omega_\theta \theta} d\theta \tag{2.57}$$

where Θ is period of $F(\theta)$ and $\omega_\theta = 2\pi/\Theta$ is the *fundamental harmonic*. Since $F(\theta)$ has a periodicity of 2π, Eqn. 2.57 becomes:

$$F_k = \frac{1}{2\pi} \int_0^{2\pi} F(\theta) e^{-ik\theta} d\theta \tag{2.58}$$

The integral of Eqn. 2.58 can be solved considering each term of the sum separate from the others:

$$F_k = \frac{1}{2\pi} \int_0^{2\pi} A_s e^{isN\theta} e^{\pm ih\theta} e^{-ik\theta} d\theta = \frac{A_s}{2\pi} \int_0^{2\pi} e^{ic\theta} d\theta =$$

$$= \frac{A_s}{2\pi}\frac{1}{ic}\Big[e^{ic\theta}\Big]_0^{2\pi} = \frac{A_s}{2i\pi c}\Big[e^{2i\pi c}-1\Big] \tag{2.59}$$

where $c = zN - k \pm h$. It can be noted that the result of Eqn. 2.59 is equal to zero when $c \neq 0$, but represents an indeterminate from $(0/0)$ when $c = 0$:

$$\lim_{c\to 0}\frac{A_s}{2i\pi c}\Big[e^{2i\pi c}-1\Big] = \frac{0}{0} \tag{2.60}$$

The indeterminate form can be solved by applying the L'Hôpital's rule:

$$\lim_{c\to 0}\frac{A_s}{2i\pi}\frac{\frac{d}{dc}[e^{2i\pi c}-1]}{\frac{d}{dc}c} = \lim_{c\to 0}\frac{A_s}{2i\pi}2i\pi e^{2i\pi c} = A_s \tag{2.61}$$

From Eqn. 2.61 it can be concluded that if $c = 0$, i.e. $k = zN \pm h$, $F_k = A_s \neq 0$.

2.3.2 Extra Harmonics Properties

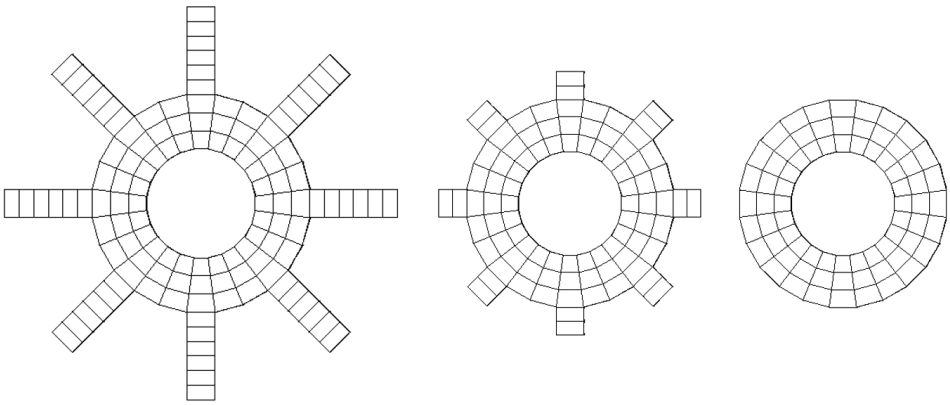

Fig. 2.17 Example of structures exhibiting different cyclic symmetry.

As already introduced at the beginning of this section, the spectrum of a modal quantity detected at the disk level shows harmonics with decreasing amplitude as the harmonic index increases (Figure 2.15). The ratio ε between the amplitudes of the dominant harmonic and the highest magnitude extra harmonic depends on the geometrical properties of the structure and cannot be a priori known. For structures exhibiting a "strong" cyclic symmetry it was observed that $\varepsilon \gg 1$. Contrarily, when an axi-symmetric structure is studied as it was cyclically symmetric, the highest magnitude extra harmonics becomes dominant, since its amplitude appears larges

than that of the h-order one. In general, the extra harmonics importance depends on the cyclic symmetry characterizing the structure: they are less important for structure exhibiting a strong cyclic symmetry, while their amplitude increases for structure showing a "weak" cyclic symmetry (Figure 2.17).

When a mode shape with h nodal diameters occurs a certain ISPA exists between adjacent sectors, or equivalently, between the left and right sector's frontiers. This phase angle has been defined in Eqn. 2.13 without any consideration for the corresponding extra harmonics pattern (Eqn. 2.51). However, for each k-order extra harmonic a new phase angle can be defined as:

$$\varphi_k = \frac{2\pi}{n_c} k \tag{2.62}$$

which gives information about the periodicity of the extra harmonic over the structure. Being the phase angle between two adjacent nodes at the disk level φ_k is here denoted as *inter-node phase angle* (INPA) (Figure 2.18)

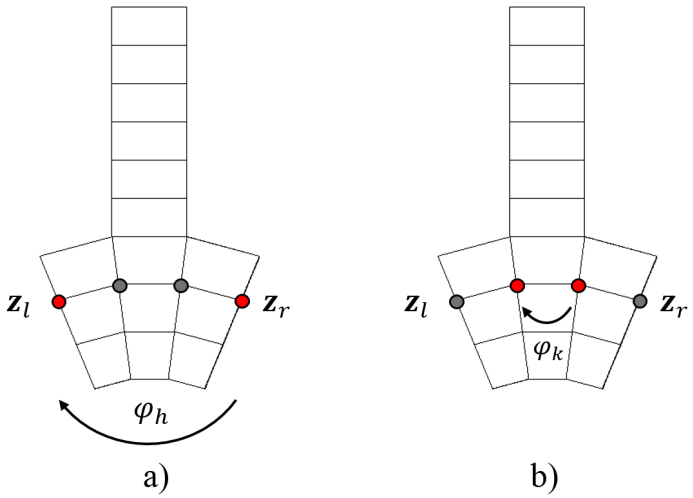

Fig. 2.18 Schematic representation of φ_h and φ_k. a) The ISPA expresses the phase lag existing between the left and right frontiers; b) the INPA expresses the phase lag between two adjacent nodes at the disk level.

Although the different definitions, φ_h and each φ_k have to be consistent to each other. In particular, the INPA φ_k has to guarantee a phase shift of φ_h between the left and right frontiers of a sector. In order to clarify this last concept, let us consider the FE model of a blisk consisting of $N = 8$ sectors having at the disk level $n_c = 24$ nodes (Figure 2.19).

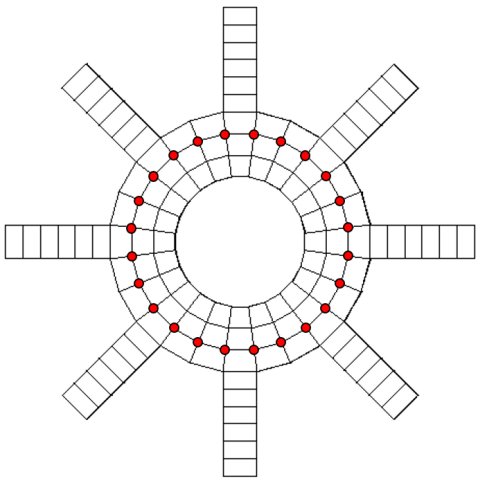

Fig. 2.19 Example of cyclic symmetry structure with $N = 8$ sectors and $n_c = 24$ nodes at the disk level.

If a mode shape with $h = 2$ nodal diameters is considered, the complete extra harmonic pattern is given by:

$$\begin{cases} k = 0 \cdot 8 \pm 2 & \rightarrow \quad k_0^- = \cancel{-2},\ k_0^+ = 2 \\ k = 1 \cdot 8 \pm 2 & \rightarrow \quad k_1^- = 6,\ \ k_1^+ = 10 \end{cases} \tag{2.63}$$

According to Eqns. 2.13 and 2.22, considering an anti-clockwise rotating mode shape, the ISPA corresponding to the dominant harmonic h is positive and equal to $\pi/2$ ($\varphi_h = \pi/2$). This kinematic condition can be schematized in Figure 2.20 by using rotating vectors on the complex plane.

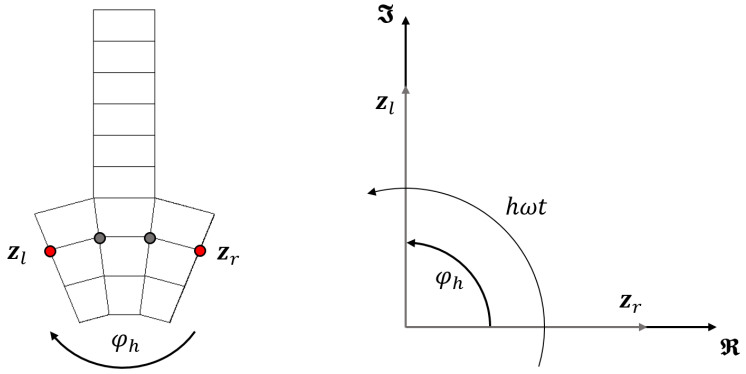

Fig. 2.20 The left frontier vibrates in anticipation with respect the right one. The phase shift between z_l and z_r is equal to the ISPA φ_h.

Here, the two arrows represent the left and right sector's interfaces, vibrating with a phase lag of φ_h. The counter-clockwise rotation of the mode shape corresponds to a counter-clockwise rotation of the vectors on the complex plane, with the left interface moving in anticipation with respect the right one.

Similar kinematic conditions can be expressed between adjacent nodes if the extra harmonics are considered. In particular, let us consider first the extra harmonic of index $k_1^- = 6$. In this case the INPA is given by:

$$\varphi_{k_1^-} = \pm\frac{2\pi}{n_c}k_1^- = \pm\frac{2\pi}{24}6 = \pm\frac{\pi}{2} \tag{2.64}$$

In order to obtain the ISPA φ_h between the left and right frontiers, $\varphi_{k_1^-}$ has to be summed up recursively $(n_{arc}-1)$ times.

$$(n_{arc}-1)\varphi_{k_1^-} = \pm(4-1)\frac{\pi}{2} = \pm 3\frac{\pi}{2} \tag{2.65}$$

If the plus sign was chosen in Eqn. 2.65, the phase lag between the left and right frontiers would be equal to $(3\pi/2)$ (Figure 2.21).

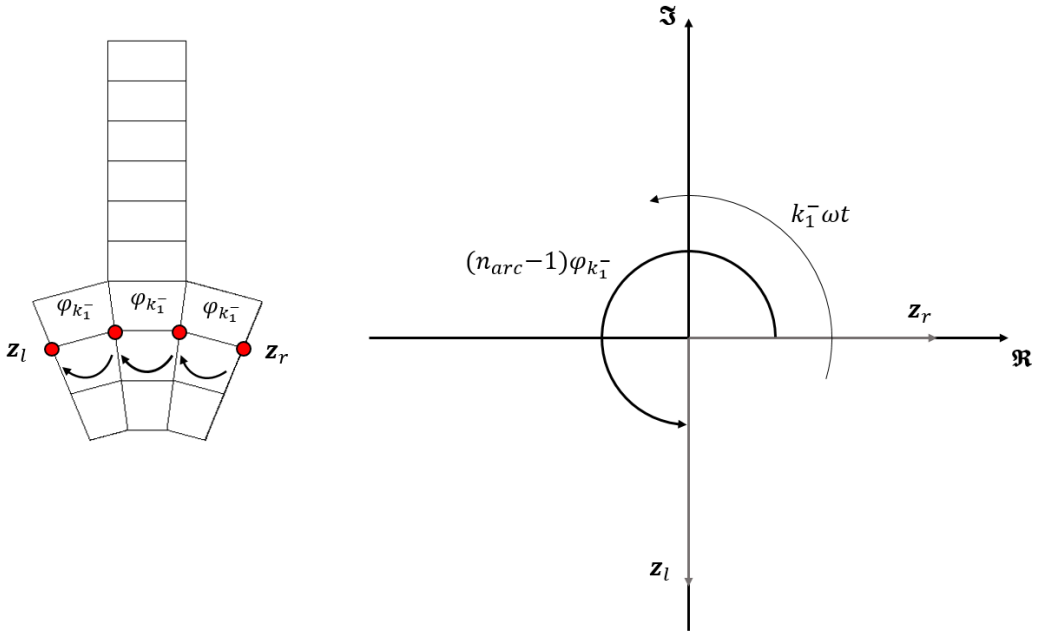

Fig. 2.21 Phase lag between the left and right sector's frontiers corresponding to an INPA $\varphi_{k_1^-} = 3\frac{\pi}{2}$. The diagram in the right shows the relative position of the frontiers by means of rotating vectors.

This choice however does not guarantee the correct mutual position between the left and right sector's frontier (compare Figure 2.21 with Figure 2.20). Contrarily, if the minus sign is considered in Eqn. 2.65, the correct relative position of the left frontier with respect the right one is found (Figure 2.22):

$$(n_{arc}-1)\varphi_{k_1^-} = -(4-1)\frac{\pi}{2} = -3\frac{\pi}{2} \tag{2.66}$$

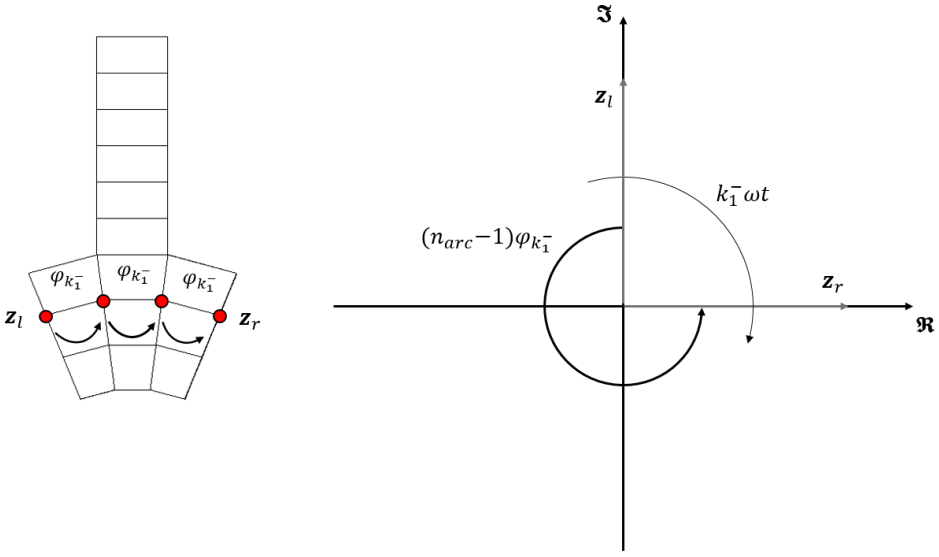

Fig. 2.22 Phase lag between the left and right sector's frontiers corresponding to an INPA $\varphi_{k_1^-} = -3\frac{\pi}{2}$. The diagram in the right shows the relative position of the frontiers by means of rotating vectors.

This last case shows that the rotation of an extra harmonic whose index k is obtained by using the minus sign in Eqn. 2.63, is opposite to that of the harmonic of index h. For the case examined since the harmonic h is counter-clockwise rotating, the extra harmonic k_1^- rotates in a clockwise direction.

Similar considerations hold for the harmonic k_1^+. In this case the correct INPA is given by:

$$\varphi_{k_1^+} = \frac{2\pi}{n_c}k_1^+ = \frac{2\pi}{24}10 = \frac{5}{6}\pi \tag{2.67}$$

which gives the following phase lag between the left and right frontiers:

$$(n_{arc}-1)\varphi_{k_1^+} = (4-1)\frac{5}{6}\pi = \frac{5\pi}{2} \tag{2.68}$$

As it can be seen from Figure 2.23, this value ensure the correct relative position between the frontiers. The extra harmonics corresponding to harmonic indexes k^+ therefore rotate in the same direction of the h order harmonic.

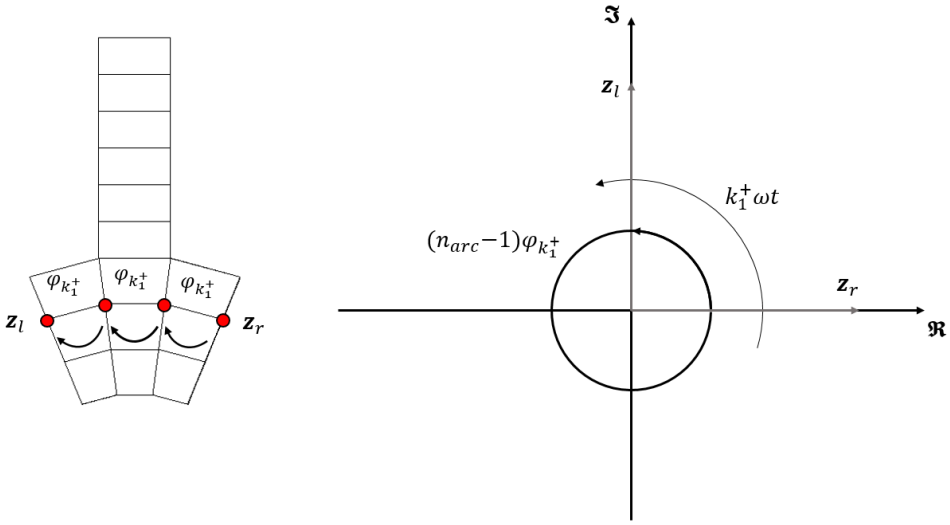

Fig. 2.23 Phase lag between the left and right sector's frontiers corresponding to an INPA $\varphi_{k_1^+} = \dfrac{5\pi}{2}$. The diagram in the right shows the relative position of the frontiers by means of rotating vectors.

It can be concluded that an extra harmonic of index k obtained by using the minus sign in Eqn. 2.51 rotates with a versus that opposite to that of the dominant harmonic h. On the contrary, the an extra harmonic of index k obtained by using the plus sign in Eqn.2.51 rotates with the same versus of the dominant harmonic h.

2.4 Tuned Bladed Disk Dynamics

As shown in the previous sections, the mode shapes of a tuned cyclic symmetric structure exhibit a periodicity described in terms of values assumed by the ISPA φ_h. Since the correlation between an observed mode shape and its value of φ_h is not so immediate, it is common to measure the periodicity of a mode shape by its number of nodal diameters h. The diagram ordinarily used to synthesize the bladed disk dynamics is the so called *FreND diagram* which represents the plot of the natural frequencies versus the number of nodal diameters characterizing the associated mode shapes. An example of FreND diagram for a blisk consisting of 24 sectors is shown

in Figure 2.24. The natural frequencies associated to the modes having the same

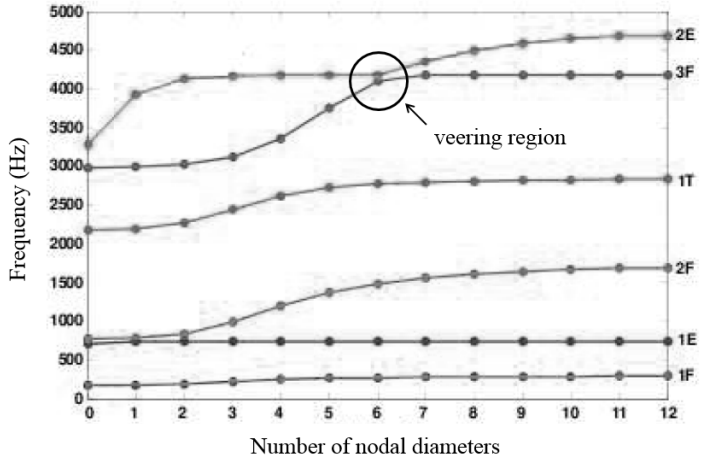

Fig. 2.24 Example of a FreND diagram of a bladed disk with $N = 24$ sectors.

sector deformed shape (e.g. flap (1F-2F), torsional (1T-2T) or edge-wise (1E-2E)) are grouped into distinct *families* of modes, each of which corresponds to a line connecting the modes from $h = 0$ to $\tilde{h}$. The number of modal families is equal to the number of fundamental sector's DoFs.

The shape of each family provides important information on the vibratory nature of the bladed disk as the number of nodal diameters h increases. In most of the cases the curve starts with a parabolic-like shape denoting disk dominated mode shapes: for low h's the blades are dragged by the disk during vibration. As the number h increases, the disk becomes stiffer leading to growing natural frequencies. After a certain value of h the modal family asymptotically approach one natural frequency, corresponding to that of the clamped, blade-alone configuration. This quasi-horizontal curve refers to blade-dominated vibration modes, where the disk is nearly motionless and the blades are weakly coupled among themselves.

Another notable feature is the presence of a *veering regions* (Figure 2.24), which occur when two different families become quite close to each other. The fifth and sixth modal families of Figure give a clear example of this phenomenon. The former starts (for low h) with disk dominated modes, the latter with blade-dominated modes: at $h = 6$ they veer away from each other, exchanging the slope between themselves. Veering regions are symptomatic of large vibration amplitudes due to mistuning phenomena [17]. For this reason they have to be avoided in order to prevent HCF problems.

The natural frequencies of rotordynamical systems often depend on the rotation speed, due to the gyroscopic phenomena, and, in the case of gas-turbine engine, to the stiffening effects induced by large centrifugal forces. The excitation frequency also depends on the rotation speed. In fact, except for mechanical impacts and self-excited phenomena, all the dynamic excitation types introduced in Chapter 1 lead to *synchronous vibrations*. This means that their excitation frequency ω is in direct ratio to the rotor angular velocity Ω according to the following relationship:

$$\omega = EO \cdot \frac{\Omega}{2\pi} \tag{2.69}$$

where ω and Ω are expressed in Hz and round per minutes (rpm) respectively and the coefficient EO, called *Engine Order*, denotes the periodicity of the excitation over the bladed disk. For instance, if the excitation is caused by the previous stator wakes, EO represents the number of stator vanes.

In order to graphically study the forced response of a bladed disk, the *Campbell diagram* is commonly used (Figure 2.22).

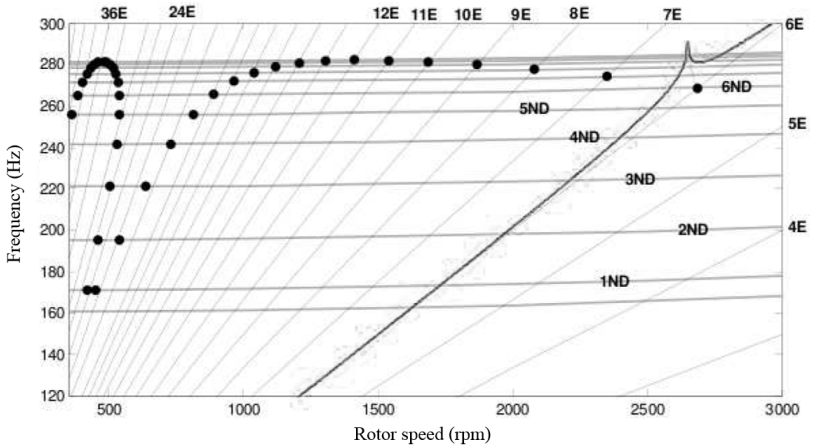

Fig. 2.25 Example of Campbell diagram.

Here, the natural frequencies are plotted as horizontal lines depending on the rotor speed Ω, while the EO excitation frequencies are shown as straight lines starting from the axis origin. The resulting intersections between the two set of lines may represent possible resonance. Among all the several crossing, just few of them correspond to actual resonance conditions, while the others, although the excitation frequencies coincide to the natural frequencies of the crossed modes, do not refer to any critical situation. In general the critical intersections are those for which the

following condition holds:

$$EO = z \cdot N \pm h \qquad \forall\, z \in \mathbb{N}^* \tag{2.70}$$

By looking at the previous equation it is quite intuitive to understand what happens when $z = 0$: the EO equals the number of nodal diameters h of the mode shape. The physical reason for which a mode shape is excited in resonance condition when $EO = h$ is intuitive: the force distribution over the structure exactly match the shape of the mode and, consequently, the maximum response amplification is achieved when the excitation frequency coincides to the natural frequency of the mode shape. Given a certain EO, the mode shapes such that $h \neq EO$ cannot be excited in resonance condition because the force projection onto the mode, i.e. the modal force, is null.

Less intuitive is the condition described by the Eqn 2.70 for $z \neq 0$. In this case a mode with h nodal diameters is critically excited by the EO force due to the *aliasing phenomenon*: the rotating force is in fact "erroneously" sampled by the sectors, which allows the disk to "see" the force as it was of $EO = h$ (Figure 2.26).

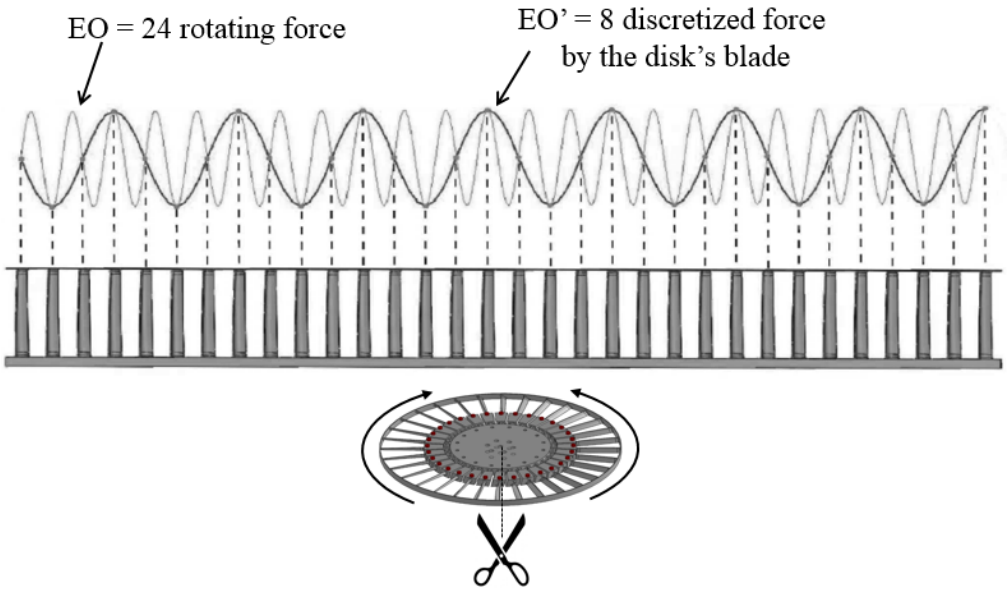

Fig. 2.26 Discretization of an EO = 24 excitation by means of a blisk with 32 blades. In this case the EO = 24 may excite in resonance condition a mode shape with $h = 8$ nodal diameters.

Chapter 3

Reduced Order Model Techniques

3.1 Introduction

In Chapter 2 most of the considerations on mode shapes of cyclic symmetric structures were carried out by assuming FE discretization of a generic rotationally periodic structure. Mass and stiffness matrices can thus be derived from FE models in order to evaluate eigenfrequencies and mode shapes through the modal analysis. However, the dynamic design of large complex structural systems requires more than a simple modal analysis. For instance, dynamic calculations aimed at predicting either the linear or non-linear forced response of real bladed disk assemblies have become essential parts of industrial practices. In general, performing such analyses on FE models consisting on hundreds of thousands (or even millions) DoFs is sometimes prohibitive due to the exceptional cost required in terms of computation time.

It was the roman emperor Julius Caesar who in ancient times introduced the principle of "divide and conquer". Ever since, this tactic has been successfully applied in a range of domains: from economics to warfare and from computer science to politics. In the past century the same idea has been successfully extended to structural dynamic analyses. In particular, the dynamic behavior of large complex structures can be evaluated by decomposing them into several smaller, simpler *substructures* (or *components*), whose dynamic behavior is generally easier to determine. Thereafter, the dynamic model of the total structure is then obtained by assembling the dynamic models of the components, an approach that is nowadays known as *dynamic substructuring* (DS). Although DS arises when the available resources in

terms of computing power were very limited, this approach remains highly relevant as the huge advances in modeling capabilities are balanced by increasingly complex engineering structures and ever shorter design cycles.

Analyzing the system's structural dynamics in such a componentwise fashion has proven to have important advantages over the methods requiring to handle the entire problems at once:

- It allows the evaluation of structures that would otherwise be large and/or complex to be simulated or measured as a whole.
- By analyzing each subsystem, local dynamic behavior can be recognized much more easily than when the entire system is analyzed. This also allows for local optimization of the design, but also for model simplification by eliminating local subsystem behavior which has no significant impact on the assembled system's dynamics.
- It gives the possibility to combine numerically modeled parts and experimentally identified components.
- When a single component is substituted, only that component needs to be reanalyzed; the total system dynamics can be evaluated at low additional cost.
- It allows sharing and combining component models design by different project groups.

3.2 Dynamic Substructuring

The most well-known DS methods combines the concepts of componentwise analysis and *model order reduction*. The basic idea behind them is quite simple: instead of describing the dynamics of a complex FE model at all its nodal DoFs, it is described in terms of dominant mode shape vectors or simply *modes*. In this way very compact descriptions of component FE models are obtained. These models are subsequently assembled to obtain the numerical model of the entire system, which can be analyzed at low computational cost to obtain the global dynamic behavior.

The development of these methods was triggered by the initial ideas of Hurty in 1960 [18], which were further worked out in [19]. Most probably these ideas

came forth from the very limited computation power in those days, making the reduction of FE models a bare necessity to analyze any realistic structure. Rapidly the scientific and engineering communities discovered the benefits of DS, which became an important research topic in the field of structural dynamics. Some major developments followed shortly, resulted in the classic methods by Guyan [20], Craig [21], Rubin [22] and MacNeal [23] in the late 1960's and 1970's.

The creation of a substructured dynamic model starts with the decomposition of the structure into non-overlapping components. For each of these components a FE model is then created. In practice, these component FE models are also used for detailed static stress analyses. Since the small geometric details often determine the stress concentrations, these often requires very fine meshes. For a few static analysis runs the computational cost associated with these models is still manageable. However, structural dynamic analysis generally requires solving many static-like problems and working with such refined models quickly becomes unfeasible. Furthermore, coarser models are usually sufficient, since the dynamic behavior is governed by the structure's global mass and stiffness distributions. The engineer thus faces a choice: either use the very fine model or create a coarser mesh. Both options are not very time efficient, as creating a good mesh can be a time consuming process too.

A more elegant approach would therefore be to decrease the number of DoFs without modifying the FE mesh. Such methods exist and are known as *model order reduction methods*. In structural dynamics these methods consist in replacing a set of physical DoFs by a much smaller set of generalized DoFs, using the principles of modal superposition and truncation. In other words, instead of describing the structure's dynamic behavior at a very large number of points along the structure, the behavior is expressed in terms of a limited number of deformation shapes with associated amplitudes.

The mathematical principle behind all the reduction methods involved in DS is basically the same: these aim at defying a reduction basis $\boldsymbol{R}$, which collects the mode shape vectors that are sufficient to well-capture the dynamic behavior of the analyzed component. The differences between the several reduction methods lie in the nature of this transformation matrix. However, it is possible to individuate two main categories in which all the techniques can be grouped:

1. *Component Mode Synthesis* (CMS) *methods*
2. *Generalized modal reduction*.

3.2.1 Component Mode Synthesis Methods

The term *component modes* is used to signify Ritz vectors, or assumed modes, that are used as basis vectors for describing the displacement of points within a substructure. Component normal modes, or eigenvectors, are just one class of component modes. For this class of methods the transformation matrix $\boldsymbol{R}$ is referred to as *component-mode matrix* and includes modes of the following types:

- *Normal* or *vibration modes*, either computed in free or constraint condition, to account for the component's dynamics.
- *Static modes* to describe the interaction with neighboring substructures.

The starting point for the derivation of the mentioned modes is the set of conservative EQM describing the linear dynamic behavior of the generic c^{th} component:

$$\boldsymbol{M}^{(c)}\ddot{\boldsymbol{x}}^{(c)}(t)+\boldsymbol{K}^{(c)}\boldsymbol{x}^{(c)}(t)=\boldsymbol{f}^{(c)}(t) \tag{3.1}$$

where, being N the number of DoFs of the whole structure, $\boldsymbol{M}^{(c)}$ and $\boldsymbol{K}^{(c)}$ are the $N\times N$ component's mass and stiffness matrices, $\boldsymbol{x}^{(c)}(t)$ the $N\times 1$ vector of physical DoFs and $\boldsymbol{f}^{(c)}(t)$ the corresponding $N\times 1$ vector of external forces. Hereafter in this section the superscript c and the explicit time dependence will be omitted for sake of clarity.

The most general type of substructure is that connected to one or more adjacent components by redundant interfaces. Figure 3.1 illustrates a simple cantilever beam that is divided into three components.

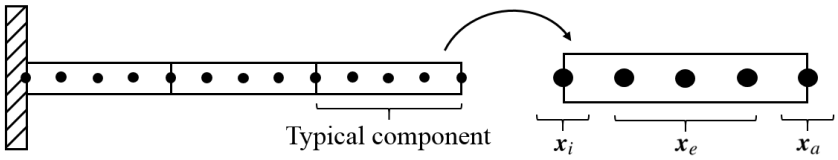

Fig. 3.1 Example of a coupled system and DoFs partitioning for a typical substructure.

As shown in the previous figure, the unconstrained DoFs of the generic substructure can be partitioned into three set of DoFs:

- *Interface* DoFs $\boldsymbol{x}_i$: denoted by the letter i, this set includes the DoFs that are shared with adjacent substructures when conforming meshes occur at the common interface.
- *Interior* or *exceeding* DoFs $\boldsymbol{x}_e$: denoted by the letter e, this set collects the DoFs that are not shared with neighboring substructures.
- *Accessories* or *active* DoFs $\boldsymbol{x}_a$: denoted by the letter a, to this set belong the DoFs used either to exert forces on the substructure or to monitor its response (see section 3.4).

The numbers of displacement coordinates belonging to the former sets are n_i, n_e and n_a respectively. Interface and active DoFs can be grouped together in a set called *boundary* that is here denoted by the letter b: $\boldsymbol{x}_b = \left\{\boldsymbol{x}_i^T \ \boldsymbol{x}_a^T\right\}^T$. The number n_b of boundary DoFs is thus given by: $n_b = n_i + n_a$. According to the previous DoFs partition, Eqn. 3.1 can be rewritten in matrix form as follows:

$$\begin{bmatrix} \boldsymbol{M}_{bb} & \boldsymbol{M}_{be} \\ \boldsymbol{M}_{eb} & \boldsymbol{M}_{ee} \end{bmatrix} \begin{Bmatrix} \ddot{\boldsymbol{x}}_b \\ \ddot{\boldsymbol{x}}_e \end{Bmatrix} + \begin{bmatrix} \boldsymbol{K}_{bb} & \boldsymbol{K}_{be} \\ \boldsymbol{K}_{eb} & \boldsymbol{K}_{ee} \end{bmatrix} \begin{Bmatrix} \boldsymbol{x}_b \\ \boldsymbol{x}_e \end{Bmatrix} = \begin{Bmatrix} \boldsymbol{f}_b \\ \boldsymbol{f}_e \end{Bmatrix} \tag{3.2}$$

where the subscripts refer to the submatrices and subvectors' dimensions.

In general, vibration and static modes can be derived by splitting the interior DoFs' response into its static and dynamic parts:

$$\boldsymbol{x}_e = \boldsymbol{x}_e^s + \boldsymbol{x}_e^d \tag{3.3}$$

Firstly, the static response is obtained by setting to zero the accelerations in Eqn. 3.2 and $\boldsymbol{x}_e^d$ in Eqn. 3.3:

$$\begin{bmatrix} \boldsymbol{K}_{bb} & \boldsymbol{K}_{be} \\ \boldsymbol{K}_{eb} & \boldsymbol{K}_{ee} \end{bmatrix} \begin{Bmatrix} \boldsymbol{x}_b \\ \boldsymbol{x}_e^s \end{Bmatrix} = \begin{Bmatrix} \boldsymbol{f}_b \\ \boldsymbol{f}_e \end{Bmatrix} \tag{3.4}$$

Assuming no external excitation at the DoFs in $\boldsymbol{x}_e$ (i.e. $\boldsymbol{f}_e = 0$), the second equation of Eqn. 3.4 gives the static part of $\boldsymbol{x}_e$ in terms of the boundary DoFs:

$$\boldsymbol{x}_e^s = -\boldsymbol{K}_{ee}^{-1}\boldsymbol{K}_{eb}\boldsymbol{x}_b = \Psi_{eb}\boldsymbol{x}_b \tag{3.5}$$

where the matrix Ψ_{eb} collects n_b *static modes*, i.e. the static deformation of the DoFs in $\boldsymbol{x}_e$ as a result of displacement or force application at the boundary DoFs $\boldsymbol{x}_b$.

Secondly, the dynamic part of $\boldsymbol{x}_e$ is approximated by a set of n_v *vibration modes* using the classic modal superposition:

$$\boldsymbol{x}_e^d \approx \sum_{j=1}^{n_v} \phi_{e,j}\eta_j = \Phi_v \eta_v \tag{3.6}$$

where the vibration modes $\phi_{e,j}$ are obtained solving the eigenvalue problem for the DoFs in $\boldsymbol{x}_e$:

$$(\boldsymbol{K}_{ee} - \omega_{e,j}^2 \boldsymbol{M}_{ee})\phi_{e,j} = 0 \tag{3.7}$$

The model reduction can be achieved by taking not all the possible n_e normal modes, but just a subset of them. Usually the modes corresponding to the lowest eigenvalues are sufficient to accurately describe the component's dynamics, since they capture most of the structure's mass and stiffness. The reduction of the dynamic part of the response is therefore effective for $n_v \ll n_e$.

By substituing Eqns. 3.5 and 3.6 into Eqn. 3.3, $\boldsymbol{x}_e$ can thus be approximated as:

$$\boldsymbol{x}_e \approx \Psi_{eb}\boldsymbol{x}_b + \Phi_v \eta_v \tag{3.8}$$

Eqn. 3.8 clearly shows the explicit dependency of $\boldsymbol{x}_e$ on $\boldsymbol{x}_b$. For this reason, $\boldsymbol{x}_e$ and $\boldsymbol{x}_b$ are commonly referred to as *slave* and *master* DoFs respectively. Considering the approximation in Eqn. 3.8, the global component's displacements vector $\boldsymbol{x} = [\boldsymbol{x}_b^T\, \boldsymbol{x}_e^T]^T$ can be expressed as:

$$\boldsymbol{x} = \begin{Bmatrix} \boldsymbol{x}_b \\ \boldsymbol{x}_e \end{Bmatrix} \approx \begin{bmatrix} \boldsymbol{I}_{bb} & \boldsymbol{0}_{bv} \\ \Psi_{eb} & \Phi_v \end{bmatrix} \begin{Bmatrix} \boldsymbol{x}_b \\ \eta_v \end{Bmatrix} = \boldsymbol{R}\boldsymbol{q} \tag{3.9}$$

where $\boldsymbol{R}$ is the component-mode, or transformation matrix, and $\boldsymbol{q}$ is the reduced vector of DoFs, which is often referred to as *generalized coordinates vector*.

When the coordinate transformation of Eqn. 3.9 is substituted into the component's EQM, the following relationship is obtained:

$$\boldsymbol{M}\boldsymbol{R}\ddot{\boldsymbol{q}} + \boldsymbol{K}\boldsymbol{R}\boldsymbol{q} = \boldsymbol{f} + \boldsymbol{r} \tag{3.10}$$

where the *residual* $\boldsymbol{r}$ comes out due to the approximation introduced by Eqn. 3.8. The reduced EQM are then obtained by setting the residual equal to zero in the space spanned by both static and vibration modes, i.e. $\boldsymbol{R}^T\boldsymbol{r} = \boldsymbol{0}$. In mathematics this is know as *Galerkin projection*[1], but in mechanics this often referred to as a *Rayleigh-Ritz procedure*. After having projected the component's EQM onto the reduction basis, the reduced component's EQM are obtained:

$$\tilde{\boldsymbol{M}}\ddot{\boldsymbol{q}} + \tilde{\boldsymbol{K}}\boldsymbol{q} = \tilde{\boldsymbol{f}} \tag{3.11}$$

where

$$\tilde{\boldsymbol{M}} = \boldsymbol{R}^T\boldsymbol{M}\boldsymbol{R} \qquad \tilde{\boldsymbol{K}} = \boldsymbol{R}^T\boldsymbol{K}\boldsymbol{R} \qquad \tilde{\boldsymbol{f}} = \boldsymbol{R}^T\boldsymbol{f} \tag{3.12}$$

Note that due to the reduction of the number of DoFs, the reduced component model will be stiffer than the full model and consequently has higher eigenfrequencies. This effect is similar to the stiffening caused by the FE discretization of the structure. The results of the analyses performed on the reduced model can be expanded in order to obtain the solution at the original set of DoFs. This procedure, which accounts for the use of the reduction matrix of Eqn. 3.9, is commonly known as *data recovery*.

The differences between the several component model reduction methods lie in the nature of the modes constituting the reduction basis $\boldsymbol{R}$. In this regard, CMS methods can be further divided in three subclasses, depending on the boundary conditions imposed to each component-alone interface [1]:

- *Fixed-interface methods*: each single component is taken with its interfaces kept fixed ($\boldsymbol{x}_b = 0$). For this class of methods the component-mode matrix $\boldsymbol{R}$ includes a set of *fixed-interface normal modes*, which however does not allow to correctly model the static deformation of the structure due to the interfaces motion. Therefore, $\boldsymbol{R}$ has to be expanded with a set of static deformed shapes, referred as *constraint modes*, which are obtained imposing, one by one, a unity displacement to one interface DoF, keeping contemporaneously fixed all the other interface DoFs (see subsection 3.3.1).

- *Free-interface methods*: each single component is taken with its interfaces kept free. As happens with fixed-interface methods, the inclusion in the component-

[1] If a different basis is chosen for the projection than for the reduction this is known as a *Petrov-Galerkin projection*.

mode matrix of the so-called *free-interface normal modes*, purified of the rigid body modes, does not allow to correctly model the static deformation of the structure. The physical information about the coupled-interfaces motion is then introduced through a set of *attachment modes*, obtained imposing, way by way, a unity force to one interface degree of freedom, keeping contemporaneously free all the other interface DoFs. For further details on the evaluation of attachment modes see [1].

- *Hybrid methods*: to this class belong the methods that are a combination of the two listed above. The component-mode matrix $\boldsymbol{R}$ may contain normal and both constraint and attachment modes [23, 24].

3.2.2 Generalized Modal Reduction

This reduction is generally utilized for structure that are not separated into component. In this case the DoFs are reduced all together by using a small subset of the structure's vibration modes. These are obtained solving the eigenvalue problem defined by the whole structure's mass and stiffness matrices:

$$(\boldsymbol{K} - \omega_j^2 \boldsymbol{M})\phi_j = \boldsymbol{0} \tag{3.13}$$

Similarly to the case of Eqn. 3.9 the whole set of DoFs $\boldsymbol{x}$ is approximated by n_v vibration modes through the modal superposition:

$$\boldsymbol{x} \approx \sum_{j=1}^{n_v} \phi_j \eta_j = \Phi_{Nn_v} \eta_v \tag{3.14}$$

where Φ_{Nn_v} is the $N \times n_v$ modal matrix and η_v the $n_v \times 1$ generalized coordinates vector. The modal reduction can be considered effective when the reduction basis contains $n_v \ll N$ vibration modes.

3.3 Fixed-interface Methods

Among the reduction techniques previously introduced, CMS fixed-interface methods are those much used by the structural dynamics community. Such techniques, as the *Guyan* and *Craig-Bampton* methods, are integrated in many FE software

packages and widely used in practical design processes. The derivation of the modes constituting the component-mode matrices of both methods is treated in the next two subsections.

3.3.1 Constraint Modes

Static *constraint modes* used in fixed-interface reduction methods can be derived by partitioning the component's displacement vector $\boldsymbol{x}$ into interior and boundary as done in Eqn. 3.2. Using the same procedure employed in the previous section, the static constraint modes can be computed from Eqn. 3.2 by neglecting the inertia forces and retaining as a master the set of boundary DoFs $\boldsymbol{x}_b$. This gives:

$$\boldsymbol{x}_e = -\boldsymbol{K}_{ee}^{-1}\boldsymbol{K}_{eb}\boldsymbol{x}_b = \boldsymbol{\Psi}_{eb}\boldsymbol{x}_b \tag{3.15}$$

The term $\boldsymbol{\Psi}_{eb} = -\boldsymbol{K}_{ee}^{-1}\boldsymbol{K}_{eb}$ is referred to as the *static condensation matrix*. Using these modes, the original set of DoFs $\boldsymbol{x}$ is therefore reduced to the set of boundary DoFs $\boldsymbol{x}_b$ as follows:

$$\boldsymbol{x} = \begin{Bmatrix} \boldsymbol{x}_b \\ \boldsymbol{x}_e \end{Bmatrix} \approx \begin{bmatrix} \boldsymbol{I}_b \\ -\boldsymbol{K}_{ee}^{-1}\boldsymbol{K}_{eb} \end{bmatrix} \boldsymbol{x}_b = \begin{bmatrix} \boldsymbol{I}_{bb} \\ \boldsymbol{\Psi}_{eb} \end{bmatrix} \boldsymbol{x}_b \tag{3.16}$$

where

$$\boldsymbol{\Psi}_{Nn_b} = \begin{bmatrix} \boldsymbol{I}_{bb} \\ \boldsymbol{\Psi}_{eb} \end{bmatrix} \tag{3.17}$$

is the $N \times n_b$ *constraint-mode matrix*. Physically, these modes represent the static deformation shape due to a unit displacement applied to one boundary DoF, while the remaining boundary DoFs are constrained and the internal DoFs are force-free. The constraint modes thus contain the substructure's static response to applied interface displacements. An example of a static constraint mode is illustrated in Figure 3.2. Here the black circles represent the boundary nodes and the grey arrow denotes an imposed interface displacement. Note that all the boundary nodes are kept fixed except that where the unit displacement is applied.

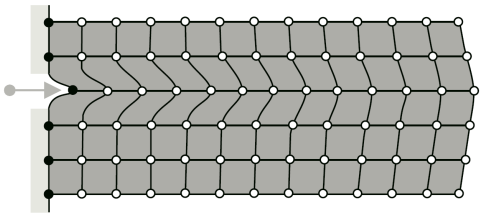

Fig. 3.2 Illustration of a static constraint mode [2]. The mode represents the static deformation of the component due to a unit displacement applied to one boundary DoF, while the others are constrained and the internal DoFs are force-free.

3.3.2 Fixed-Interface Normal Modes

The *fixed-interface normal modes* are the component's vibration shapes when it is constrained at the boundary. Similar to the constraint modes, the first step in their computation is the partitioning of the DoFs vector into interior and boundary DoFs. Component fixed-interface normal modes are then obtained by restraining all the boundary DoFs and solving the following eigenproblem:

$$\left(\boldsymbol{K}_{ee} - \omega_{e,j}^2 \boldsymbol{M}_{ee}\right) \boldsymbol{\phi}_{e,j} = \boldsymbol{0}_{ee} \tag{3.18}$$

where $\omega_{e,j}^2$ and $\boldsymbol{\phi}_{e,j}$ are the j^{th} eigenvalue and mass normalized eigenvector. The complete set of n_e fixed-interface normal mode can be labeled as $\boldsymbol{\Phi}_{ee}$ and assembled for increasing $\omega_{e,j}^2$ as columns of the following modal matrix:

$$\boldsymbol{\Phi}_{Ne} = \begin{bmatrix} \boldsymbol{0}_{be} \\ \boldsymbol{\Phi}_{ee} \end{bmatrix} \tag{3.19}$$

Figure 3.3 gives an illustration of a fixed-interface vibration mode.

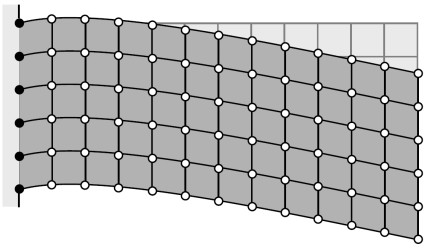

Fig. 3.3 Illustration of a fixed-interface normal mode [2]: it represent the one component's vibration shape obtained by constraining all the boundary DoFs.

Finally, note that the fixed-interface vibration modes, like the static constraint modes, are hard to obtain experimentally. This is due to the fact that the interface DoFs need to be constrained, a condition that is very difficult to realize in practice.

In the previous two sections the most common types of modes used for fixed-interface CMS methods have been outlined. The following two sections addresses the Guyan and Craig-Bampton methods by defining the corresponding component-mode matrices by mixing the static and dynamic components modes provided in the previous sections.

3.3.3 Guyan Method

One of the oldest reduction methods is the Guyan reduction. In his classic half page long paper [20], Guyan proposed in 1965 an idea that is still actively used in structural dynamics today. This method is also referred to as the Guyan-Irons method, since Irons proposed the same idea five years later [25].

Starting from the component EQM in Eqn. 3.1 and assuming the global DoFs vector partitioned as done in Eqn. 3.2, the Guyan method condenses the set $\boldsymbol{x}_e$ to the boundary DoFs by just employing static constraint modes (see subsection 3.3.1):

$$\boldsymbol{u}_e = \Psi_{eb}\boldsymbol{x}_b \tag{3.20}$$

Therefore, the Guyan coordinate transformation/reduction can be expressed as:

$$\boldsymbol{x} = \begin{Bmatrix} \boldsymbol{x}_b \\ \boldsymbol{x}_e \end{Bmatrix} \approx \begin{bmatrix} \boldsymbol{I}_{bb} \\ \Psi_{eb} \end{bmatrix} \boldsymbol{x}_b = \Psi_{Nb}\boldsymbol{x}_b = \boldsymbol{R}_G\, \boldsymbol{x}_b \tag{3.21}$$

where the columns of the Guyan component-mode matrix $\boldsymbol{R}_G$ consists of static constraint modes only. By projecting Eqn. 3.1 onto the reduction basis $\boldsymbol{R}_G$, the following reduced system of equation is obtained:

$$\boldsymbol{M}_G\, \ddot{\boldsymbol{x}}_b + \boldsymbol{K}_G\, \boldsymbol{x}_b = \boldsymbol{f}_G \tag{3.22}$$

where

$$\begin{aligned} \boldsymbol{M}_G &= \boldsymbol{R}_G^T \boldsymbol{M} \boldsymbol{R}_G = \boldsymbol{M}_{bb} - \boldsymbol{K}_{be}\boldsymbol{K}_{ee}^{-1}\boldsymbol{M}_{eb} - \boldsymbol{M}_{be}\boldsymbol{K}_{ee}^{-1}\boldsymbol{K}_{eb} + \boldsymbol{K}_{be}\boldsymbol{K}_{ee}^{-1}\boldsymbol{M}_{ee}\boldsymbol{K}_{ee}\boldsymbol{K}_{eb} \\ \boldsymbol{K}_G &= \boldsymbol{R}_G^T \boldsymbol{K} \boldsymbol{R}_G = \boldsymbol{K}_{bb} - \boldsymbol{K}_{be}\boldsymbol{K}_{ee}^{-1}\boldsymbol{K}_{eb} \end{aligned} \tag{3.23}$$

are the Guyan condensed mass and stiffness matrices and

$$\boldsymbol{f}_G = \boldsymbol{R}_G^T \boldsymbol{f} = \boldsymbol{f}_b - \boldsymbol{K}_{be}\boldsymbol{K}_{ee}^{-1}\boldsymbol{f}_e \tag{3.24}$$

is the condensed vector of generalized forces.

Since in the derivation of the condensed stiffness the inertia forces are neglected, the exact solution is found if this technique is applied to static problems. If it is applied to dynamic problems, an approximate solution is found. This is due to the fact that the internal inertia forces of the substructure are statically condensed on the boundary. This approximation is valid as long as the highest eigenfrequency one wants to compute for the entire structure is much lower than the lowest eigenfrequency of the substructure clamped at its interface.

Since the interface DoFs of the substructure model are retained, assembly to other (reduced) models is very straightforward. Due to this property, such reduced models are referred to as *superelements*.

3.3.4 Craig-Bampton Method

To overcome the main drawback of the Guyan method, the classic Craig-Bampton technique (*CB*-CMS) proposes an expansion of this method by including information on the internal dynamics in the reduced component model [21]. This is achieved by expanding the reduction basis with fixed-interface vibration modes, thereby obtaining a more complete and versatile basis to describe the component's dynamic behavior.

Starting again from the EQM partitioned into boundary and interior DoFs, the latter can be approximated as follows:

$$\boldsymbol{x}_e \approx \Psi_{ee}\boldsymbol{x}_b + \Phi_{ek}\eta_k \tag{3.25}$$

Here Φ_{ek} denotes the reduced set of $n_k \ll n_e$ fixed-interface normal modes, obtained by keeping the the n_e lowest eigenvalues modes of the full fixed-interface modal

matrix Φ_{ee} (Eqn. 3.19). As in the case of the Guyan method the boundary DoFs are retained as master, leading to the following coordinate transformation:

$$\boldsymbol{x} = \begin{Bmatrix} \boldsymbol{x}_b \\ \boldsymbol{x}_e \end{Bmatrix} \approx \begin{bmatrix} \boldsymbol{I}_{bb} & \boldsymbol{0}_{bk} \\ \Psi_{eb} & \Phi_{ek} \end{bmatrix} \begin{Bmatrix} \boldsymbol{x}_b \\ \eta_k \end{Bmatrix} = \boldsymbol{R}_{CB}\, \boldsymbol{x}_{CB} \tag{3.26}$$

where $\boldsymbol{R}_{CB}$ is the *CB*-CMS component-mode matrix. The application of the reduction basis in the usual fashion gives the reduced equations of motion:

$$\begin{bmatrix} \tilde{\boldsymbol{M}}_{bb} & \tilde{\boldsymbol{M}}_{bk} \\ \tilde{\boldsymbol{M}}_{kb} & \boldsymbol{I}_{kk} \end{bmatrix} \begin{Bmatrix} \ddot{\boldsymbol{x}}_b \\ \ddot{\eta}_k \end{Bmatrix} + \begin{bmatrix} \tilde{\boldsymbol{K}}_{bb} & \boldsymbol{0} \\ \boldsymbol{0} & \Omega^2_{kk} \end{bmatrix} \begin{Bmatrix} \boldsymbol{x}_b \\ \eta_k \end{Bmatrix} = \begin{Bmatrix} \tilde{\boldsymbol{f}}_b \\ \tilde{\boldsymbol{f}}_k \end{Bmatrix} \tag{3.27}$$

with

$$\begin{aligned} \tilde{\boldsymbol{M}}_{bb} &= \boldsymbol{M}_{bb} - \boldsymbol{M}_{be}\boldsymbol{K}_{ee}^{-1}\boldsymbol{M}_{eb} - \boldsymbol{K}_{be}\boldsymbol{K}_{ee}^{-1}\boldsymbol{M}_{eb} + \boldsymbol{K}_{be}\boldsymbol{K}_{ee}^{-1}\boldsymbol{M}_{ee}\boldsymbol{K}_{ee}^{-1}\boldsymbol{K}_{eb} \\ \tilde{\boldsymbol{K}}_{bb} &= \boldsymbol{K}_{bb} - \boldsymbol{K}_{be}\boldsymbol{K}_{ee}^{-1}\boldsymbol{K}_{eb} \\ \boldsymbol{M}_{kb} &= \boldsymbol{M}_{bk}^T = \Phi_{ek}^T\left(\boldsymbol{M}_{eb} - \boldsymbol{M}_{ee}\boldsymbol{K}_{ee}^{-1}\boldsymbol{K}_{eb}\right) \\ \tilde{\boldsymbol{f}}_b &= \boldsymbol{f}_b - \boldsymbol{K}_{be}\boldsymbol{K}_{ee}^{-1}\boldsymbol{f}_e \\ \tilde{\boldsymbol{f}}_k &= \Phi_{ek}^T\boldsymbol{f}_e \end{aligned} \tag{3.28}$$

and Ω^2_{kk} is a diagonal matrix containing the first n_k fixed-interface eigenfrequencies $\omega^2_{e,j}$.

One of the strengths of the *CB*-CMS method is the straightforward calculation of its reduction basis. Secondly, like in the Guyan method, the physical boundary DoFs $\boldsymbol{x}_b$ are retained in the reduced model, which facilitates easy assembly of the reduced substructure as a superelement in common FE codes.

3.4 Interface Reduction Methods

In the previous sections a complete classification of the component-mode reduction techniques has been given. Furthermore, the component-modes utilized in fixed-interface CMS methods have been deeply discussed in order to introduce the most used reduction techniques, i.e the Guyan and *CB*-CMS method. As already stated, both methods aim at building superelements by condensating most of the component's DoFs on a smaller set of boundary DoFs, but just a subset of them

enables either the static or dynamic coupling with neighboring components. In this way the reduced order model (ROM) of a complex structure can be finally created.

From the definition of constraint-mode given in section 3.3.1 it is clear the important role they play in describing the motion of the boundary DoFs. However, there is a high computational cost associated with these modes, since the resulting CMS models must have one DoF for each DoF at the boundary. This means that, whereas dramatic order reduction may be achieved for individual substructures (reduction of the normal-mode generalized DoFs), there is no order reduction of the DoFs at the interfaces between components. In particular, complex engineering structures generally consist in a large number of components, and an even larger number of interfaces between them may exists. These interfaces may be extensive and complex, meaning that when the dynamic model of such structures is created in a componentwise fashion, the ratio of interface DoFs over the whole set of generalized DoFs becomes unacceptably high. This can make the CMS model cumbersome to use especially for analysis of large-scale structures with many components.

The difficulty of handling such large number of interface DoFs can be overcome using *interface reduction* techniques. Similar to component-mode methods, these consist in the approximation of the boundary DoFs by means of a truncated set of deformation shapes, called *interface modes*. As such, they constitute a second reduction step that leads to more compact EQM as well as smaller sized component reduction matrices. Depending on the geometric and structural characteristics of the component, the interface reduction can be performed by following two different approaches:

1. When the interface is located on a stiff part of a substructure, or its dimensions are relatively small compared to those of the total substructure, one could approximate its behavior with a local rigid region. The resulting rigidification hence neglects local deformation of the interface, being this described by only six rigid motions, i.e. three translations and three rotations. Therefore a very compact representation of the substructure interface is obtained.

2. In many other cases however, interfaces can not be assumed to behave rigidly. A more accurate method, which can be seen as a generalization of the previous approach, is then to apply a modal reduction to the interface DoFs. Similar to the component reduction techniques of section 3.2, a modal basis is computed for the interface DoFs by solving an eigenvalue problem. By truncating the

resulting interface modes the physical interface DoFs can be replaced by a smaller subset of modal coordinates.

Interface reduction can be applied either on substructure level or on assembly level. Since the interface behavior is dependent on all components that it connects, it is likely that component's interface reduction in general gives less accurate results than when information of the assembled structure are used to reduce the interface DoFs. However, it has been demonstrated how a component level reduction of the interface is successful when the interfaces of components connected together are reduced using the same basis [4]. For this reason in the following much emphasis will be given to the approach accounting for the interface modal reduction at substructure level. This idea will then be employed on applications concerning the dynamic coupling of extended moving interfaces and the reduction of cyclic symmetric structures (Chapter 4).

Although the interface DoFs approximation by rigid motions is useful for some structures, it is often preferred to allow interface deformation. In those cases the more general modal truncation method can be applied. The methodology here presented is based on the observation that the interface behavior does not require in general detailed insight in the components' dynamics, since an accurate representation of the static behavior at the interface is often sufficient. This condition is guaranteed by both Guyan and *CB*-CMS method. In fact, for these methods the component's interface motion is uniquely described by a subset constraint modes[2], whose number n_i strictly depends on the FE mesh at the boundary.

For large and complex component's interfaces the number of constraint modes (and the number of interface DoFs they involve) is usually large and a further reduction is often desirable. In this regard, among the various approaches proposed, that of the *Characteristic Constraint modes* (*CC* modes) [5] appears as the most appealing. According to this method, the interface DoFs $\boldsymbol{x}_i$ can be reduced by using a new set of modes that correspond to the more natural physical motion of the interface. Generally, this is posed as an eigenvalue problem for the constraint mode partitions of the previously condensed Guyan or *CB*-CMS mass and stiffness matrices (Eqns. 3.23 and 3.28). This idea was first proposed in [26] and later worked out by Tran [27, 28] for the reduction of cyclic symmetric structures.

[2]In general the interface DoFs are included into the set of boundary DoFs: $\boldsymbol{x}_b = \left\{\boldsymbol{x}_i^T \; \boldsymbol{x}_a^T\right\}^T$ (see subsection 3.2.2).

In this section the original *Gram-Schmidt Interface* (*GSI*) reduction method for the modal reduction of interface DoFs is presented. Such technique, already proposed in [4], is an upgrade of the pre-existing method based on the *CC* modes formulation given by Castanier et al. [5] and has as a main objective the extension of its applicability to the following two cases:

1. Dynamic assembly of components having non-conforming meshes at the coupling interfaces.
2. Modal reduction of the DoFs at independent frontier of a bladed disk sector treated in cyclic symmetry conditions.

3.4.1 Modal Reduction of Interface Displacements

The starting point for the formulation of the interface reduction method is given by the component's *CB*-CMS EQM (Eqn. 3.27):

$$\begin{bmatrix} \tilde{\boldsymbol{M}}_{bb} & \tilde{\boldsymbol{M}}_{bk} \\ \tilde{\boldsymbol{M}}_{kb} & \boldsymbol{I}_{kk} \end{bmatrix} \begin{Bmatrix} \ddot{\boldsymbol{x}}_b \\ \ddot{\eta}_k \end{Bmatrix} + \begin{bmatrix} \tilde{\boldsymbol{K}}_{bb} & \boldsymbol{0} \\ \boldsymbol{0} & \Omega_{kk}^2 \end{bmatrix} \begin{Bmatrix} \boldsymbol{x}_b \\ \eta_k \end{Bmatrix} = \begin{Bmatrix} \tilde{\boldsymbol{f}}_b \\ \tilde{f}_k \end{Bmatrix}$$

By taking only the constraint modes partitions $\tilde{\boldsymbol{M}}_{bb}$ and $\tilde{\boldsymbol{K}}_{bb}$ of the *CB*-CMS mass and stiffness matrices, one finds:

$$\tilde{\boldsymbol{M}}_{bb}\,\ddot{\boldsymbol{x}}_b + \tilde{\boldsymbol{K}}_{bb}\,\boldsymbol{x}_b = \tilde{\boldsymbol{f}}_b \tag{3.29}$$

Assuming the external forces equal to zero and looking for the non-trivial solution, the following eigenproblem is found:

$$(\tilde{\boldsymbol{K}}_{bb} - \omega_{b,j}^2 \tilde{\boldsymbol{M}}_{bb})\varphi_{b,j} = \boldsymbol{0} \qquad \forall\ j = 1,\ldots,n_b \tag{3.30}$$

where $\omega_{b,j}^2$ and $\varphi_{b,j}$ are the j^{th} eigenvalue and mass normalized *CC* mode respectively. The complete set of *CC* modes can be arranged (for increasing eigenvalues) as the columns of the following *CC* modal matrix:

$$\Phi_{bb} = \begin{bmatrix} \varphi_{b,1} & \varphi_{b,2} & \ldots & \varphi_{b,n_b} \end{bmatrix} \tag{3.31}$$

However, the definition of a subset with $n_w \ll n_b$ *CC* modes necessary to operate the component's interface reduction, depends on which sets of DoFs are actually included into $\boldsymbol{x}_b$. In this regard, the method based on the *CC* modes has been improved by Battiato et al. [4] since two different cases may occur:

1. The boundary DoFs coincides with the interface DoFs: $\boldsymbol{x}_b \equiv \boldsymbol{x}_i$;
2. The boundary DoFs includes the sets of interface and active DoFs: $\boldsymbol{x}_b \equiv \left\{\boldsymbol{x}_i^T \; \boldsymbol{x}_a^T\right\}^T$.

Boundary Including Only Interface DoFs

When $\boldsymbol{x}_b \equiv \boldsymbol{x}_i$ the whole modal matrix of Eqn. 3.31 can be employed to express the interface displacements $\boldsymbol{x}_i$ in terms of the modal coordinates η_i:

$$\boldsymbol{x}_i = \boldsymbol{\Phi}_{bb}\eta_b = \boldsymbol{\Phi}_{ii}\eta_i \tag{3.32}$$

where the subscript "b" has been replaced by "i". If a subset of $n_w \ll n_i$ *CC* modes describing the dominant physical modes at the interface is retained, Eqn. 3.32 is no more an equality and the following approximation occurs:

$$\boldsymbol{x}_i \approx \sum_{j=1}^{n_w} \varphi_{i,j}\eta_j = \boldsymbol{\Phi}_{iw}\eta_w \tag{3.33}$$

Finally, starting from the *CB*-CMS generalized coordinate vector, the transformation leading to a reduced set of interface DoFs is:

$$\boldsymbol{x}_{CB} = \begin{Bmatrix} \boldsymbol{x}_i \\ \eta_k \end{Bmatrix} \approx \begin{bmatrix} \boldsymbol{\Phi}_{iw} & \boldsymbol{0}_{ik} \\ \boldsymbol{0}_{kw} & \boldsymbol{I}_{kk} \end{bmatrix} \begin{Bmatrix} \eta_w \\ \eta_k \end{Bmatrix} = \boldsymbol{R}_{CC} \begin{Bmatrix} \eta_w \\ \eta_k \end{Bmatrix} \tag{3.34}$$

where the new reduction basis is thus given by:

$$\boldsymbol{R}_{CC} = \begin{bmatrix} \boldsymbol{\Phi}_{iw} & \boldsymbol{0}_{ik} \\ \boldsymbol{0}_{kw} & \boldsymbol{I}_{kk} \end{bmatrix} \tag{3.35}$$

By projecting Eqn. 3.27 onto $\boldsymbol{R}_{CC}$, a further reduction of the equations of motion is obtained:

$$\boldsymbol{M}_{CC}\,\ddot{\boldsymbol{x}}_{CC} + \boldsymbol{K}_{CC}\,\boldsymbol{x}_{CC} = \boldsymbol{f}_{CC} \tag{3.36}$$

where

$$\begin{aligned} \boldsymbol{M}_{CC} &= \boldsymbol{R}_{CC}^{T}\boldsymbol{M}_{CB}\boldsymbol{R}_{CC} = \begin{bmatrix} \boldsymbol{I}_{ww} & \boldsymbol{\Phi}_{iw}^{T}\tilde{\boldsymbol{M}}_{ik} \\ \tilde{\boldsymbol{M}}_{ki}\boldsymbol{\Phi}_{iw} & \boldsymbol{I}_{kk} \end{bmatrix} \\ \boldsymbol{K}_{CC} &= \boldsymbol{R}_{CC}^{T}\boldsymbol{K}_{CB}\boldsymbol{R}_{CC} = \begin{bmatrix} \Omega_{ww}^{2} & \boldsymbol{0}_{ik} \\ \boldsymbol{0}_{kw} & \Omega_{kk}^{2} \end{bmatrix} \end{aligned} \tag{3.37}$$

are the *CC* component's mass and stiffness matrices and:

$$\boldsymbol{x}_{CC} = \begin{Bmatrix} \eta_w \\ \eta_k \end{Bmatrix} \qquad \boldsymbol{f}_{CC} = \begin{Bmatrix} \boldsymbol{\Phi}_{iw}^{T}\tilde{\boldsymbol{f}}_i \\ \tilde{\boldsymbol{f}}_k \end{Bmatrix} \tag{3.38}$$

are the *CC* generalized coordinates and force vectors. Note that $\boldsymbol{K}_{CC}$ is now fully diagonal since the partition Ω_{ww}^{2} is a diagonal matrix containing the first n_w eigenvalues $\omega_{b,j}^{2}$ (Eqn. 3.30).

Boundary Including Interface and Active DoFs

For general applications concerning dynamic analyses on ROM of complex structures, no other sets of master DoFs have to be retained besides those belonging to the interfaces. For instance, ROMs of bladed disks do not necessarily require active DoFs for the direct application of physical excitations. In fact, in the case of complex pressure distributions acting on the blades' airfoils it is common to modalize the nodal forces. Moreover, if stresses and strains have to be determined on already condensed physical DoFs, their distributions can be easily recovered by expanding the component's response through the component-mode matrix $\boldsymbol{R}$. However, retaining a set of active DoFs as a master may be convenient when the following two scenarios occur:

1. For non-linear dynamic analyses involving contacts phenomena occurring at the interface between adjacent substructures, a set of active DoFs may help in the direct estimation of the physical contact forces.

2. The storage of the component-mode matrix is often prohibitive when the full FE model of a structure consists on a huge number of DoFs. Hence, at a preliminary design stage when sensitivity analyses on model parameters (geometric, contact, ect.) have to be performed, a further set of master DoFs

may be retained either for the physical forces application or the component's response monitoring.

For these reasons it is often required to create the ROM of substructures where besides the interface DoFs also an active set of DoFs is retained. Therefore, the modal transformation based on the *CC* modes has to be applied only to the interface DoFs partition, leaving the active DoFs physical as they are. In this regard, the *CC* modal transformation involving the whole set of boundary DoFs is given by:

$$\boldsymbol{x}_b = \begin{Bmatrix} \boldsymbol{x}_i \\ \boldsymbol{x}_a \end{Bmatrix} = \boldsymbol{\Phi}_{bb} \begin{Bmatrix} \eta_i \\ \eta_a \end{Bmatrix} = \begin{bmatrix} \boldsymbol{\Phi}_{ii} & \boldsymbol{\Phi}_{ia} \\ \boldsymbol{\Phi}_{ai} & \boldsymbol{\Phi}_{aa} \end{bmatrix} \begin{Bmatrix} \eta_i \\ \eta_a \end{Bmatrix} \tag{3.39}$$

where the modal matrix $\boldsymbol{\Phi}_{bb}$ has been partitioned according to the two sets of modal coordinates η_i and η_a with size n_i and n_a respectively. By solving the second equation for η_a and substituting the result into the first, Eqn. 3.39 becomes:

$$\boldsymbol{x}_b = \begin{Bmatrix} \boldsymbol{x}_i \\ \boldsymbol{x}_a \end{Bmatrix} = \begin{bmatrix} \boldsymbol{\Phi}_{ii} - \boldsymbol{\Phi}_{ia}\boldsymbol{\Phi}_{aa}^{-1}\boldsymbol{\Phi}_{ai} & \boldsymbol{\Phi}_{ia}\boldsymbol{\Phi}_{aa}^{-1} \\ \boldsymbol{0}_{ai} & \boldsymbol{I}_{aa} \end{bmatrix} \begin{Bmatrix} \eta_i \\ \boldsymbol{x}_a \end{Bmatrix} \tag{3.40}$$

Eqn. 3.40 clearly shows the coupling between $\boldsymbol{x}_i$ and $\boldsymbol{x}_a$. Since the *CC* modal matrix $\boldsymbol{\Phi}_{bb}$ has been built by ordering the *CC* modes for increasing eigenvalues (Eqn. 3.31), a first DoFs' reduction can be achieved by performing the modal truncation of the highest eigenvalues *CC* modes. Under this consideration, the coupling between $\boldsymbol{x}_i$ and $\boldsymbol{x}_a$ might be removed by truncating the last n_a columns (*CC* modes) of the modal matrix in Eqn. 3.39, which corresponds to get rid of the submatrices $\boldsymbol{\Phi}_{ia}$ and $\boldsymbol{\Phi}_{aa}$. Hence, the coordinates transformation of Eqn. 3.40 becomes:

$$\boldsymbol{x}_b = \begin{Bmatrix} \boldsymbol{x}_i \\ \boldsymbol{x}_a \end{Bmatrix} = \begin{bmatrix} \boldsymbol{\Phi}_{ii} - \cancel{\boldsymbol{\Phi}_{ia}\boldsymbol{\Phi}_{aa}^{-1}\boldsymbol{\Phi}_{ai}} & \cancel{\boldsymbol{\Phi}_{ia}\boldsymbol{\Phi}_{aa}^{-1}} \\ \boldsymbol{0}_{ai} & \boldsymbol{I}_{aa} \end{bmatrix} \begin{Bmatrix} \eta_i \\ \boldsymbol{x}_a \end{Bmatrix} \approx \begin{bmatrix} \boldsymbol{\Phi}_{ii} & \boldsymbol{0}_{ia} \\ \boldsymbol{0}_{ai} & \boldsymbol{I}_{aa} \end{bmatrix} \begin{Bmatrix} \eta_i \\ \boldsymbol{x}_a \end{Bmatrix} \tag{3.41}$$

and the interface DoFs partition of the *CB*-CMS generalized coordinates vector would thus be modalized by means of the following coordinates transformation:

$$\boldsymbol{x}_{CB} = \begin{Bmatrix} \boldsymbol{x}_b \\ \eta_k \end{Bmatrix} = \begin{Bmatrix} \boldsymbol{x}_i \\ \boldsymbol{x}_a \\ \eta_k \end{Bmatrix} \approx \begin{bmatrix} \boldsymbol{\Phi}_{ii} & \boldsymbol{0}_{ia} & \boldsymbol{0}_{ik} \\ \boldsymbol{0}_{ai} & \boldsymbol{I}_{aa} & \boldsymbol{0}_{ak} \\ \boldsymbol{0}_{ki} & \boldsymbol{0}_{ka} & \boldsymbol{I}_{kk} \end{bmatrix} \begin{Bmatrix} \eta_i \\ \boldsymbol{x}_a \\ \eta_k \end{Bmatrix} \tag{3.42}$$

Being the eigenvectors of the eigenproblem in Eqn. 3.30, the columns of Φ_{bb} are linearly independent to each other by definition. However, the same does not hold for the columns of Φ_{ii}, which is just a submatrix of Φ_{bb} (Eqn. 3.39). In fact, Φ_{ii} appears to be in general ill-conditioned, meaning that some of its columns are nearly aligned to each other, i.e. they are nearly linear depended. This may lead to some null eigenvalues when an eigenanalisys on the $\boldsymbol{M}_{CC}$ and $\boldsymbol{K}_{CC}$ is performed, even if the substructure is constrained so that no rigid body modes occur. In order to avoid this problem, the columns of Φ_{ii} may be orthonormalized by using the Gram-Schmidt algorithm:

$$\Phi_{ii} \xrightarrow{\textit{Gram-Schmidt}} \hat{\Phi}_{ii} \tag{3.43}$$

The principle of the Gram-Schmidt algorithm is graphically explained in Figure 3.4. Two modes, nearly linear dependent to each other (represented by the two vectors $\varphi_{i,1}$ and $\varphi_{i,2}$, almost parallel) are replaced by two orthonormalized modes (vectors $\hat{\varphi}_{i,1}$ and $\hat{\varphi}_{i,2}$). At the end of this process the columns of $\hat{\Phi}_{ii}$ satisfy the following conditions:

$$\hat{\varphi}_{i,j}^T \hat{\varphi}_{i,z} = \begin{cases} 0 & \text{when } j \neq z \quad (\textbf{\textit{orthogonal}} \textit{ vectors}) \\ 1 & \text{when } j = z \quad (\textbf{\textit{unit}} \textit{ vectors: } \|\hat{\varphi}_{i,j}\| = 1) \end{cases} \tag{3.44}$$

and Eqn. 3.42 becomes:

$$\boldsymbol{x}_{CB} = \begin{Bmatrix} \boldsymbol{x}_i \\ \boldsymbol{x}_a \\ \eta_k \end{Bmatrix} \approx \begin{bmatrix} \hat{\Phi}_{ii} & \boldsymbol{0}_{ia} & \boldsymbol{0}_{ik} \\ \boldsymbol{0}_{ai} & \boldsymbol{I}_{aa} & \boldsymbol{0}_{ak} \\ \boldsymbol{0}_{ki} & \boldsymbol{0}_{ka} & \boldsymbol{I}_{kk} \end{bmatrix} \begin{Bmatrix} \eta_i \\ \boldsymbol{x}_a \\ \eta_k \end{Bmatrix} \tag{3.45}$$

Henceforth in this section the "hat" is omitted and the Gram-Schmidt orthonormalization is considered applied to the columns of Φ_{ii} unless otherwise specified.

The number of interface DoFs can actually be reduced if a subset of $n_w \ll n_i$ columns of Φ_{ii} is kept. Therefore, Eqn. 3.45 can be further approximated as:

$$\boldsymbol{x}_{CB} = \begin{Bmatrix} \boldsymbol{x}_i \\ \boldsymbol{x}_a \\ \eta_k \end{Bmatrix} \approx \begin{bmatrix} \Phi_{iw} & \boldsymbol{0}_{ia} & \boldsymbol{0}_{ik} \\ \boldsymbol{0}_{aw} & \boldsymbol{I}_{aa} & \boldsymbol{0}_{ak} \\ \boldsymbol{0}_{kw} & \boldsymbol{0}_{ka} & \boldsymbol{I}_{kk} \end{bmatrix} \begin{Bmatrix} \eta_w \\ \boldsymbol{x}_a \\ \eta_k \end{Bmatrix} = \boldsymbol{R}_{GS} \begin{Bmatrix} \eta_w \\ \boldsymbol{x}_a \\ \eta_k \end{Bmatrix} \tag{3.46}$$

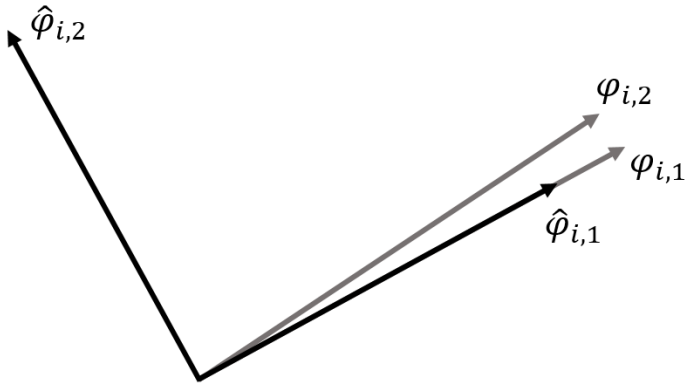

Fig. 3.4 Gram-Schmidt orthonormalization of two modes. Two modes, nearly linear dependent to each other (represented by the two vectors $\varphi_{i,1}$ and $\varphi_{i,2}$, almost parallel) are replaced by two orthonormalized modes (vectors $\hat{\varphi}_{i,1}$ and $\hat{\varphi}_{i,2}$).

where Φ_{iw} is the truncated basis of *Gram-Schmidt Interface* modes (*GSI* modes) and $\boldsymbol{R}_{GS}$ represents the new reduction basis. Finally, the reduced EQM have the same form of those in Eqn. 3.36. The component's reduced matrices and force vector are obtained by employing the matrix $\boldsymbol{R}_{GS}$ instead of $\boldsymbol{R}_{CC}$ in the transformations of Eqns. 3.37 and 3.38.

3.4.2 Multiple Interfaces Reduction

Components sharing more than one interface with their neighbors are no exceptions. For example, any of the middle components of the beam shown in Figure 3.1 could be representative of the mentioned situation. In those cases the various sets of interface DoFs have to be reduced one by one. The procedure adopted to carry out these subsequent reductions is still that accounting for a partitioning of the boundary DoFs $\boldsymbol{x}_b$ into the sets $\boldsymbol{x}_i$ and $\boldsymbol{x}_a$ (Eqn. 3.39). In particular, let us consider the *CB*-CMS ROM of a component having N_i interfaces (Figure 3.5). The global vector of interface DoFs $\boldsymbol{x}_i$ can therefore be partitioned by grouping the DoFs interface by interface:

$$\boldsymbol{x}_i = \left\{ \boldsymbol{x}_{i_1}^T \ \ldots \ \boldsymbol{x}_{i_j}^T \ \ldots \ \boldsymbol{x}_{i_{N_i}}^T \right\}^T \tag{3.47}$$

When reducing the size of the j^{th} interface, a new set of active DoFs $\boldsymbol{x}'_{a_j}$ has to be defined as:

$$\boldsymbol{x}'_{a_j} = \left\{ \boldsymbol{x}_{i_1}^T \ \ldots \ \boldsymbol{x}_{i_{j-1}}^T \quad \boldsymbol{x}_{i_{j+1}}^T \ \ldots \ \boldsymbol{x}_{i_{N_i}}^T \quad \boldsymbol{x}_a^T \right\}^T \tag{3.48}$$

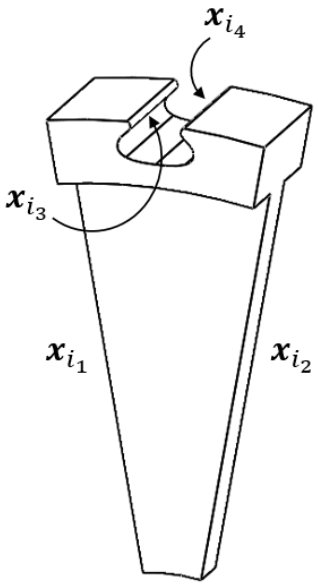

Fig. 3.5 Example of component with multiple interfaces.

which collects the DoFs of all the interfaces except those of the j^{th} and the original set of active DoFs $\boldsymbol{x}_a$. Therefore, as done in Eqn. 3.41 the boundary DoFs can be partitioned as:

$$\boldsymbol{x}_b = \begin{Bmatrix} \boldsymbol{x}_{i_j} \\ \boldsymbol{x}'_{a_j} \end{Bmatrix} \tag{3.49}$$

To this point the procedure leading to the matrix $\boldsymbol{\Phi}_{i_j w_j}$, aimed at reducing the j^{th} interface with n_{w_j} *GSI* modes, is exactly that defined by all the equations between Eqn. 3.39 and Eqn. 3.43. Once this procedure is carried out for all the interfaces, N_i matrices $\boldsymbol{\Phi}_{i_j w_j}$ are found and the *CB*-CMS generalized coordinate vector can be further condensed as:

$$\boldsymbol{x}_{CB} = \begin{Bmatrix} \boldsymbol{x}_{i_1} \\ \vdots \\ \boldsymbol{x}_{i_{N_i}} \\ \boldsymbol{x}_a \\ \eta_k \end{Bmatrix} \approx \begin{bmatrix} \boldsymbol{\Phi}_{i_1 w_1} & \cdots & \boldsymbol{0}_{i_1 w_{N_i}} & \boldsymbol{0}_{i_1 a} & \boldsymbol{0}_{i_1 k} \\ \vdots & \ddots & \vdots & \vdots & \vdots \\ \boldsymbol{0}_{i_{N_i} w_1} & \cdots & \boldsymbol{\Phi}_{i_{N_i} w_{N_i}} & \boldsymbol{0}_{i_{N_i}, a} & \boldsymbol{0}_{i_{N_i} k} \\ \boldsymbol{0}_{a, w_1} & \cdots & \boldsymbol{0}_{a, w_{N_i}} & \boldsymbol{I}_{aa} & \boldsymbol{0}_{ak} \\ \boldsymbol{0}_{k, w_1} & \cdots & \boldsymbol{0}_{k, w_{N_i}} & \boldsymbol{0}_{ka} & \boldsymbol{I}_{kk} \end{bmatrix} \begin{Bmatrix} \eta_{w_1} \\ \vdots \\ \eta_{w_{N_i}} \\ \boldsymbol{x}_a \\ \eta_k \end{Bmatrix} \tag{3.50}$$

where

$$\boldsymbol{R}_{GS} = \begin{bmatrix} \boldsymbol{\Phi}_{i_1 w_1} & \cdots & \boldsymbol{0}_{i_1 w_{N_i}} & \boldsymbol{0}_{i_1 a} & \boldsymbol{0}_{i_1 k} \\ \vdots & \ddots & \vdots & \vdots & \vdots \\ \boldsymbol{0}_{i_{N_i} w_1} & \cdots & \boldsymbol{\Phi}_{i_{N_i} w_{N_i}} & \boldsymbol{0}_{i_{N_i} a} & \boldsymbol{0}_{i_{N_i} k} \\ \boldsymbol{0}_{a w_1} & \cdots & \boldsymbol{0}_{a w_{N_i}} & \boldsymbol{I}_{aa} & \boldsymbol{0}_{ak} \\ \boldsymbol{0}_{k w_1} & \cdots & \boldsymbol{0}_{k w_{N_i}} & \boldsymbol{0}_{ka} & \boldsymbol{I}_{kk} \end{bmatrix} \tag{3.51}$$

is the interface reduction basis, which transforms the *CB*-CMS EQM into the form of Eqn. 3.36. The component's reduced matrices and force vector are therefore obtained by employing the matrix $\boldsymbol{R}_{GS}$ of Eqn. 3.50, in the transformations of Eqns. 3.37 and 3.38.

Besides reducing the total number of component's DoFs, interface reduction methods can also be used to decrease the size of the component-mode matrix. Thereby, handling with the large component-mode matrices, which can easily take up many gigabytes of memory and storage space, is greatly simplified if a data recovery has to be performed. This can be achieved by simply combining the two subsequent coordinate transformations that have led Eqn. 3.36:

1. Component's reduction using the *CB*-CMS method:

$$\begin{Bmatrix} \boldsymbol{x}_i \\ \boldsymbol{x}_e \end{Bmatrix} \approx \begin{bmatrix} \boldsymbol{I}_{ie} & \boldsymbol{0} \\ \boldsymbol{\Psi}_{ee} & \boldsymbol{\Phi}_{ek} \end{bmatrix} \begin{Bmatrix} \boldsymbol{x}_i \\ \eta_k \end{Bmatrix} = \boldsymbol{R}_{CB} \boldsymbol{x}_{CB}$$

2. Application of the interface reduction basis:

$$\begin{Bmatrix} \boldsymbol{x}_i \\ \eta_k \end{Bmatrix} \approx \begin{bmatrix} \boldsymbol{\Phi}_{iw} & \boldsymbol{0}_{ik} \\ \boldsymbol{0}_{kw} & \boldsymbol{I}_{kk} \end{bmatrix} \begin{Bmatrix} \eta_w \\ \eta_k \end{Bmatrix} = \boldsymbol{R}_{GS} \begin{Bmatrix} \eta_w \\ \eta_k \end{Bmatrix}$$

In general, due to the large number of interior DoFs, the first transformation requires the largest amount of memory space. By combining the two transformation the reduced component-mode matrix can be found:

$$\begin{Bmatrix} \boldsymbol{x}_i \\ \boldsymbol{x}_e \end{Bmatrix} \approx \begin{bmatrix} \boldsymbol{I}_{ie} & \boldsymbol{0} \\ \boldsymbol{\Psi}_{ee} & \boldsymbol{\Phi}_{ek} \end{bmatrix} \begin{bmatrix} \boldsymbol{\Phi}_{iw} & \boldsymbol{0}_{ik} \\ \boldsymbol{0}_{kw} & \boldsymbol{I}_{kk} \end{bmatrix} \begin{Bmatrix} \eta_w \\ \eta_k \end{Bmatrix} = \boldsymbol{R}_{CB} \boldsymbol{R}_{GS} \begin{Bmatrix} \eta_w \\ \eta_k \end{Bmatrix} = \boldsymbol{R}_{TOT} \begin{Bmatrix} \eta_w \\ \eta_k \end{Bmatrix} \tag{3.52}$$

Due to the interface reduction, the size of $\boldsymbol{R}_{TOT}$ is much smaller than that of $\boldsymbol{R}_{CB}$. Therefore handling with the *GSI* reduced system becomes much easier, while the

results for the condensed DoFs can still be obtained by expanding the solutions found by means of $\boldsymbol{R}_{TOT}$.

3.4.3 Interface Reduction Via Gram-Schmidt Interface Modes: Procedure Summary

The *GSI* reduction method presented in the previous sections is particularly useful when the interface DoFs partitions of a previously condensed *CB*-CMS model have to be reduced is size. The *GSI* reduction method can be summarized in the following few steps:

1. Create the *CB*-CMS ROM of the analyzed component by retaining as master a set of boundary DoFs $\boldsymbol{x}_b$ (Eqn. 3.27);
2. For each set of interface DoFs $\boldsymbol{x}_{i_j}$ contained in $\boldsymbol{x}_b$, rearrange the DoFs as done in Eqn. 3.49 and partition the corresponding *CB*-CMS matrices accordingly;
3. For each couple of *CB*-CMS matrices, i.e. the *CB*-CMS mass and stiffness matrices, compute the *CC* modal matrix Φ_{bb} by solving the eigenproblem of Eqn. 3.30;
4. Apply the Gram-Schmidt ortonormalization process to the columns of $\Phi_{i_j i_j}$ (partition of Φ_{bb}) and retain the first n_{w_j} *GSI* modes;
5. Reduce the *CB*-CMS model by using the coordinate transformation of Eqn. 3.49.

3.5 Assembly of Component Models

After having created the ROMs of components according to the methods presented in the previous sections, the next step is to assemble these models so that the structural dynamic model of the whole system can be obtained. The idea behind the classic components' assembly procedure is the same adopted for regular FE models. Here the physical DoFs at coincident interfaces are enforced to be equal by writing simple *compatibility equations*. As it will be shown in the next sections, this procedure is straightforward for either FE models or superelements having *conforming* interfaces,

meaning that their nodes share the same geometric locations and the element shape functions are matching. Differently, the assembly of substructures featuring non-conforming meshes leads to a further approximated ROM of the assembled structure.

This section outlines the most common substructures' assembly approaches and highlights the advantages of performing the component's coupling by enforcing the compatibility conditions in a space spanned by the interface modes. Such coupling process appears particularly useful when components with non-conforming meshes at the coupling interfaces are assembled.

3.5.1 Assembly of Components with Conforming Interfaces

Let us consider the superelements created by applying the *CB*-CMS method on two substructures denoted by α and β. The *CB*-CMS generalized coordinates vectors for the two components are $\boldsymbol{x}_{CB}^{\alpha}$ and $\boldsymbol{x}_{CB}^{\beta}$ respectively (Eqs. 3.26). Moreover, for both components let us assume the sets of boundary DoFs $\boldsymbol{x}_{b_\alpha}^{\alpha}$ and $\boldsymbol{x}_{b_\beta}^{\beta}$ consisting of both interface and active DoFs:

$$\boldsymbol{x}_{b_\alpha}^{\alpha} = \begin{Bmatrix} \boldsymbol{x}_{i_\alpha}^{\alpha} \\ \boldsymbol{x}_{a_\alpha}^{\alpha} \end{Bmatrix} \qquad \boldsymbol{x}_{b_\beta}^{\beta} = \begin{Bmatrix} \boldsymbol{x}_{i_\beta}^{\beta} \\ \boldsymbol{x}_{a_\beta}^{\beta} \end{Bmatrix} \tag{3.53}$$

where

$$\begin{cases} \boldsymbol{x}_{i_\alpha}^{\alpha} \in \mathbb{R}^{n_{i_\alpha} \times 1} & \boldsymbol{x}_{i_\beta}^{\beta} \in \mathbb{R}^{n_{i_\beta} \times 1} & \text{with} \quad n_{i_\alpha} = n_{i_\beta} = n_i \\ \boldsymbol{x}_{a_\alpha}^{\alpha} \in \mathbb{R}^{n_{a_\alpha} \times 1} & \boldsymbol{x}_{a_\beta}^{\beta} \in \mathbb{R}^{n_{a_\beta} \times 1} & \text{with} \quad n_{a_\alpha} \neq n_{a_\beta} \end{cases} \tag{3.54}$$

Physical Compatibility Conditions

If conforming interfaces were present in the original FE models, the superelements coupling can be easily performed by just writing the following compatibility conditions:

$$\boldsymbol{x}_i^{\alpha} = \boldsymbol{x}_i^{\beta} = \boldsymbol{x}_i \tag{3.55}$$

These can be enforced by means of the boolean matrix $\boldsymbol{C}_{CB}$ that is here named as *compatibility matrix*:

$$\begin{Bmatrix} \boldsymbol{x}_{CB}^{\alpha} \\ \boldsymbol{x}_{CB}^{\beta} \end{Bmatrix} = \begin{Bmatrix} \boldsymbol{x}_{i}^{\alpha} \\ \boldsymbol{x}_{a_\alpha}^{\alpha} \\ \eta_{k_\alpha}^{\alpha} \\ \boldsymbol{x}_{i}^{\beta} \\ \boldsymbol{x}_{a_\beta}^{\beta} \\ \eta_{k_\beta}^{\beta} \end{Bmatrix} = \begin{bmatrix} \boldsymbol{0} & \boldsymbol{0} & \boldsymbol{I} & \boldsymbol{0} & \boldsymbol{0} \\ \boldsymbol{I} & \boldsymbol{0} & \boldsymbol{0} & \boldsymbol{0} & \boldsymbol{0} \\ \boldsymbol{0} & \boldsymbol{0} & \boldsymbol{0} & \boldsymbol{I} & \boldsymbol{0} \\ \boldsymbol{0} & \boldsymbol{0} & \boldsymbol{I} & \boldsymbol{0} & \boldsymbol{0} \\ \boldsymbol{0} & \boldsymbol{I} & \boldsymbol{0} & \boldsymbol{0} & \boldsymbol{0} \\ \boldsymbol{0} & \boldsymbol{0} & \boldsymbol{0} & \boldsymbol{0} & \boldsymbol{I} \end{bmatrix} \begin{Bmatrix} \boldsymbol{x}_{a_\alpha}^{\alpha} \\ \boldsymbol{x}_{a_\beta}^{\beta} \\ \boldsymbol{x}_{i} \\ \eta_{k_\alpha}^{\alpha} \\ \eta_{k_\beta}^{\beta} \end{Bmatrix} = \boldsymbol{C}_{CB} \begin{Bmatrix} \boldsymbol{x}_{a_\alpha}^{\alpha} \\ \boldsymbol{x}_{a_\beta}^{\beta} \\ \boldsymbol{x}_{i} \\ \eta_{k_\alpha}^{\alpha} \\ \eta_{k_\beta}^{\beta} \end{Bmatrix} \tag{3.56}$$

Lastly, the assembled *CB*-CMS matrices and vectors are given by:

$$\boldsymbol{M}_{CB}^{A} = \boldsymbol{C}_{CB}^{T} \begin{bmatrix} \boldsymbol{M}_{CB}^{\alpha} & \boldsymbol{0} \\ \boldsymbol{0} & \boldsymbol{M}_{CB}^{\beta} \end{bmatrix} \boldsymbol{T}_{CB} \qquad \boldsymbol{K}_{CB}^{A} = \boldsymbol{C}_{CB}^{T} \begin{bmatrix} \boldsymbol{K}_{CB}^{\alpha} & \boldsymbol{0} \\ \boldsymbol{0} & \boldsymbol{K}_{CB}^{\beta} \end{bmatrix} \boldsymbol{C}_{CB}$$

$$\boldsymbol{x}_{CB}^{A} = \begin{Bmatrix} \boldsymbol{x}_{a_\alpha}^{\alpha} \\ \boldsymbol{x}_{a_\beta}^{\beta} \\ \boldsymbol{x}_{i} \\ \eta_{k_\alpha}^{\alpha} \\ \eta_{k_\beta}^{\beta} \end{Bmatrix} \qquad \boldsymbol{f}_{CB}^{A} = \boldsymbol{C}_{CB}^{T} \begin{Bmatrix} \boldsymbol{f}_{CB}^{\alpha} \\ \boldsymbol{f}_{CB}^{\beta} \end{Bmatrix} \tag{3.57}$$

where the superscript A stands for assembled. Once the assembled ROM is obtained, the assembled interface DoFs $\boldsymbol{x}_i$ may be reduced by employing the method proposed in section 3.4.1.

Modal Compatibility Conditions

An alternative assembly procedure is that involving the modal coordinates of a set of interface *GSI* modes. This however is not straightforward as in the case previously discussed. In particular, let us suppose the substructures α and β reduced by using the coordinates transformation of Eqn. 3.46. Since the interface modal coordinates $\eta_{w_\alpha}^{\alpha}$ and $\eta_{w_\beta}^{\beta}$ refer to different reduction bases of *GSI* modes, the coupling between the two substructure can not be directly imposed. The compatibility conditions between these sets of modal coordinates can be enforced if and only if a common basis $\Phi_{iw_\gamma}^{\gamma}$ of n_{w_γ} *GSI* modes is defined from the truncated bases $\Phi_{iw_\alpha}^{\alpha}$ and $\Phi_{iw_\beta}^{\beta}$. The new modal matrix $\Phi_{iw_\gamma}^{\gamma}$ can then be used to reduce both the interfaces according to

the following transformations:

$$\boldsymbol{x}_i^{\alpha} \approx \boldsymbol{\Phi}_{iw_\gamma}^{\gamma} \eta_{w_\gamma}^{\alpha} \qquad \boldsymbol{x}_i^{\beta} \approx \boldsymbol{\Phi}_{iw_\gamma}^{\gamma} \eta_{w_\gamma}^{\beta} \tag{3.58}$$

The assembled ROM is thus obtained by enforcing the compatibility conditions $\eta_{w_\gamma}^{\alpha} = \eta_{w_\gamma}^{\beta} = \eta_{w_\gamma}$. Therefore, considering for each substructure the reduced order vector at the right-hand side of Eqn. 3.46, the assembled ROM is obtained by using the boolean matrix $\boldsymbol{C}_{GS}$:

$$\begin{Bmatrix} \eta_{w_\gamma}^{\alpha} \\ \boldsymbol{x}_{a_\alpha}^{\alpha} \\ \eta_{k_\alpha}^{\alpha} \\ \eta_{w_\gamma}^{\beta} \\ \boldsymbol{x}_{a_\beta}^{\beta} \\ \eta_{k_\beta}^{\beta} \end{Bmatrix} = \begin{bmatrix} \boldsymbol{0} & \boldsymbol{0} & \boldsymbol{I} & \boldsymbol{0} & \boldsymbol{0} \\ \boldsymbol{I} & \boldsymbol{0} & \boldsymbol{0} & \boldsymbol{0} & \boldsymbol{0} \\ \boldsymbol{0} & \boldsymbol{0} & \boldsymbol{0} & \boldsymbol{I} & \boldsymbol{0} \\ \boldsymbol{0} & \boldsymbol{0} & \boldsymbol{I} & \boldsymbol{0} & \boldsymbol{0} \\ \boldsymbol{0} & \boldsymbol{I} & \boldsymbol{0} & \boldsymbol{0} & \boldsymbol{0} \\ \boldsymbol{0} & \boldsymbol{0} & \boldsymbol{0} & \boldsymbol{0} & \boldsymbol{I} \end{bmatrix} \begin{Bmatrix} \boldsymbol{x}_{a_\alpha}^{\alpha} \\ \boldsymbol{x}_{a_\beta}^{\beta} \\ \eta_{w_\gamma} \\ \eta_{k_\alpha}^{\alpha} \\ \eta_{k_\beta}^{\beta} \end{Bmatrix} = \boldsymbol{C}_{GS} \begin{Bmatrix} \boldsymbol{x}_{a_\alpha}^{\alpha} \\ \boldsymbol{x}_{a_\beta}^{\beta} \\ \eta_{w_\gamma} \\ \eta_{k_\alpha}^{\alpha} \\ \eta_{k_\beta}^{\beta} \end{Bmatrix} \tag{3.59}$$

Finally, the assembled reduced order matrices and vectors are given by:

$$\boldsymbol{M}_{GS}^{A} = \boldsymbol{C}_{GS}^{T} \begin{bmatrix} \boldsymbol{M}_{GS}^{\alpha} & \boldsymbol{0} \\ \boldsymbol{0} & \boldsymbol{M}_{GS}^{\beta} \end{bmatrix} \boldsymbol{C}_{GS} \qquad \boldsymbol{K}_{GS}^{A} = \boldsymbol{C}_{GS}^{T} \begin{bmatrix} \boldsymbol{K}_{GS}^{\alpha} & \boldsymbol{0} \\ \boldsymbol{0} & \boldsymbol{K}_{GS}^{\beta} \end{bmatrix} \boldsymbol{C}_{GS}$$

$$\boldsymbol{x}_{GS}^{A} = \begin{Bmatrix} \boldsymbol{x}_{a_\alpha}^{\alpha} \\ \boldsymbol{x}_{a_\beta}^{\beta} \\ \eta_{w_\gamma} \\ \eta_{k_\alpha}^{\alpha} \\ \eta_{k_\beta}^{\beta} \end{Bmatrix} \qquad \boldsymbol{f}_{GS}^{A} = \boldsymbol{C}_{GS}^{T} \begin{Bmatrix} \boldsymbol{f}_{GS}^{\alpha} \\ \boldsymbol{f}_{GS}^{\beta} \end{Bmatrix} \tag{3.60}$$

Since the interface modes evidence the characteristic motion of the interfaces, the assembly procedure here presented provides a physical insight into the transmission of vibration energy between substructures. In detail, the substructures can be dynamically coupled, and then the energy be transferred from one to the other, if their interfaces' motion is described by the same basis of *GSI* modes. This approach definitely appears as more beneficial than the previous, due to the less number of interface DoFs involved in the coupling procedure.

3.5.2 Assembly of Components with Non-Conforming Interfaces

In the subsection 3.5.1 interface meshes with coincident nodes and matching element shape functions were assumed. However, substructure models are often created by different engineers groups without any consideration for the design of neighboring substructures. Since the models are meshed independently, it is likely that their interface meshes are incompatible. In this case the substructures coupling may require special procedures.

Physical Compatibility Conditions

Instead of remeshing the substructures, one approach would be using the *node collocation method* [29], for which the physical displacements at the nodes of one interface are interpolated at the nodes of the other by using the element shape functions.

Without loss of generality, let us consider again to assemble two superelements obtained by performing *CB*-CMS reductions on the FE models of the generic α and β component. Furthermore it is assumed that the numbers n_{i_α} and n_{i_β} of interface DoFs are different to each other ($n_{i_\alpha} < n_{i_\beta}$). Due to the unequal number of interface DoFs, the compatibility conditions can not longer be expressed using the boolean matrices as in Eqn. 3.56. Instead, a coordinate transformation is needed in order to force the number of interface DoFs of one component (β) to be equal to those of the adjacent one (α). This can be achieved by transforming the nodal displacements at the finer interface (β) into the corresponding displacements at the nodes of the coarser interface (α). The mentioned transformation therefore requires to consider the DoFs $\boldsymbol{x}_{i_\alpha}^{\alpha}$ as *master*, while $\boldsymbol{x}_{i_\beta}^{\beta}$ as *slave*:

$$\boldsymbol{x}_{i_\beta}^{\beta} = \boldsymbol{D}_{\beta\alpha}\boldsymbol{x}_{i_\alpha}^{\beta} \tag{3.61}$$

where $\boldsymbol{D}_{\beta\alpha}$ is the so called *collocation matrix* of size $n_{i_\beta} \times n_{i_\alpha}$, containing the values of the α interface element shape functions at the locations of the β interface nodes, while $\boldsymbol{x}_{i_\alpha}^{\beta}$ are the nodal displacements of the β interface interpolated at the nodes of the coarser grid α (Figure 3.6)
According to Eqn. 3.61 the generalized *CB*-CMS coordinates vector $\boldsymbol{x}_{CB}^{\beta}$ can then be

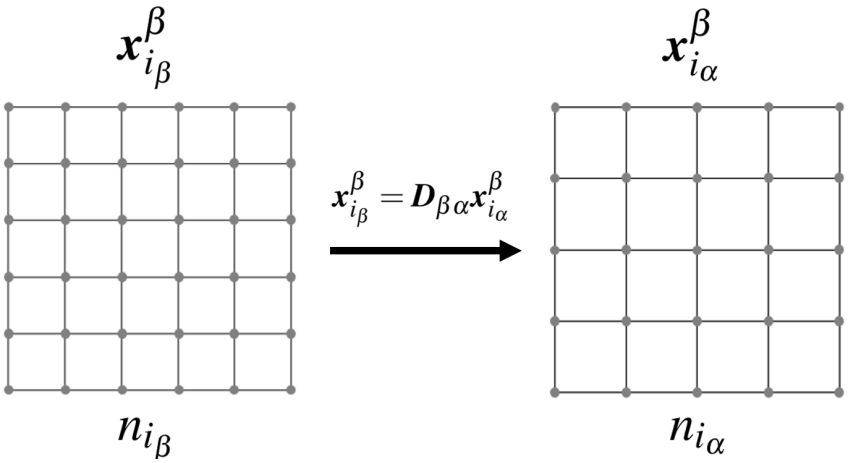

Fig. 3.6 Coordinates transformation operated by the collocation matrix $\boldsymbol{D}_{\beta\alpha}$: the nodal displacements at the finer interface $\boldsymbol{x}^{\beta}_{i_\beta}$ are transformed into the corresponding displacements at the nodes of the coarser interface $\boldsymbol{x}^{\beta}_{i_\alpha}$.

written as:

$$\boldsymbol{x}^{\beta}_{CB} = \begin{Bmatrix} \boldsymbol{x}^{\beta}_{i_\beta} \\ \boldsymbol{x}^{\beta}_{a_\beta} \\ \eta^{\beta}_{k_\beta} \end{Bmatrix} = \boldsymbol{R}_D \begin{Bmatrix} \boldsymbol{x}^{\beta}_{i_\alpha} \\ \boldsymbol{x}^{\beta}_{a_\beta} \\ \eta^{\beta}_{k_\beta} \end{Bmatrix} = \begin{bmatrix} \boldsymbol{D}_{\beta\alpha} & \boldsymbol{0} & \boldsymbol{0} \\ \boldsymbol{0} & \boldsymbol{I} & \boldsymbol{0} \\ \boldsymbol{0} & \boldsymbol{0} & \boldsymbol{I} \end{bmatrix} \begin{Bmatrix} \boldsymbol{x}^{\beta}_{i_\alpha} \\ \boldsymbol{x}^{\beta}_{a_\beta} \\ \eta^{\beta}_{k_\beta} \end{Bmatrix} \tag{3.62}$$

where the matrix $\boldsymbol{R}_D$ includes the collocation matrix $\boldsymbol{D}_{\beta\alpha}$ and the interpolated *CB*-CMS matrices and vectors for the β substructure are:

$$\bar{\boldsymbol{M}}^{\beta}_{CB} = \boldsymbol{R}^T_D \boldsymbol{M}^{\beta}_{CB} \boldsymbol{R}_D \qquad \bar{\boldsymbol{K}}^{\beta}_{CB} = \boldsymbol{R}^T_D \boldsymbol{K}^{\beta}_{CB} \boldsymbol{R}_D$$

$$\bar{\boldsymbol{x}}^{\beta}_{CB} = \begin{Bmatrix} \boldsymbol{x}^{\beta}_{i_\alpha} \\ \boldsymbol{x}^{\beta}_{a_\beta} \\ \eta^{\beta}_{k_\beta} \end{Bmatrix} \qquad \bar{\boldsymbol{f}}^{\beta}_{CB} = \boldsymbol{R}^T_D \boldsymbol{f}^{\beta}_{CB} \tag{3.63}$$

Finally, the assembled ROM can be obtained as already done in Eqn. 3.56, where the matrices and vectors for the β component are those of Eqn. 3.63. The assembly procedure is summarized in Figure 3.7

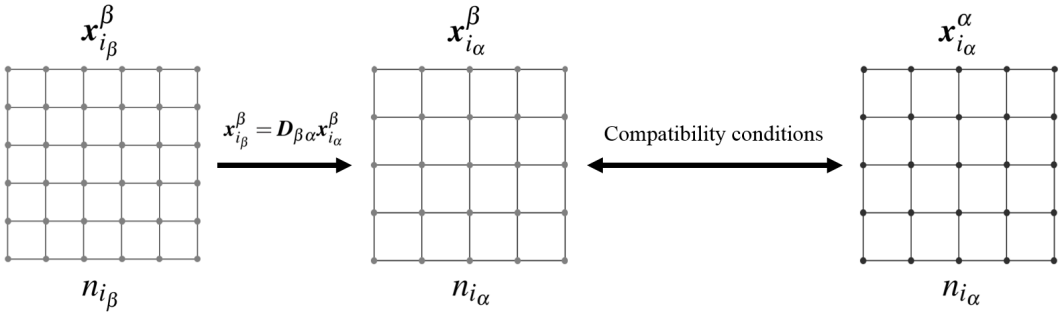

Fig. 3.7 Coordinates transformation and subsequent compatibility between the α and β interfaces. The interpolated displacements $\boldsymbol{x}^{\beta}_{i_\alpha}$ are enforced to be equal to the nodal displacement at the α interface $\boldsymbol{x}^{\alpha}_{i_\beta}$.

Modal Compatibility Conditions

The substructure coupling procedure discussed in the previous paragraph solves the problem of non-conforming meshes without significantly reducing the size of the interfaces. In order to cope with such limitation a novel assembly procedure involving interface *GSI* modes has been proposed in [4]. This methodology overcomes the problem of non-conforming meshes in an elegant manner, being based on the idea of vibration energy transmission between components. Moreover, as already shown in the subsection 3.5.1 the assembly methodology takes also huge advantages from the drastic reduction of the interface DoFs.

Let us consider again the assembly of superelements resulting from the *CB*-CMS reduction of two substructures denoted by α and β. An additional interface reduction for both superelements may be achieved by using two different reduced bases, $\boldsymbol{\Phi}_{i_\alpha w_\alpha}$ and $\boldsymbol{\Phi}_{i_\beta w_\beta}$, obtained by selecting the first n_{w_α} and n_{w_β} columns of the matrices $\boldsymbol{\Phi}_{i_\alpha i_\alpha}$ and $\boldsymbol{\Phi}_{i_\beta i_\beta}$ respectively. However, due to the unequal number of interface DoFs ($n_{i_\alpha} < n_{i_\beta}$), the full matrices of *GSI* modes have different number of rows:

$$\boldsymbol{\Phi}_{i_\alpha i_\alpha} \in \mathbb{R}^{n_{i_\alpha} \times n_{i_\alpha}} \qquad \boldsymbol{\Phi}_{i_\beta i_\beta} \in \mathbb{R}^{n_{i_\beta} \times n_{i_\beta}} \tag{3.64}$$

This means that $\boldsymbol{\Phi}_{i_\alpha w_\alpha}$ and $\boldsymbol{\Phi}_{i_\beta w_\beta}$ can not be directly compared and the common basis of *GSI* modes can not be found. This problem can be overcome by interpolating the columns of $\boldsymbol{\Phi}_{i_\beta i_\beta}$ at the node locations of the α interface by using the shape function of the element at the β interface:

$$\boldsymbol{\Phi}_{i_\alpha i_\beta} = \boldsymbol{D}_{\alpha\beta} \boldsymbol{\Phi}_{i_\beta i_\beta} \quad \rightarrow \quad \boldsymbol{\Phi}_{i_\alpha i_\beta} \in \mathbb{R}^{n_{i_\alpha} \times n_{i_\beta}} \tag{3.65}$$

where $\Phi_{i_\alpha i_\beta}$ are the *GSI* mode of the β interface interpolated at the node location of the α interface, while $\boldsymbol{D}_{\alpha\beta}$ is the *interpolation matrix*[3].

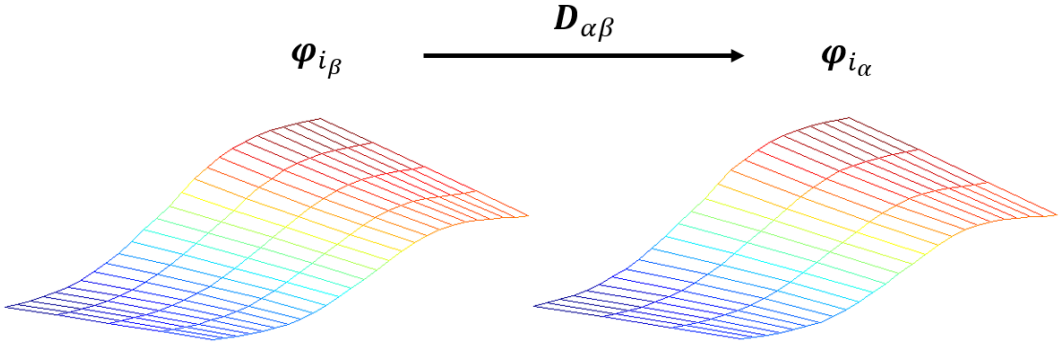

Fig. 3.8 Interpolation of a *GSI* mode: in to compare the *GSI* modes those belonging to the basis $\Phi_{i_\beta w_\beta}$ are interpolated at the node locations of the α interface.

Being $\Phi_{i_\alpha i_\beta}$ a rectangular matrix, its rank is at most equal to n_{i_α}, meaning that not all its columns are linear independent to each other. By reducing $\Phi_{i_\alpha i_\beta}$ to its *reduced row echelon form*[4], n_{i_α} linear independent *GSI* modes can be found:

$$\Phi_{i_\alpha i_\beta} \xrightarrow{\textit{row echelon form}} \bar{\Phi}_{i_\alpha i_\alpha} \in \mathbb{R}^{n_i^\alpha \times n_i^\alpha} \tag{3.66}$$

The bases $\Phi_{i_\alpha i_\alpha}$ and $\bar{\Phi}_{i_\alpha i_\alpha}$ have now the same dimensions and the common reduced basis $\Phi^\gamma_{i_\alpha w_\gamma}$ can thus be determined as already described in the subsection 3.5.1. Although this basis can be directly used to reduce the size of the α interface, it can not be used for the β interface since the number of its DoFs is larger than the size of each interpolated *GSI* mode. For this reason $\Phi^\gamma_{i_\alpha w_\gamma}$ has to be expanded back by interpolating each of its columns at the DoFs location of the β interface by using the shape functions of the elements at the α interface:

$$\Phi^\gamma_{i_\beta w_\gamma} = \boldsymbol{D}_{\beta\alpha}\Phi^\gamma_{i_\alpha w_\gamma} \quad \rightarrow \quad \Phi^\gamma_{i_\beta w_\gamma} \in \mathbb{R}^{n_{i_\beta} \times n_{w_\gamma}} \tag{3.67}$$

[3] $\boldsymbol{D}_{\alpha\beta}$ is built with the same logic used for the collocation matrix of Eqn. 3.58.

[4] A matrix that has undergone Gauss-Jordan elimination is said to be in *reduced row echelon form*. Such a matrix has the following characteristics:

1. All zero rows are at the bottom of the matrix;
2. The *pivot* (leading entry) of each nonzero row after the first occurs to the right of the pivot of the previous row;
3. The pivot in any nonzero row is equal to 1;
4. All entries in the column above and below a leading 1 are zero.

Although the *GSI* modes collected by $\Phi^{\gamma}_{i_\alpha w_\gamma}$ and $\Phi^{\gamma}_{i_\beta w_\gamma}$ refer to different mesh grids, they basically represents same spatial shapes. Therefore, by reducing the corresponding interface DoFs as follows:

$$\boldsymbol{x}^{\alpha}_{i_\alpha} \approx \Phi^{\gamma}_{i_\alpha w_\gamma} \eta^{\alpha}_{w_\gamma} \qquad \boldsymbol{x}^{\beta}_{i_\beta} \approx \Phi^{\gamma}_{i_\beta w_\gamma} \eta^{\beta}_{w_\gamma} \tag{3.68}$$

the corresponding set of modal coordinates $\eta^{\alpha}_{w_\gamma}$ and $\eta^{\beta}_{w_\gamma}$ can be enforced to be equal exactly as done in Eqn. 3.56:

$$\begin{Bmatrix} \eta^{\alpha}_{w_\gamma} \\ \boldsymbol{x}^{\alpha}_{a_\alpha} \\ \eta^{\alpha}_{k_\alpha} \\ \eta^{\beta}_{w_\gamma} \\ \boldsymbol{x}^{\beta}_{a_\beta} \\ \eta^{\beta}_{k_\beta} \end{Bmatrix} = \begin{bmatrix} \boldsymbol{0} & \boldsymbol{0} & \boldsymbol{I} & \boldsymbol{0} & \boldsymbol{0} \\ \boldsymbol{I} & \boldsymbol{0} & \boldsymbol{0} & \boldsymbol{0} & \boldsymbol{0} \\ \boldsymbol{0} & \boldsymbol{0} & \boldsymbol{0} & \boldsymbol{I} & \boldsymbol{0} \\ \boldsymbol{0} & \boldsymbol{0} & \boldsymbol{I} & \boldsymbol{0} & \boldsymbol{0} \\ \boldsymbol{0} & \boldsymbol{I} & \boldsymbol{0} & \boldsymbol{0} & \boldsymbol{0} \\ \boldsymbol{0} & \boldsymbol{0} & \boldsymbol{0} & \boldsymbol{0} & \boldsymbol{I} \end{bmatrix} \begin{Bmatrix} \boldsymbol{x}^{\alpha}_{a_\alpha} \\ \boldsymbol{x}^{\beta}_{a_\beta} \\ \eta_{w_\gamma} \\ \eta^{\alpha}_{k_\alpha} \\ \eta^{\beta}_{k_\beta} \end{Bmatrix} = \boldsymbol{C}_{GS} \begin{Bmatrix} \boldsymbol{x}^{\alpha}_{a_\alpha} \\ \boldsymbol{x}^{\beta}_{a_\beta} \\ \eta_{w_\gamma} \\ \eta^{\alpha}_{k_\alpha} \\ \eta^{\beta}_{k_\beta} \end{Bmatrix} = \boldsymbol{C}_{GS} \boldsymbol{x}^{A}_{GS} \tag{3.69}$$

Finally, the assembled reduced order matrices and vectors are given by:

$$\boldsymbol{M}^{A}_{GS} = \boldsymbol{C}^{T}_{GS} \begin{bmatrix} \boldsymbol{M}^{\alpha}_{GS} & \boldsymbol{0} \\ \boldsymbol{0} & \boldsymbol{M}^{\beta}_{GS} \end{bmatrix} \boldsymbol{C}_{GS} \qquad \boldsymbol{K}^{A}_{GS} = \boldsymbol{C}^{T}_{GS} \begin{bmatrix} \boldsymbol{K}^{\alpha}_{GS} & \boldsymbol{0} \\ \boldsymbol{0} & \boldsymbol{K}^{\beta}_{GS} \end{bmatrix} \boldsymbol{C}_{GS}$$

$$\boldsymbol{x}^{A}_{GS} = \begin{Bmatrix} \boldsymbol{x}^{\alpha}_{a_\alpha} \\ \boldsymbol{x}^{\beta}_{a_\beta} \\ \eta_{w_\gamma} \\ \eta^{\alpha}_{k_\alpha} \\ \eta^{\beta}_{k_\beta} \end{Bmatrix} \qquad \boldsymbol{f}^{A}_{GS} = \boldsymbol{C}^{T}_{GS} \begin{Bmatrix} \boldsymbol{f}^{\alpha}_{GS} \\ \boldsymbol{f}^{\beta}_{GS} \end{Bmatrix} \tag{3.70}$$

3.6 Application to Cyclic Symmetric Structures

In Chapter 2 the main properties of cyclic symmetric structures were presented in order to give an insight into how dynamic analyses on bladed disks could be performed in a very simple manner. It was shown that performing analyses on FE models of fundamental sectors instead on full structures is convenient, since a reduction of the EQM can be achieved by isolating the solution for certain harmonic

indexes. However, the DoFs reduction resulting from the application of simple cyclic constraints (Eqn. 2.22) is not sufficient to drastically reduce the size of the dynamic problem. For this reasons cyclic constraints can be combined with CMS methods in order to obtain highly reduced models. In this regard the method proposed by Tran is one of the most successful [27]. In his paper a methodology used to reduce the DoFs at the independent frontier of a sector is presented. As it will be shown in the following, the Tran's method employs more than one CMS condensation to achieve the mentioned reduction, while the interface reduction method presented in section 3.5 does not requires such large amount of offline reduction costs.

The aforementioned methodologies are here described by taking as reference the FE fundamental sector of a dummy blisk (Figure 3.9).

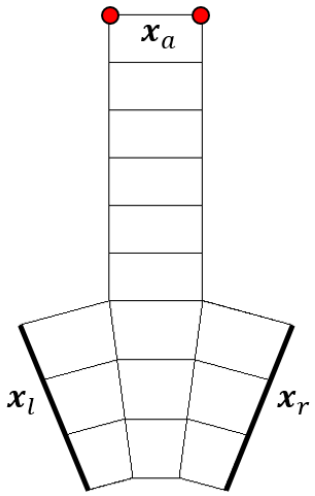

Fig. 3.9 FE model of a fundamental sector.

Due to the subsequent application of cyclic constraints and CMS methods it is found useful to partition the DoFs of the fundamental sector as follows:

$$\boldsymbol{x}_s = \begin{Bmatrix} \boldsymbol{x}_a \\ \boldsymbol{x}_l \\ \boldsymbol{x}_r \\ \boldsymbol{x}_e \end{Bmatrix} \tag{3.71}$$

where the partitions with subscripts a, l, r and e refer to the vector of active, left frontier, right frontier and exceeding DoFs respectively.

3.6.1 Tran's Method

For real turbomachinery bladed disks the FE model of fundamental sectors can have many thousands of DoFs. This led Tran to develop a methodology aimed at reducing the size of these models by combining the properties of cyclic symmetric structures with CMS methods. In particular, this technique appears beneficial when a significant reduction of the independent frontier of a cyclic symmetric sector has to be performed.

The first step towards the complete sector's reduction is represented by the *CB*-CMS condensations, which requires considering the active DoFs and those at both frontiers as boundary DoFs:

$$\boldsymbol{x}_s = \begin{Bmatrix} \boldsymbol{x}_b \\ \boldsymbol{x}_e \end{Bmatrix} = \begin{Bmatrix} \boldsymbol{x}_a \\ \boldsymbol{x}_l \\ \boldsymbol{x}_r \\ \boldsymbol{x}_e \end{Bmatrix} \tag{3.72}$$

The coordinate transformation leading to the sector's *CB*-CMS reduced vector is same as Eqn. 3.26:

$$\begin{Bmatrix} \boldsymbol{x}_b \\ \boldsymbol{x}_e \end{Bmatrix} \approx \begin{bmatrix} \boldsymbol{I}_{be} & \boldsymbol{0}_{bk} \\ \boldsymbol{\Psi}_{ee} & \boldsymbol{\Phi}_{ek} \end{bmatrix} \begin{Bmatrix} \boldsymbol{x}_b \\ \eta_k \end{Bmatrix} = \boldsymbol{R}_{CB} \boldsymbol{x}_{CB} \tag{3.73}$$

where a subset of n_k fixed-interface normal modes has been retained. Since the former reduction preserves the physical DoFs at the left and right frontier, $\boldsymbol{x}_r$ can be

expressed in terms of $\boldsymbol{x}_l$ by using the cyclic constraints given in Eqn. 2.22:

$$\boldsymbol{x}_{CB} = \begin{Bmatrix} \boldsymbol{x}_b \\ \eta_k \end{Bmatrix} = \begin{Bmatrix} \boldsymbol{x}_a \\ \boldsymbol{x}_l \\ \boldsymbol{x}_r \\ \eta_k \end{Bmatrix} = \begin{bmatrix} \boldsymbol{I} & \boldsymbol{0} & \boldsymbol{0} \\ \boldsymbol{0} & \boldsymbol{I} & \boldsymbol{0} \\ \boldsymbol{0} & \boldsymbol{I}e^{\iota\varphi_h} & \boldsymbol{0} \\ \boldsymbol{0} & \boldsymbol{0} & \boldsymbol{I} \end{bmatrix} \begin{Bmatrix} \boldsymbol{x}_a^h \\ \boldsymbol{x}_l^h \\ \eta_k^h \end{Bmatrix} = \boldsymbol{T}_{CB,cs}^h \boldsymbol{x}_{CB,cs}^h \tag{3.74}$$

where:

$$\boldsymbol{T}_{CB,cs} = \begin{bmatrix} \boldsymbol{I} & \boldsymbol{0} & \boldsymbol{0} \\ \boldsymbol{0} & \boldsymbol{I} & \boldsymbol{0} \\ \boldsymbol{0} & \boldsymbol{I}e^{\iota\varphi_h} & \boldsymbol{0} \\ \boldsymbol{0} & \boldsymbol{0} & \boldsymbol{I} \end{bmatrix} \qquad \boldsymbol{x}_{CB,cs}^h = \begin{Bmatrix} \boldsymbol{x}_a^h \\ \boldsymbol{x}_l^h \\ \eta_k^h \end{Bmatrix} \tag{3.75}$$

Then, a new Guyan ROM is created by retaining as master the left and right frontiers DoFs only. By grouping $\boldsymbol{x}_l$ and $\boldsymbol{x}_r$ into the set of interface DoFs $\boldsymbol{x}_i$, the Guyan ROM is obtained by using the following coordinates transformation:

$$\boldsymbol{x}_s = \begin{Bmatrix} \boldsymbol{x}_l \\ \boldsymbol{x}_r \\ \boldsymbol{x}_e \end{Bmatrix} = \begin{Bmatrix} \boldsymbol{x}_i \\ \boldsymbol{x}_e \end{Bmatrix} \approx \begin{bmatrix} \boldsymbol{I}_{ie} \\ \Psi_{ee} \end{bmatrix} \boldsymbol{x}_i = \Psi_c \boldsymbol{x}_i = \boldsymbol{R}_G \boldsymbol{x}_i \tag{3.76}$$

which allows obtaining the Guyan condensed mass and stiffness matrices by using Eqn. 3.23. Again, $\boldsymbol{x}_r$ can be expressed in terms of $\boldsymbol{x}_l$ by employing the cyclic constraints:

$$\boldsymbol{x}_i = \begin{Bmatrix} \boldsymbol{x}_l \\ \boldsymbol{x}_r \end{Bmatrix} = \begin{bmatrix} \boldsymbol{I} \\ \boldsymbol{I}e^{i\varphi_h} \end{bmatrix} \boldsymbol{x}_l^h = \boldsymbol{R}_{G,cs}^h \boldsymbol{x}_l^h \tag{3.77}$$

By projecting the Guyan EQM onto the basis $\boldsymbol{R}_{G,cs}^h$, the following cyclic EQM are obtained:

$$\boldsymbol{M}_{G,cs}\, \ddot{\boldsymbol{x}}_l^h + \boldsymbol{K}_{G,cs}\, \boldsymbol{x}_l^h = \boldsymbol{f}_{G,cs} \tag{3.78}$$

where

$$\boldsymbol{M}_{G,cs} = (\boldsymbol{R}_{G,cs}^h)^* \boldsymbol{M}_G \boldsymbol{R}_{G,cs}^h \qquad \boldsymbol{K}_{G,cs} = (\boldsymbol{R}_{G,cs}^h)^* \boldsymbol{K}_G \boldsymbol{R}_{G,cs}^h$$
$$\boldsymbol{f}_{G,cs} = (\boldsymbol{R}_{G,cs}^h)^* \boldsymbol{f}_G \tag{3.79}$$

The interface modes reducing the independent frontier $\boldsymbol{x}_l^h$ are given by the lowest eigenfrequecies eigenvectors found by solving the following eigenproblem:

$$\left(\boldsymbol{K}_{G,cs} - \omega_j^2 \boldsymbol{M}_{G,cs}\right) \phi_j = \boldsymbol{0} \qquad \forall\, j = 1, \ldots, n_l \tag{3.80}$$

If a subset of n_u interface mode is arranged as the columns of a matrix Φ^h_{lu}, $\boldsymbol{x}^h_{CB}$ can be further reduced as:

$$\boldsymbol{x}^h_{CB} = \begin{Bmatrix} \boldsymbol{x}^h_a \\ \boldsymbol{x}^h_l \\ \eta^h_k \end{Bmatrix} \approx \begin{bmatrix} \boldsymbol{I} & \boldsymbol{0} & \boldsymbol{0} \\ \boldsymbol{0} & \Phi^h_{lu} & \boldsymbol{0} \\ \boldsymbol{0} & \boldsymbol{0} & \boldsymbol{I} \end{bmatrix} \begin{Bmatrix} \boldsymbol{x}^h_a \\ \eta^h_u \\ \eta^h_k \end{Bmatrix} \tag{3.81}$$

where

$$\boldsymbol{x}^h_T = \begin{Bmatrix} \boldsymbol{x}^h_a \\ \eta^h_u \\ \eta^h_k \end{Bmatrix} \tag{3.82}$$

is the Tran generalized coordinate vector. The coordinate transformation of Eqn. 3.81 is clearly effective for $n_u \ll n_l$.

Note that the Guyan reduction and the subsequent application of cyclic constraints (Eqn. 3.76 and 3.77) led to a ROM having as a master the cyclic DoFs $\boldsymbol{x}^h_l$ only (Eqn. 3.78). This allowed Tran to compute the modes ϕ_j at the left frontier without the need to separate them from the active ones[5]. However, the Tran's method requires two reductions of the original FE model (both *CB*-CMS and Guyan), which makes it more costly than the *GSI* method (see section 3.4).

3.6.2 Independent Frontier Reduction via *GSI* modes

As seen in the subsection 3.6.1 the method by Tran allows the evaluation of the cyclic frontier modes on a Guyan ROM treated in cyclic symmetry conditions. The procedure employed to compute these modes is straightforward, since the ROM of Eqn. 3.78 is condensed on the independent frontier only. However, the creation of two different CMS models considerably increases the offline reductions costs, especially when the size of the FE sector is large.

Besides their use for coupling either conforming or non-conforming interfaces of component's ROMs, the interface *GSI* modes can be adopted to overcome the drawback of the Tran's method. In particular, starting from the coordinate transformation of Eqn. 3.74, the independent $\boldsymbol{x}^h_l$ can be directly reduced using the *GSI*

[5]This approach is typical of the *GSI* reduction technique.

modes according to the procedure of described in the subsection 3.4.1:

$$\begin{Bmatrix} \boldsymbol{x}_a^h \\ \boldsymbol{x}_l^h \\ \eta_k^h \end{Bmatrix} \approx \begin{bmatrix} \boldsymbol{I}_{aa} & \boldsymbol{0}_{aw} & \boldsymbol{0}_{ak} \\ \boldsymbol{0}_{la} & \boldsymbol{\Phi}_{lw}^h & \boldsymbol{0}_{lk} \\ \boldsymbol{0}_{ka} & \boldsymbol{0}_{kw} & \boldsymbol{I}_{kk} \end{bmatrix} \begin{Bmatrix} \boldsymbol{x}_a^h \\ \eta_w^h \\ \eta_k^h \end{Bmatrix} = \boldsymbol{T}_{CC}^h \begin{Bmatrix} \boldsymbol{x}_a^h \\ \eta_w^h \\ \eta_k^h \end{Bmatrix} \tag{3.83}$$

where

$$\boldsymbol{x}_{GS}^h = \begin{Bmatrix} \boldsymbol{x}_a^h \\ \eta_w^h \\ \eta_k^h \end{Bmatrix} \tag{3.84}$$

is the *GSI* generalized coordinates vector. In this way the independent frontier reduction may be achieved without performing the further Guyan reduction required by the Tran's approach.

3.7 Example

In this section the performances of the *GSI* reduction technique are tested on the FE model of a dummy bladed disk's sector. The reference model consists of one dummy blade attached to the corresponding disk's sector by the *dove tail joint* (Figure 3.10).

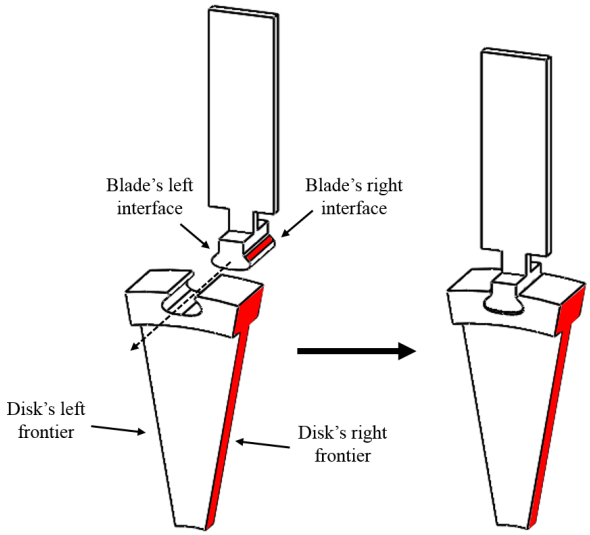

Fig. 3.10 Reference model: dummy blade attached to the fundamental sector.

Hereafter the term "interface" is used to identify one of the coupling interfaces between the blade and sector, while the term "frontier" refers to the disk's sector boundaries shared with adjacent sectors (Figure 3.11).

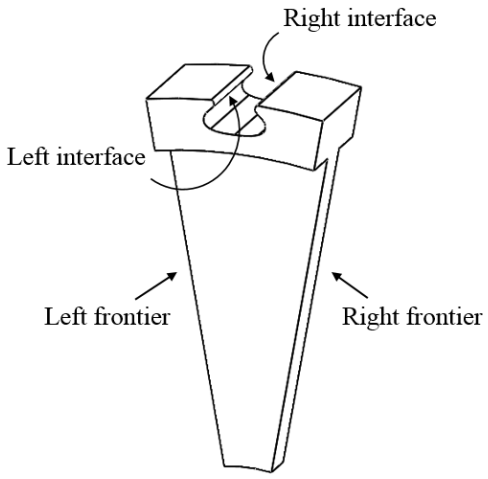

Fig. 3.11 Interfaces and frontiers of the disk's sector.

According to the description given in the previous sections, the methodology is here applied in order to perform two different tasks:

1. *Blade-Disk's sector coupling*: as it will be shown in the next subsection the blade and sector's interfaces were appositely meshed with non-collocated nodes. Hence, besides reducing the interface DoFs, the *GSI* method is also used to couple the two components by enforcing the compatibility conditions in the modal space instead on the physical one.

2. *Reduction of the sector's frontier after the application of cyclic constraints*: after having performed the reduction of the disk's coupling interfaces, cyclic constraints are applied to the left and right sector's frontiers (Eqn. 2.32). The DoFs at the independent frontier may then be reduced by using a suitable basis of *GSI* modes.

The two tasks are tackled one by one going through different steps of reduction. The correctness of the employed procedures is checked by comparing the output of the reduced models with those of the full ones on a case-by-case basis.

3.7.1 Models Description

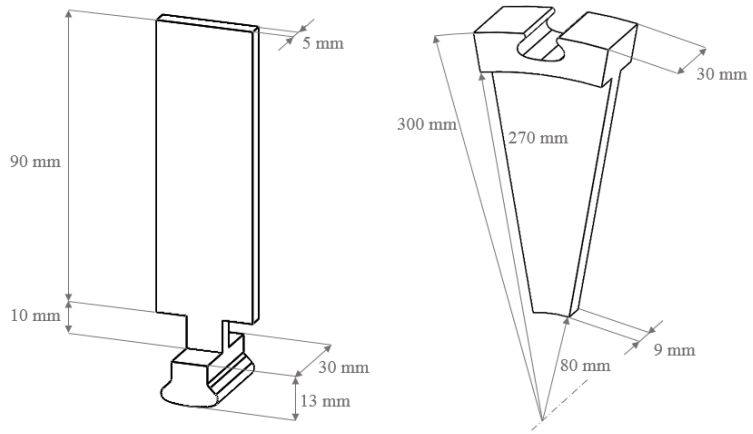

Fig. 3.12 Reference model dimensions.

The structure used as a reference can be thought as the assembly resulting from the coupling of one dummy blade with the corresponding disk's sector (Figure 3.10). The geometry of both components was created according to the dimensions specified

in Figure 3.12. These were meshed using the commercial FE software ANSYS by employing the solid quadratic elements SOLID 185 with the following material properties: Young's modulus E = 210 GPa, Poisson's ration ν = 0.33 and density ρ = 7800 kg/m^3. These discretizations resulted into two FE models having $N_B = 6888$ and $N_{DS} = 5496$ DoFs for the blade and sector respectively (Figure 3.13).

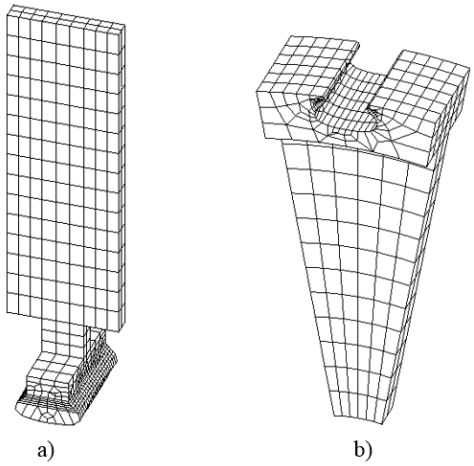

Fig. 3.13 FE models of the dummy blade a) and disk's sector b).

The blade and sector models were appositely created with non-collocated nodes at the common interfaces. In particular, two regular grids of $n_{i_b} = 100$ and $n_{i_s} = 130$ nodes were used to mesh the blade and sector interfaces. These grids are here denoted by $\mathsf{Cl_b}$ and $\mathsf{Cl_d}$. $\mathsf{Cl_b}$ discretizes both right and left blade's interfaces, while $\mathsf{Cl_d}$ does the same for the sector interfaces (Figure 3.14).

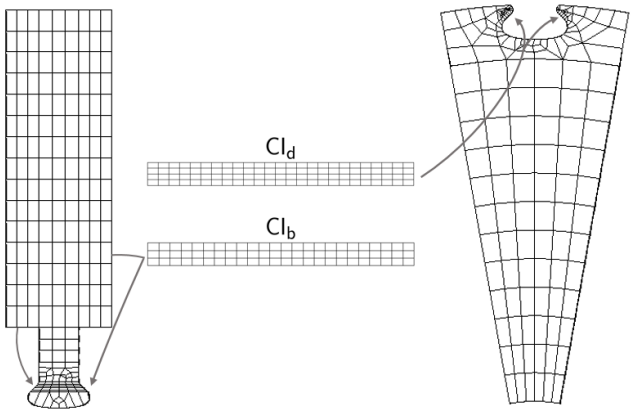

Fig. 3.14 Interface mesh grids for the left and right interfaces.

The number of elements, nodes and corresponding DoFs for both FE models is listed in the Table 3.1.

Table 3.1 Features of the blade and sector FE models.

FE Model	# elements	# nodes	# DoFs	# DoFs per interface
Blade	4992	2296	6888	300
Disk'sector	4776	1832	5496	390

3.7.2 Craig-Bampton Reduced Order Models

By using the *CB*-CMS method the FE models were reduced down to $n_{b_b} = 692$ and $n_{b_d} = 1196$ boundary DoFs, which are almost the 10% and 21.5% of the original FE models size. The *CB*-CMS generalized coordinates vector for the blade can be written as:

$$\boldsymbol{x}^b_{CB} = \begin{Bmatrix} \boldsymbol{x}^b_{a_b} \\ \boldsymbol{x}^b_{li_b} \\ \boldsymbol{x}^b_{ri_b} \\ \eta^b_{k_b} \end{Bmatrix} \tag{3.85}$$

where $\boldsymbol{x}^b_{a_b}$, $\boldsymbol{x}^b_{li_b}$ and $\boldsymbol{x}^b_{ri_b}$ are the active, left and right interface DoFs retained in the *CB*-CMS reduction (Figure 3.15), while $\eta^b_{k_b}$ is the vector of modal coordinates corresponding to the reduced set n_{k_b} fixed-interface normal modes.

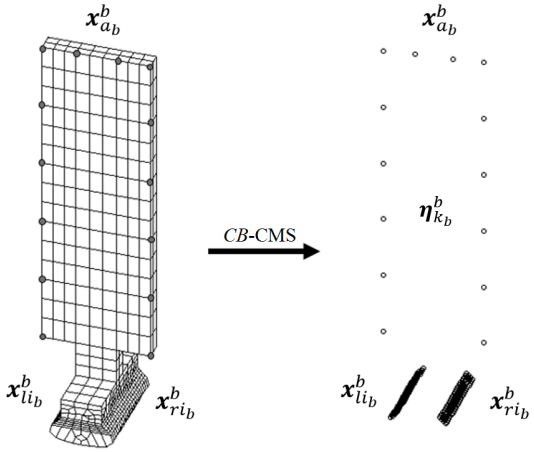

Fig. 3.15 *CB*-CMS reduction of the blade FE model: the black circles denote the physical DoFs retained in the *CB*-CMS condensation.

The set of active DoFs $\boldsymbol{x}_{a_b}^b$ was chosen in order to perform two different tasks:

1. Similarly to the case of forced response calculations on real FE models of turbine blades, where the aerodynamic forces are spread over the blades's pressure side, the active DoFs in this case allows for the application of distributed forces over the blade's perimeter;

2. The distribution of the active DoFs over the blade's perimeters allows for a satisfactory check on the mode shape of the ROM when compared to those of the full FE model.

The sizes of the former subvectors are listed in Table 3.2.

Table 3.2 Sizes of the $\boldsymbol{x}_{CB}^b$ subvectors.

Set	# DoFs
$\boldsymbol{x}_{a_b}^b$	42
$\boldsymbol{x}_{li_b}^b$	300
$\boldsymbol{x}_{ri_b}^b$	300
$\eta_{k_b}^b$	50
$\boldsymbol{x}_{CB}^b$	692

For reference, the first 50 natural frequencies of the blade *CB*-CMS ROM are all within 0.8% of the corresponding FE natural frequencies (Figure 3.16). The percentage difference between these values was evaluated by using the following relationship:

$$e_{\%} = \frac{|f_{CB} - f_{FE}|}{f_{FE}} \cdot 100 \tag{3.86}$$

where the FE quantities were considered as reference.

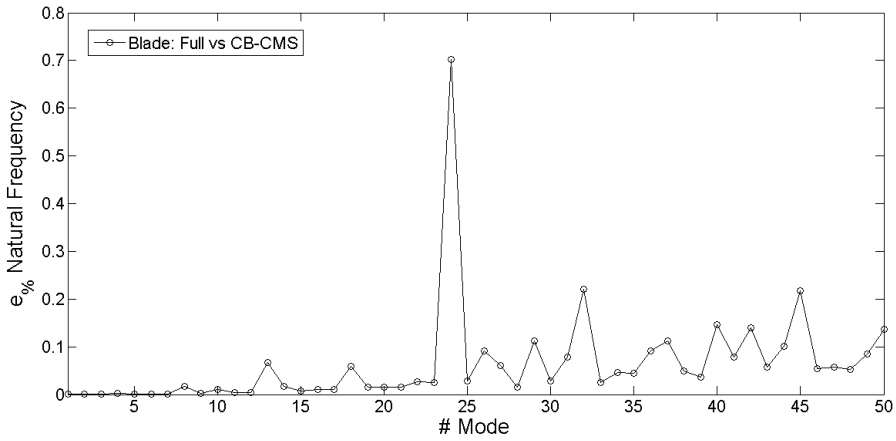

Fig. 3.16 Percentage errors in term of natural frequencies between the blade's FE model and the corresponding *CB*-CMS ROM. The plot shows the typical upward trend of $e_{\%}$ as the natural frequency of the mode shapes increases. The error on the mode 24, significantly higher than the others, depends on the nature of the mode shape itself. From Figure 3.17 it can be noted that for mode 24 most of the blade acts as if it was clamped (blue zone). This means that the active DoFs $\boldsymbol{x}^b_{a_b}$ at the blade's perimeter do not significantly contribute to the approximation of a mode shape mainly localized at the blade's root.

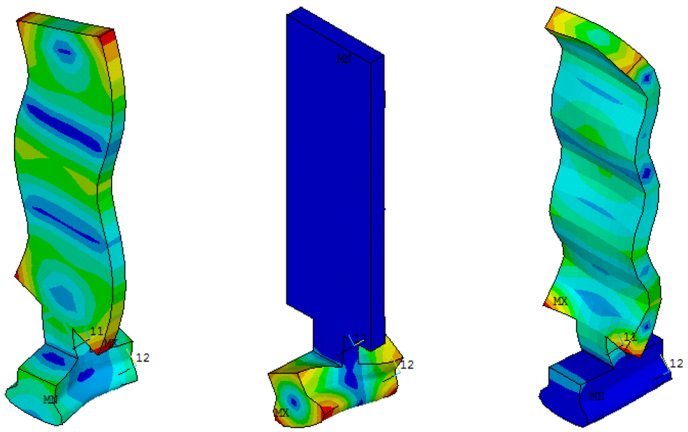

Fig. 3.17 Representation of the blade's mode shapes 23, 24 and 25: the blade's structure participates more when the mode 23 and 25 occur as compared to the mode 24.

Although the blade FE model was condensed in free-free condition, the sector was reduced by clamping all the nodes having radial coordinate equal to 80 mm (Figure 3.12). The *CB*-CMS generalized coordinates vector for the sector ROM can

be expressed as:

$$\boldsymbol{x}_{CB}^{d} = \begin{Bmatrix} \boldsymbol{x}_{li_d}^{d} \\ \boldsymbol{x}_{ri_d}^{d} \\ \boldsymbol{x}_{lf_d}^{d} \\ \boldsymbol{x}_{rf_d}^{d} \\ \eta_{k_d}^{d} \end{Bmatrix} \tag{3.87}$$

where $\boldsymbol{x}_{li_d}^{d}$ and $\boldsymbol{x}_{ri_d}^{d}$ are the master DoFs at the left and right coupling interfaces, $\boldsymbol{x}_{lf_d}^{d}$ and $\boldsymbol{x}_{rf_d}^{d}$ the sector's left and right frontier DoFs and $\eta_{k_d}^{d}$ the modal coordinates corresponding to the retained fixed-interface normal modes (Figure 3.18).

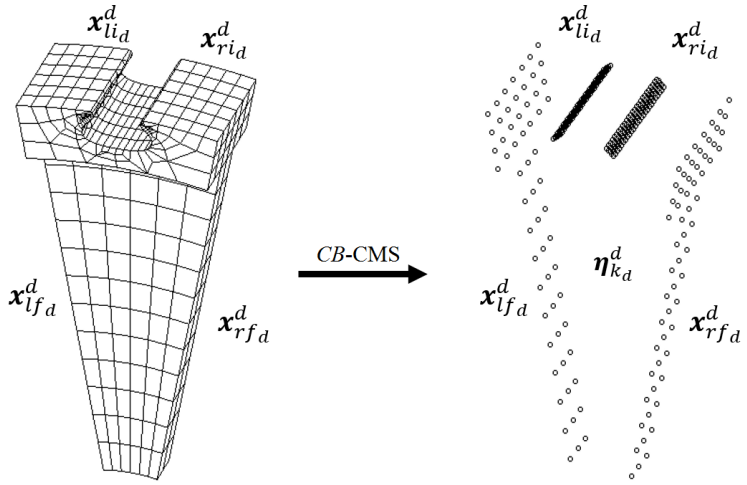

Fig. 3.18 *CB*-CMS reduction of the disk's sector FE model: the black circles denote the physical DoFs retained in the *CB*-CMS condensation.

The size of each subvector is given in Table3.3.

Table 3.3 Sizes of the $\boldsymbol{x}_{CB}^{d}$ subvectors.

Set	# DoFs
$\boldsymbol{x}_{li_d}^{d}$	390
$\boldsymbol{x}_{ri_d}^{d}$	390
$\boldsymbol{x}_{lf_d}^{d}$	183
$\boldsymbol{x}_{rf_d}^{d}$	183
$\eta_{k_d}^{d}$	50
$\boldsymbol{x}_{CB}^{d}$	1196

For reference, the first 50 natural frequencies of the sector *CB*-CMS ROM are all within 1.1% of the corresponding FE natural frequencies (Figure 3.19).

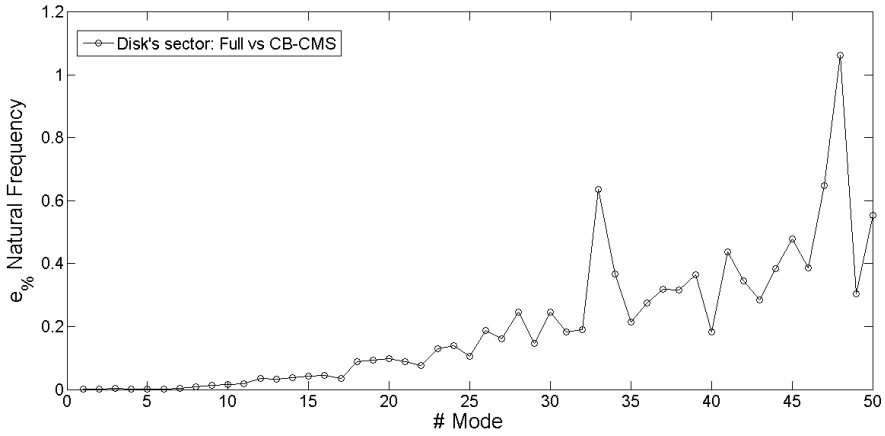

Fig. 3.19 Percentage errors in term of natural frequencies between the sector's FE model and the corresponding *CB*-CMS ROM. The plot shows the typical upward trend of $e_{\%}$ as the natural frequency of the mode shapes increases. The errors on the modes 33 and 48, significantly higher than the others, depend on the nature of the mode shapes themselves. As in the case of the blade from Figure 3.20 it can be noted that some of the active DoFs (e.i. those at the frontiers for the mode 33 and those at the interfaces for the mode 48) do not significantly contribute to the definition of the mode shapes.

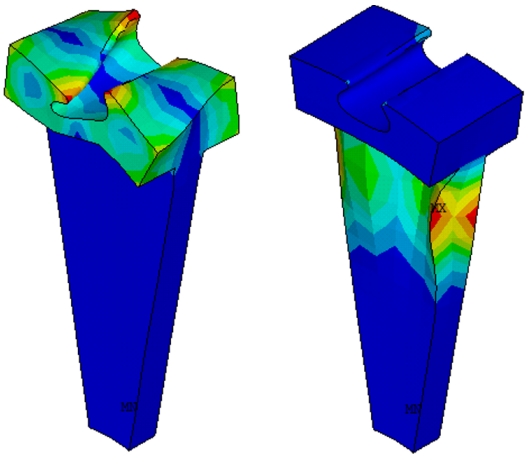

Fig. 3.20 Representation of the mode shape 33 and 48 for the disk's sector.

3.7.3 Interfaces Reduction

After having created the *CB*-CMS ROMs of blade and sector, further modal interface reductions were carried out according to the *GSI* method (see the subsection 3.4.1). In particular, the method was first applied to the blade and sector interfaces and later to the independent sector frontier after the application of cyclic constraints.

Blade Interfaces Reduction

In this case the interface DoFs $\boldsymbol{x}^b_{li_b}$ and $\boldsymbol{x}^b_{ri_b}$ were reduced by applying the *GSI* method. The modal reduction of these sets led to a new ROM whose vector of generalized coordinates can be written as:

$$\boldsymbol{x}^b_{GS} = \begin{Bmatrix} \boldsymbol{x}^b_{a_b} \\ \eta^b_{li_b} \\ \eta^b_{ri_b} \\ \eta^b_{k_b} \end{Bmatrix} \tag{3.88}$$

where $\eta^b_{li_b}$ and $\eta^b_{ri_b}$ represent the modal coordinates corresponding to the retained set of interface *GSI* modes. An investigation on the number of modes used to reduce both interfaces was then carried out. Several simulations were performed, where the effect of 10, 20, 30, and 50 modes on the interfaces reduction was evaluated. In order to estimate the goodness of this second reduction, the first 50 natural frequencies of the blade *GSI* ROMs were compared to those of the corresponding *CB*-CMS ROM. The comparison was performed again by using the relationship of Eqn. 3.86, where the *CB*-CMS quantities were taken as reference. For all the mentioned test campaigns the highest $e_{\%}$ are listed in Table 3.4.

Table 3.4 Highest $e\%$ between the blade natural frequencies evaluated by using the *CB*-CMS and *GSI* ROM.

# *GSI* modes	10	20	30	50
$e_{\%}$ (*CB* vs *GSI*)	14.05%	2.6%	$9.6 \cdot 10^{-3}\%$	$9 \cdot 10^{-4}\%$

From the previous table it can be noted that reducing the interfaces with either 30 or 50 *GSI* modes each ensures high accuracy in the prediction of the blade natural frequencies. These were collected into two different bases (one for the left and one

for the right interface), which were exploited for the blade-sector coupling procedure. The selected bases of *GSI* modes will be denoted by Φ_l^b and Φ_r^b.

The check of the blade *GSI* ROM was finally concluded by comparing its eigenvectors with those of the *CB*-CMS ROM. The comparison was carried out on the eigenvectors partition corresponding to the set of active DoFs $\boldsymbol{x}_{a_b}^b$ by using the *Modal Assurance Criterion* (MAC):

$$\texttt{MAC} = \frac{\|\phi_{CB}^T \phi_{GS}\|^2}{\left(\phi_{CB}^T \phi_{CB}\right)\left(\phi_{GS}^T \phi_{GS}\right)} \tag{3.89}$$

where ϕ_{CB} and ϕ_{GS} are the physical partitions of the *CB*-CMS and *GSI* eigenvectors. From Figure. 3.21 it can be noted that the mode shapes of both ROMs are identical to each other, since all the terms on the main diagonal are equal to one. These results gives confidence in the *GSI* reduction of the blade interfaces.

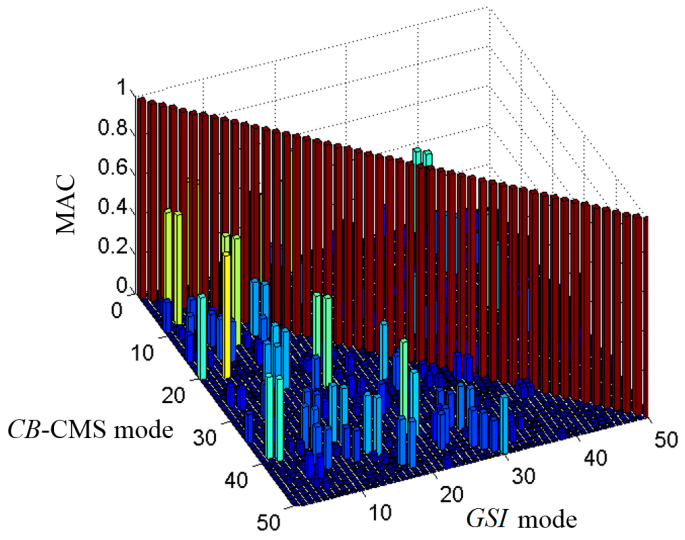

Fig. 3.21 MAC between the *CB-CMS* and *GSI* blade eigenvectors: the terms on the main diagonal confirm the perfect agreement between the two sets of eigenvectors. Note that the off-diagonal terms give just an insight into how similar are two different eigenvectors arbitrarily chosen from the bases under comparison.

Disk Interfaces Reduction

The sector's interface DoFs $\boldsymbol{x}^d_{li_d}$ and $\boldsymbol{x}^d_{ri_d}$ were reduced in order to obtain a ROM corresponding to the following vector of generalized coordinates:

$$\boldsymbol{x}^d_{GS} = \begin{Bmatrix} \eta^d_{li_d} \\ \eta^d_{ri_d} \\ \boldsymbol{x}^d_{lf_d} \\ \boldsymbol{x}^d_{rf_d} \\ \eta^d_{k_d} \end{Bmatrix} \tag{3.90}$$

where $\eta^d_{li_d}$ and $\eta^d_{ri_d}$ represent the modal coordinates of a reduced set of *GSI* modes. In particular, the effect of 10, 20, 30 and 50 *GSI* modes on the interfaces reduction was evaluated. For all the former cases the fist 50 sector's natural frequencies were compared to those of the corresponding *CB*-CMS model by using the relationship of Eqn. 3.86. The highest values of $e_{\%}$ for all the mentioned cases are listed in Table 3.5.

Table 3.5 Highest $e\%$ between the sector natural frequencies evaluated by using the *CB*-CMS and *GSI* ROM.

# *GSI* modes	10	20	30	50
$e_{\%}$ (CB vs *GSI*)	4.63%	0.09%	$1.7 \cdot 10^{-3}\%$	$4.9 \cdot 10^{-6}\%$

It can be noted that 20 *GSI* modes are sufficient to perform a satisfactory interface condensation, guaranteeing high precision in the prediction of the sector natural frequencies. Hereafter these basis of 20 *GSI* modes are denoted as Φ^d_l and Φ^d_r.

3.7.4 Interface Coupling and Cyclic Constraints

As already shown in section 3.4, the *GSI* method gives the possibility to assemble two or more substructures even if non-conforming meshes are present at the respective interfaces. This can be achieved by finding a common basis of modes reducing the left and right interfaces of both blade and sector ROMs.

The criteria adopted here consisted to bring together the smallest subsets of *GSI* modes that were sufficient to satisfactorily represent the components' dynamics.

Hence, the bases here denoted as $\Phi^b_{l(r)}$ and $\Phi^d_{l(r)}$ were put together in order to define the basis $\Phi^C_{l(r)}$ reducing the left (right) interface of both blade and sector. In order to remove any possible linear dependence between the modes of $\Phi^b_{l(r)}$ and $\Phi^d_{l(r)}$, a Gram-Schmidt orthonormalization of $\Phi^C_{l(r)}$ was performed (see the subsection 3.4.1). At the end of this process the common basis $\Phi^C_{l(r)}$ was therefore used to reduce the size of both blade and sector left (right) interface. For the case under study the common basis $\Phi^C_{l(r)}$ reducing the left (right) interface was obtained by collecting the first 30 and 20 *GSI* modes for the blade and sector left (right) interface respectively (see subsection 3.7.3).

According to the DoFs partitions of Eqns. 3.88 and 3.90, the size of the resulting subvectors is given in Table 3.7:

Table 3.6 Sizes of the $\boldsymbol{x}^b_{GS}$ and $\boldsymbol{x}^d_{GS}$ subvectors.

Set	# DoFs	Set	# DoFs
$\boldsymbol{x}^b_{a_b}$	42	-	-
$\eta^b_{li_b}$	50	$\eta^d_{li_d}$	50
$\eta^b_{ri_b}$	50	$\eta^d_{ri_d}$	50
-	-	$\boldsymbol{x}^d_{lf_d}$	183
-	-	$\boldsymbol{x}^d_{rf_d}$	183
$\eta^b_{k_b}$	50	$\eta^d_{k_d}$	50
$\boldsymbol{x}^b_{GS}$	192	$\boldsymbol{x}^d_{GS}$	516

Figures 3.22 and 3.23 shows the errors on the first 50 natural frequencies obtained by performing modal analyses on the *CB*-CMS and *GSI* ROMs of blade and sector respectively. It can be noted how the expansion of the reduction bases increased the accuracy of both *GSI* ROMs. In fact, for the blade the maximum difference on the natural frequencies decreased from $9.6 \cdot 10^{-3}\%$ (Table 3.4) to less than $6 \cdot 10^{-4}\%$. Similar considerations can be carried out for the sector; in this case the maximum difference decreased from 0.09% (Table 3.5) to less than 0.01%.

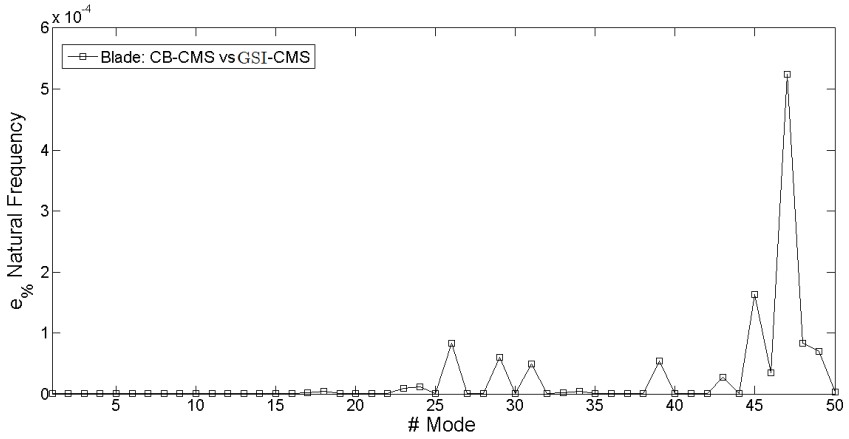

Fig. 3.22 Percentage errors in term of natural frequencies between the blade *CB*-CMS and *GSI* ROM.

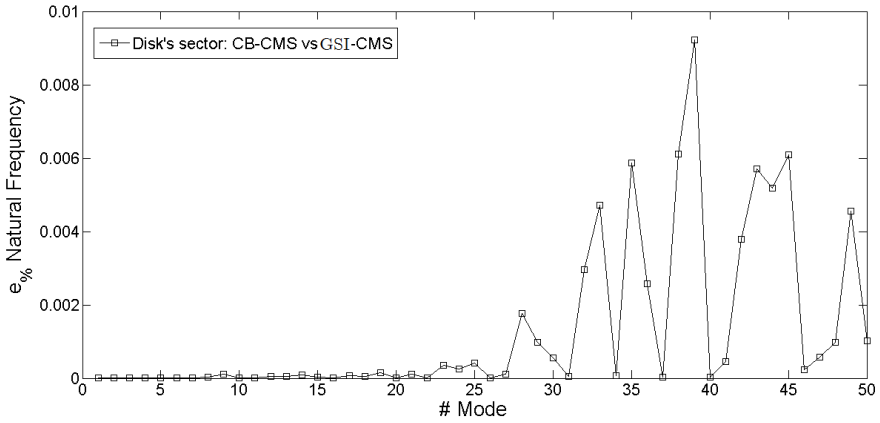

Fig. 3.23 Percentage errors in term of natural frequencies between the sector *CB*-CMS and *GSI* ROM.

Note that the different magnitude of the errors in Figures 3.22 and 3.23 depends on the original number of *GSI* modes employed in both component's reduction. In particular, before employing the common basis the sector's ROM showed a maximum $e_{\%}$ that was already one order of magnitude larger than that of the blade's one (0.09% vs $9.6 \cdot 10^{-3}$%). Although the use of the common bases decreased the mention errors, their difference still remained (0.01% vs $6 \cdot 10^{-4}$%). Furthermore, by looking at the Figures 3.22 and 3.23 other two interesting facts can be highlighted:

1. For both components the highest values of $e_{\%}$ corresponds to higher frequency mode shapes. In the case of the blade (sector) it was shown that reducing both interfaces with 30 (20) *GSI* modes guaranteed high accuracy in the prediction

of the first 50 blade's (sector's) eigenfrequencies (Tables 3.4 and 3.5). It was also stressed that this condition was improved when the common bases were employed. However, 30 (20) *GSI* modes approximately guarantee high accuracy in the prediction of the first 30 (20) mode shapes. The highest errors on the subsequent modes, still being minimized by the common bases, depend on the poorest approximation of their interfaces motion (i.e. the *GSI* modes in the common basis do not allow the same approximation for all the examined modes).

2. Figure 3.23 shows a rather sharp error increase from mode 30 on, with some subsequent modes still being exact: the first 30 *GSI* modes retained for the blade's interface reduction ensure high accuracy in the prediction of the first 30 blade's mode. When using the common basis some of the sector's *GSI* modes may contribute for a better definition of the blade's subsequent modes.

Before performing the coupling, cyclic constraints were applied to the sector frontiers for all the admissible values of φ_h:

$$\boldsymbol{x}_{GS}^{d} = \begin{Bmatrix} \eta_{li_d}^{d} \\ \eta_{ri_d}^{d} \\ \boldsymbol{x}_{lf_d}^{d} \\ \boldsymbol{x}_{rf_d}^{d} \\ \eta_{k_d}^{d} \end{Bmatrix} = \begin{bmatrix} \boldsymbol{I} & \boldsymbol{0} & \boldsymbol{0} & \boldsymbol{0} \\ \boldsymbol{0} & \boldsymbol{I} & \boldsymbol{0} & \boldsymbol{0} \\ \boldsymbol{0} & \boldsymbol{0} & \boldsymbol{I} & \boldsymbol{0} \\ \boldsymbol{0} & \boldsymbol{0} & \boldsymbol{I}e^{\iota\varphi_h} & \boldsymbol{0} \\ \boldsymbol{0} & \boldsymbol{0} & \boldsymbol{0} & \boldsymbol{I} \end{bmatrix} \begin{Bmatrix} \eta_{li_d}^{d,h} \\ \eta_{ri_d}^{d,h} \\ \boldsymbol{x}_{lf_d}^{d,h} \\ \eta_{k_d}^{d,h} \end{Bmatrix} \tag{3.91}$$

Thereby the modal analysis of each cyclic symmetric eigenproblem was performed and the disk's FreND diagram for the first 5 modal families was carried out:

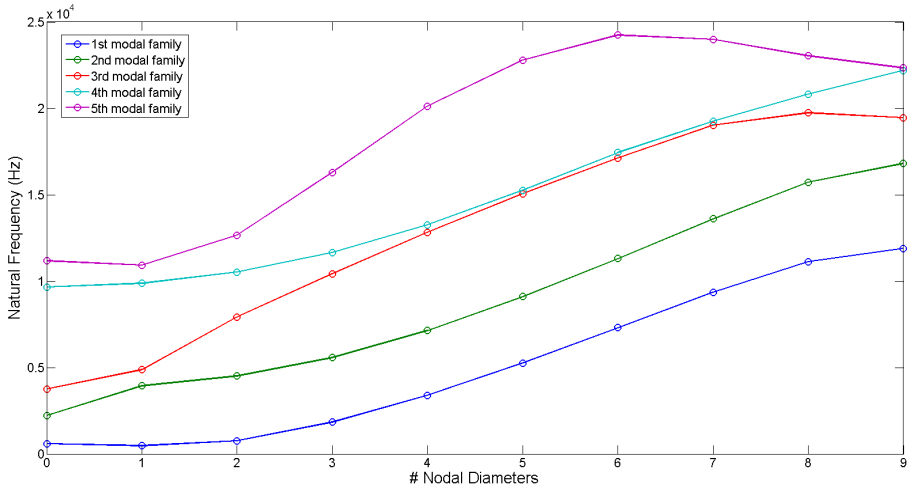

Fig. 3.24 Disk's FreND diagram.

Such results were used as a benchmark in order to test the goodness of the approaches used to reduce the independent frontier of the sector. In particular, starting from the transformation of Eqn 3.91, for each value of φ_h, other two ROMs were created by employing the *GSI* and the Tran's method. For both cases just 20 *GSI* modes were retained. The generalized coordinate vectors corresponding to these ROMs can be expressed as:

$$\boldsymbol{x}_T^{d,h} = \left\{ \begin{array}{c} \eta_{li_d}^{d,h} \\ \eta_{ri_d}^{d,h} \\ \eta_{lf_d,Tran}^{d,h} \\ \eta_{k_d}^{d,h} \end{array} \right\} \qquad \boldsymbol{x}_{GS}^{d,h} = \left\{ \begin{array}{c} \eta_{li_d}^{d,h} \\ \eta_{ri_d}^{d,h} \\ \eta_{lf_d,GS}^{d,h} \\ \eta_{k_d}^{d,h} \end{array} \right\} \tag{3.92}$$

where $\eta_{lf_d,Tran}^{d,h}$ and $\eta_{lf_d,Int}^{d,h}$ are the left frontier modal coordinates in the two cases. Hereafter these ROMs will be denoted as DS_{Int} and DS_{Tran} respectively.

A new modal analysis on both cyclic ROMs was performed and the corresponding FreND diagrams were evaluated. The resulting modal families were then compared to those of Figure 3.24 by computing the $e_{\%}$ as usual. Both comparisons led to maxima errors smaller than $10^{-4}\%$, meaning that an excellent reduction of the independent frontier may be achieved by employing both methods. However, the DS_{Int} ROM has to be preferred over the DS_{Tran} one for obvious reasons: while the method by Tran requires a further Guyan condensation of the model (see the section 3.6.1), the *GSI* method does not. Therefore, although the time spent for solving the

cyclic eigenproblem is the same and the eigenfrequencies are practically identical, the off-line reduction costs required by the Tran's method are much larger than those of the *GSI* one. For this reason the ROM of the assembled structure will be obtained by coupling the blade *GSI* ROM with DS_{Int}.

Finally, the assembled ROM was obtained by enforcing the following compatibility conditions in the space of interface modes:

$$\begin{cases} \eta^{b}_{li_b} = \eta^{d,h}_{li_d} = \eta_{li} \\ \eta^{b}_{ri_b} = \eta^{d,h}_{ri_d} = \eta_{li} \end{cases} \qquad \forall\, h = 0, \ldots, \tilde{h} \tag{3.93}$$

The generalized coordinate vector of the resulting ROM can then be written as:

$$\boldsymbol{x}^{h}_{GS} = \begin{Bmatrix} \boldsymbol{x}^{b,h}_{a_b} \\ \eta^{h}_{li} \\ \eta^{h}_{ri} \\ \eta^{d,h}_{lf_{d,Int}} \\ \eta^{d,h}_{k_b} \\ \eta^{d,h}_{k_d} \end{Bmatrix} \tag{3.94}$$

whose subvectors dimensions are listed in the following table:

Table 3.7 Sizes of the $\boldsymbol{x}^{h}_{GS}$ subvectors.

Set	# DoFs
$\boldsymbol{x}^{b,h}_{a_b}$	42
η^{h}_{li}	50
η^{h}_{ri}	50
$\eta^{d,h}_{lf_{d,Int}}$	20
$\eta^{d,h}_{k_b}$	50
$\eta^{d,h}_{k_d}$	50
$\boldsymbol{x}^{h}_{GS}$	262

These ROMs were directly compared with the full FE model in terms of natural frequencies, mode shapes and linear forced responses of the system. In particular, by comparing the FreND diagram of the full FE model (Figure 3.25) with that obtained from the assembled ROM, the percentage errors of Figure 3.26 can be found:

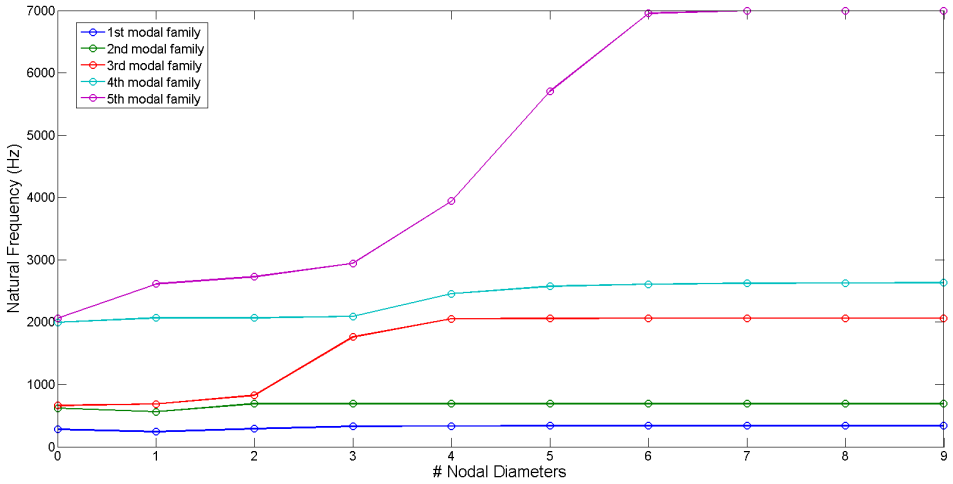

Fig. 3.25 FreND diagram of the assembled structure.

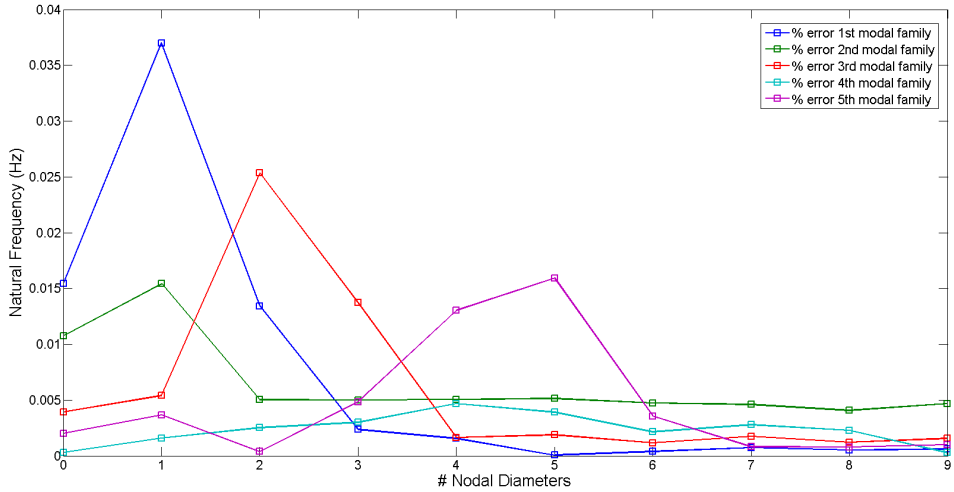

Fig. 3.26 Errors on the natural frequencies.

which shows maxima $e_{\%}$ less than 0.04% for all the modal families. From Figure 3.26 it can be noted that larger errors on the natural frequencies occur for lower nodal diameter mode shapes. The physical reason of such trend is quite intuitive: for low nodal diameters the disk significantly participates to the assembly dynamics by dragging the blades during vibration. This means that the errors found for small nodal diameters strongly depend on both disk and blade's reductions. Differently, for large nodal diameters the disk becomes stiffer and the blades behave as if they were clamped at the root. In this second case the effect of the disk's interfaces reduction is much less important.

The physical partition of the reduced eigenvectors (corresponding to $\boldsymbol{x}_{a_b}^b$ in Figure 3.15) were then compared with the full ones. Figure 3.25 shows the MAC number for the mode shapes computed by isolating the harmonic index $h = 2$.

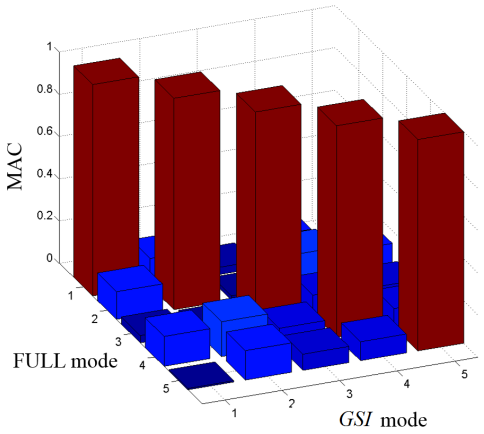

Fig. 3.27 Errors on the natural frequencies of the assembled structure.

The unitary values on the main diagonal of the plot denote a perfect matching between the two sets of modes. Identical results were found for all the other mode shapes.

Lastly, the forced response of the system for the mode shape with $h = 2$ nodal diameters was computed. In particular, the dynamic response was calculated assuming a clockwise traveling wave excitation with EO = 2 and a modal damping ratio of $\zeta = 0.001$. The results of the analyses performed on the two models are shown in Figure 3.28.

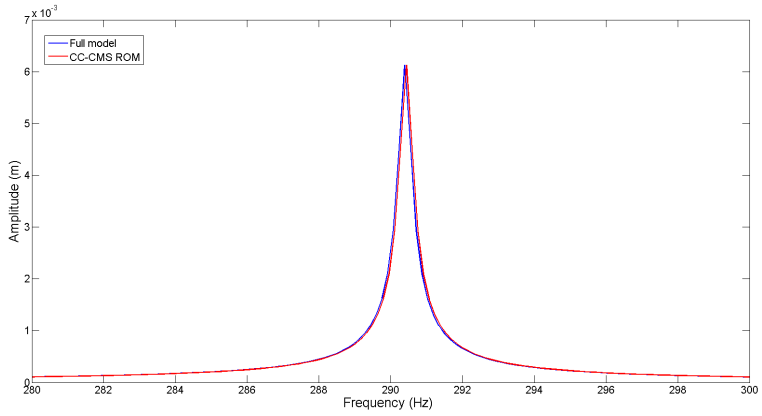

Fig. 3.28 MAC between the full model and *GSI* eigenvectors the term on the main diagonal confirm the perfect agreement between the two sets of eigenvectors.

The negligible stiffening effect characterizing the ROM is clearly the result of several reductions. However, no substantial differences can be found between the two plots, neither in terms of resonance frequency nor in terms of response amplitude. Therefore, the use of the ROM instead of the full one leads to evident advantages, which mainly lie on the drastic reduction of the DoFs (262 vs $\sim$ 12000) and corresponding computational costs (9 s vs $\sim$ 600 s for the forced response of Figure 3.28).

3.8 Discussion

In this chapter the novel *GSI* reduction technique for the modal reduction of the interface DoFs is presented. The methodology goes through different reduction steps of the components' FE models belonging to the same complex structure. In particular, starting from the *Craig-Bampton* reduced order model of each substructure, further model condensations can be achieved by using a suitable set of few *Gram-Schmidt Interface* modes (*GSI* modes). The main advantages of this method are mainly two:

1. Besides reducing the interface DoFs, the method allows the components coupling even in the case on non-conforming interface meshes. This task is carried out by reducing the components' interfaces using the same basis of interface modes and then by writing the compatibility equations not in the domain of the physical DoFs but in the modal space of spanned by the selected Gram-Schmidted *GSI* modes.

2. It can be used as a valid alternative of the Tran's method for the reduction of cyclic symmetric structures. In particular, the independent frontier of a sector treated in cyclic symmetry conditions can be condensed without performing ulterior Guyan condensations of the full FE model. In this way the offline reduction costs can be considerably lowered.

The high precision exhibited in the prediction of the dynamic behavior of assembled structures in terms of natural frequencies, mode shapes and forced response calculations, makes the *GSI* technique suitable not only for turbomachinery applications, but also for many other fields involving dynamic substructuring.

Chapter 4

Multi-Stage Reduced Order Models

4.1 Introduction

The architecture of current aircraft turbojet engines mainly consists of multi-stage structures resulting from the coupling of bladed disks by means of bolted flange joints. Despite of the high complexity of the whole system, the design of a multi-stage assembly is still based on the finite element analyses of its single component. However, the prediction of their dynamic coupling represents a crucial issue requiring high computational efforts and the development of innovative numerical techniques. In this frame ROM techniques become necessary tools for making the FE analyses faster without losing the accuracy of the full FE model.

ROMs in the class of CMS (see Chapter 3) are being used in the turbomachinery field for the prediction of the forced response of isolated bladed disks and just few studies concern their application on multi-stage systems. Nonetheless, the relevance of bladed disks coupling has been numerically proved and few efficient ROM exist to precisely determine the mode shapes and the forced response of a linear multi-stage assembly by overcoming high computational costs.

Although much research has been conducted on single-stage bladed disks, far less has been done for multi-stage bladed disk systems. Indeed, the main challenge associated with modeling multi-stage assemblies is strictly related to the possible different cyclic symmetry of the stages, since the number of sectors is different from stage to stage. In this case a sector representative of the whole system geometry does not exist in general, and typical dynamic calculations based on cyclic constraints can

not be performed as in the case of single bladed disks. Therefore, when dealing with multi-stage systems the single-stage approach is no more valid and the effects of dynamic coupling between stages has to be taken into account.

Early ROMs for multi-stage problems used the well-known dynamic substructuring in the class of the CMS methods [18, 21], which involve dividing the system into components for faster analyses and combining them by using different approaches like fixed-interface, free interface normal modes or hybrid methods (see Chapter 2). An investigation of FE models of multi-stage bladed disks with blade mistuning was conducted by Bladh et al. [30, 31]. It was shown that single-stage bladed disks do not preserve their dynamic behavior when coupled together. In particular, multi-stage effects due to the inter-stage coupling occur in a certain frequency range where the motion of the disk is dominant.

As already stated, in general multi-stage structures do not satisfy cyclic symmetry requirements. Rare exceptions would be those where the coupled stages have numbers of sectors that admit a common divisor[1]. For this reason early multi-stage problems have been tackled trying to combine integral models of bladed disk, which unavoidably leads to solve very large systems of equations. An approach used to obtain ROMs of multi-stage assemblies was proposed by Song et al. [32, 33]. In his technique each stage is treated as a separate component, while the physical displacements characterizing the coupling interface between adjacent stages are projected onto a common set of harmonic basis functions. In Chapter 2 these harmonics were named as *dominant* and describe the typical nodal diameters patterns of a bladed disks. This method has been recently improved by Battiato et al. [6], by expanding the set of dominant basis functions with a suitable pattern of *extra harmonics*, which represent small wave-length spatial phenomena observable at the inter-stage boundary where the continuity of the material is guaranteed (see Chapter 2). For both ROMs the geometric compatibility conditions needed to dynamically couple the full stages are enforced in the space of the Fourier coefficients so that the problem of incompatible meshes at the coupling interface can be easily solved.

From the observation that most of the mode shapes of multi-stage structures are similar to those of isolated disks, especially for the simultaneous occurrence of the same nodal diameters pattern for all the disks, multi-stage ROMs were later

[1]The common divisor can actually be used to divide the whole multi-stage system into a discrete number of fundamental sectors, allowing dynamic computations in cyclic symmetry conditions.

formulated in cyclic symmetry conditions. The first multi-stage reduction technique involving cyclic constraints was proposed by Laxalde et al. [34, 35], who imposed linear constraints for the inter-stage coupling. Later, Sternchüss et al. [36, 3] employed CMS methods in order to create superelements of the stages' reference sectors, which are subsequently coupled by intermediate rings. Besides reducing the size of the full model, this approach gives a solution to the problem of incompatible meshes at the inter-stage boundary. As schematized in Figure 4.1 the ring mesh has to match those at inter-stage boundaries.

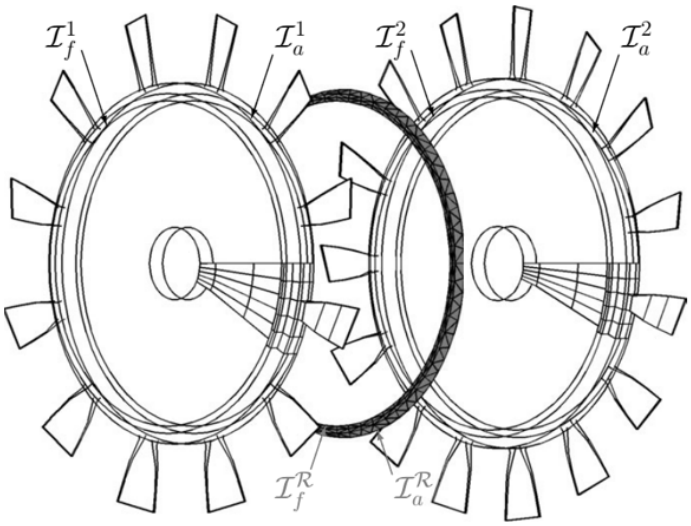

Fig. 4.1 Example of coupled multi-stage system by means of on intermediate ring [3].

However, one should be aware that introducing further components into the model leads to increase the offline computational costs. Indeed, the amount of time spent for their modeling and the subsequent reduction is often not negligible.

The strength of the introduced methods mainly lies in the ability of modeling the dynamic coupling of stages despite their different rotational periodicity. In practical cases this condition is much more severe than actually appears, since the FE models of assembled stages have in general incompatible meshes at the inter-stage boundary (Figure 4.2). Another important feature of such techniques is the capability of reducing the size of complex models that otherwise would be extremely hard to analyze. In this context the best reduction technique for multi-stage systems would be that satisfying all the following requirements:

- It has to ensure the coupling of stages with different cyclic periodicity and incompatible meshes at the inter-stage boundary.
- It has to handle with ROMs of fundamental sectors treated in cyclic symmetry conditions (see Chapter 2).
- The geometric compatibility conditions between the stages ROMs have to be enforced in a simple manner, without using inter-stage connection elements.

In this Chapter a novel reduction technique fulfilling all these conditions is presented. The methodology takes its basis from the approach developed in [32] and goes further to obtain the optimal method allowing better single-stage reductions and multi-stage coupling in the reduced order space only.

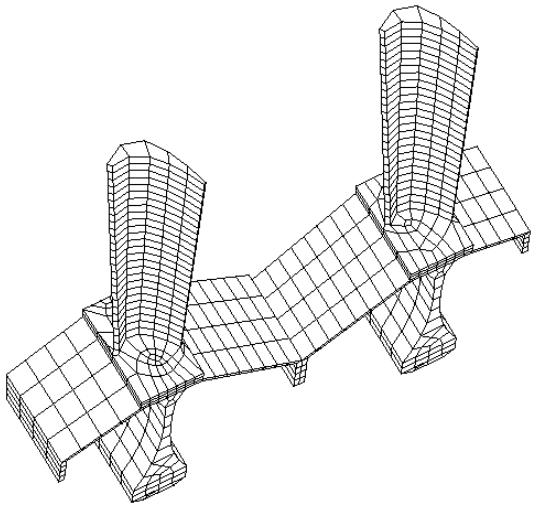

Fig. 4.2 Fundamental sectors of bladed disks having different rotational periodicity. The sectors feature incompatible meshes at the inter-stage boundary.

4.2 Multi-stage Achitectures

Most aircraft turbojet engines consist of bladed disks coupled to each other by means of bolted flange joints. This arrangement is used in both multi-stage compressor and turbine assemblies and ensures the torque transmission from one stage to the adjacent one. Although the working principle of compressors and turbines remains unaltered,

several solutions for stages coupling are currently employed by the manufacturers. Figure 4.3 shows three architectures adopted to joint together the last stages of a HPT assembly.

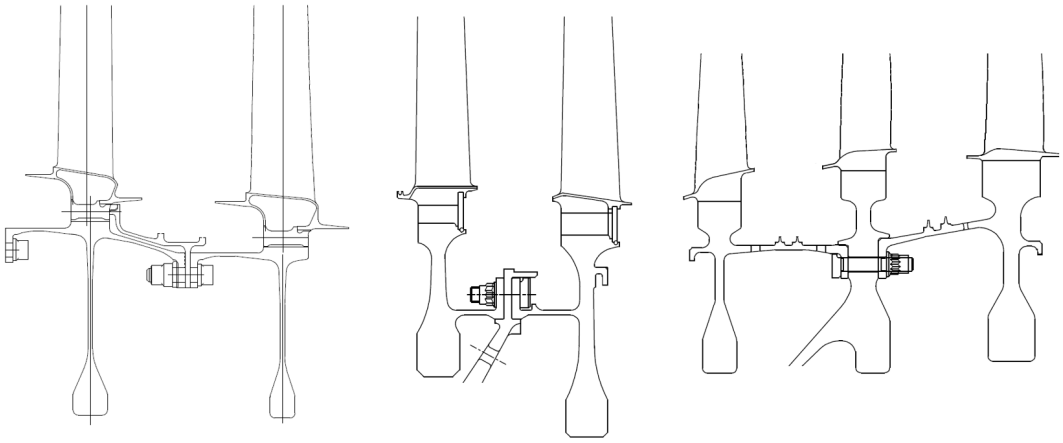

Fig. 4.3 Example of flange joint architectures.

These configurations only differ for the geometry of the bolted flange joint connecting neighboring stages that unavoidably involves a different disk's design. However, besides the flange joint the any disk architecture always shows the features summarized Figure 4.4: The shape of the disk cross section comes out from design

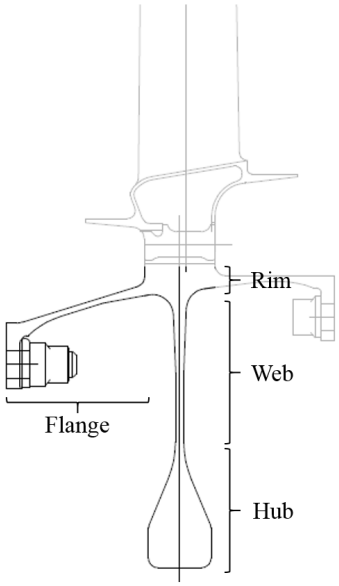

Fig. 4.4 Disk cross section's nomenclature.

criteria mainly based on static considerations. These are related to the necessity of controlling centrifugal loads and related stresses under the prescribed limits.

In the next sections the multi-stage reduction techniques are presented thinking their application on the a) geometry of Figure 4.3. Nonetheless, the developed methods still remain valid for all the bladed disks architectures and generic multi-stage structures.

4.3 Multi-Stage ROM for Full Stages

In this section most of the considerations carried out for cyclic symmetric structures will be exploited to introduce the novel ROM technique presented in [6, 7]. For a better understanding of the reduction procedure some of the equations already derived in Chapter 2 will be recalled.

A bladed disk can be ideally considered as a cyclic symmetric structure consisting of N identical sectors. In the most simple case the fundamental sector representative of the whole structure geometry is composed by one portion of disk with an attached blade (Figure 4.5).

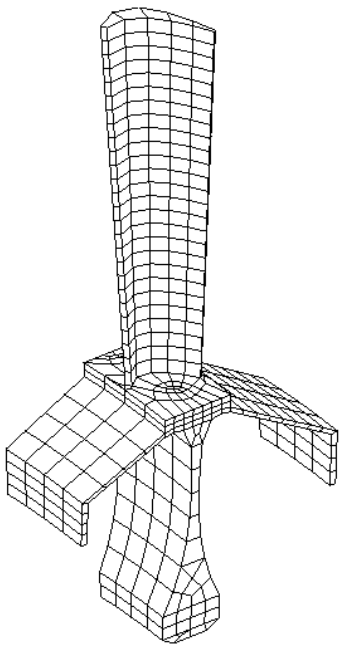

Fig. 4.5 FE model of a fundamental sector.

The conservative EQM describing the linear dynamic behavior of a perfect cyclic symmetric bladed disk is given by:

$$\boldsymbol{M}\ddot{\boldsymbol{x}} + \boldsymbol{K}\boldsymbol{x} = \boldsymbol{f} \tag{4.1}$$

where $\boldsymbol{M}$ and $\boldsymbol{K}$ are the real mass and stiffness matrices, $\boldsymbol{x}$ is the vector of physical displacements and $\boldsymbol{f}$ is the corresponding vector of external forces. As explained in Chapter 2, if Eqn. 4.1 is written in a cylindrical coordinate system having the z-axis coincident with the disk's revolution one (Figure 2.3), and the DoFs grouped sector by sector, the matrices $\boldsymbol{M}$ and $\boldsymbol{K}$ and the vectors $\boldsymbol{x}$ and $\boldsymbol{f}$ can be written as follows:

$$\boldsymbol{M} = \begin{bmatrix} \boldsymbol{M}_0 & \boldsymbol{M}_1 & \boldsymbol{M}_2 & \dots & \boldsymbol{M}_2 & \boldsymbol{M}_1 \\ \boldsymbol{M}_1 & \boldsymbol{M}_0 & \boldsymbol{M}_1 & \dots & \boldsymbol{M}_3 & \boldsymbol{M}_2 \\ \boldsymbol{M}_2 & \boldsymbol{M}_1 & \boldsymbol{M}_0 & \dots & \boldsymbol{M}_4 & \boldsymbol{M}_3 \\ \vdots & \vdots & \vdots & \ddots & \vdots & \vdots \\ \boldsymbol{M}_2 & \boldsymbol{M}_3 & \boldsymbol{M}_4 & \dots & \boldsymbol{M}_0 & \boldsymbol{M}_1 \\ \boldsymbol{M}_1 & \boldsymbol{M}_2 & \boldsymbol{M}_3 & \dots & \boldsymbol{M}_1 & \boldsymbol{M}_0 \end{bmatrix} \qquad \boldsymbol{K} = \begin{bmatrix} \boldsymbol{K}_0 & \boldsymbol{K}_1 & \boldsymbol{K}_2 & \dots & \boldsymbol{K}_2 & \boldsymbol{K}_1 \\ \boldsymbol{K}_1 & \boldsymbol{K}_0 & \boldsymbol{K}_1 & \dots & \boldsymbol{K}_3 & \boldsymbol{K}_2 \\ \boldsymbol{K}_2 & \boldsymbol{K}_1 & \boldsymbol{K}_0 & \dots & \boldsymbol{K}_4 & \boldsymbol{K}_3 \\ \vdots & \vdots & \vdots & \ddots & \vdots & \vdots \\ \boldsymbol{K}_2 & \boldsymbol{K}_3 & \boldsymbol{K}_4 & \dots & \boldsymbol{K}_0 & \boldsymbol{K}_1 \\ \boldsymbol{K}_1 & \boldsymbol{K}_2 & \boldsymbol{K}_3 & \dots & \boldsymbol{K}_1 & \boldsymbol{K}_0 \end{bmatrix}$$

$$\boldsymbol{x} = \begin{Bmatrix} \boldsymbol{x}_1 \\ \boldsymbol{x}_2 \\ \boldsymbol{x}_3 \\ \vdots \\ \boldsymbol{x}_{N-1} \\ \boldsymbol{x}_N \end{Bmatrix} \qquad \boldsymbol{f} = \begin{Bmatrix} \boldsymbol{f}_1 \\ \boldsymbol{f}_2 \\ \boldsymbol{f}_3 \\ \vdots \\ \boldsymbol{f}_{N-1} \\ \boldsymbol{f}_N \end{Bmatrix} \tag{4.2}$$

The matrices $\boldsymbol{M}$ and $\boldsymbol{K}$ have a *block circulant symmetric* structure and the blocks $\boldsymbol{M}_i$ and $\boldsymbol{K}_i$ ($i = 0, \dots, \text{int}(N/2)$ if N is even or $i = 0, \dots, \text{int}\big((N-1)/2\big)$ if N is odd) are symmetric matrices whose dimension is equal to the number of DoFs of each bladed disk sector. When the mass and stiffness matrices are set up from the FE models, the eigenproblem corresponding to Eqn. 4.1 can be solved:

$$(\boldsymbol{K} - \omega_i^2 \boldsymbol{M})\boldsymbol{u}_i = \boldsymbol{0} \qquad i = 1, \dots, Nn_s \tag{4.3}$$

where n_s is the number of DoFs for each disk's sector, while ω_i^2 and $\boldsymbol{u}_i$ are the i^{th} eigenfrequency and eigenvector respectively.

Dynamic analyses of cyclic symmetric structures can be performed on sectors instead on full FE models. According to the DoF partition adopted in Eqn. (4.2), the motion of the n^{th} sector can be described by the following Fourier series [37, 6, 7]:

$$\boldsymbol{x}_n = \frac{1}{\sqrt{N}}\boldsymbol{a}_0 + \sqrt{\frac{2}{N}}\sum_{h=1}^{\tilde{h}-1}\boldsymbol{a}_h^c \cos[(n-1)\varphi_h] + \\ + \sqrt{\frac{2}{N}}\sum_{h=1}^{\tilde{h}-1}\boldsymbol{a}_h^s \sin[(n-1)\varphi_h] + \frac{1}{\sqrt{N}}(-1)^{n-1}\boldsymbol{a}_{\tilde{h}} \quad (4.4)$$

where $\boldsymbol{a}$ is the vector of spatial Fourier coefficients with subscripts c and s identifying the cosine and sine components respectively, h is the dominant harmonic index of the mode shape, $\varphi_h = 2\pi h/N$ represents the *inter-blade phase angle* (IBPA) and $\tilde{h}$, which is equal to $N/2$ if N is even or $(N-1)/2$ if N is odd, denotes the maximum number of the nodal diameters admitted by the disk mode shapes. The last term in Eqn. (4.4) does not exist if N is odd. By grouping the spatial Fourier coefficients as follows:

$$\boldsymbol{a} = \left\{(\boldsymbol{a}_0)^T, (\boldsymbol{a}_1^c)^T, (\boldsymbol{a}_2^c)^T, \ldots, (\boldsymbol{a}_{\tilde{h}-1}^c)^T, (\boldsymbol{a}_{\tilde{h}})^T, (\boldsymbol{a}_{\tilde{h}-1}^s)^T, \ldots, (\boldsymbol{a}_2^s)^T, (\boldsymbol{a}_1^s)^T\right\}^T \quad (4.5)$$

the vector of physical DoF $\boldsymbol{x}(t)$ can be expressed as:

$$\boldsymbol{x}(t) = (\boldsymbol{F}_{N,N} \otimes \boldsymbol{I}_s)\boldsymbol{a}(t) \quad (4.6)$$

where $\boldsymbol{I}_s$ is the identity matrix of size n_s and $\boldsymbol{F}_{N,N}$ is the real valued $N \times N$ Fourier matrix. $\boldsymbol{F}_{N,N}$ is an orthogonal matrix, i.e. $\boldsymbol{F}_{N,N}^T\boldsymbol{F}_{N,N} = \boldsymbol{I}_N$, whose elements are defined

as:

$$f_{nh} = \begin{cases} \dfrac{1}{\sqrt{N}} & \text{if } h = 1 \\ \sqrt{\dfrac{2}{N}} \cos\left[\dfrac{2\pi(h-1)(n-1)}{N}\right] & \text{if } 1 < h < \dfrac{N+2}{2} \\ \dfrac{(-1)^{n-1}}{\sqrt{N}} & \text{if } h = \dfrac{N+2}{2} \\ \sqrt{\dfrac{2}{N}} \sin\left[\dfrac{2\pi(h-1)(n-1)}{N}\right] & \text{if } \dfrac{N+2}{2} < h \leq N \end{cases} \tag{4.7}$$

Since the eigenvectors of the block circulant symmetric matrices $\boldsymbol{M}$ and $\boldsymbol{K}$ are arranged as columns of $\boldsymbol{F}_{N,N}$, the coordinates transformation expressed by Eqn. (4.6) allows the eigenproblem in Eqn. (4.3) to be brought into a block diagonal form. Therefore, N new cyclic symmetric eigenproblems of size equal to n_d can be solved separately [12]. By solving the n^{th} eigenproblem, eigenvalues and eigenvectors for a specific h can be determined without any approximation (see Chapter 2).

4.3.1 Master Nodes

FE dynamic analyses on multi-stage bladed disks are often impracticable due to the large number of DoFs involved in the simulation. For this reason substructuring methods are currently employed in order to create ROMs of the disk's sub-components that are subsequently assembled. The ROM technique treated in this section is based on the *CB*-CMS ROM of each bladed disk constituting the multi-stage structure (see Chapter 3 for further details on the Craig-Bampton method). This methodology requires that at least the DoFs belonging to the inter-stage boundaries of both stages (also called interfaces) are retained as a master. In the case of a real turbine bladed disk these set of interface DoFs belongs to the flange joint (Figure 4.6). Hereafter this set of n_i inter-stage boundary DoFs will be identified as $\boldsymbol{x}_i$.

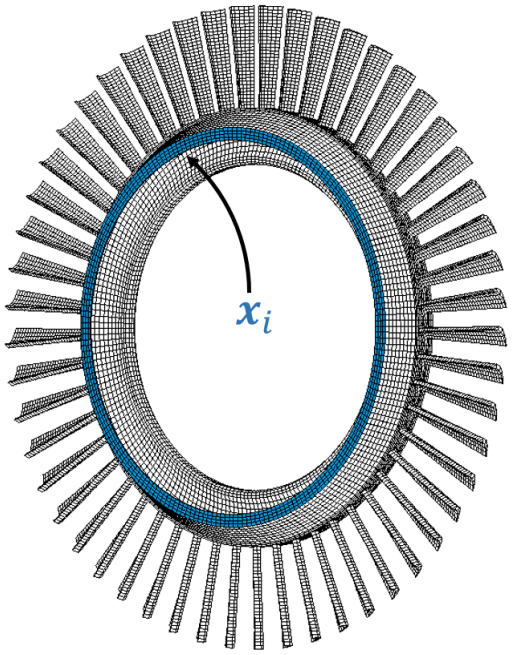

Fig. 4.6 Interface DoFs at the inter-stage boundary of a bladed disk.

In general, for applications concerning dynamic analyses on FE models of real bladed disks no other sets of master DoFs would be required. Due to the complex pressure distribution on the blade airfoils and the need to determine the stresses and strains in extended regions of the structure, it is common to modalize the nodal forces and to reconstruct the physical response in an offline post-processing. Although such approach does not appears as costly from a computational point of view, it requires the storage of the component-mode matrix. This task could be prohibitive when the full FE model consists of a huge number of DoFs, and definitely leads to increase the total duration of the process from the FE model definition to the output results.

For this reason at a preliminary design stage, when sensitivity analyses on certain geometric quantities should be performed, a further set of master DoFs would be desirable. This second set is identified as $\boldsymbol{x}_a$ and contains n_a *active* DoFs, which are those where the forces are applied and the response monitored (Figure. 4.7).

By following the same logic of the *GSI* method for the interfaces reduction (see Chapter 3), in the next subsections it will be shown how the inter-stage boundary DoFs can be reduced by exploiting the harmonic basis functions describing the disk's mode shapes, leaving the active DoFs physical as they are.

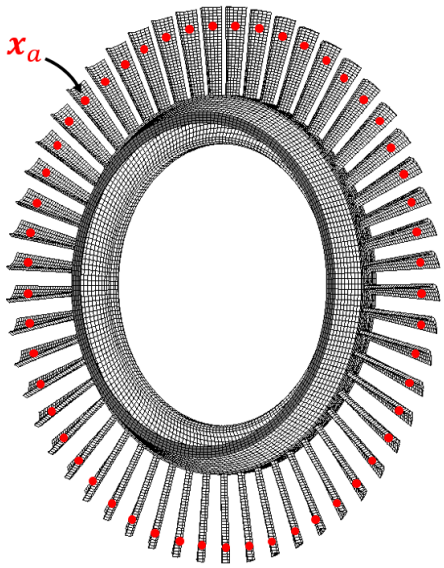

Fig. 4.7 Active DoFs at the blades' airfoils.

4.3.2 Single Stage Reduction

This subsection shows how a strongly reduced model of a single-stage bladed disk can be obtained starting from its *CB*-CMS ROM. The methodology adopted here takes his basis from Song [32] and D'Souza [37] and shows the importance of considering the extra harmonics in the reduction of the interface DoFs.

Consider now the full FE model of a bladed disk and let us denote as $\boldsymbol{x}$ the vector of all its DoFs. Similarly as done for the reduction techniques in Chapter 3, the vector $\boldsymbol{x}$ can be considered as composed by the sets of interface DoFs $\boldsymbol{x}_i$, active DoFs $\boldsymbol{x}_a$ and exceeding DoFs $\boldsymbol{x}_e$, which represent all the DoFs neither on the interface nor active. The number of exceeding DoFs is denoted by n_e. It is named as boundary the set $\boldsymbol{x}_b$ that gathers the interface and active DoFs together: $\boldsymbol{x}_b = \left\{\boldsymbol{x}_i^T \; \boldsymbol{x}_a^T\right\}^T$. According with this DoFs partitions the *CB*-CMS coordinate transformation is defined as (Eqn 3.26):

$$\boldsymbol{x} = \begin{Bmatrix} \boldsymbol{x}_b \\ \boldsymbol{x}_e \end{Bmatrix} \approx \begin{bmatrix} \mathbf{I}_{bb} & \boldsymbol{0}_{bk} \\ \boldsymbol{\Psi}_{eb} & \boldsymbol{\Phi}_{ek} \end{bmatrix} \begin{Bmatrix} \boldsymbol{x}_b \\ \eta_k \end{Bmatrix} = \boldsymbol{R}_{CB}\boldsymbol{x}_{CB} \tag{4.8}$$

where:

- $\left[\boldsymbol{I}_{bb} \; \boldsymbol{\Phi}_{eb}^T\right]^T$ is the constraint modes matrix.

- $\left[\boldsymbol{\theta}_{bk}^T \ \boldsymbol{\Phi}_{ek}^T\right]^T$ is the reduced matrix of n_k fixed-interface normal modes.
- η_k is the reduced vector of modal coordinates corresponding to the reduced set of fixed-interface normal modes.
- $\boldsymbol{R}_{CB}$ is the *CB*-CMS reduction basis.
- $\boldsymbol{x}_{CB}$ is the *CB*-CMS generalized coordinates vector.

By projecting Eqn. (4.1) onto the space spanned by the columns of $\boldsymbol{R}_{CB}$, a reduced set of EQM is obtained:

$$\boldsymbol{M}_{CB}\ddot{\boldsymbol{x}}_{CB} + \boldsymbol{K}_{CB}\boldsymbol{x}_{CB} = \boldsymbol{f}_{CB} \tag{4.9}$$

where

$$\boldsymbol{M}_{CB} = \boldsymbol{R}_{CB}^T \boldsymbol{M} \boldsymbol{R}_{CB} \qquad \boldsymbol{K}_{CB} = \boldsymbol{R}_{CB}^T \boldsymbol{K} \boldsymbol{R}_{CB}$$
$$\boldsymbol{f}_{CB} = \boldsymbol{R}_{CB}^T \boldsymbol{f} \tag{4.10}$$

are the reduced *CB*-CMS mass and stiffness matrices and the *CB*-CMS generalized forces vector.

A further reduction of $\boldsymbol{x}_i$ is possible since they can be approximated by few harmonics describing the trend of the displacement field at the interface. Consider the case where a stage is composed by N identical sectors. The FE model of the sector representative of the whole bladed disk geometry is constructed such that groups of nodes at its interface have the same angle in a cylindrical coordinate system that is aligned with the axis of the stage itself. These groups of nodes are referred to as *radial line segments* [37, 6], and Z of them exist within each sector (Fig. 4.8). Therefore, NZ is the total number of radial line segments at the stage interface. The number of DoFs per radial line segment is n_r.

According to the radial line segments definition, the vector $\boldsymbol{x}_i$ can be partitioned as follows:

$$\boldsymbol{x}_i = \begin{Bmatrix} \boldsymbol{x}_{R_1} \\ \boldsymbol{x}_{R_2} \\ \vdots \\ \boldsymbol{x}_{R_{NZ}} \end{Bmatrix} \tag{4.11}$$

where the subscript "R" stands for radial line segment and the DoFs at the interface of the n^{th} sector correspond to the radial line segments $\boldsymbol{x}_{R_j}$ for $1+(n-1)Z \leq r \leq nZ$.

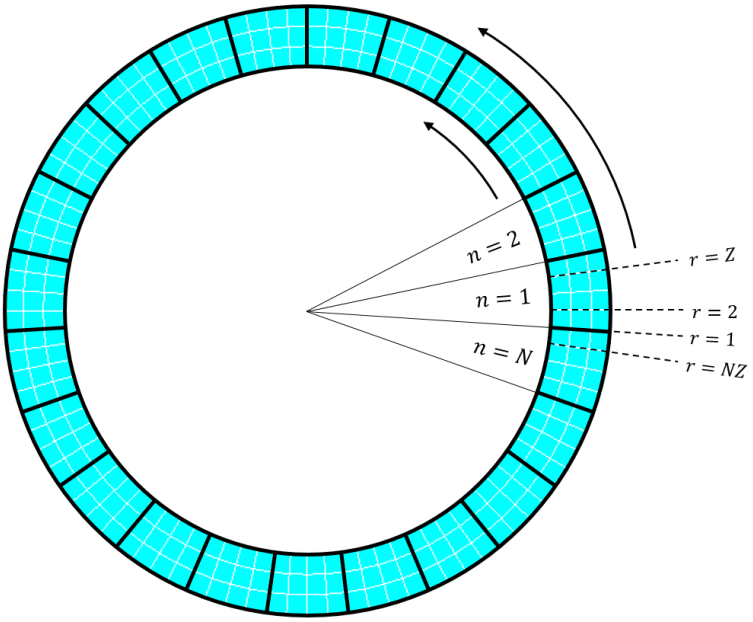

Fig. 4.8 Inter-stage boundary of a cyclic symmetric stage. Sectors and radial line segments are denoted by n and r respectively.

If the r^{th} radial line segment is thought as if it was the r^{th} sector of a bladed disk with NZ sectors, the motion of the r^{th} radial line segment can thus be expressed using the same Fourier series introduced in Eqn. 4.4:

$$\boldsymbol{x}_{R_r} = \frac{1}{\sqrt{NZ}}\boldsymbol{a}_{i_0} + \sqrt{\frac{2}{NZ}}\sum_{h=1}^{\tilde{R}-1}\boldsymbol{a}_{i_h}^{c}\cos[(r-1)\varphi_k] + \\ + \sqrt{\frac{2}{NZ}}\sum_{h=1}^{\tilde{R}-1}\boldsymbol{a}_{i_h}^{s}\sin[(r-1)\varphi_k] + \frac{1}{\sqrt{NZ}}(-1)^{r-1}\boldsymbol{a}_{i_{\tilde{R}}} \quad (4.12)$$

where $\varphi_k = 2\pi k/(NZ)$, $\boldsymbol{a}_i$ denote a vector of interface spatial Fourier coefficients with subscripts c or s identifying the cosine and sine components respectively and $\tilde{R} = NZ/2$ if NZ is even or $\tilde{R} = (NZ-1)/2$ if NZ is odd. The last term Eqn. (4.12) does not exist if NZ is odd.

If the spatial Fourier coefficients are grouped as follows:

$$\boldsymbol{a}_i = \left\{(\boldsymbol{a}_{i_0})^T, (\boldsymbol{a}_{i_1}^{c})^T, (\boldsymbol{a}_{i_2}^{c})^T, \ldots, (\boldsymbol{a}_{i_{\tilde{R}-1}}^{c})^T, (\boldsymbol{a}_{i_{\tilde{R}}})^T, \right. \\ \left. (\boldsymbol{a}_{i_{\tilde{R}-1}}^{s})^T, \ldots, (\boldsymbol{a}_{i_2}^{s})^T, (\boldsymbol{a}_{i_1}^{s})^T\right\}^T \quad (4.13)$$

the interface DoFs can be transformed as:

$$\boldsymbol{x}_i = (\boldsymbol{F}_{NZ,NZ} \otimes \boldsymbol{I}_{n_r})\boldsymbol{a}_i = \boldsymbol{F}_e \boldsymbol{a}_i \tag{4.14}$$

where $\boldsymbol{I}_{n_r}$ is the identity matrix of size n_r, $\boldsymbol{F}_{NZ,NZ}$ is the $NZ \times NZ$ real valued Fourier matrix and $\boldsymbol{F}_e$ is the expansion of $\boldsymbol{F}_{NZ,NZ}$ to all the interface DoFs by the Kronecker product.

By applying the transformation of Eqn. (4.14), the *CB*-CMS generalized coordinates vector $\boldsymbol{x}_{CB}$ becomes:

$$\boldsymbol{x}_{CB} = \begin{Bmatrix} \boldsymbol{x}_i \\ \boldsymbol{x}_a \\ \eta_k \end{Bmatrix} = \begin{bmatrix} \boldsymbol{F}_e & \boldsymbol{0}_{ia} & \boldsymbol{0}_{ik} \\ \boldsymbol{0}_{ai} & \boldsymbol{I}_{aa} & \boldsymbol{0}_{ak} \\ \boldsymbol{0}_{ki} & \boldsymbol{0}_{ka} & \boldsymbol{I}_{kk} \end{bmatrix} \begin{Bmatrix} \boldsymbol{a}_i \\ \boldsymbol{x}_a \\ \eta_k \end{Bmatrix} \tag{4.15}$$

Eqn. 4.15 clearly represents a pure coordinate transformation and does not introduce any reduction of the interface DoFs $\boldsymbol{x}_i$. However, a further reduction of the Fourier coefficients $\boldsymbol{a}_i$ can be achieved by truncating the columns of $\boldsymbol{F}_{NZ,NZ}$ that do not significantly contribute to the definition of the mode shapes at the stage's interface. In fact, a satisfactory representation of a mode shape can be obtained by considering the columns of $\boldsymbol{F}_{NZ,NZ}$ corresponding to the disk's dominant harmonics ($0 \leq h \leq \tilde{h}$) and the small subset of extra harmonics satisfying Eqn. 2.51.

When a bladed disk is subjected to an engine order traveling wave excitation not all the mode shapes can be excited in resonance condition. In particular, if EO is the excitation order and h is the number of nodal diameters of the mode shape, Eqn. 2.70 holds:

$$EO = z \cdot N \pm h \qquad \forall\, z \in \mathbb{N}^+$$

In this case the bladed disk reduction can be performed only for the dominant and extra harmonics corresponding to h. In particular, the Fourier matrix $\boldsymbol{F}_{NZ,NZ}$ can be reduced by retaining just the columns referring to the dominant harmonic index h and the extra ones linked to it (Eqn. (2.51)). Moreover, for a certain dominant harmonic index h, the extra harmonics of order k that significantly contribute to the definition of a mode shape are those selected by the following relationship:

$$|F_k| \geq \varepsilon \cdot F^{max} \qquad \varepsilon \in \mathbb{R}^+ \tag{4.16}$$

where $|F_k|$ is the amplitude of the k^{th} order extra harmonics, $F^{max} = \max(|F_k|)$ and ε is an positive real number arbitrary small (Figure 4.9). The harmonic indexes corresponding to the harmonics of Eqn. 4.16 can thus be grouped into the set σ_h.

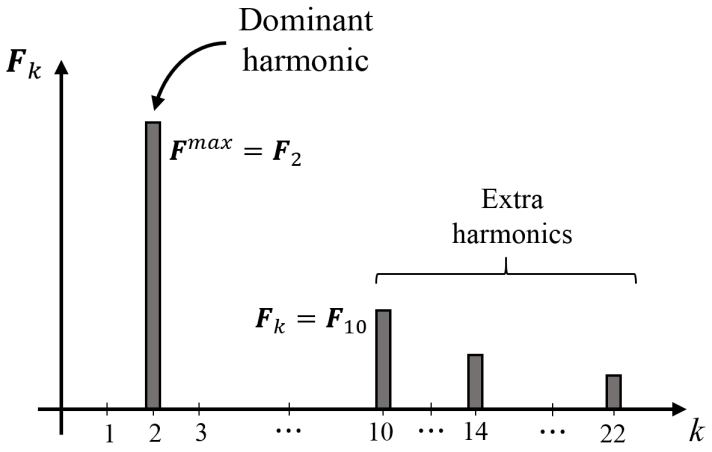

Fig. 4.9 Representation of the highest amplitude harmonics and the generic extras.

If a complete reduction of the bladed disk has to be performed, the former procedure should be carried out all the dominant harmonic indexes h. Hence, the global set of harmonic indexes (referring to both dominant and extra harmonics) that satisfactory reduced the bladed disk's interface is defined as:

$$\Sigma = \bigcup_{h=1}^{\tilde{h}} \sigma_h \tag{4.17}$$

Finally, by picking the columns of $\boldsymbol{F}_{NZ,NZ}$ corresponding to the harmonic indexes collected into Σ, $\boldsymbol{x}_i$ can be reduced as follows:

$$\boldsymbol{x}_i \approx (\boldsymbol{F}_{NZ,\Sigma} \otimes \boldsymbol{I}_{n_d})\tilde{\boldsymbol{a}}_i = \tilde{\boldsymbol{F}}_e \tilde{\boldsymbol{a}}_i \tag{4.18}$$

and the *CB*-CMS generalized coordinates vector becomes:

$$\boldsymbol{x}_{CB} = \begin{Bmatrix} \boldsymbol{x}_i \\ \boldsymbol{x}_a \\ \eta_k \end{Bmatrix} \approx \begin{bmatrix} \boldsymbol{0}_{ia} & \tilde{\boldsymbol{F}}_e & \boldsymbol{0}_{ik} \\ \boldsymbol{I}_{aa} & \boldsymbol{0}_{ai} & \boldsymbol{0}_{ak} \\ \boldsymbol{0}_{ka} & \boldsymbol{0}_{ki} & \boldsymbol{I}_{kk} \end{bmatrix} \begin{Bmatrix} \boldsymbol{x}_a \\ \tilde{\boldsymbol{a}}_i \\ \eta_k \end{Bmatrix} = \boldsymbol{\Phi}_{\boldsymbol{F}}\, \boldsymbol{x}_{\boldsymbol{F}} \tag{4.19}$$

where the tilde (˜) identifies the reduced order matrices and vectors. By projecting Eqn. 4.9 onto Φ_{bmF_e}, a further reduced set of EQM is obtained:

$$\boldsymbol{M}_{F_e}\ddot{\boldsymbol{x}}_{F_e} + \boldsymbol{K}_{F_e}\boldsymbol{x}_{F_e} = \boldsymbol{f}_{F_e} \tag{4.20}$$

where

$$\boldsymbol{M}_{\mathscr{F}} = \Phi_{F_e}^T \boldsymbol{M}_{CB} \Phi_{F_e} \qquad \boldsymbol{K}_{F_e} = \Phi_{F_e}^T \boldsymbol{K}_{CB} \Phi_{F_e} \qquad \boldsymbol{f}_{F_e} = \Phi_{F_e}^T \boldsymbol{f}_{F_e} \tag{4.21}$$

are the reduced mass and stiffness matrices and generalized forces vector.

Example: Single-Stage Reduction

The importance of the extra harmonics in the reduction of the coupling interface DoFs $\boldsymbol{x}_i$ can be evaluated by the following example. Let us consider a blisk having the simple geometry of a flat plate (Figure 4.10).

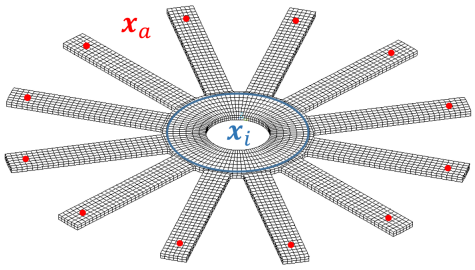

Fig. 4.10 Blisk with geometry of a flat plate and cantilever beams as blades.

The FE model was created by employing the ANSYS elements SOLID186[2] with the following material properties: Young's modulus $E = 78$ GPa, Poisson's ratio $\nu = 0.33$ and density $\rho = 2800$ kg/m^3. The blisk can be supposed to be coupled to another blisk through its interface, which is represented by the blue circumference highlighted in Figure 4.10. The set of active DoFs $\boldsymbol{x}_a$ was defined by selecting one node per blades in homologous locations (red circles in Figure 4.10). Both the interface and active DoFs were then retained as master when the *CB*-CMS ROM of the blisk was created. According to Eqn. 4.18 $\boldsymbol{x}_i$ was further reduced such that only the mode with 2 nodal diameters could be represented at the interface, while

[2]The SOLID186 element is used for 3-D modeling of solid structures. It is defined by 20 nodes having three DoFs at each node: translations in the nodal x, y, and z directions.

the active DoFs were kept physical to facilitate the force application. The set of harmonic indexes Σ in this case coincides to the set σ_2, which is defined as:

$$\sigma_2 = 2, 10, 14, 22, 26 \tag{4.22}$$

which is the largest set of extra harmonics satisfying the Eqn. 2.51. Different ROMs were then created considering the following three reduced sets of harmonic coefficients:

$$\begin{cases} \Sigma_I = 2 \\ \Sigma_{II} = 2, 10 \\ \Sigma_{III} = 2, 10, 14 \end{cases} \tag{4.23}$$

According to Eqn. 4.18 the interface reduction was performed for each set of harmonics listed in Eqn. 4.23 and the blisk's frequency response function (FRF) was evaluated case by case. By assuming a traveling wave excitation on the blades of order 2 (EO = 2) and a modal damping $\zeta = 0.001$, the FRFs were compared to that of the *CB*-CMS ROM calculated in the same conditions (Figure 4.11). From Figure 4.11 it is clear that the correct description of the mode shape $h = 2$ requires at the interface more than one harmonic. In fact, the set Σ_I leads to a ROM that is stiffer than the *CB*-CMS one. As the number of harmonics increases the FRF's peak of the Fourier ROM moves towards that of the *CB*-CMS ROM. The physical reason for that lies on the additional flexibility introduced at the blisk's interface by the harmonics $k = 10$ and $k = 14$.

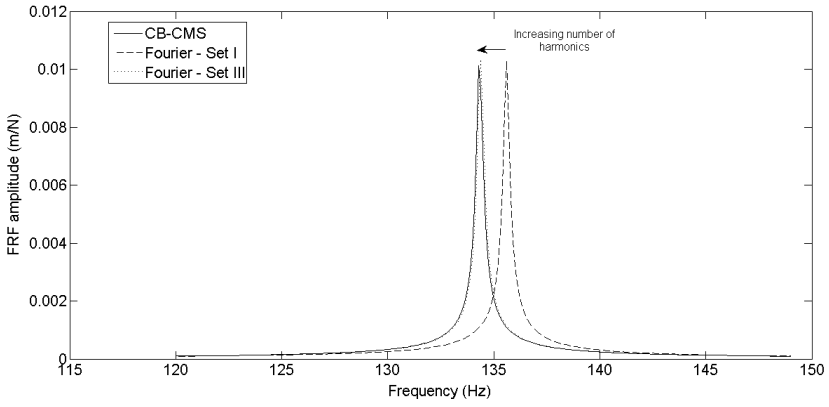

Fig. 4.11 Comparison in terms of FRFs between the *CB*-CMS ROM and the ROMs corresponding to the sets Σ_I and Σ_{III}.

4.3.3 Multi-stage Coupling Procedure

As already introduced at the beginning of this chapter the different cyclic symmetry characterizing the single-stages of a more complex multi-stage system could make their coupling challenging. The most efficient and commonest approach for modeling a bladed disk is based on the definition of the fundamental sector's FE model, which is repeated as many time as the number of blades is. Hence, the different number of sectors of adjacent stages generally results in non-compatible interface meshes, i.e. the nodes of adjacent interfaces do not share the same geometric locations in the circumferential direction. In fact, although the interfaces' modeling can be apriori performed by adopting an element discretization characterized by compatible radial line segments of nodes (i.e. the nodes at the disks' interfaces are located at the same radial coordinates), the different stages' periodicity cannot ensure compatible node locations in the circumferential direction. In this frame the classic coupling procedure based on the equalities of the interface DoFs cannot be applied.

The procedure described in the subsection 4.3.2 easily solves the problem of mismatching meshes introduced above. By assuming compatible radial line segments of nodes at the stages' interfaces, the coupling procedure can be performed by enforcing the compatibility conditions not in the physical space, but in the space of the harmonic Fourier functions approximating the interfaces' motion along each circumference of nodes. The multi-stage coupling procedure is here presented in the case of two stages, but can be extended when more than two stages are involved.

Consider a multi-stage FE model composed by two stages denoted by α and β with N_α and N_β sectors respectively. Z_α and Z_β are the numbers of radial line segments at the interface of the fundamental sectors α and β respectively. The number of the DoFs of the α and β radial line segments is assumed to be the same (under the hypothesis of compatible radial line segments $n_{r_\alpha} = n_{r_\beta} = n_r$). The total numbers of radial line segments are $N_\alpha Z_\alpha$ for the stage α and $N_\beta Z_\beta$ for the stage β. Once the sets of harmonic indexes Σ_α and Σ_β (Eqn. 4.17) are defined a new set of the common harmonic indexes Σ_γ has to be defined as:

$$\Sigma_\gamma = \Sigma_\alpha \cap \Sigma_\beta \tag{4.24}$$

whose is in general smaller than those of Σ_α and Σ_β. The harmonic indexes collected into the set Σ_γ select the columns of the Fourier matrices $\boldsymbol{F}_{N_\alpha Z_\alpha, N_\alpha Z_\alpha}$ and $\boldsymbol{F}_{N_\beta Z_\beta, N_\beta Z_\beta}$

referring to the harmonic functions that describe the same motion at the α and β interfaces. Therefore, the physical interface DoFs of the two stages can be approximated as follows:

$$\boldsymbol{x}_i^{\alpha} \approx (\boldsymbol{F}_{N_\alpha Z_\alpha, \Sigma_\gamma} \otimes \boldsymbol{I}_{n_d}) \tilde{\boldsymbol{a}}_i^{\alpha} = \boldsymbol{F}_e^{\alpha} \tilde{\boldsymbol{a}}_i^{\alpha}$$

$$\boldsymbol{x}_i^{\beta} \approx (\boldsymbol{F}_{N_\beta Z_\beta, \Sigma_\gamma} \otimes \boldsymbol{I}_{n_d}) \tilde{\boldsymbol{a}}_i^{\beta} = \boldsymbol{F}_e^{\beta} \tilde{\boldsymbol{a}}_i^{\beta} \tag{4.25}$$

According to the Eqn. 4.19 the *CB*-CMS generalized coordinates vectors $\boldsymbol{x}_{CB}^{\alpha}$ and $\boldsymbol{x}_{CB}^{\beta}$ can be then expressed as:

$$\boldsymbol{x}_{CB}^{\alpha} = \begin{Bmatrix} \boldsymbol{x}_i^{\alpha} \\ \boldsymbol{x}_a^{\alpha} \\ \eta_k^{\alpha} \end{Bmatrix} \approx \begin{bmatrix} \boldsymbol{0}_{ia} & \boldsymbol{F}_e^{\alpha} & \boldsymbol{0}_{ir} \\ \boldsymbol{I}_{aa} & \boldsymbol{0}_{ai} & \boldsymbol{0}_{ar} \\ \boldsymbol{0}_{ra} & \boldsymbol{0}_{ri} & \boldsymbol{I}_{rr} \end{bmatrix} \begin{Bmatrix} \boldsymbol{x}_a^{\alpha} \\ \tilde{\boldsymbol{a}}_i^{\alpha} \\ \eta_k^{\alpha} \end{Bmatrix} = \Phi_{\boldsymbol{F}_e}^{\alpha} \boldsymbol{x}_{\boldsymbol{F}_e}^{\alpha}$$

$$\boldsymbol{x}_{CB}^{\beta} = \begin{Bmatrix} \boldsymbol{x}_i^{\beta} \\ \boldsymbol{x}_a^{\beta} \\ \eta_k^{\beta} \end{Bmatrix} \approx \begin{bmatrix} \boldsymbol{0}_{ia} & \boldsymbol{F}_e^{\beta} & \boldsymbol{0}_{ir} \\ \boldsymbol{I}_{aa} & \boldsymbol{0}_{ai} & \boldsymbol{0}_{ar} \\ \boldsymbol{0}_{ra} & \boldsymbol{0}_{ri} & \boldsymbol{I}_{rr} \end{bmatrix} \begin{Bmatrix} \boldsymbol{x}_a^{\beta} \\ \tilde{\boldsymbol{a}}_i^{\beta} \\ \eta_k^{\beta} \end{Bmatrix} = \Phi_{\boldsymbol{F}_e}^{\beta} \boldsymbol{x}_{\boldsymbol{F}_e}^{\beta} \tag{4.26}$$

The coupling between the stages is performed by enforcing the compatibility conditions $\tilde{\boldsymbol{a}}_i^{\alpha} = \tilde{\boldsymbol{a}}_i^{\beta} = \tilde{\boldsymbol{a}}_i$ that holds either in the case of compatible or non-compatible meshes at the interfaces. The compatibility conditions are thus enforced through the compatibility matrix $\boldsymbol{C}_{\boldsymbol{F}}$ as:

$$\begin{Bmatrix} \boldsymbol{x}_{\boldsymbol{F}_e}^{\alpha} \\ \boldsymbol{x}_{\boldsymbol{F}_e}^{\beta} \end{Bmatrix} = \begin{Bmatrix} \boldsymbol{x}_a^{\alpha} \\ \tilde{\boldsymbol{a}}_i^{\alpha} \\ \eta_k^{\alpha} \\ \boldsymbol{x}_a^{\beta} \\ \tilde{\boldsymbol{a}}_i^{\beta} \\ \eta_k^{\beta} \end{Bmatrix} = \begin{bmatrix} \boldsymbol{I} & \boldsymbol{0} & \boldsymbol{0} & \boldsymbol{0} & \boldsymbol{0} \\ \boldsymbol{0} & \boldsymbol{0} & \boldsymbol{I} & \boldsymbol{0} & \boldsymbol{0} \\ \boldsymbol{0} & \boldsymbol{0} & \boldsymbol{0} & \boldsymbol{I} & \boldsymbol{0} \\ \boldsymbol{0} & \boldsymbol{I} & \boldsymbol{0} & \boldsymbol{0} & \boldsymbol{0} \\ \boldsymbol{0} & \boldsymbol{0} & \boldsymbol{I} & \boldsymbol{0} & \boldsymbol{0} \\ \boldsymbol{0} & \boldsymbol{0} & \boldsymbol{0} & \boldsymbol{0} & \boldsymbol{I} \end{bmatrix} \begin{Bmatrix} \boldsymbol{x}_a^{\alpha} \\ \boldsymbol{x}_a^{\beta} \\ \tilde{\boldsymbol{a}}_i \\ \eta_k^{\alpha} \\ \eta_k^{\beta} \end{Bmatrix} = \boldsymbol{C}_{\boldsymbol{F}} \begin{Bmatrix} \boldsymbol{x}_a^{\alpha} \\ \boldsymbol{x}_a^{\beta} \\ \hat{\boldsymbol{a}}_i \\ \eta_k^{\alpha} \\ \eta_k^{\beta} \end{Bmatrix} = \boldsymbol{C}_{\boldsymbol{F}} \boldsymbol{x}_{\boldsymbol{F}}^{MS} \tag{4.27}$$

where the superscript ^{MS} stands for *Multi-Stage*. Lastly, the assembled and reduced matrices and force vector are given by:

$$\boldsymbol{M}_{\boldsymbol{F}}^{MS} = \boldsymbol{C}_{\boldsymbol{F}}^T \begin{bmatrix} \boldsymbol{M}_{\boldsymbol{F}}^{\alpha} & \boldsymbol{0} \\ \boldsymbol{0} & \boldsymbol{M}_{\boldsymbol{F}}^{\beta} \end{bmatrix} \boldsymbol{C}_{\boldsymbol{F}} \qquad \boldsymbol{K}_{\boldsymbol{F}}^{MS} = \boldsymbol{C}_{\boldsymbol{F}}^T \begin{bmatrix} \boldsymbol{K}_{\boldsymbol{F}}^{\alpha} & \boldsymbol{0} \\ \boldsymbol{0} & \boldsymbol{K}_{\boldsymbol{F}}^{\beta} \end{bmatrix} \boldsymbol{C}_{\boldsymbol{F}}$$

$$\boldsymbol{f}_{\boldsymbol{F}}^{MS} = \boldsymbol{C}_{\boldsymbol{F}}^{T} \begin{Bmatrix} \boldsymbol{f}_{\boldsymbol{F}}^{\alpha} \\ \boldsymbol{f}_{\boldsymbol{F}}^{\beta} \end{Bmatrix} \tag{4.28}$$

For sake of clarity Σ_γ contains all the harmonic indexes corresponding to the harmonic coefficients for which the compatibility conditions between stages can be enforced (Figure 4.12). The harmonic coefficients corresponding to harmonic indexes either belonging only to Σ_α or Σ_β are automatically enforced to be zero when the coupling is performed.

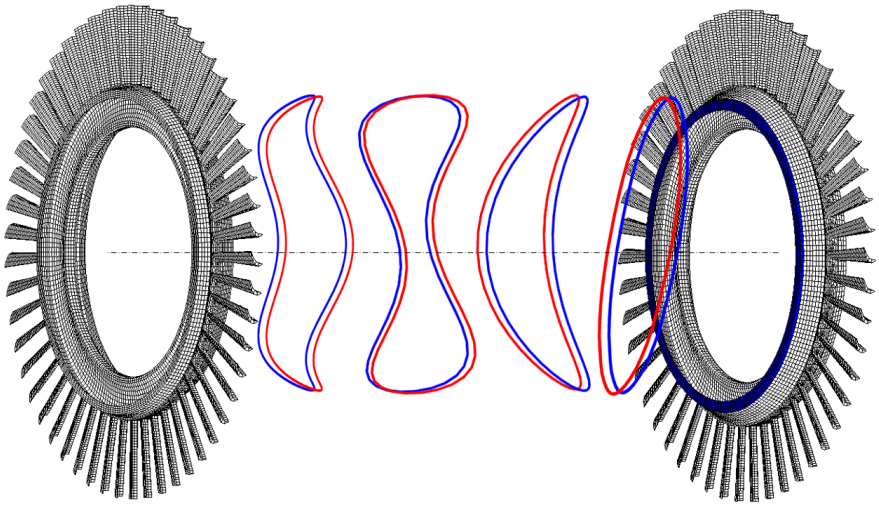

Fig. 4.12 The harmonic compatibility conditions between stages are enforced through the equality of the harmonic coefficients representing the common harmonic functions.

As in the case of the method described in chapter 3 the selected harmonic basis functions describe the characteristic motion of the interfaces. Therefore, the two single-stage ROMs can be dynamically coupled, and then the vibration energy be transferred from one to the other, if the harmonic function reducing both interfaces are the same.

Example: Multi-Stage Coupling

The multi-stage system composed by two bladed disks is considered as the reference example. It can be thought as the assembly resulting from the coupling of the two stages with $N_\alpha = 50$ and $N_\beta = 53$ sectors. The FE models of the two stages were generated by repeating the FE models of the fundamental sectors N_α and N_β times respectively (the FE models of Figure 4.12 are considered as reference). The

stages were meshed using the SOLID185 [3] ANSYS elements to which the following material properties were associated: Young's modulus $E = 210$ GPa, Poisson's ratio $\nu = 0.33$ and density $\rho = 7800$ kg/m^3. For both stages the number of radial line segments per sector is equal to four ($Z_\alpha = Z_\beta = 4$). The radial line segments of the stage α are compatible to those of the stage β, meaning that they both have five nodes at the same radial coordinates. The different periodicity characterizing the two stages leads to different meshes at the coupling interfaces.

The *CB*-CMS ROMs were then created by retaining for both stages the sets of interface ($\boldsymbol{x}_i^\alpha$ and $\boldsymbol{x}_i^\beta$) and active DoFs ($\boldsymbol{x}_a^\alpha$ and $\boldsymbol{x}_a^\beta$). The number of nodes and DoFs of the two FE models and the size of the interface and active sets of DoFs are listed in the Table 4.1.

Table 4.1 Features of the stages α and β FE models.

Stage	# nodes	# DoFs	# interface DoFs (n_i)	# active DoFs (n_a)
α	42250	126750	3000	150
β	44202	132606	3180	159

In addition, the first 200 fixed-interface normal modes were also considered for both the stages, yielding two *CB*-CMS ROMs with 3350 and 3539 DoFs. For reference, the first 200 natural frequencies of both *CB*-CMS ROMs are all within 0.4% of the corresponding FE natural frequencies. The mentioned difference was evaluated by the following relationship:

$$e_{\%} = \frac{|f_{CB} - f_{FE}|}{f_{FE}} \cdot 100 \tag{4.29}$$

where the FE quantities were considered as reference.

After having created the *CB*-CMS ROMs of the two stages, the sets Σ_α and Σ_β of extra harmonics indexes corresponding to different values of ε were defined (Eqn. 4.16). The values of ε and the corresponding sets of harmonic indexes are listed in Table 4.2. where Σ_γ represents the intersection between Σ_α and Σ_β.

The ROMs of the two stages were created using as reduction basis the harmonic functions corresponding to the three sets Σ_γ listed in Table 4.2. After having solved the corresponding eigenproblems, the percentage differences in term of natural

[3]The SOLID185 element is used for 3-D modeling of solid structures. It is defined by eight nodes having three DoFs at each node: translations in the nodal x, y, and z directions.

Table 4.2 Sets of harmonic indexes used for the reduction of the stages α and β.

ε	Σ_α	Σ_β	Σ_γ
0.5	$0 \rightarrow 25$	$0 \rightarrow 27$	$0 \rightarrow 25$
10^{-1}	$0 \rightarrow 29$	$0 \rightarrow 31$	$0 \rightarrow 29$
10^{-2}	$0 \rightarrow 35$	$0 \rightarrow 37$	$0 \rightarrow 35$

frequencies with respect the *CB*-CMS ROMs were evaluated by using the Eqn. 4.29. Figure 4.13 shows the values of $e_{\%}$ corresponding to the set Σ_γ obtained for $\varepsilon = 0.5$.

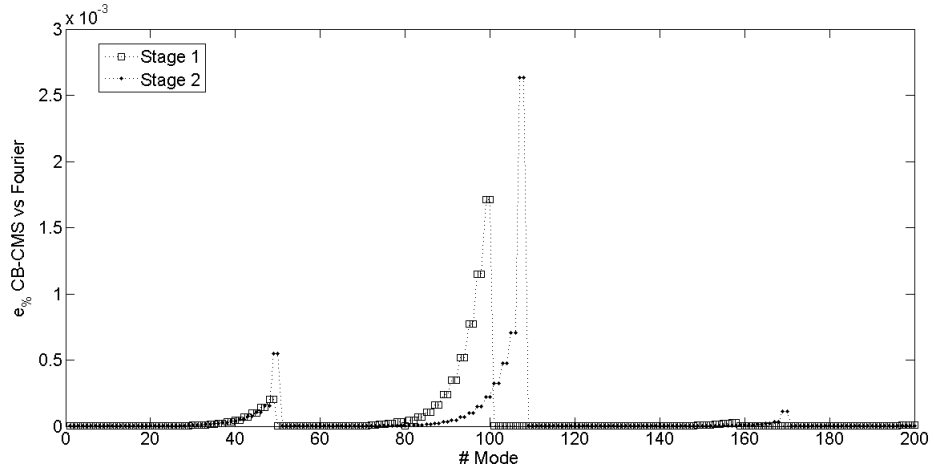

Fig. 4.13 $e_{\%}$ for the first 200 modes of the stages α and β when the first set of hamonic indexes Σ_γ is considered.

From Figure 4.13 it can be noted that the stages' ROMs obtained by using only the set of dominant harmonics ($h = 0, 1, 2, \ldots, 25$) leads to small differences on frequencies when with respect the *CB*-CMS ones ($\max(e_{\%}) \approx 2.6 \cdot 10^{-3}\%$). If the sets Σ_γ corresponding to $\varepsilon = 10^{-1}$ and $\varepsilon = 10^{-2}$ are used, the maxima differences decrease to $e_{\%} \approx 3.5 \cdot 10^{-4}\%$ and $e_{\%} \approx 3.2 \cdot 10^{-5}\%$ respectively. These results confirm the importance of expanding the interface reduction basis if a better approximation of the stage's dynamics is required.

By following the stages' coupling procedure described above, three multi-stage ROMs were created by enforcing the compatibility conditions as suggested in Eqn. 4.27. Eigenfrequencies and mode shapes of the assembled ROMs were then compared to those of the full FE model by using Eqn. 4.29 and the Modal Assur-

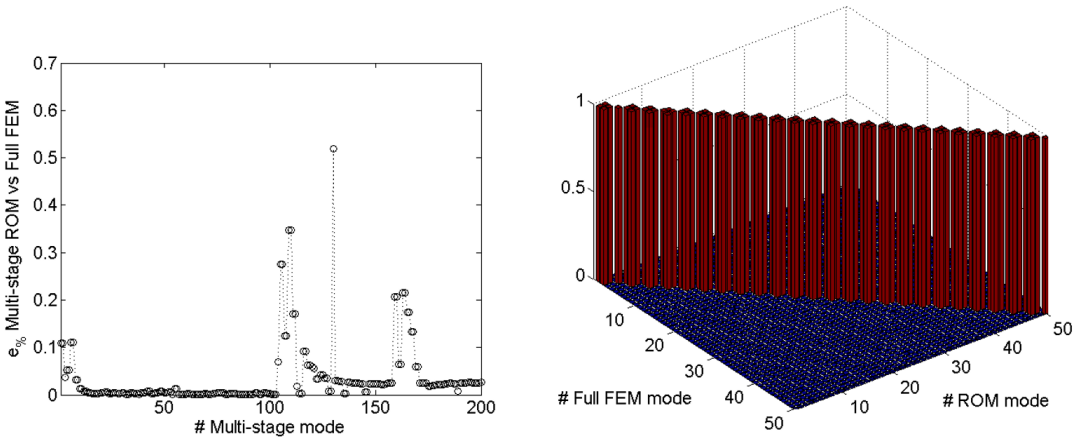

a) b)

Fig. 4.14 $e_{\%}$ for the first 200 modes obtained by comparing the frequencies from the full FE model with those of the multi-stage ROM a), MAC between the the first 50 full FE modes and ROM modes b).

ance Criterion (Figure 4.14). The plots refer to the case where only the dominant harmonics ($h = 0, 1, 2, \ldots, 25$) were used to reduce the interfaces of the two stages.

The comparison between the full and reduced multi-stage models was completed by computing the forced response of the system when a traveling wave excitation with EO = 2 was applied to the active DoFs in the z. Due to the excellent results already obtained for the eigenvalues and eigenvectors comparisons, this further check was performed on the smaller size ROM.

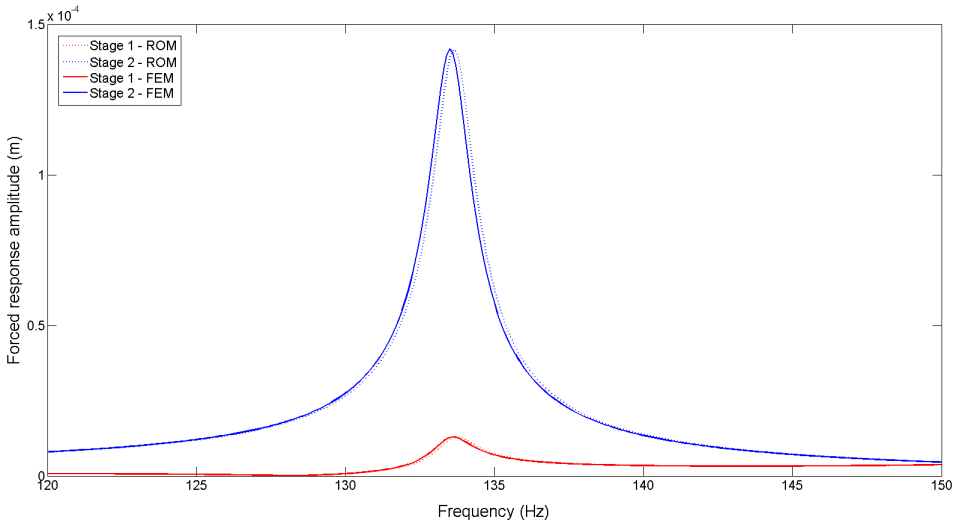

Fig. 4.15 Forced response comparison between the FE and reduced multi-stage model.

From Figure 4.15 no significant differences can be noted neither in frequency nor in amplitude between two plots. However, performing forced response calculations on the ROM was much more efficient than doing the same for the full assembled FE model. In fact, due to the different model size (1306 vs $\sim$ 260000) the computational time spent for the forced response on the full configuration was almost 138 times larger than that spent for the reduced one ($\sim$15 s vs $\sim$ 2075 s).

The small differences on the natural frequencies ($\max(e\%) \approx 0.55\%$), the perfect matching on the eigenvectors and the accuracy of the forced response calculations, make the reduction technique suitable for fast dynamic analyses on complex multi-stage systems.

Note that the straightforward application of the methodology here described implies two different conditions:

1. The mesh at each stage's interface has to be characterized by equally spaced radial line segments of nodes;
2. The radial line segments at the interface between two adjacent stages have nodes located at the same radial coordinates.

Although the first condition cannot be relaxed, since it allows the coordinate transformation of Eqn. 4.18, the second one can be overcome by first interpolating the harmonic Fourier functions of one interface at the circumferences of nodes of the adjacent one, and then by enforcing the compatibility condition as done in Eqn. 4.27.

4.4 Multi-stage ROM for Sectors in Cyclic Symmetry Conditions

The number of inter-stage boundary DoFs is often large and creating *CB*-CMS ROMs of full stages could be a time consuming process. For this reason a ROM technique involving FE models of fundamental sectors instead of full stages would be much more efficient. In this section an original reduction technique for multi-stage structures involving cyclic constraints on fundamental sectors is presented. The methods starts from the *cyclic Craig-Bampton* method (CS-CB) developed by Bladh et al. [9] and goes further giving a smart solution for the sectors' interfaces reduction.

4.4.1 Cyclic Craig-Bampton Method

The CS-CB method is here formulated for bladed disk sectors consisting of one disk's sector with an attached blade (Figure 4.2). By using the notation of Figure 4.16 the sector's DoFs may be partitioned as:

$$\boldsymbol{x}_S = \begin{Bmatrix} \boldsymbol{x}_i \\ \boldsymbol{x}_a \\ \boldsymbol{x}_l \\ \boldsymbol{x}_r \\ \boldsymbol{x}_e \end{Bmatrix} \tag{4.30}$$

where:

- $\boldsymbol{x}_i$ is the vector of DoFs at the inter-stage boundary non including those at the left and right sector's frontier.
- $\boldsymbol{x}_a$ is the vector of active DoFs.
- $\boldsymbol{x}_l$ is the vector of DoFs at sector's left frontier.
- $\boldsymbol{x}_r$ is the vector of DoFs at sector's right frontier.
- $\boldsymbol{x}_e$ is the vector of exceeding DoFs, i.e. those not belonging to the previous sets.

The corresponding sector's matrices and force vector can thus be partitioned as follows:

$$\boldsymbol{M}_S = \begin{bmatrix} \boldsymbol{M}_{ii} & \boldsymbol{M}_{ia} & \boldsymbol{M}_{il} & \boldsymbol{M}_{ir} & \boldsymbol{M}_{ie} \\ \boldsymbol{M}_{ai} & \boldsymbol{M}_{aa} & \boldsymbol{M}_{al} & \boldsymbol{M}_{ar} & \boldsymbol{M}_{ae} \\ \boldsymbol{M}_{li} & \boldsymbol{M}_{la} & \boldsymbol{M}_{ll} & \boldsymbol{M}_{lr} & \boldsymbol{M}_{le} \\ \boldsymbol{M}_{ri} & \boldsymbol{M}_{ra} & \boldsymbol{M}_{rl} & \boldsymbol{M}_{rr} & \boldsymbol{M}_{re} \\ \boldsymbol{M}_{ei} & \boldsymbol{M}_{ea} & \boldsymbol{M}_{el} & \boldsymbol{M}_{er} & \boldsymbol{M}_{ee} \end{bmatrix} \quad \boldsymbol{K}_S = \begin{bmatrix} \boldsymbol{K}_{ii} & \boldsymbol{K}_{ia} & \boldsymbol{K}_{il} & \boldsymbol{K}_{ir} & \boldsymbol{K}_{ie} \\ \boldsymbol{K}_{ai} & \boldsymbol{K}_{aa} & \boldsymbol{K}_{al} & \boldsymbol{K}_{ar} & \boldsymbol{K}_{ae} \\ \boldsymbol{K}_{li} & \boldsymbol{K}_{la} & \boldsymbol{K}_{ll} & \boldsymbol{K}_{lr} & \boldsymbol{K}_{le} \\ \boldsymbol{K}_{ri} & \boldsymbol{K}_{ra} & \boldsymbol{K}_{rl} & \boldsymbol{K}_{rr} & \boldsymbol{K}_{re} \\ \boldsymbol{K}_{ei} & \boldsymbol{K}_{ea} & \boldsymbol{K}_{el} & \boldsymbol{K}_{er} & \boldsymbol{K}_{ee} \end{bmatrix}$$

$$\boldsymbol{f}_S = \begin{Bmatrix} \boldsymbol{f}_i \\ \boldsymbol{f}_a \\ \boldsymbol{f}_l \\ \boldsymbol{f}_r \\ \boldsymbol{f}_e \end{Bmatrix} \tag{4.31}$$

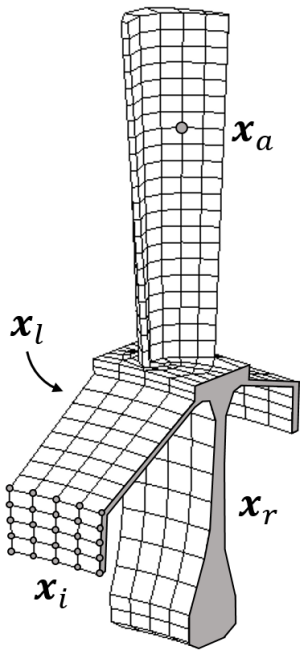

Fig. 4.16 FE model of the fundamental sector: DoFs notation.

According to Eqn. 2.22 cyclic constraints can be enforced between the sector's left and right frontiers so that $\boldsymbol{x}_r$ can be expressed in terms of $\boldsymbol{x}_l$ as follows:

$$\boldsymbol{x}_r = \boldsymbol{x}_l e^{\pm \imath \varphi_h} \tag{4.32}$$

Therefore, the vector of physical coordinates $\boldsymbol{x}_S$ can be turned into cyclic coordinates by using the following transformation:

$$\boldsymbol{x}_s = \begin{Bmatrix} \boldsymbol{x}_i \\ \boldsymbol{x}_a \\ \boldsymbol{x}_l \\ \boldsymbol{x}_r \\ \boldsymbol{x}_e \end{Bmatrix} = \begin{bmatrix} \boldsymbol{I}_{ii} & \boldsymbol{0}_{ia} & \boldsymbol{0}_{il} & \boldsymbol{0}_{ie} \\ \boldsymbol{0}_{ai} & \boldsymbol{I}_{aa} & \boldsymbol{0}_{al} & \boldsymbol{0}_{ae} \\ \boldsymbol{0}_{li} & \boldsymbol{0}_{la} & \boldsymbol{I}_{ll} & \boldsymbol{0}_{le} \\ \boldsymbol{0}_{ri} & \boldsymbol{0}_{ra} & \boldsymbol{I}_{rr} e^{\pm \imath \varphi_h} & \boldsymbol{0}_{re} \\ \boldsymbol{0}_{ei} & \boldsymbol{0}_{ea} & \boldsymbol{0}_{el} & \boldsymbol{I}_{ee} \end{bmatrix} \begin{Bmatrix} \boldsymbol{x}_i^h \\ \boldsymbol{x}_a^h \\ \boldsymbol{x}_l^h \\ \boldsymbol{x}_e^h \end{Bmatrix} = \boldsymbol{T}_{CS}^h \boldsymbol{x}_{CS}^h \tag{4.33}$$

where $\boldsymbol{T}_{CS}^h$ is the cyclic transformation matrix, $\boldsymbol{x}_{CS}^h$ is the cyclic coordinates vector and the superscript h denotes the harmonic index for which the cyclic reduction has been performed. The cyclic mass and stiffness matrices and the external forces are finally obtained by using the following relationships:

$$\boldsymbol{M}_{CS}^h = (\boldsymbol{T}_{CS}^h)^* \boldsymbol{M}_S \boldsymbol{T}_{CS}^h \qquad \boldsymbol{K}_{CS}^h = (\boldsymbol{T}_{CS}^h)^* \boldsymbol{K}_S \boldsymbol{T}_{CS}^h$$

$$\boldsymbol{f}_{CS} = (\boldsymbol{T}^h_{CS})^* \boldsymbol{f}_S \tag{4.34}$$

The size of the cyclic symmetric sector can be further reduced by resorting to the *CB*-CMS reduction technique. In this regard two new vectors of cyclic boundary and exceeding DoFs can be defined as:

$$\boldsymbol{x}^h_b = \begin{Bmatrix} \boldsymbol{x}^h_i \\ \boldsymbol{x}^h_a \end{Bmatrix} \qquad \boldsymbol{x}^h_{e'} = \begin{Bmatrix} \boldsymbol{x}^h_l \\ \boldsymbol{x}^h_e \end{Bmatrix} \tag{4.35}$$

which leads to the following partitioning of the the cyclic coordinates vector:

$$\boldsymbol{x}^h_{CS} = \begin{Bmatrix} \boldsymbol{x}^h_b \\ \boldsymbol{x}^h_{e'} \end{Bmatrix} \tag{4.36}$$

The cyclic matrices and force vector of Eqn. 4.55 can then be partitioned accordingly as:

$$\boldsymbol{M}^h_{CS} = \begin{bmatrix} \boldsymbol{M}^h_{bb} & \boldsymbol{M}^h_{be'} \\ \boldsymbol{M}^h_{e'b} & \boldsymbol{M}^h_{e'e'} \end{bmatrix} \qquad \boldsymbol{K}^h_{CS} = \begin{bmatrix} \boldsymbol{K}^h_{bb} & \boldsymbol{K}^h_{be'} \\ \boldsymbol{K}^h_{e'b} & \boldsymbol{K}^h_{e'e'} \end{bmatrix} \qquad \boldsymbol{f}^h_{CS} = \begin{Bmatrix} \boldsymbol{f}^h_b \\ \boldsymbol{f}^h_{e'} \end{Bmatrix} \tag{4.37}$$

For each harmonic index h the cyclic DoFs $\boldsymbol{x}^h_{e'}$ can be statically condensed on the cyclic boundary DoFs exactly as done in Eqn. 3.15:

$$\boldsymbol{x}^h_{e'} = -\boldsymbol{K}^h_{e'e'}\boldsymbol{K}^h_{e'b}\boldsymbol{x}^h_b = \Psi^h_{e'b}\boldsymbol{x}^h_b \tag{4.38}$$

where the term $\Psi^h_{e'b} = -\boldsymbol{K}^h_{e'e'}\boldsymbol{K}^h_{e'b}$ is here referred to as the *cyclic static condensation matrix*. Eqn. 4.38 can then be used to express $\boldsymbol{x}^h_{CS}$ in terms of $\boldsymbol{x}^h_b$:

$$\boldsymbol{x}^h_{CS} = \begin{Bmatrix} \boldsymbol{x}^h_b \\ \boldsymbol{x}'^h_e \end{Bmatrix} \approx \begin{bmatrix} \boldsymbol{I}^h_b \\ \Psi^h_{e'b} \end{bmatrix} \boldsymbol{x}^h_b \tag{4.39}$$

where:

$$\Psi^h_{sb} = \begin{bmatrix} \boldsymbol{I}^h_b \\ \Psi^h_{e'b} \end{bmatrix} \tag{4.40}$$

is the $n_s \times n_b$ *cyclic constraint-mode matrix*.

Moreover, the *cyclic fixed-interface normal modes* are computed for each harmonic index h from the cyclic eigenproblem:

$$\left(\boldsymbol{K}^h_{e'e'} - \omega^2_{e',j}\boldsymbol{M}^h_{e'e'}\right)\boldsymbol{\phi}^h_{e',j} = \boldsymbol{0}_{e'} \qquad \forall\ j = 1,\ldots,n_{e'} \tag{4.41}$$

where $\omega^2_{e',j}$ and $\boldsymbol{\phi}^h_{e',j}$ are the j^{th} eigenvalue and mass normalized eigenvector. The complete set of $n_{e'}$ cyclic fixed-interface normal modes can be labeled as $\boldsymbol{\Phi}^h_{e'e'}$ and assembled for increasing eigenvalues as columns of the following modal matrix:

$$\boldsymbol{\Phi}^h_{se'} = \begin{bmatrix} \boldsymbol{0}_{be'} \\ \boldsymbol{\Phi}^h_{e'e'} \end{bmatrix} \tag{4.42}$$

Therefore, by keeping a subset of $n_k \ll n'_e$ cyclic fixed-interface normal modes, $\boldsymbol{x}^h_{CS}$ can reduced as (Eqn. 3.26):

$$\boldsymbol{x}^h_{CS} = \begin{Bmatrix} \boldsymbol{x}^h_b \\ \boldsymbol{x}^h_{e'} \end{Bmatrix} \approx \begin{bmatrix} \boldsymbol{I}^h_b & \boldsymbol{0}_{bk} \\ \boldsymbol{\Psi}^h_{e'b} & \boldsymbol{\Phi}^h_{e'k} \end{bmatrix} \begin{Bmatrix} \boldsymbol{x}^h_b \\ \eta^h_k \end{Bmatrix} = \boldsymbol{R}^h_{CB}\boldsymbol{x}^h_{CB} \tag{4.43}$$

where $\boldsymbol{R}^h_{CB}$ is the cyclic *CB*-CMS component-mode matrix. By projecting the sector's EQM onto the space spanned by the columns of $\boldsymbol{R}^h_{CB}$, the following reduced set of EQM is obtained:

$$\begin{bmatrix} \tilde{\boldsymbol{M}}^h_{bb} & \tilde{\boldsymbol{M}}^h_{bk} \\ \tilde{\boldsymbol{M}}^h_{kb} & \boldsymbol{I}^h_{kk} \end{bmatrix} \begin{Bmatrix} \ddot{\boldsymbol{x}}^h_b \\ \ddot{\eta}^h_k \end{Bmatrix} + \begin{bmatrix} \tilde{\boldsymbol{K}}^h_{bb} & \boldsymbol{0} \\ \boldsymbol{0} & \left(\Omega^2_{kk}\right)^h \end{bmatrix} \begin{Bmatrix} \boldsymbol{x}^h_b \\ \eta^h_k \end{Bmatrix} = \begin{Bmatrix} \tilde{\boldsymbol{f}}^h_b \\ \tilde{\boldsymbol{f}}^h_k \end{Bmatrix} \tag{4.44}$$

The submatrices and subvectors of Eqn. 4.44 are defined exactly as already done in Eqn. 3.28.

4.4.2 Cyclic Interface DoFs Reduction and Inter-Stage Coupling

The ROM obtained at the end of the former procedure well approximate the single-stage dynamics for mode shapes having h nodal diameters. However, although a significant reduction of the exceeding DoFs was achieved, the set of cyclic interface DoFs ($\boldsymbol{x}^h_i$) remained preserved (Figure 4.17). In general, disk sectors characterized by different sector angles have non-matching nodes at the inter-stage boundaries. Therefore, the direct coupling between the cyclic ROMs obtained by employing the

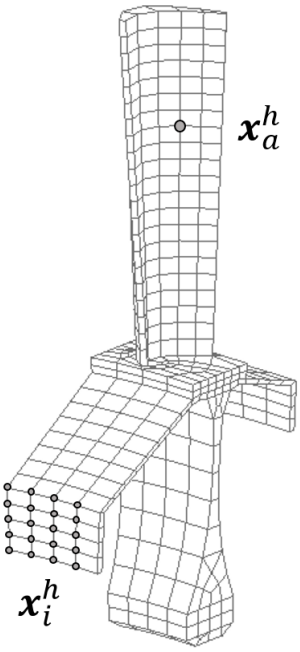

Fig. 4.17 Cyclic DoFs retained as a master in the CS-CB ROM.

CS-CB method can take place if a further transformation of the interface DoFs is performed.

In the previous section it was assumed to have regular meshes at the stages' interfaces, a condition that allowed to group the DoFs in radial line segments. By using the same logic for fundamental sectors, the interface mesh can be created in order to have Z radial line segments of DoFs (Figure 4.18):

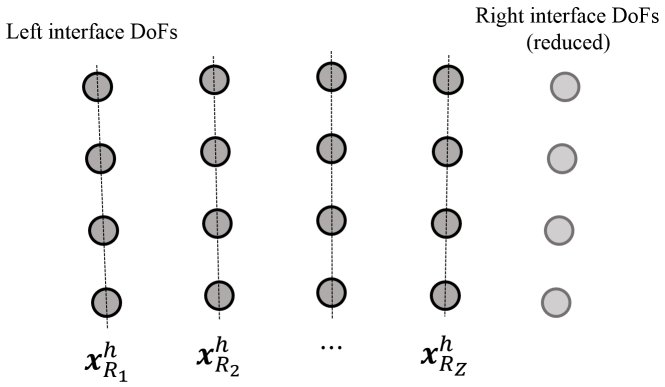

Fig. 4.18 Radial line segments of DoFs at the cyclic sector interface.

In this way the interface DoFs can be partitioned as follows:

$$\boldsymbol{x}_i^h = \begin{Bmatrix} \boldsymbol{x}_{R_1}^h \\ \vdots \\ \boldsymbol{x}_{R_r}^h \\ \vdots \\ \boldsymbol{x}_{R_Z}^h \end{Bmatrix} \qquad \forall\, r = 1,\ldots,Z \tag{4.45}$$

where $\boldsymbol{x}_{R_r}^h$ are the cyclic DoFs belonging to the r^{th} radial line segment. The reduction method proposed in this section aims at reducing all the cyclic interface DoFs $\boldsymbol{x}_i^h$ to those of the first radial line segment $\boldsymbol{x}_{R_1}^h$. By performing the mentioned reduction for both cyclic symmetric sectors it will be shown how the compatibility conditions leading to a highly reduced multi-stage ROM can be enforced in a simple manner.

Before going into the details of this methodology, let us remember the physical meaning of the generic cyclic eigenvector. As already discussed in Chapter 2 it represents a vector giving information about the amplitude and phase of the h^{th} order spatial harmonic used to perform the cyclic reduction (Figure 2.10). However, the dominant harmonic of order h is not the only one describing the stage's mode at the interface, since the importance of the corresponding set of extra harmonics pattern was also proved (Eqn. 2.51). The interface reduction proposed in this section can thus be achieved by writing kinematic relationships similar to Eqn. 2.32 between the radial line segments for all the harmonic indexes linked to h by the Eqn. 2.51.

According to the previous description the cyclic eigenvector corresponding to the generic radial line segment $\boldsymbol{x}_{R_r}^h$ can be thought as the sum of dominant and extra harmonic components:

$$\boldsymbol{X}_{R_r}^h = \boldsymbol{X}_{R_r}^{h,d} + \sum_{k\in\sigma_h} \boldsymbol{X}_{R_r}^{h,k} \qquad \forall\, r = 1,\ldots,Z \tag{4.46}$$

where σ_h is the set collecting extra harmonics indexes linked to h (see subsection 4.3.2). As already explained in Chapter 2 the same relationship must hold for the corresponding physical DoFs:

$$\boldsymbol{x}_{R_j}^h = \boldsymbol{x}_{R_j}^{h,d} + \sum_{k\in\sigma_h} \boldsymbol{x}_{R_j}^{h,k} \tag{4.47}$$

By extending Eqn. 4.47 to the all Z radial line segments, $\boldsymbol{x}_i^h$ can then be rewritten as:

$$\boldsymbol{x}_i^h = \begin{Bmatrix} \boldsymbol{x}_{R_1}^h \\ \vdots \\ \boldsymbol{x}_{R_r}^h \\ \vdots \\ \boldsymbol{x}_{R_Z}^h \end{Bmatrix} = \begin{Bmatrix} \boldsymbol{x}_{R_1}^{h,d} \\ \vdots \\ \boldsymbol{x}_{R_r}^{h,d} \\ \vdots \\ \boldsymbol{x}_{R_Z}^{h,d} \end{Bmatrix} + \sum_{k \in \sigma_h} \begin{Bmatrix} \boldsymbol{x}_{R_1}^{h,k} \\ \vdots \\ \boldsymbol{x}_{R_r}^{h,k} \\ \vdots \\ \boldsymbol{x}_{R_Z}^{h,k} \end{Bmatrix} \rightarrow \boldsymbol{x}_i^h = \boldsymbol{x}_i^{h,d} + \sum_{k \in \sigma_h} \boldsymbol{x}_i^k \tag{4.48}$$

Each vector at the right-hand side of Eqn. 4.48 can be further reduced by writing the kinematic constraint equations between adjacent radial line segments. In particular, let us start with the vector of dominant cyclic coordinates $\boldsymbol{x}_i^{h,d}$. Due to the cyclic constraints enforced at the beginning of the reduction (Eqn. 4.32), the cyclic DoFs of the r^{th} radial line segment are linked to those of the first one by the following relationship:

$$\boldsymbol{x}_{R_r}^{h,d} = \boldsymbol{x}_{R_1}^{h,d} e^{\pm \imath (r-1)\varphi_{h_r}} \tag{4.49}$$

where φ_{h_r} is called *dominant inter-line phase angle* and represents the phase shift between two radial line segments when the disk's interface is forced to vibrate with a spatial harmonic of order h:

$$\varphi_{h_r} = \frac{\varphi_h}{Z} \tag{4.50}$$

Hence, the whole vector of dominant cyclic interface DoFs can be expresses as:

$$\boldsymbol{x}_i^{h,d} = \begin{Bmatrix} \boldsymbol{x}_{R_1}^{h,d} \\ \vdots \\ \boldsymbol{x}_{R_r}^{h,d} \\ \vdots \\ \boldsymbol{x}_{R_Z}^{h,d} \end{Bmatrix} \approx \begin{bmatrix} \boldsymbol{I} \\ \vdots \\ \boldsymbol{I} e^{\pm \imath (r-1)\varphi_{h_r}} \\ \vdots \\ \boldsymbol{I} e^{\pm \imath (Z-1)\varphi_{h_r}} \end{bmatrix} \boldsymbol{x}_{R_1}^{h,d} = \Gamma_d \boldsymbol{x}_{R_1}^{h,d} \tag{4.51}$$

where Γ_d is the matrix reducing the dominant cyclic interface DoFs to the first radial line segment (Figure 4.19).

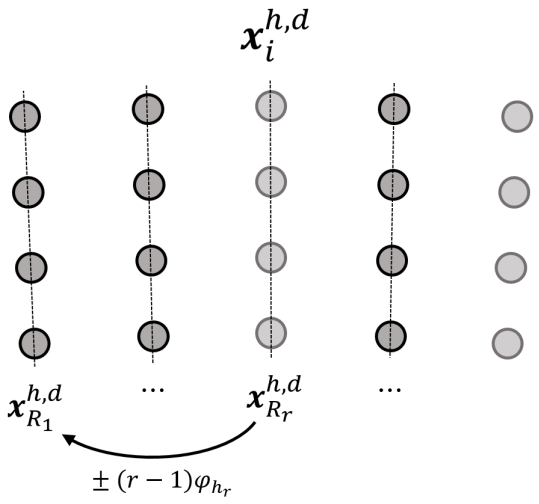

Fig. 4.19 Reduction of r^{th} radial line segments for the dominant harmonics.

Similar considerations can be carried out for all the terms of the sum at the right-hand side of Eqn. 4.48. In particular, let us assume σ_h collecting a number of n_m extra harmonics indexes:

$$\sigma_h = k_1, \ldots, k_m, \ldots, k_{n_m} \tag{4.52}$$

For the m^{th} index let us define the *extra inter-line phase angle* as:

$$\varphi_{k_m} = \frac{2\pi}{NZ} k_m \qquad k_m \in \sigma_h \tag{4.53}$$

which represents the phase shift between two adjacent radial line segments when the disk's interface is forced to vibrate with a spatial harmonic of order k_m. Therefore, according to the definition of extra harmonic given in Chapter 2, the generic vector $\boldsymbol{x}_i^{k_m}$ can be approximated as follows:

$$\boldsymbol{x}_i^{k_m} = \begin{Bmatrix} \boldsymbol{x}_{R_1}^{k_m} \\ \vdots \\ \boldsymbol{x}_{R_r}^{k_m} \\ \vdots \\ \boldsymbol{x}_{R_Z}^{k_m} \end{Bmatrix} \approx \begin{bmatrix} \boldsymbol{I} \\ \vdots \\ \boldsymbol{I} e^{\pm \imath (-1)^m (r-1) \varphi_{k_m}} \\ \vdots \\ \boldsymbol{I} e^{\pm \imath (-1)^m (Z-1) \varphi_{k_m}} \end{bmatrix} \boldsymbol{x}_{R_1}^{k_m} = \Gamma_{k_m} \boldsymbol{x}_{R_1}^{k_m} \tag{4.54}$$

where Γ_{k_m} is a reduction matrix similar to Γ_h consistent with the extra harmonic index k_m (Figure 4.20).

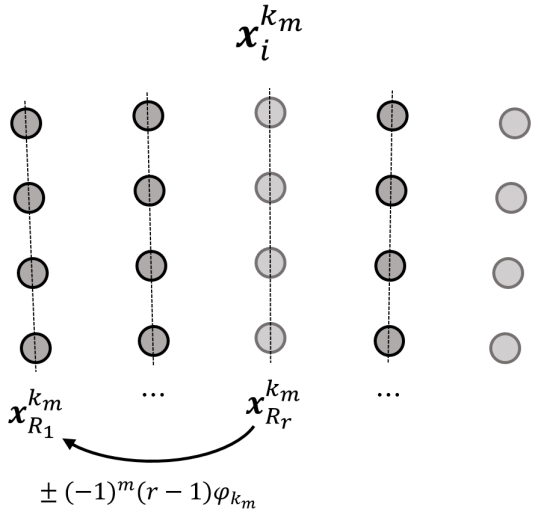

Fig. 4.20 Reduction of r^{th} radial line segments for the extra harmonics of order k_m.

By substituting Eqns. 4.51 and 4.54 into the Eqn. 4.48 the cyclic interface DoFs can be expressed as[4]:

$$\boldsymbol{x}_i^h = \begin{bmatrix} \Gamma_h & \Gamma_{k_1} & \cdots & \Gamma_{k_m} \end{bmatrix} \begin{Bmatrix} \boldsymbol{x}_{R_1}^h \\ \boldsymbol{x}_{R_1}^{k_1} \\ \vdots \\ \boldsymbol{x}_{R_1}^{k_m} \end{Bmatrix} \tag{4.55}$$

and the CS-CB vector generalized coordinates vector be finally approximated as follows:

$$\boldsymbol{x}_{CB}^h = \begin{Bmatrix} \boldsymbol{x}_a^h \\ \boldsymbol{x}_i^h \\ \eta_k^h \end{Bmatrix} \approx \begin{bmatrix} \boldsymbol{I} & \boldsymbol{0} & \boldsymbol{0} & \cdots & \boldsymbol{0} & \boldsymbol{0} \\ \boldsymbol{0} & \Gamma_h & \Gamma_{k_1} & \cdots & \Gamma_{k_m} & \boldsymbol{0} \\ \boldsymbol{0} & \boldsymbol{0} & \boldsymbol{0} & \cdots & \boldsymbol{0} & \boldsymbol{I} \end{bmatrix} \begin{Bmatrix} \boldsymbol{x}_a^h \\ \boldsymbol{x}_{R_1}^h \\ \boldsymbol{x}_{R_1}^{k_1} \\ \vdots \\ \boldsymbol{x}_{R_1}^{k_m} \\ \eta_k^h \end{Bmatrix} =$$

$$= \boldsymbol{R}_{\Gamma_h} \boldsymbol{x}_{CB}^{\Gamma_h} \tag{4.56}$$

By projecting the EQM of Eqn. 4.44 onto the space spanned by the matrix $\boldsymbol{R}_{\Gamma_h}$ a new highly reduced cyclic ROM is obtained (Figure 4.21)

[4]Hereafter the superscripts h,d and h,k_m are replaced by h and k_m respectively.

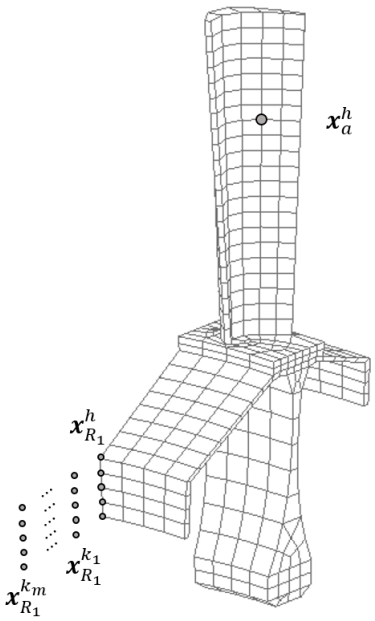

Fig. 4.21 Cyclic ROM for the dominant harmonics of order h and the corresponding extras.

Once the former reduction is performed for both sectors and for all the possible nodal diameter patterns, the compatibility conditions between the ROMs can be enforced by equaling the cyclic DoFs at their first radial line segments referring to the same harmonics (Figure 4.22).

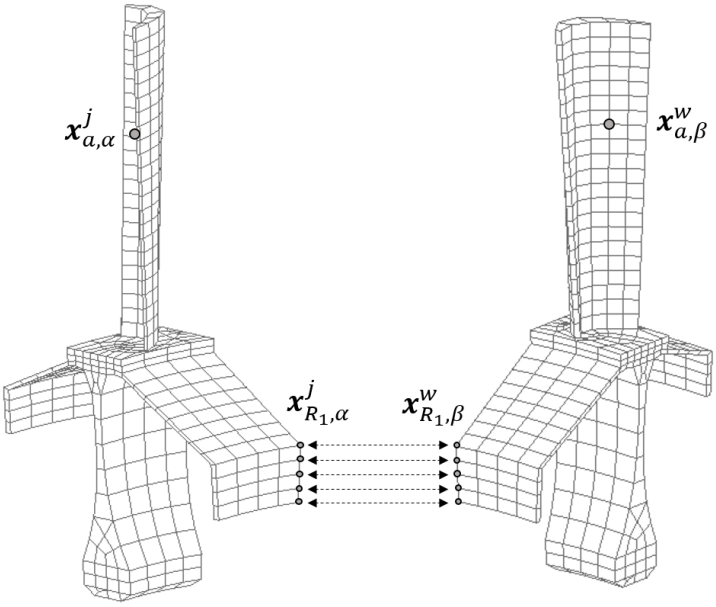

Fig. 4.22 Compatibility conditions between two cyclic ROMs.

In particular, if $\boldsymbol{x}^{j}_{R_1,\alpha}$ denotes the cyclic DoFs of order j at the first radial line segment of the stage α and $\boldsymbol{x}^{w}_{R_1,\beta}$ denotes the cyclic DoFs of order w at the first radial line segment of the stage β, the multi-stage coupling can be performed by writing the following equations:

$$\boldsymbol{x}^{j}_{R_1,\alpha} = \boldsymbol{x}^{w}_{R_1,\beta} \quad \Leftrightarrow \quad j = w \tag{4.57}$$

The harmonic indexes for which the compatibility equations are written can be determined exactly as already done in the previous section, i.e. by finding the set Σ_γ containing the best harmonic indexes for both stages (Eqn. 4.24).

Note that due to the presence of the extra harmonics patterns and the different cyclic periodicity of the stages, the multi-stage coupling process may involve more than two cyclic ROMs. However, in the most simple case where the dynamic behavior of the multi-stage system has to be predicted for a certain value of h, the model assembly can be performed by coupling just the DoFs referring to the dominant harmonic indexes (Figure 4.23).

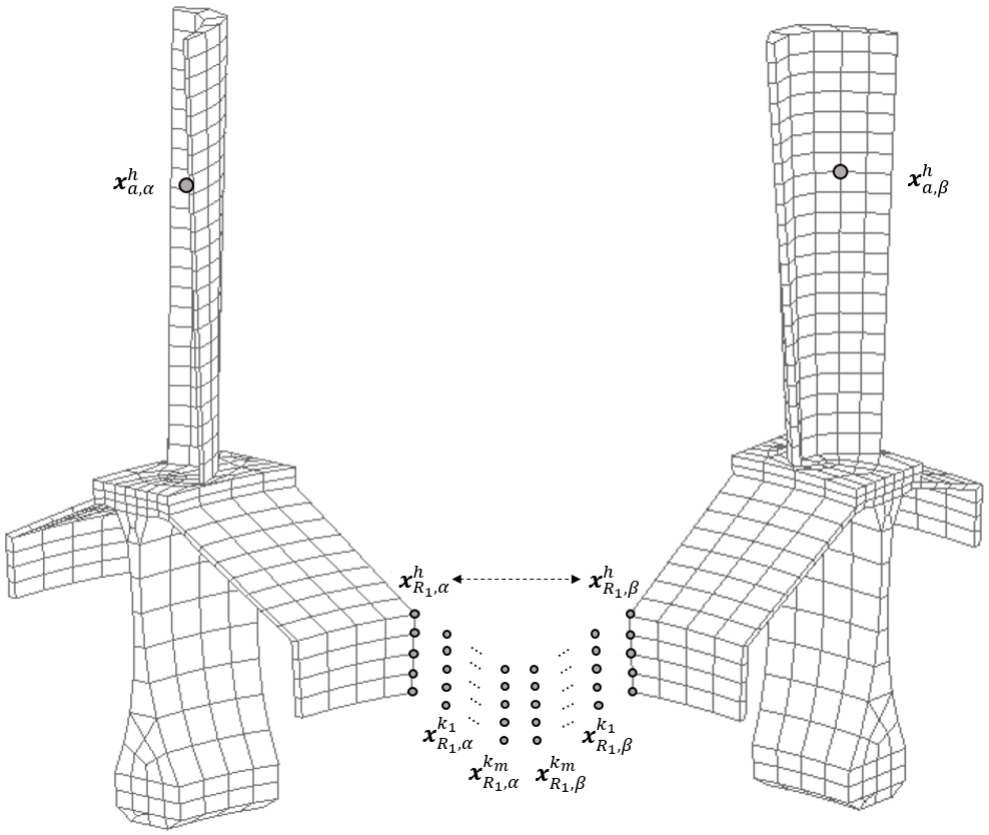

Fig. 4.23 Compatibility conditions between two cyclic ROMs just for the dominant harmonics of index h.

In such cases the presence of the uncoupled extra harmonics DoFs still ensures additional flexibility to the inter-stage boundaries and then a better approximation of the multi-stage system's dynamics.

Example: Multi-stage Coupling

The multi-stage reduction technique involving cyclic ROMs was tested on the reference model of section 4.2. A preliminary CS-CB reduction was performed for both α and β sectors for all the common dominant harmonic indexes ($h = 0, 1, \ldots, 25$). The size of the full FE models and those of the resulting CS-CB ROMs are reported in Table 4.3:

Table 4.3 Features of the sectors α and β FE models.

Sector	# DoFs full FE model	# DoFs CS-CB ROM
α	5736	53
β	5670	53

The number of DoFs of each sector's ROM results from the sum of:

- 5×3 interface DoFs at the first radial line for the dominant harmonic h ($\boldsymbol{x}^h_{R_1}$).
- 5×3 interface DoFs at the first radial line for the highest amplitude extra harmonics k ($\boldsymbol{x}^{k_1}_{R_1}$).
- 3 active DoFs at the blade airfoil ($\boldsymbol{x}^h_a$).
- 20 cyclic fixed-interface modal coordinates due to the cyclic *CB*-CMS reduction.

Figure 4.24 shows the DoFs retained for each cyclic ROM. For reference, first 20 natural frequencies of each ROM are within 0.53% of the corresponding FE natural frequencies. Also in this case this value was evaluated by using the relationship:

$$e_{\%} = \frac{|f_{CS\text{-}CB} - f_{FE}|}{f_{FE}} \tag{4.58}$$

where the FE quantities were considered as reference.

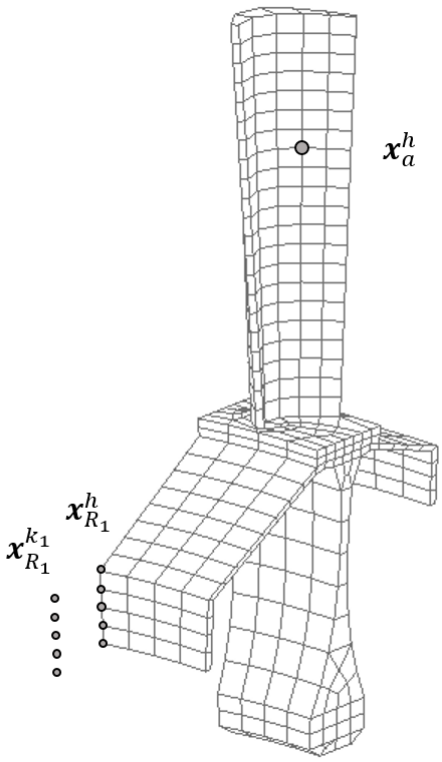

Fig. 4.24 Cyclic DoFs retained for each cyclic ROM. Two sets of cyclic DoFs are retained: $x_{R_1}^h$ refers to the dominant harmonic, while $x_{R_1}^{k_1}$ refers to the highest amplitude extra harmonics.

By employing the coupling procedure described above, 26 multi-stage ROMs were created by enforcing the compatibility conditions just for the dominant harmonic indexes, since it was chosen to predict the the dynamic behavior of the multi-stage for isolated nodal diameters patterns. Figure 4.25 shows the comparison between the forced response calculations obtained from the full FE model and the multi-stage ROM corresponding to the harmonic index $h = 2$. The calculations were performed by exciting the models with a traveling wave excitation of order EO = 2.

As in the case of the multi-stage technique presented in section 4.2, no significant differences can be found neither in terms of resonance frequencies ($< 0.005\%$) nor in terms of vibration amplitude. However, performing forced response calculations on the ROM was much more efficient than doing the same for the full assembled FE model. In fact, due to the different model size (53 vs $\sim$ 260000) the computational time spent for the forced response on the full configuration was almost 10^3 times larger than that spent for the reduced one ($\sim$2 s vs $\sim$ 2075 s).

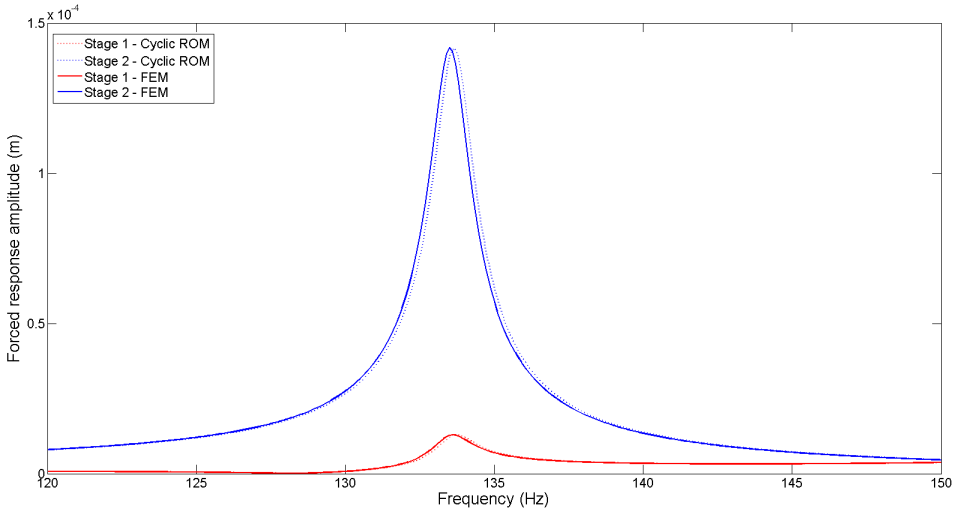

Fig. 4.25 Forced response comparison between the FE and cyclic reduced multi-stage model.

4.5 Discussion

This Chapter presents two novel reduction techniques for multi-stage systems based on the same theory background of cyclic symmetric structures, but different mathematical approaches:

1. The first method starts from the finite element models of isolated full stages. These are individually reduced and then assembled leading to a reduced order model of the complete multi-stage structure. The first reduction step for each single-stage is the application of the well-known Craig-Bampton method, which requires that at least the DoFs at the inter-stage boundary are retained as master. Later, such physical DoFs are approximated by few spatial harmonic basis functions taking into account the presence of either dominant of extra harmonic patterns. Once the mentioned reduction is performed for both stages' interfaces, the multi-stage coupling procedure is performed by equaling the same order spatial Fourier coefficients (i.e. the generalized coordinates) of the functions adopted for the interfaces reduction. The main idea behind this coupling process can be summarized as follows: *the vibration energy can be transferred from one stage to the adjacent ones if their motion at the interface has the same spatial shape*.

   It can be noted that the stages' coupling is performed for all the harmonic functions approximating the motion at the stage's interfaces. The assembled

multi-stage ROM then allows the force response prediction for any traveling wave excitation applied to the stages. In the example of section 4.3, the application of this method led to an effective model size compression (1306 vs 260000) that guaranteed to lower the computational costs of almost 140 times.

2. The second method just requires the finite element models of stand-alone fundamental sectors representative of the stages' geometries. Each sector is reduced by applying a modified version of the *cyclic Craig-Bampton* method proposed by Bladh [9], which takes into account a further reduction of the interface DoFs considering the extra harmonic pattern related to the dominant harmonic index for which the starting cyclic reduction is performed. At the end of each stage's reduction the interface is modeled by few cyclic physical DoFs. The final multi-stage reduced order model is this time obtained by enforcing the compatibility conditions in the space of such cyclic DoFs.

   For this second case the model size compression was much more effective than that achieved with the first reduction method (53 vs 1306 vs 260000). However, the stages reduction is in this case valid just for one dominant harmonic function. This means that the forced response calculations can be performed for traveling wave excitations having engine order compatible with the order of the harmonic function used for the cyclic reduction of the sectors.

It has been proved that the application of both methods on a multi-stage bladed disks model allows an excellent prediction of its dynamics in terms of natural frequencies, eigenvectors and forced response calculations. The choice of one method over the other depends on the objective of the dynamic calculations on a multi-stage ROM. If the complete system dynamics has to be modeled, the first method is preferred since it allows to enforce the harmonic compatibility conditions for all the desired set of harmonic basis functions. Differently, if the behavior of the system for few nodal diameter patterns is of interest, the second method appears much more efficient and easily applicable.

Although the methods were applied in order to solve linear dynamic problems, they appear also promising for modeling non-linear problems concerning friction contacts at the flange joint connecting two stages (see chapter 5). In particular, the extra harmonics can be exploited to better approximate the displacements at the interface between two stages when the damping capability of the flange joint has to be captured by employing suitable contact models.

Chapter 5

ROM for Multi-Stage Bladed Disks with Friction at the Flange Joint

5.1 Introduction

The interests of the scientific community in the development of non-linear models for friction prediction in turbomachinery has been grown recently. Most of them concern problems related to the presence of possible sources of friction at specific blade's locations. In this frame the modeling of non-linearities caused by underplatform dampers [38–41], blade's root [42] and shroud contacts [43, 44], has been proved as effective in predicting of the non-linear blade's dynamics. Such models have also become standard tools widely employed by the industries in the design of single-wheels bladed disk.

Recently the focus of research is moving towards other types of joint involved in aircraft engines, whose non-linear behavior may affect the dynamics of the whole system. In this regard, the bolted flange joint connecting neighboring stages of a complex multi-stage system may represent a possible source of non-linearities due friction contacts. As in the case of other types of joints used in bladed disk assemblies, such friction phenomena may lead to a significant amount of damping that can be exploited to lower the dynamic response of the system under the prescribed limits.

Nowadays the most used and simplest approach to model a flange joint consists in linking the nodes at the disks' interfaces either by means of rigid connections or by a set of springs having equal stiffness. In both cases the resulting coupled

structure is stiffer than the actual one and may provide high resonance frequencies since possible stick-slip phenomena at the contact interface are completely prevented. In order to improve the previous approaches the energy dissipation due to the friction at the contact surfaces must then be taken into account.

Single bolted joints actually show an evident non-linear behavior that was experimentally observed and numerically proved in [45–47]. Later, the non-linear nature of flange joints involved in the casing of aircraft engines was numerically demonstrated by using non-linear three-dimensional friction elements applied at the contact interfaces [48–50]. A similar application featuring friction contacts is that of the flange joints connecting adjacent bladed disks of a real turbofan engine. In this regard, a novel contact model for the microslip prediction in the flange joint of a multi-stage bladed disk assembly was proposed by Firrone et al. [7]. Localized non-linearities associated to the mentioned typologies of joints are not in general well captured when linear FE models are used. Recently, delli Carri et al. proposed an extention of existing modal testing techniques in order to enhance the elements of the FE model that is used to predict the non-linear behavior of the system [51, 52].

In this Chapter the multi-stage ROM techniques developed in Chapter 4 are combined with the macroslip contact model involving the classic spring-slider contact element (also known as *Jenkins*). In this way the non-linear forced response of a multi-stage bladed disk with friction contacts at the bolted flange joint can be easily evaluated.

The non-linear numerical solver developed to predict the non-linear forced responses in the frequency domain is based on the *Harmonic Balance Method* (HBM). Here, the periodic response of the system subjected to periodic excitation is studied as a superposition of harmonics and allows to turn the differential EQM into a system of non-linear, complex, algebraic equations.

5.2 Reduced Balance Equations and Harmonic Balance Method

In Chapter 3 and 4 it was shown how the linear dynamics of large complex structures can be efficiently predicted on highly condensed models. Reduction techniques have also become essential tools used for non-linear forced response calculations

on large mechanical systems involving friction contacts. In this regard the case of a multi-stage bladed disk assembly with friction contacts at the bolted flange joint has no exceptions. The EQM of such system can be expressed as:

$$\boldsymbol{M}\ddot{\boldsymbol{x}}(t)+\boldsymbol{C}\dot{\boldsymbol{x}}(t)+\boldsymbol{K}\boldsymbol{x}(t)=\boldsymbol{f}_e(t)-\boldsymbol{f}_n(\boldsymbol{x},\dot{\boldsymbol{x}},t) \tag{5.1}$$

where $\boldsymbol{M}$, $\boldsymbol{C}$ and $\boldsymbol{K}$ are the mass, viscous damping and stiffness matrices, $\boldsymbol{x}(t)$ is the vector of physical DoFs, $\boldsymbol{f}_e$ is the vector of the external harmonic forces acting on the system and $\boldsymbol{f}_n$ is the vector of the nonlinear contact forces, generated by the relative displacement of the contact DoFs.

A multi-stage ROM can be obtained by either using the conventional methods presented in Chapter 3 or one of the most suitable reduction techniques developed in Chapter 4. When one of these method is employed, the system dynamics is expressed in terms of a smaller set of generalized DoFs and the following reduced non-linear EQM are obtained:

$$\boldsymbol{M}_r\ddot{\boldsymbol{x}}_r(t)+\boldsymbol{C}_r\dot{\boldsymbol{x}}_r(t)+\boldsymbol{K}_r\boldsymbol{x}_r(t)=\boldsymbol{f}_{r,e}(t)-\boldsymbol{f}_{r,n}(\boldsymbol{x}_r,\dot{\boldsymbol{x}}_r,t) \tag{5.2}$$

where $\boldsymbol{M}_r$, $\boldsymbol{C}_r$ and $\boldsymbol{K}_r$ are the reduced mass, viscous damping and stiffness matrices, $\boldsymbol{x}_r(t)$ is the reduced vector of generalized DoFs, $\boldsymbol{f}_{r,e}$ is the reduced vector of the external harmonic forces acting on the system and $\boldsymbol{f}_{r,n}$ is the reduced vector of the nonlinear contact forces. Hereafter matrices and vectors are assumed to be reduced and the subscript r will be omitted in order to simplify the following notation.

In order to reduce the large calculation times typical of numerical integration of non-linear systems, the HBM can be used to compute the steady-state response of the system [53–55]. In particular, due to the periodicity of the traveling wave excitations acting on both stages, the displacements $\boldsymbol{x}$ and the non-linear contact forces $\boldsymbol{f}_n$ are periodical at steady-state. Therefore, they can be expressed as the real part of the following truncated series of harmonic terms:

$$\begin{aligned}\boldsymbol{x}(t)&=\Re\left(\sum_{f=0}^{n_h}\boldsymbol{X}^f\cdot e^{if\mathrm{EO}\Omega t}\right)\\ \boldsymbol{f}_n(\boldsymbol{x},\dot{\boldsymbol{x}},t)&=\Re\left(\sum_{f=0}^{n_h}\boldsymbol{F}_n^f\cdot e^{if\mathrm{EO}\Omega t}\right)\end{aligned} \tag{5.3}$$

where Ω is the rotation speed of the multi-stage bladed disk and n_h is the number of harmonics that has to be chosen in order to approximate the dynamics of the system with sufficient accuracy. If Eqns. 5.3 are replaced into Eqn. 5.2, the reduced set of EQM is turned into a set of non-linear, complex, algebraic equations:

$$\boldsymbol{D}^f(\Omega)\boldsymbol{X}^f = \boldsymbol{F}_e^f - \boldsymbol{F}_n^f \qquad \forall\, f = 0,\ldots,n_h \tag{5.4}$$

where

$$\boldsymbol{D}^f = \boldsymbol{K} + if\Omega\boldsymbol{C} - (f\mathrm{EO}\Omega)^2\boldsymbol{M} \qquad \forall\, f = 0,\ldots,n_h \tag{5.5}$$

is the f^{th} order dynamic stiffness matrix and the 0^{th} order represents the static balance equation.

Since the non-linear contact forces $\boldsymbol{f}_n$ depend on the relative displacement of the contact DoFs, whose number is typically much lower than the total number of DoFs, it is convenient to rearrange Eqn. 5.4 in order to decouple the solution of the non-linear part of the problem from its linear part. To do this, the receptance matrix $\boldsymbol{H}^f$, which is the inverse of $\boldsymbol{D}^f$, can be computed and the set of balance equations can be written in the receptance form as:

$$\boldsymbol{X}^f = \boldsymbol{X}_e^f - \boldsymbol{H}^f\boldsymbol{F}_n^f \tag{5.6}$$

where the first term at the right-harnd side of Eqn. 5.6 represents the linear response due to the external excitation, i.e. $\boldsymbol{X}_e = \boldsymbol{H}^f\boldsymbol{F}_e^f$, while the second term takes into account the contribution of the non-linear forces.

The complex displacement vector $\tilde{\boldsymbol{X}}^f$ can be grouped as:

$$\boldsymbol{X}^f = \begin{Bmatrix} \boldsymbol{X}_n^f \\ \boldsymbol{X}_l^f \end{Bmatrix} \tag{5.7}$$

where $\boldsymbol{X}_n^f$ is the vector of the non-linear DoFs, i.e. those where the non-linear contact forces act, and $\boldsymbol{X}_l^f$ are all the remaining linear DoFs. By using the DoFs partition of Eqn. 5.7, Eqn. 5.6 becomes:

$$\begin{Bmatrix} \boldsymbol{X}_n^f \\ \boldsymbol{X}_l^f \end{Bmatrix} = \begin{Bmatrix} \boldsymbol{X}_{e,n}^f \\ \boldsymbol{X}_{e,l}^f \end{Bmatrix} - \begin{bmatrix} \boldsymbol{H}_{nn}^f & \boldsymbol{H}_{nl}^f \\ \boldsymbol{H}_{ln}^f & \boldsymbol{H}_{ll}^f \end{bmatrix} \begin{Bmatrix} \boldsymbol{F}_n^f \\ \boldsymbol{0} \end{Bmatrix} \tag{5.8}$$

Since the non-linear contact forces $\boldsymbol{F}_n^f$ only depend on the non-linear displacement $\boldsymbol{X}_n^f$, only the first matrix equation:

$$\boldsymbol{X}_n^f = \boldsymbol{X}_{e,n}^f - \boldsymbol{H}_{nn}^f \boldsymbol{F}_n^f \tag{5.9}$$

is non-linear and has to be solved iteratively with a non-linear solver. Once the non-linear forces $\boldsymbol{F}_n^f$ are obtained from Eqn. 5.9, the response of the linear DoFs $\boldsymbol{X}_l^f$ can be computed by solving the following equation:

$$\boldsymbol{X}_l^f = \boldsymbol{X}_{e,l}^f - \boldsymbol{H}_{ln}^f \boldsymbol{F}_n^f \tag{5.10}$$

It must be observed that Eqns.5.9 are coupled to each other, because the arbitrary harmonic component $\boldsymbol{F}_n^f$ of the non-linear contact forces depends on all the harmonic components of the displacement of non-linear DoFs $\boldsymbol{X}_n^f$. In order to solve Eqn. 5.9 a contact model is necessary to compute the harmonic components $\boldsymbol{F}_n^f$ of the periodical contact forces from a given set of harmonics components $\boldsymbol{X}_n^f$ of the non-linear nodal displacements.

5.3 Contact Models

In order to solve the reduced set of non-linear algebraic EQM given in Eqn. (5.9) it is required to compute the periodic contact forces due to the relative displacement occurring for each couple of nodes in contact.

The the problem of modeling periodical contact forces due to friction contacts and their implementation in numerical solvers for the forced response calculation of mechanical systems has been addressed by several authors. Most of these models are based on the so called *Alternating Frequency Time* (AFT) method [56], also known as the *Hybrid Frequency Time* (HFT) method [57].
According to the flow-chart shown in Figure 5.1 the AFT method can be thought as composed by the following steps:

- For a given set of harmonic Fourier coefficients $\boldsymbol{X}_n^f$ representing the absolute displacements of the contact nodes, the relative displacements $\Delta\boldsymbol{X}_n^f$ are computed from the contact kinematics.

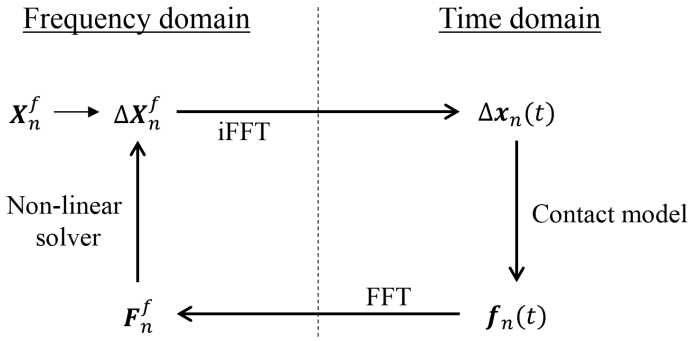

Fig. 5.1 Diagram of the AFT/HFT method.

- The periodical time history of the relative displacements is obtained by performing the *Inverse Fourier Transform* (IFFT) of $\Delta \boldsymbol{X}_n^f$.
- The periodical time history of non-linear contact forces is computed by using the constitutive laws of the contact model.
- The *Fast Fourier Transform* is applied to $\boldsymbol{f}_n$ in order to compute the harmonic components $\boldsymbol{F}_n^f$ of the periodical contact forces, which are then substituted into the Eqn. (5.10).

Among the contact models existing in the technical literature for the forced response calculation of mechanical systems, the following two are used in the application dealt in the present Chapter:

1. One-dimensional contact model with constant normal load [54].
2. One-dimensional contact model with normal load variation [58, 55].

5.3.1 1-D Contact Model with Constant Normal Load

This contact model (Figure 5.2) was described and used for the first time by Griffin in 1980 [54]. It is able to model a 1-D relative displacement in the tangential direction by taking into account the effect of a constant normal load acting on the contact. According to the nomenclature used in Figure 5.2, $x_1(t)$ denotes the periodic relative displacement between two nodes in contact, while $x_2(t)$ is the amount of tangential slip between the contact surfaces. A friction coefficient μ is assumed between the contact surfaces, while a constant normal load f_0 keeps the two bodies in contact.

The tangential contact stiffness is modeled by a spring with elastic constant k_t.

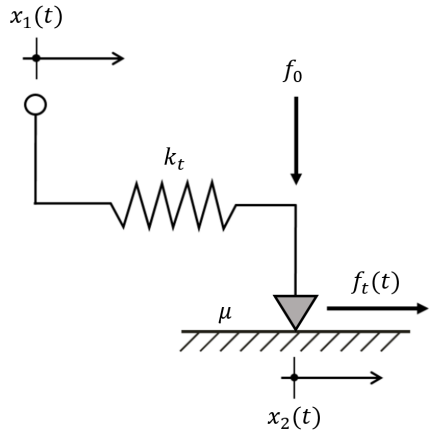

Fig. 5.2 1-D contact model with constant normal load.

Only two contact states can be modeled: stick and slip. In the sticking mode the contact is elastic, no slip occurs and the tangential force at the contact is:

$$f_c = k_t \cdot (x_1 - x_2) \quad \text{with} \quad \dot{x}_2 = 0 \tag{5.11}$$

In the slipping mode, the modulus of the tangential force is equal to the Coulomb limit value and its versus depends on the versus of the slipping velocity according to the following relationship:

$$f_t = \text{sgn}(\dot{x}_2) \cdot \mu \cdot f_0 \tag{5.12}$$

where $\text{sgn}(\dot{x}_2)$ is the sign function which assumes two possible values:

$$\text{sgn}(\dot{x}_2) = \begin{cases} -1 & \text{if } \dot{x}_2 < 0 \text{ (negative slip)} \\ \\ 1 & \text{if } \dot{x}_2 > 0 \text{ (positive slip)} \end{cases} \tag{5.13}$$

Stick and slip alternate each other according to the transition criteria shown in Table 5.1

Table 5.1 1-D contact element with constant normal load: transition criteria.

Contact state	Transition criterion
Stick to Slip	$\lvert f_t \rvert = \mu \cdot f_0$
Slip to Stick	$\dot{x}_2 = 0$

5.3.2 1-D Contact Model With Normal Load Variation

The contact model described in the previous subsection does not allow to model the effect of the normal load variation. However, this important feature helps in a better modeling of the actual contact state, especially when *separation* or *lift-off* occurs. This model was first proposed by Yang et al. [58] for single HBM and then extended by Petrov and Ewins [55] in the case of *multi-harmonic balance method* (MHBM).

A schematic view of this contact model can be found in Figure 5.3, where the two-dimensional relative displacement is decomposed into two perpendicular directions: two in-plane tangential component represented by x_1 and x_2 components, and one out-of-plane normal component x_n.

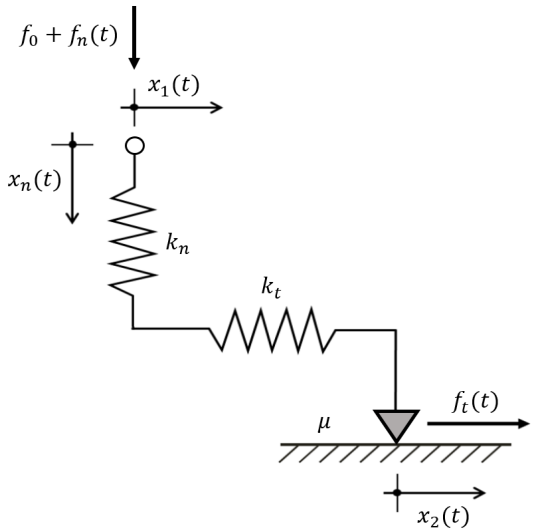

Fig. 5.3 1-D contact model with normal load variation.

The one-dimensional contact model with normal load variation is used to compute the periodic friction forces for a given periodic relative displacement by taking into account possible separation of the normal contact. Hence, in this case three possible contact states can be modeled: stick, slip and separation.

The contact model's parameters are represented by the tangential and normal contact stiffnesses, which are modeled by two springs with stiffness k_t and k_n respectively, the coefficient of friction μ and the normal preload f_0 (see Figure). The normal contact force $f_n(t)$ is defined as:

$$f_n = \max(f_0 + k_n \cdot x_n, 0) \tag{5.14}$$

If f_0 is positive, the bodies are in contact before vibration starts, while if f_0 is negative an initial gap $g_0 = -\frac{f_0}{k_n}$ exists between the two bodies.

Along the tangential direction, the contact force is defined as:

$$f_t = \begin{cases} k_t \cdot (x_1 - x_2) & \text{sticking mode} \\ \text{sgn}(\dot{x}_2)\mu f_n & \text{slipping mode} \\ 0 & \text{lift-off mode} \end{cases} \tag{5.15}$$

Stick, slip and lift-off (see Eqn. 5.14 for the constitutive equations) may alternate each other during the periodic vibration, according to the transition criteria shown in Table 5.2.

Table 5.2 1-D contact element with variable normal load: transition criteria.

Initial stage	Final state	Transition criterion
Stick	Slip	$\lvert f_t \rvert = \mu \cdot f_n$
Stick	Lift-off	$f_n = 0$ and $\dot{f}_n < 0$
Slip	Stick	$\dot{x}_n = 0$
Slip	Lift-off	$f_n = 0$ and $\dot{f}_n < 0$
Lift-off	Stick	$f_n = 0$, $\dot{f}_n > 0$ and $\lvert \dot{f}_t \rvert < \mu \cdot \lvert \dot{f}_n \rvert$
Lift-off	Slip	$f_n = 0$, $\dot{f}_n > 0$ and $\lvert \dot{f}_t \rvert > \mu \cdot \lvert \dot{f}_n \rvert$

5.4 Model's Hypotheses

In the following sections the reduced non-linear EQM of a multi-stage bladed disk with friction contacts at the flange joint are derived by using the reduction techniques presented in Chapter 4. For all these cases the capability of the flange joint in damping the blades vibrations is tested. In this way the results coming from different mathematical approaches can be compared in order to identify the best reduction strategy.

The performances of the mentioned methods are tested on a simplified multi-stage bladed disk model satisfying the following hypotheses:

1. *The traveling wave excitation acting on both stages have the same EO*. The forced response calculations carried out in Chapter 4 clearly show an important feature of the multi-stage bladed disks dynamics: at a resonance frequency the response of a multi-stage system is mainly localized on one of the two stages (Figure 5.4)

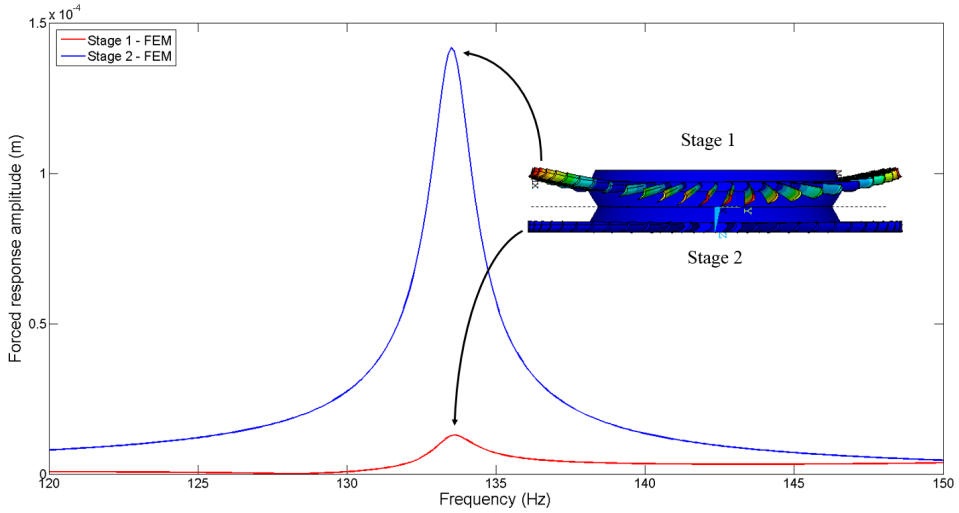

Fig. 5.4 Typical forced response of a multi-stage bladed disk: the system's response is mainly localized on the stage 1.

The transmission of vibration energy from the most resonant stage to the other one allows the assembly vibrating according to just one harmonic index h. Hence, the maximum amplification of the response is obtained when both stages are excited by traveling wave excitations having the same EO. When the disks are subjected to rotating excitation having different EOs, just one of

them give rise to the resonance, while the other, being orthogonal to the mode shape, does not contribute to the response amplification.

However, this hypothesis is no more valid when modeling the dynamic behavior of bladed disks having critical resonances excitable by different traveling wave EO excitations in a narrow range of rotation speed. The mentioned case could be that shown by the Campbell diagram of Figure 5.5.

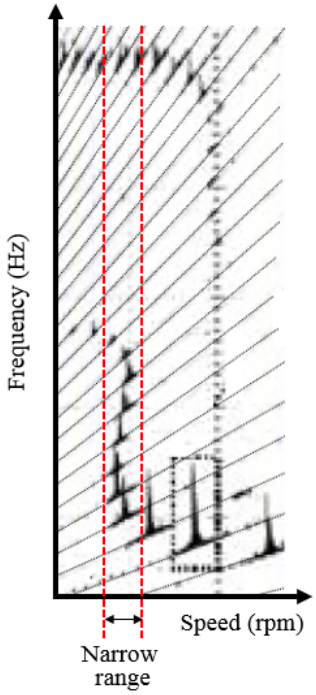

Fig. 5.5 Example of an experimental Campbell diagram of a bladed disk. In a narrow range of rotation speed the bladed disk shows several resonances corresponding to different EO excitations. Therefore, when multiple EO patterns excite the structure, the bladed disk's response results from the superposition of the excited resonance.

Here, several critical resonances corresponding to different EOs occur at the same rotation speed. In such particular case the superposition of the effects generated by all the excited resonances should be taken into account.

2. *The multi-stage ROM is obtained from the ROMs of the single-stages by enforcing the compatibility conditions just in the axial direction*. Due to the presence of several bolted connection at the flanges, adjacent stages are tightened together and no relative axial displacement is allowed between them. The goodness of this hypothesis is proved by the application of the contact models presented in section 5.3 on a simplified multi-stage system.

The mentioned check is performed by modeling the friction contacts at the inter-stage boundary and quantifying their effect in mitigating the blades' vibrations.

3. *The steady state displacements and non-linear contact forces are approximated with their* 1^{st} *order Fourier coefficients (Single-HBM).* Although this hypothesis could be interpreted as restrictive of the current practice, considering the recent state of the art focused on applications where Multi-HBM is used, Single-HBM can be used to well approximate the multi-stage dynamics since no strong non-linearities are expected. In fact, due to the several bolted connections along the flange partial lift-off is prevented. Moreover, considering the harmonic trend of the displacement along the flanges [7], the alternation of regions where stick and slip are present results in a global microslip phenomenon (Figure 5.6)

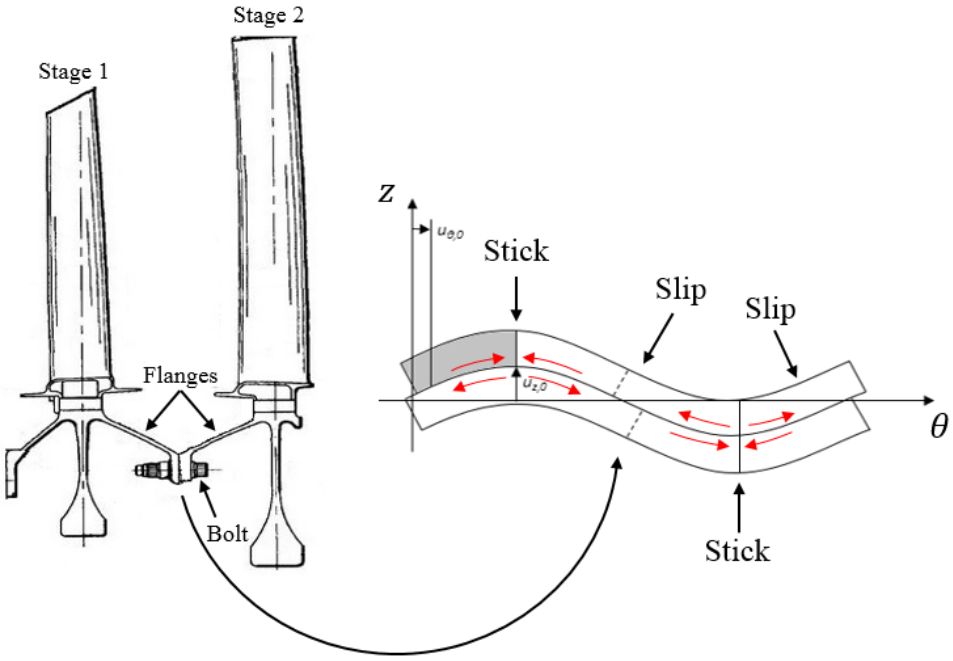

Fig. 5.6 Alternation of stick and slip regions along the flanges joint. Stick takes place where no relative displacement occurs between the two flanges, i.e. at the locations where the flanges show the largest vibration amplitude. Slip occurs between two stick regions, due to the extension and compression of the material close to the contact interface.

5.5 Multi-Stage CB-CMS ROM & Friction Contacts

In section 5.2 the balance equations of a reduced mechanical system with friction contacts were derived under the hypothesis of external harmonic excitation (Eqn. 5.6). In this section similar equations will be obtained for a multi-stage ROM resulting from the coupling of two *CB*-CMS ROMs of the single-stages.

According to the DoFs notation adopted in the previous Chapters, the *CB*-CMS generalized coordinates vector for the j^{th} stage's ROM can be expressed as:

$$\boldsymbol{x}_{CB_j} = \begin{Bmatrix} \boldsymbol{x}_{i_j} \\ \boldsymbol{x}_{a_j} \\ \eta_{k_j} \end{Bmatrix} \qquad \forall\ j = 1,2 \tag{5.16}$$

where $\boldsymbol{x}_{i_j}$ are the physical DoFs at the inter-stage boundary, $\boldsymbol{x}_{a_j}$ is the vector of active DoFs defined by selecting one node per blade at homologous locations and η_{k_j} is the vector of modal coordinates corresponding to n_{k_j} fixed-interface normal modes retained in the *CB*-CMS reduction.

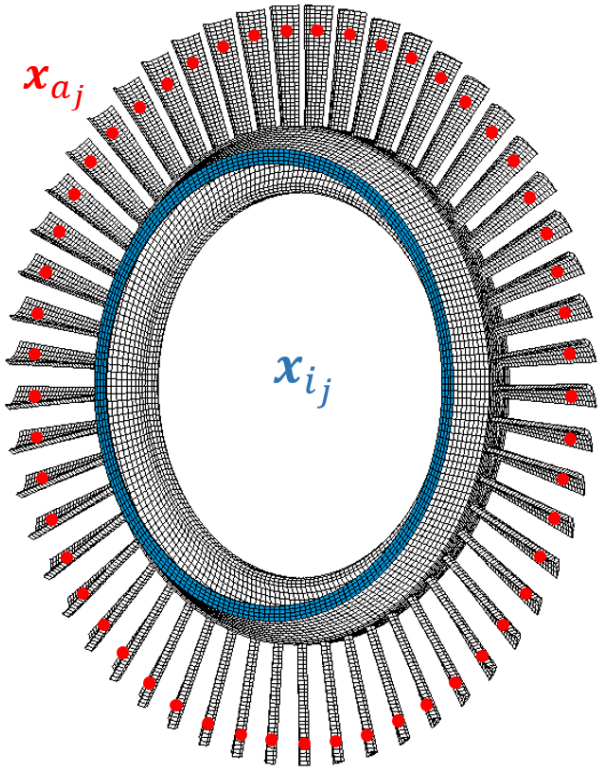

Fig. 5.7 *CB*-CMS physical coordinates for the j^{th} stage.

By putting the vectors $\boldsymbol{x}_{CB_j}$ together and grouping the subvectors concerning the same class of DoFs, the *CB*-CMS generalized coordinate vector for the multi-stage system is obtained:

$$\boldsymbol{x}_{CB} = \begin{Bmatrix} \boldsymbol{x}_{i_1} \\ \boldsymbol{x}_{i_2} \\ \boldsymbol{x}_{a_1} \\ \boldsymbol{x}_{a_2} \\ \eta_{k_1} \\ \eta_{k_2} \end{Bmatrix} \tag{5.17}$$

From the former equation it can be noted that no compatibility conditions have been applied between the interface DoFs, since the friction contact forces depending on their relative displacements have to be evaluated[1]. Therefore, Eqn. 5.2 can in this case be expressed as:

$$\boldsymbol{M}_{CB}\ddot{\boldsymbol{x}}_{CB}(t) + \boldsymbol{C}_{CB}\dot{\boldsymbol{x}}_{CB}(t) + \boldsymbol{K}_{CB}\boldsymbol{x}_{CB}(t) = \boldsymbol{f}_{CB,e}(t) - \boldsymbol{f}_{CB,n}(\boldsymbol{x}_r, t) \tag{5.18}$$

Under the hypothesis n.3 the balance equations given in Eqn. 5.18 can be turned into the following set of algebraic complex equations:

$$\boldsymbol{D}^1_{CB}(\Omega) \cdot \boldsymbol{X}_{CB}{}^1 = \boldsymbol{F}^1_{CB,e} - \boldsymbol{F}^1_{CB,n} \tag{5.19}$$

where the superscript "1" indicates the first harmonic component of the corresponding quantity. Hereafter this superscript will be omitted in order to simplify the notation.

According to the DoFs partition given in Eqn. 5.17, the Fourier coefficients of the displacement and force vectors can be expressed as:

$$\boldsymbol{X}_{CB} = \begin{Bmatrix} \boldsymbol{X}_{i_1} \\ \boldsymbol{X}_{i_2} \\ \boldsymbol{X}_{a_1} \\ \boldsymbol{X}_{a_2} \\ \boldsymbol{E}_{k_1} \\ \boldsymbol{E}_{k_2} \end{Bmatrix} \quad \boldsymbol{F}_{CB,e} = \begin{Bmatrix} \boldsymbol{0} \\ \boldsymbol{0} \\ \boldsymbol{F}_{e_1} \\ \boldsymbol{F}_{e_2} \\ \boldsymbol{0} \\ \boldsymbol{0} \end{Bmatrix} \quad \boldsymbol{F}_{CB,n} = \begin{Bmatrix} \boldsymbol{F}_{n_1} \\ \boldsymbol{F}_{n_2} \\ \boldsymbol{0} \\ \boldsymbol{0} \\ \boldsymbol{0} \\ \boldsymbol{0} \end{Bmatrix} \tag{5.20}$$

where:

[1]Note that for *CB*-CMS ROMs the contact forces evaluation can be performed exclusively in the case of compatible meshes at the inter-stage boundary.

- $\boldsymbol{X}_{i_j}$ and $\boldsymbol{X}_{a_j}$ are the 1^{st} order Fourier coefficients of the physical DoFs $\boldsymbol{x}_{i_j}$ and $\boldsymbol{x}_{a_j}$;
- $\boldsymbol{E}_{k_j}$ are the 1^{st} order Fourier coefficients of the *CB*-CMS modal coordinates η_{k_j};
- $\boldsymbol{F}_{e_j}$ are the 1^{st} order Fourier coefficients of the traveling wave EO excitation discretized at the blades of the j^{th} stage;
- $\boldsymbol{F}_{n_j}$ are the 1^{st} order Fourier coefficients of the contact forces distributed at the interface of the j^{th} stage.

Since the non-linear contact forces depend on the relative displacements of equally collocated nodes, the 1^{st} order Fourier coefficients of the relative displacements at the inter-stage boundary can be calculated as:

$$\Delta \boldsymbol{X}_i = \boldsymbol{X}_{i_1} - \boldsymbol{X}_{i_2} \tag{5.21}$$

Therefore, the coordinates transformation linking the absolute to the relative complex displacements is given by:

$$\boldsymbol{X}_{CB} = \begin{Bmatrix} \boldsymbol{X}_{i_1} \\ \boldsymbol{X}_{i_2} \\ \boldsymbol{X}_{a_1} \\ \boldsymbol{X}_{a_2} \\ \boldsymbol{H}_{k_1} \\ \boldsymbol{H}_{k_2} \end{Bmatrix} = \begin{bmatrix} \boldsymbol{I} & \boldsymbol{I} & \boldsymbol{0} & \boldsymbol{0} & \boldsymbol{0} & \boldsymbol{0} \\ \boldsymbol{0} & \boldsymbol{I} & \boldsymbol{0} & \boldsymbol{0} & \boldsymbol{0} & \boldsymbol{0} \\ \boldsymbol{0} & \boldsymbol{0} & \boldsymbol{I} & \boldsymbol{0} & \boldsymbol{0} & \boldsymbol{0} \\ \boldsymbol{0} & \boldsymbol{0} & \boldsymbol{0} & \boldsymbol{I} & \boldsymbol{0} & \boldsymbol{0} \\ \boldsymbol{0} & \boldsymbol{0} & \boldsymbol{0} & \boldsymbol{0} & \boldsymbol{I} & \boldsymbol{0} \\ \boldsymbol{0} & \boldsymbol{0} & \boldsymbol{0} & \boldsymbol{0} & \boldsymbol{0} & \boldsymbol{I} \end{bmatrix} \begin{Bmatrix} \Delta \boldsymbol{X}_i \\ \boldsymbol{X}_{i_2} \\ \boldsymbol{X}_{a_1} \\ \boldsymbol{X}_{a_2} \\ \boldsymbol{H}_{k_1} \\ \boldsymbol{H}_{k_2} \end{Bmatrix} = \boldsymbol{T}_{rel} \boldsymbol{X}_{CB}^{rel} \tag{5.22}$$

where $\boldsymbol{T}_{rel}$ is the matrix transforming the interface displacements from absolute to relative. By substituting Eqn. 5.22 into Eqn. 5.19 and pre-multiplying both sides by $\boldsymbol{T}_{rel}^T$, the following system of equation is obtained:

$$\boldsymbol{T}_{rel}^T \boldsymbol{D}_{CB} \boldsymbol{T}_{rel} \boldsymbol{X}_{CB}^{rel} - \boldsymbol{T}_{rel}^T \boldsymbol{F}_{CB,e} + \boldsymbol{T}_{rel}^T \boldsymbol{F}_{CB,n} \approx \boldsymbol{0} \tag{5.23}$$

Although the pre-multiplication by $\boldsymbol{T}_{rel}^T$ leaves $\boldsymbol{F}_{CB,e}$ unchanged, more attention has to be paid on the term $\boldsymbol{T}_{rel}^T \boldsymbol{F}_{CB,n}$:

$$\boldsymbol{T}_{rel}^T \boldsymbol{F}_{CB,n} = \begin{bmatrix} \boldsymbol{I} & \boldsymbol{0} & \boldsymbol{0} & \boldsymbol{0} & \boldsymbol{0} & \boldsymbol{0} \\ \boldsymbol{I} & \boldsymbol{I} & \boldsymbol{0} & \boldsymbol{0} & \boldsymbol{0} & \boldsymbol{0} \\ \boldsymbol{0} & \boldsymbol{0} & \boldsymbol{I} & \boldsymbol{0} & \boldsymbol{0} & \boldsymbol{0} \\ \boldsymbol{0} & \boldsymbol{0} & \boldsymbol{0} & \boldsymbol{I} & \boldsymbol{0} & \boldsymbol{0} \\ \boldsymbol{0} & \boldsymbol{0} & \boldsymbol{0} & \boldsymbol{0} & \boldsymbol{I} & \boldsymbol{0} \\ \boldsymbol{0} & \boldsymbol{0} & \boldsymbol{0} & \boldsymbol{0} & \boldsymbol{0} & \boldsymbol{I} \end{bmatrix} \begin{Bmatrix} \boldsymbol{F}_{n_1} \\ \boldsymbol{F}_{n_2} \\ \boldsymbol{0} \\ \boldsymbol{0} \\ \boldsymbol{0} \\ \boldsymbol{0} \end{Bmatrix} = \begin{Bmatrix} \boldsymbol{F}_{n_1} \\ \boldsymbol{F}_{n_2} + \boldsymbol{F}_{n_2} \\ \boldsymbol{0} \\ \boldsymbol{0} \\ \boldsymbol{0} \\ \boldsymbol{0} \end{Bmatrix} \tag{5.24}$$

Since the contact forces at the two contact interfaces are equal in amplitude but opposite in sign, the term $\boldsymbol{F}_{n_1} + \boldsymbol{F}_{n_2}$ is null:

$$\boldsymbol{T}_{rel}^T \boldsymbol{F}_{CB,n} = \begin{Bmatrix} \boldsymbol{F}_{n_1} \\ \boldsymbol{0} \\ \boldsymbol{0} \\ \boldsymbol{0} \\ \boldsymbol{0} \\ \boldsymbol{0} \end{Bmatrix} = \begin{Bmatrix} \boldsymbol{F}_{n} \\ \boldsymbol{0} \\ \boldsymbol{0} \\ \boldsymbol{0} \\ \boldsymbol{0} \\ \boldsymbol{0} \end{Bmatrix} \tag{5.25}$$

In this way only the non-linear equations corresponding to the term $\boldsymbol{F}_n$ have to be iteratively solved. It must be pointed out that thanks to the coordinates transformation of Eqn. 5.23 the number of non-linear algebraic equations results halved with respect that of Eqn. 5.19.

Example

In this subsection a simplified multi-stage bladed disk with friction contacts at the bolted flange joint is analyzed. By employing the contact models described in section 5.3, friction contacts at the interface between the stages will be modeled and their capability in damping the blades' vibrations is quantified by means of forced response calculations.

A multi-stage system consisting of two different bladed disks with $N = 50$ sectors each was taken as reference (Figure 5.8). The FE models of the two stages were generated in ANSYS by repeating the FE models of the fundamental sectors N times around the z-axis. The stages 1 and 2 consist of 43200 and 40300 4-node brick

elements with 42250 and 38900 node respectively (the stages have the same number of sectors, but different number of elements per sector). The material properties were chosen according to the standard values of the steel: Young's modulus $E = 210$ GPa, Poisson's ration $\nu = 0.33$ and density $\rho = 7800$ kg/m^3. For both stages the number of radial line segments per sector is $Z = 4$. All the radial line segments have five equally spaced nodes, meaning that the two stages have perfectly matching meshes at the contact interface.

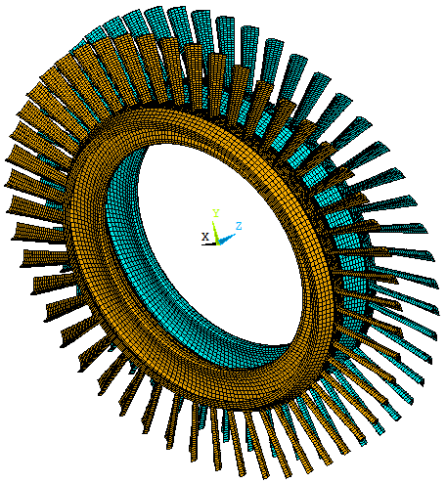

Fig. 5.8 FE model of the reference multi-stage system.

The *CB*-CMS ROMs of the stages were created by retaining as master the sets of interface and active DoFs $\left\{\boldsymbol{x}_{i_1}^T \; \boldsymbol{x}_{a_1}^T\right\}^T$ and $\left\{\boldsymbol{x}_{i_2}^T \; \boldsymbol{x}_{a_2}^T\right\}^T$ for the stage 1 and 2 respectively. The sets $\boldsymbol{x}_{i_1}$ and $\boldsymbol{x}_{i_2}$ are the DoFs of the nodes lying on the medium radius circumference of the contact surface, while $\boldsymbol{x}_{a_1}$ and $\boldsymbol{x}_{a_2}$ were defined by selecting one node per blade in the middle of the blades' airfoils (Figure 5.9). The size of the mentioned set of master DoFs is listed in Table 5.3.

Table 5.3 Number of master DoFs retained in the *CB*-CMS reduction of the stages.

Set	# DoFs
$\boldsymbol{x}_{i_1}$	600
$\boldsymbol{x}_{a_1}$	150
$\boldsymbol{x}_{i_2}$	600
$\boldsymbol{x}_{a_2}$	150

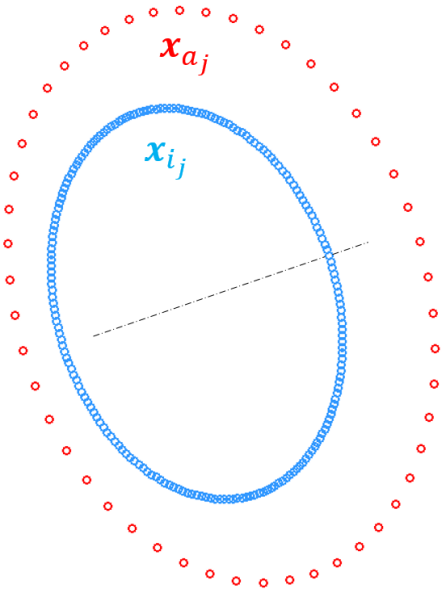

Fig. 5.9 Master nodes of the single-stage *CB*-CMS ROM.

In addition the first 200 fixed-interface normal modes were employed in the reduction of the two stages, yielding two *CB*-CMS ROMs with 950 DoFs each. For reference, the first 200 natural frequencies of the *CB*-CMS ROMs are within the 0.3% of the corresponding FE natural frequencies. The size of the full and reduced model are compared in Table 5.4.

Table 5.4 Size of the full and reduced models of the stages 1 and 2.

Stage	# DoFs full FE model	# DoFs *CB*-CMS ROM
Stage 1	126750	950
Stage 2	116700	950

A first multi-stage ROM allowing friction contact at the inter-stage boundary was obtained from the *CB*-CMS ROMs of the two stages. In particular, the master DoFs at the stages' interfaces were coupled in all the directions (ρ, θ and z) by means of friction contact elements involving the normal load variation (see subsection 5.3.2). For each couple of nodes two contact elements were employed. In fact, projecting their in-plane relative displacement onto two directions (ρ and θ), still guarantees to catch the fundamental features of the real bi-dimensional trajectory of the contact [59]. The tangential contact stiffnesses in the radial and circumferential direction

were set equal to 10^8 N/m ($k_\rho = k_\theta = 10^8$), while the normal contact stiffness k_z was assumed equal to $1.5 \cdot 10^8$ N/m.

Due to the perfect matching positions of the master nodes at the stages' interfaces, the contact model was therefore applied to all the $NZ = 200$ pairs of nodes, leading to 1200 non-linear EQM. This number was finally halved by employing the coordinates transformation of Eqn. 5.22, since the non-linear contact forces only depend on the relative displacements characterizing each couple of nodes in contact. The resulting multi-stage ROM is here denoted by I and the dynamic analyses performed on it are henceforth considered as a benchmark.

The generalized coordinates vector of the multi-stage ROM can thus be written:

$$\boldsymbol{x}_I = \begin{Bmatrix} \Delta\boldsymbol{x}_i \\ \boldsymbol{x}_{i_2} \\ \boldsymbol{x}_{a_1} \\ \boldsymbol{x}_{a_2} \\ \boldsymbol{\eta}_{k_1} \\ \boldsymbol{\eta}_{k_2} \end{Bmatrix} \tag{5.26}$$

whose corresponding mass and stiffness matrices are here denoted as $\boldsymbol{M}_I$ and $\boldsymbol{K}_I$. The structural damping matrix $\boldsymbol{C}_I$ was built by using the eigenvectors of the system and an assumed value of modal damping ratio ζ. In particular, under the hypothesis of proportional damping, the matrix $\boldsymbol{C}_I$ can be diagonalized by the modal matrix of the reduced system $\boldsymbol{\Phi}_I$:

$$\boldsymbol{\Phi}_I^T \boldsymbol{C}_I \boldsymbol{\Phi}_I = \mathrm{diag}(2\zeta_i \omega_i) \tag{5.27}$$

where ζ_i and ω_i represent the modal damping ratio and the eigenfrequecy associated to the i^{th} mode. By assuming the same modal damping $\zeta = 0.005$ for all the modes, the reduced damping matrix can be easily obtained as follows:

$$\boldsymbol{C}_I = 2\zeta \left(\boldsymbol{\Phi}_I^T\right)^{-1} \mathrm{diag}(\omega_i) \left(\boldsymbol{\Phi}_I\right)^{-1} \tag{5.28}$$

The non-linear forced response calculations were performed by forcing the stages with two clocked traveling waves excitations of order EO = 2 in the z direction. The discrete values of such rotating forces can be calculated blade by blade as follows:

$$f_e e^{i\mathrm{EO}\frac{2\pi}{N}n_b} \qquad n_b = 0, 1, \ldots, (50-1) \tag{5.29}$$

where f_e is the amplitude of the traveling waves exciting on both stages and n_b is an integer denoting the blade number.

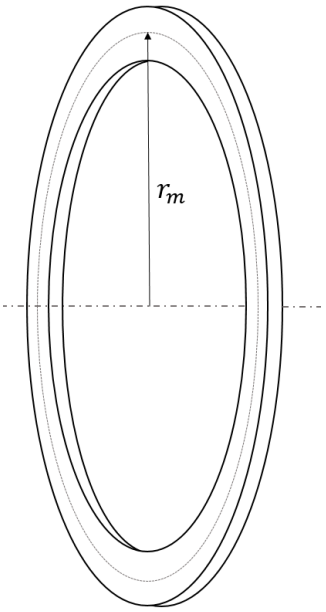

Fig. 5.10 Mean radius of the contact interface.

Several forced response calculations corresponding to different values of f_e were performed in order to evaluate the effect of the friction damping produced by the flange joint on the blades' response. For all these cases the value of normal preload f_0 for each contact element was set equal to 350 N, a value that was deducted from practical considerations on the power transmission between the two stages. In particular, if P is the power and Ω is the rotation speed of the multi-stage system, the corresponding transmitted torque can be calculated as:

$$T = \frac{P}{\Omega} \tag{5.30}$$

By denoting with r_m the medium radius of the annular ring representing the area at the contact interface (Figure 5.10), the tangential force producing the torque T is given by:

$$F_t = \frac{T}{r_m} \tag{5.31}$$

Finally, assuming a friction coefficient μ at the contact interface, the normal preload F_0 can be evaluated by applying the Coulomb friction law:

$$F_0 = \frac{F_t}{\mu} \tag{5.32}$$

By dividing F_0 for the number n_c of contact node pairs, the normal preload associated to each contact element is given by:

$$f_0 = \frac{F_0}{n_c} \tag{5.33}$$

Therefore, according to the given description, the constant normal preload $f_0 = 350$ N was calculated by assuming the following data:

Table 5.5 Data used for the estimation of the normal preload for each pair of nodes in contact.

Quantity		Value
P	(kW)	7000
Ω	(rpm)	11330
r_m	(m)	0.43112
μ	(-)	0.5

Under the hypothesis of SHBM (hypothesis n.3) the non-linear algebraic system of equation was obtained (Eqn. 5.23), and its solution found by using the Newton-Raphson algorithm. Typical results of such simulations are shown in Figure 5.11 and 5.12, where the non-linear forced response calculations for the stage 1 and 2, normalized with respect the amplitude of the traveling wave excitations f_e, are plotted. The forced response of Figure 5.11 and 5.12 exhibit the typical behavior of joints where friction is present. In particular, for low amplitudes of the harmonic excitation ($f_e = 1$ N) the *fully stick* condition is obtained. In this case no large relative displacements occur at the contact interface, no slip is present and then no energy dissipation can take place. From a mathematical point of view the contact elements act as springs[2], linking both sides of the joint and then contributing to increase the stiffness of the system. By increasing the excitation amplitude slip starts, energy dissipation occurs and the resonance frequency of the system moves towards the *free* condition. Here, the large relative displacements at the joint interface are caused by

[2]The small relative displacements for each couple of contact nodes lead to tangential contact forces whose amplitudes are lower than the Coulomb limit μf_0.

large vibration amplitudes that make friction unable to introduce further damping into the system.

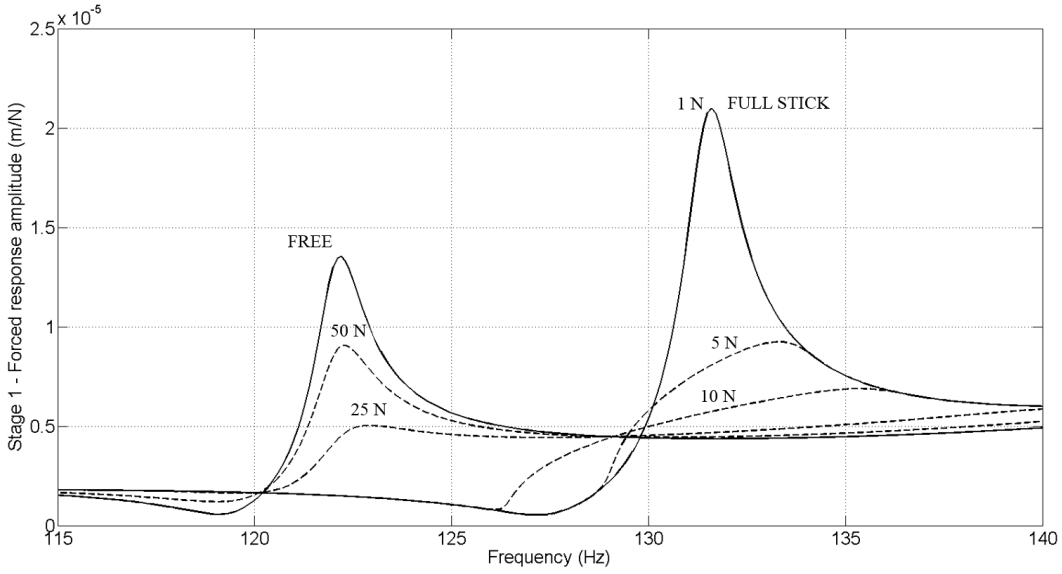

Fig. 5.11 Normalized forced responses for the Stage 1.

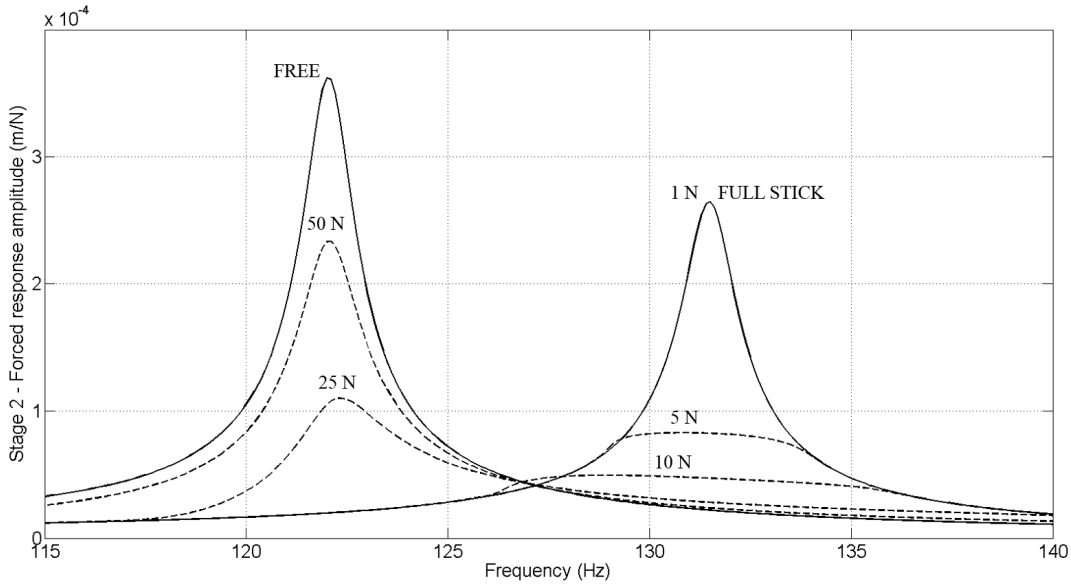

Fig. 5.12 Normalized forced responses for the Stage 2.

Note that the forced responses of Figures 5.11 and 5.12 were obtained by assuming an uniform pressure distribution along the flange, which is clearly an approxi-

mation. In reality the contact pressure along the flange can be considered stationary (non time-varying) but non-uniform, being mainly localized in the areas where the bolts are tightened. However, due to the large number of bolts generally involved (i.e. one third of the number of blades), it was demonstrated that the resulting pressure localization does not lead to significant modification of the force response neither in terms of vibration amplitude nor in terms of resonance frequency [60]. Therefore, a stationary and uniform pressure distribution at the flange interface can be considered as a valid approximation.

A second multi-stage ROM was created by enforcing the equality of the interface displacements in the z direction. In particular, by assuming the vectors $\boldsymbol{x}_{i_j}$ partitioned as $\boldsymbol{x}_{i_j} = \left\{ \left(\boldsymbol{x}_{i_j}^{\rho}\right)^T \left(\boldsymbol{x}_{i_j}^{\theta}\right)^T \left(\boldsymbol{x}_{i_j}^{z}\right)^T \right\}^T$, the mentioned compatibility conditions can be expressed as $\boldsymbol{x}_{i_1}^{z} = \boldsymbol{x}_{i_1}^{z} = \boldsymbol{x}_{i}^{z}$. The remaining two DoFs per contact node (ρ and θ) were coupled by means of Jenkins contact elements (see subsection 5.3.1). For this ROM the number of non-linear EQM would be equal to 800. However, by employing the coordinates transformation of Eqn. 5.22, relative displacement at the interface were obtained from the absolute ones and the number of non-linear EQM decreased from 800 to 400. Hence, by denoting with *II* this new ROM the corresponding generalized coordinates vector can be written as:

$$\boldsymbol{x}_{II} = \begin{Bmatrix} \Delta\boldsymbol{x}_{i}^{\rho} \\ \boldsymbol{x}_{i_2}^{\rho} \\ \Delta\boldsymbol{x}_{i}^{\theta} \\ \boldsymbol{x}_{i_2}^{\theta} \\ \boldsymbol{z}_{i}^{z} \\ \boldsymbol{x}_{i_2} \\ \boldsymbol{x}_{a_1} \\ \boldsymbol{x}_{a_2} \\ \eta_{k_1} \\ \eta_{k_2} \end{Bmatrix} \tag{5.34}$$

The size of the multi-stage ROMs *I* and *II*, and the corresponding number of non-linear EQM are compared in Table 5.6

By assuming a modal damping ratio of $\zeta = 0.005$, the structural damping matrix $\boldsymbol{C}_{II}$ was obtained exactly as done for $\boldsymbol{C}_{I}$. Considering the same contact parameters and excitation amplitudes used in the previous case, new forced response calculation

Table 5.6 Size of the multi-stage ROM *I* and *II* and corresponding number of non-linear EQM.

Multi-stage ROM	# DoFs	# non-linear EQM
ROM_I	1900	600
ROM_{II}	1700	400

were performed and compared to those of Figure 5.11 and 5.12. Figure 5.13 and 5.14 clearly show a perfect match between the non-linear forced responses obtained by using both ROMs. There results actually prove the goodness of the hypotheses n.2 and n.3 made in section 5.4. In particular, the large value of constant normal preload assumed for each pair of nodes in contact ($f_0 = 350$ N) prevents separation at the inter-stage boundary. For this reason the stages' coupling in the z direction and the use simple Jenkins contact elements do not introduce further approximations of the solution. Moreover, the absence of lift-off during the contact confirms the hypothesis of a "weak" non-linear behavior of the joint and then justifies the use of the SHMB approximation.

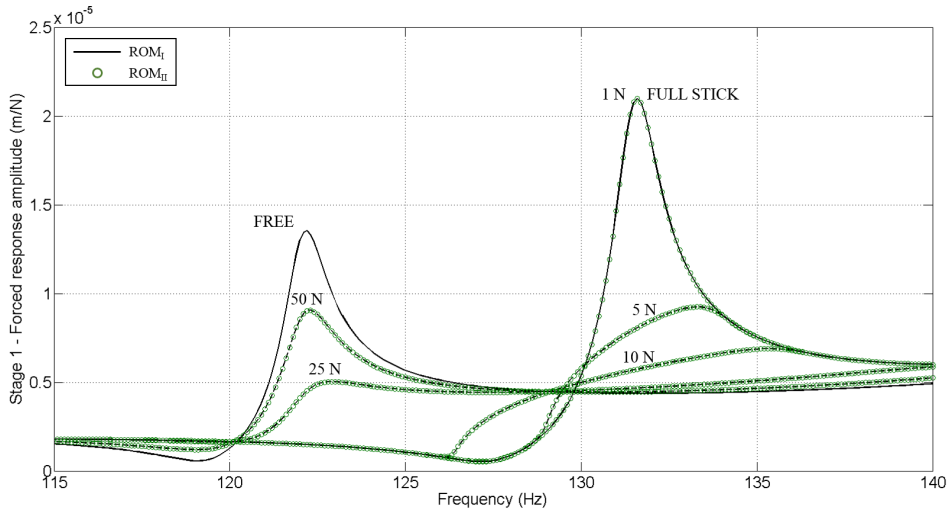

Fig. 5.13 Comparison of forced response calculation obtained from the ROM_I and ROM_{II}. The plots refer to displacements detected at the blades of the stage 1.

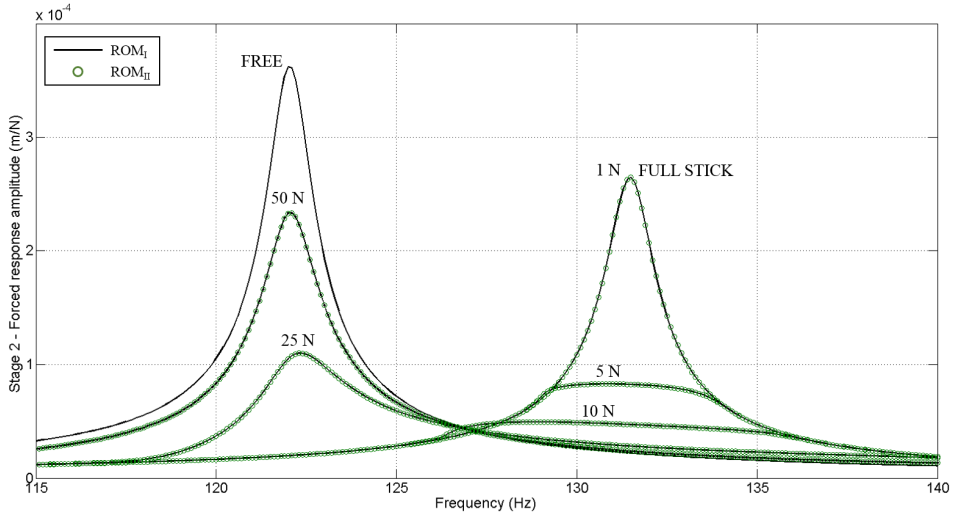

Fig. 5.14 Comparison of forced response calculation obtained from the ROM$_I$ and ROM$_{II}$. The plots refer to displacements detected at the blades of the stage 2.

Finally, although identical results were obtained in the two cases, the ROM$_{II}$ has to be preferred over the ROM$_I$ for the smaller number of DoFs involved (1700 vs 1900), the smaller partition of non-linear EQM (400 vs 600) and the least time spent for the computation of each nonlinear forced response ($\sim$ 890 s vs $\sim$ 2700 s).

5.6 Multi-Stage ROM for Full Stages & Friction Contacts

The number of non-linear EQM can be strongly reduced by employing the multi-stage reduction technique presented in section 4.3. It was shown that starting from the *CB*-CMS ROMs of two stages, the displacement field at the inter-stage boundary in all the directions (ρ, θ, z) could be approximated by few spatial harmonic functions. The set of harmonic indexes corresponding to such functions was denoted by Σ (Eqn. 4.17). Due to the hypothesis n.1 Σ must contain at least the dominant harmonic indexes h linked to the EO of the traveling waves exciting both stages (Eqn. 2.70). Hence, as shown in section 4.3, this condition would allow to write compatibility equations between stages at least for the harmonic indexes h. However, such compatibility is here enforced only for the harmonic functions describing the interfaces motion in the z direction, in order to prevent the contact between the

flanges in the axial direction. Differently, no geometric compatibility conditions are enforced along ρ and θ, since a relative displacement along these two directions is expected. Therefore, when the interface reduction is performed for both stages and the mentioned compatibility conditions are enforced, a new multi-stage ROM is obtained. The generalized coordinates vector associated to such ROM can be written as:

$$\boldsymbol{x}_{MS} = \begin{Bmatrix} \boldsymbol{a}_{i_1}^{\rho} \\ \boldsymbol{a}_{i_2}^{\rho} \\ \boldsymbol{a}_{i_1}^{\theta} \\ \boldsymbol{a}_{i_2}^{\theta} \\ \boldsymbol{a}_{i}^{z} \\ \boldsymbol{x}_{a_1} \\ \boldsymbol{x}_{a_1} \\ \boldsymbol{\eta}_{k_1} \\ \boldsymbol{\eta}_{k_2} \end{Bmatrix} \tag{5.35}$$

where

- $\boldsymbol{a}_{i_j}^{d}$ are the Fourier coefficients of the spatial harmonic function approximating the displacement at the interface of the j^{th} stage in the d direction ($d = \rho, \theta, z$).
- $\boldsymbol{x}_{a_j}$ are the active DoFs of the j^{th} stage.
- η_{k_j} are the modal coordinates corresponding to n_{k_j} fixed-interface normal modes retained in the *CB*-CMS reduction of the j^{th} stage.

Therefore, Eqn. 5.2 can in this case be expressed as:

$$\boldsymbol{M}_{MS}\ddot{\boldsymbol{x}}_{MS}(t) + \boldsymbol{C}_{MS}\dot{\boldsymbol{x}}_{MS}(t) + \boldsymbol{K}_{MS}\boldsymbol{x}_{MS}(t) = \boldsymbol{f}_{MS,e}(t) - \boldsymbol{f}_{MS,n}(\boldsymbol{x}_{MS}, t) \tag{5.36}$$

Under the hypothesis n.3, the balance equations given in Eqn. 5.36 can be turned into the following set of algebraic complex equations:

$$\boldsymbol{D}_{MS}^{1}(\Omega) \cdot \boldsymbol{X}_{MS}^{1} = \boldsymbol{F}_{MS,e}^{1} - \boldsymbol{F}_{MS,n}^{1} \tag{5.37}$$

According to the DoFs partition given in Eqn. 5.35, the Fourier coefficients of the displacement and force vectors can be expressed as:

$$\boldsymbol{X}_{MS} = \begin{Bmatrix} \boldsymbol{A}_{i_1}^{\rho} \\ \boldsymbol{A}_{i_2}^{\rho} \\ \boldsymbol{A}_{i_1}^{\theta} \\ \boldsymbol{A}_{i_2}^{\theta} \\ \boldsymbol{A}_{i}^{z} \\ \boldsymbol{X}_{a_1} \\ \boldsymbol{X}_{a_2} \\ \boldsymbol{E}_{k_1} \\ \boldsymbol{E}_{k_1} \end{Bmatrix} \quad \boldsymbol{F}_{MS,e} = \begin{Bmatrix} \boldsymbol{0} \\ \boldsymbol{0} \\ \boldsymbol{0} \\ \boldsymbol{0} \\ \boldsymbol{0} \\ \boldsymbol{F}_{e_1} \\ \boldsymbol{F}_{e_2} \\ \boldsymbol{0} \\ \boldsymbol{0} \end{Bmatrix} \quad \boldsymbol{F}_{MS,n} = \begin{Bmatrix} \bar{\boldsymbol{F}}_{n_1}^{\rho} \\ \bar{\boldsymbol{F}}_{n_2}^{\rho} \\ \bar{\boldsymbol{F}}_{n_1}^{\theta} \\ \bar{\boldsymbol{F}}_{n_2}^{\theta} \\ \boldsymbol{0} \\ \boldsymbol{0} \\ \boldsymbol{0} \\ \boldsymbol{0} \\ \boldsymbol{0} \end{Bmatrix} \tag{5.38}$$

where:

- $\boldsymbol{A}_{i_j}^{d}$ are the complex amplitudes of the spatial Fourier coefficient $\boldsymbol{a}_{i_j}^{d}$. $\boldsymbol{A}_{i_j}^{d}$ gives information about the amplitude and phase of the cosine and sine harmonic functions, or simply *waveforms*, describing the motion at the interface of the j^{th} stage;
- $\boldsymbol{X}_{a_j}$ are the complex amplitudes of the active DoF of the j^{th} stage;
- $\boldsymbol{E}_{k_j}$ are the complex amplitudes of the *CB*-CMS modal coordinates η_{k_j} for the j^{th} stage;
- $\boldsymbol{F}_{e_j}$ are the 1^{st} order Fourier coefficients of the traveling wave EO excitation discretized at the blades of the j^{th} stage.
- $\bar{\boldsymbol{F}}_{n_j}^{d}$ are the complex amplitudes of the spatial Fourier coefficients describing the distribution of the contact force at the interface of the j^{th} stage in the d direction.

When the difference between $\boldsymbol{A}_{i_1}^{d}$ and $\boldsymbol{A}_{i_2}^{d}$ is performed, the complex amplitudes of the dominant and extra waveforms referring to the relative displacement at the joint interface in the d direction are obtained:

$$\Delta\boldsymbol{A}_{i}^{d} = \boldsymbol{A}_{i_1}^{d} - \boldsymbol{A}_{i_2}^{d} \qquad d = \rho, \theta \tag{5.39}$$

Therefore, the coordinates transformation linking the absolute to the relative complex amplitudes is given by:

$$\begin{Bmatrix} \boldsymbol{A}_{i_1}^{\rho} \\ \boldsymbol{A}_{i_2}^{\rho} \\ \boldsymbol{A}_{i_1}^{\theta} \\ \boldsymbol{A}_{i_2}^{\theta} \\ \boldsymbol{A}_{i}^{z} \\ \boldsymbol{X}_{a_1} \\ \boldsymbol{X}_{a_2} \\ \boldsymbol{E}_{k_1} \\ \boldsymbol{E}_{k_1} \end{Bmatrix} = \begin{bmatrix} \boldsymbol{I} & \boldsymbol{I} & \boldsymbol{0} & \boldsymbol{0} & \boldsymbol{0} & \boldsymbol{0} & \boldsymbol{0} & \boldsymbol{0} & \boldsymbol{0} \\ \boldsymbol{0} & \boldsymbol{I} & \boldsymbol{0} & \boldsymbol{0} & \boldsymbol{0} & \boldsymbol{0} & \boldsymbol{0} & \boldsymbol{0} & \boldsymbol{0} \\ \boldsymbol{0} & \boldsymbol{0} & \boldsymbol{I} & \boldsymbol{0} & \boldsymbol{0} & \boldsymbol{0} & \boldsymbol{0} & \boldsymbol{0} & \boldsymbol{0} \\ \boldsymbol{0} & \boldsymbol{0} & \boldsymbol{0} & \boldsymbol{I} & \boldsymbol{0} & \boldsymbol{0} & \boldsymbol{0} & \boldsymbol{0} & \boldsymbol{0} \\ \boldsymbol{0} & \boldsymbol{0} & \boldsymbol{0} & \boldsymbol{0} & \boldsymbol{I} & \boldsymbol{0} & \boldsymbol{0} & \boldsymbol{0} & \boldsymbol{0} \\ \boldsymbol{0} & \boldsymbol{0} & \boldsymbol{0} & \boldsymbol{0} & \boldsymbol{0} & \boldsymbol{I} & \boldsymbol{0} & \boldsymbol{0} & \boldsymbol{0} \\ \boldsymbol{0} & \boldsymbol{0} & \boldsymbol{0} & \boldsymbol{0} & \boldsymbol{0} & \boldsymbol{0} & \boldsymbol{I} & \boldsymbol{0} & \boldsymbol{0} \\ \boldsymbol{0} & \boldsymbol{0} & \boldsymbol{0} & \boldsymbol{0} & \boldsymbol{0} & \boldsymbol{0} & \boldsymbol{0} & \boldsymbol{I} & \boldsymbol{0} \\ \boldsymbol{0} & \boldsymbol{0} & \boldsymbol{0} & \boldsymbol{0} & \boldsymbol{0} & \boldsymbol{0} & \boldsymbol{0} & \boldsymbol{0} & \boldsymbol{I} \end{bmatrix} \begin{Bmatrix} \Delta\boldsymbol{A}_{i}^{\rho} \\ \boldsymbol{A}_{i_2}^{\rho} \\ \Delta\boldsymbol{A}_{i}^{\theta} \\ \boldsymbol{A}_{i_2}^{\theta} \\ \boldsymbol{A}_{i}^{z} \\ \boldsymbol{X}_{a_1} \\ \boldsymbol{X}_{a_2} \\ \boldsymbol{E}_{k_1} \\ \boldsymbol{E}_{k_1} \end{Bmatrix} = \boldsymbol{T}_{rel}\boldsymbol{X}_{MS}^{rel} \tag{5.40}$$

where $\boldsymbol{T}_{rel}$ is the coordinates transformation matrix. By substituting Eqn. (5.40) into Eqn. (5.36) and pre-multiplying both sides by $\boldsymbol{T}_{rel}^{T}$, the following system of equation is obtained:

$$\boldsymbol{T}_{rel}^{T}\boldsymbol{D}_{MS}\boldsymbol{T}_{rel}\boldsymbol{X}_{MS}^{rel} - \boldsymbol{T}_{rel}^{T}\boldsymbol{F}_{MS,e} + \boldsymbol{T}_{rel}^{T}\boldsymbol{F}_{MS,n} \approx \boldsymbol{0} \tag{5.41}$$

Although the pre-multiplication by $\boldsymbol{T}_{rel}^{T}$ leaves $\mathbf{F}_{MS,e}$ unchanged, more attention has to be paid on $\boldsymbol{T}_{rel}^{T}\mathbf{F}_{MS,n}$:

$$\boldsymbol{T}_{rel}^{T}\mathbf{F}_{MS,n} = \begin{bmatrix} \boldsymbol{I} & \boldsymbol{0} & \boldsymbol{0} & \boldsymbol{0} & \boldsymbol{0} & \boldsymbol{0} & \boldsymbol{0} & \boldsymbol{0} & \boldsymbol{0} \\ \boldsymbol{I} & \boldsymbol{I} & \boldsymbol{0} & \boldsymbol{0} & \boldsymbol{0} & \boldsymbol{0} & \boldsymbol{0} & \boldsymbol{0} & \boldsymbol{0} \\ \boldsymbol{0} & \boldsymbol{0} & \boldsymbol{I} & \boldsymbol{0} & \boldsymbol{0} & \boldsymbol{0} & \boldsymbol{0} & \boldsymbol{0} & \boldsymbol{0} \\ \boldsymbol{0} & \boldsymbol{0} & \boldsymbol{0} & \boldsymbol{I} & \boldsymbol{0} & \boldsymbol{0} & \boldsymbol{0} & \boldsymbol{0} & \boldsymbol{0} \\ \boldsymbol{0} & \boldsymbol{0} & \boldsymbol{0} & \boldsymbol{0} & \boldsymbol{I} & \boldsymbol{0} & \boldsymbol{0} & \boldsymbol{0} & \boldsymbol{0} \\ \boldsymbol{0} & \boldsymbol{0} & \boldsymbol{0} & \boldsymbol{0} & \boldsymbol{0} & \boldsymbol{I} & \boldsymbol{0} & \boldsymbol{0} & \boldsymbol{0} \\ \boldsymbol{0} & \boldsymbol{0} & \boldsymbol{0} & \boldsymbol{0} & \boldsymbol{0} & \boldsymbol{0} & \boldsymbol{I} & \boldsymbol{0} & \boldsymbol{0} \\ \boldsymbol{0} & \boldsymbol{0} & \boldsymbol{0} & \boldsymbol{0} & \boldsymbol{0} & \boldsymbol{0} & \boldsymbol{0} & \boldsymbol{I} & \boldsymbol{0} \\ \boldsymbol{0} & \boldsymbol{0} & \boldsymbol{0} & \boldsymbol{0} & \boldsymbol{0} & \boldsymbol{0} & \boldsymbol{0} & \boldsymbol{0} & \boldsymbol{I} \end{bmatrix} \begin{Bmatrix} \bar{\boldsymbol{F}}_{n_1}^{\rho} \\ \bar{\boldsymbol{F}}_{n_2}^{\rho} \\ \bar{\boldsymbol{F}}_{n_1}^{\theta} \\ \bar{\boldsymbol{F}}_{n_2}^{\theta} \\ \boldsymbol{0} \\ \boldsymbol{0} \\ \boldsymbol{0} \\ \boldsymbol{0} \\ \boldsymbol{0} \end{Bmatrix} = \begin{Bmatrix} \bar{\boldsymbol{F}}_{n_1}^{\rho} \\ \bar{\boldsymbol{F}}_{n_1}^{\rho} + \bar{\boldsymbol{F}}_{n_2}^{\rho} \\ \bar{\boldsymbol{F}}_{n_1}^{\theta} \\ \bar{\boldsymbol{F}}_{n_1}^{\theta} + \bar{\boldsymbol{F}}_{n_2}^{\theta} \\ \boldsymbol{0} \\ \boldsymbol{0} \\ \boldsymbol{0} \\ \boldsymbol{0} \\ \boldsymbol{0} \end{Bmatrix} \tag{5.42}$$

The contact forces at the two contact interfaces are equal in amplitude but opposite in sign, meaning that the terms $\bar{\boldsymbol{F}}^{\rho}_{n_1} + \bar{\boldsymbol{F}}^{\rho}_{n_2}$ and $\bar{\boldsymbol{F}}^{\theta}_{n_1} + \bar{\boldsymbol{F}}^{\theta}_{n_2}$ are both null:

$$\boldsymbol{T}^{T}_{rel}\mathbf{F}_{MS,nl} = \begin{Bmatrix} \bar{\boldsymbol{F}}^{\rho}_{n_1} \\ \boldsymbol{0} \\ \bar{\boldsymbol{F}}^{\theta}_{n_1} \\ \boldsymbol{0} \\ \boldsymbol{0} \\ \boldsymbol{0} \\ \boldsymbol{0} \\ \boldsymbol{0} \\ \boldsymbol{0} \end{Bmatrix} = \begin{Bmatrix} \bar{\boldsymbol{F}}^{\rho}_{n} \\ \boldsymbol{0} \\ \bar{\boldsymbol{F}}^{\theta}_{n} \\ \boldsymbol{0} \\ \boldsymbol{0} \\ \boldsymbol{0} \\ \boldsymbol{0} \\ \boldsymbol{0} \\ \boldsymbol{0} \end{Bmatrix} \tag{5.43}$$

In this way the non-linear partition of the EQM was reduced of the 50% with respect that of the system given in Eqn. (5.37).

The Jenkins contact element is used for classical node-to-node contact problems. However, due to the coordinates transformation defined by the Eqn. (4.18) and the application of the SHBM, the relative displacements at the inter-stage boundaries are expressed in term of complex coefficients $\Delta\boldsymbol{A}^{d}_{i}$. Therefore, the application of the mentioned contact model requires to rebuild the physical relative displacements so that the contact forces $f_{n,t}$ can be evaluated in the physical space too.

The vector of spatial Fourier coefficients $\boldsymbol{a}_i$ contains cosine and sine components referring to the waveforms approximating the motion at the contact interface (Eqn. 4.13). If ς is the generic harmonic index included into the set Σ, $\boldsymbol{a}_i$ can be expressed as:

$$\boldsymbol{a}_i = \Big(\bigcup_{\varsigma} \boldsymbol{a}^{c}_{i_\varsigma}\Big) \cup \Big(\bigcup_{\varsigma} \boldsymbol{a}^{s}_{i_\varsigma}\Big) \qquad \forall\, \varsigma \in \Sigma \tag{5.44}$$

When Eqn. 5.36 is turned in the frequency domain and the coordinates transformation of Eqn. 5.40 is employed, the Fourier coefficients $\boldsymbol{a}_i$ are converted into the following set of complex cosine and sine amplitudes:

$$\Delta\boldsymbol{A}_i = \Big(\bigcup_{\varsigma} \Delta\boldsymbol{A}^{c}_{i_\varsigma}\Big) \cup \Big(\bigcup_{\varsigma} \Delta\boldsymbol{A}^{s}_{i_\varsigma}\Big) \qquad \forall\, \varsigma \in \Sigma \tag{5.45}$$

The cosine and sine waveforms at the contact interface can be obtained by expanding the complex coefficients of Eqn. 5.45 through the following relationships:

$$\Delta \boldsymbol{x}_i^c(\theta_i) = \Re\left(\sum_{\varsigma} g|\Delta A_{i_\varsigma}^c| e^{\imath(\varsigma\theta_i + \varphi_{\Delta A_{i_\varsigma}^c})}\right)$$

$$\Delta \boldsymbol{x}_i^s(\theta_i) = \Re\left(\sum_{\varsigma} g|\Delta A_{i_\varsigma}^s| e^{\imath(\varsigma\theta_i + \varphi_{\Delta A_{i_\varsigma}^s})}\right) \tag{5.46}$$

where:

- g is defined as (see Eqns. 4.4 and 4.12):

$$g = \begin{cases} \dfrac{1}{\sqrt{NZ}} & \text{if} \quad \varsigma = 0, \tilde{R} \\ \\ \sqrt{\dfrac{2}{NZ}} & \text{for all the other } \varsigma \end{cases} \tag{5.47}$$

- $|\Delta A_{i_\varsigma}^c|$ and $|\Delta A_{i_\varsigma}^s|$ are the absolute values of the complex coefficients of Eqn. 5.45[3];
- $\varphi_{\Delta A_{i_\varsigma}^c}$ and $\varphi_{\Delta A_{i_\varsigma}^s}$ are the phase angles of the complex coefficients of Eqn. 5.44;
- θ_i is the vector listing the angular locations along the contact interface where the Jenkins contact elements are employed;

The complex waveform approximating the relative physical displacement field at the contact interface is finally given by:

$$\Delta \boldsymbol{x}_i(\theta_i) = \Delta \boldsymbol{x}_i^c(\theta_i) + i\Delta \boldsymbol{x}_i^s(\theta_i) \tag{5.48}$$

The physical contact forces $\boldsymbol{f}_n^d(\theta_i)$ in the d direction are then computed applying the Jenkins contact element at all the locations θ_i chosen to discretize the physical relative displacement $\Delta \boldsymbol{x}_i^d$ ($d = \rho, \theta$). The real and imaginary parts of $\boldsymbol{f}_n^d(\theta_i)$ can be

[3]Note that $\Delta A_{i_\varsigma}^c$ and $\Delta A_{i_\varsigma}^s$ can be written as $\Delta A_{i_\varsigma}^c = |\Delta A_{i_\varsigma}^c| e^{\imath\varphi_{\Delta A_{i_\varsigma}^c}}$ and $\Delta A_{i_\varsigma}^s = |\Delta A_{i_\varsigma}^s| e^{\imath\varphi_{\Delta A_{i_\varsigma}^s}}$ respectively.

expressed according to the following Fourier series:

$$\Re\left[\boldsymbol{f}_n^d(\theta_i)\right] = \Re\left(\sum_{\varsigma} \bar{\boldsymbol{F}}_{i_\varsigma}^{c,d} \cdot e^{\imath\varsigma\theta_i}\right)$$

$$\Im\left[\boldsymbol{f}_n^d(\theta_i)\right] = \Re\left(\sum_{\varsigma} \bar{\boldsymbol{F}}_{i_\varsigma}^{s,d} \cdot e^{\imath\varsigma\theta_i}\right) \tag{5.49}$$

where $\bar{\boldsymbol{F}}_{i_\varsigma}^{c,d}$ and $\bar{\boldsymbol{F}}_{i_\varsigma}^{s,d}$ represent the spatial Fourier coefficients of the physical contact force $\boldsymbol{f}_n^d(\theta_i)$ having harmonic index $\varsigma \in \Sigma$. Therefore, the cosine and sine components of $\boldsymbol{F}_n^d$ are defined as:

$$\boldsymbol{F}_n^{c,d} = \bigcup_{\varsigma} \frac{1}{g} \bar{\boldsymbol{F}}_{i_\varsigma}^{c,d} \qquad \boldsymbol{F}_n^{c,d} = \bigcup_{\varsigma} \frac{1}{g} \bar{\boldsymbol{F}}_{i_\varsigma}^{s,d} \tag{5.50}$$

and the complex coefficients of the harmonics contact force balancing the non-linear EQM in Eqn. 5.41 are given by:

$$\boldsymbol{F}_n^d = \left[(\boldsymbol{F}_n^{c,d})^T \ (\boldsymbol{F}_n^{s,d})^T\right]^T \tag{5.51}$$

Example

The application already presented in section 5.5 is here studied by applying the multi-stage reduction technique introduced above. Thereby, starting from the *CB*-CMS ROMs of the two stages, further reductions of the interface DoFs were achieved by resorting to the transformation of Eqn. (4.18). The harmonic indexes for which the mentioned reduction could be performed were deduced from the assumed value of the EO. In particular, by setting $z = 0$ in Eqn. 2.70, the dominant harmonic index reducing the interface of both stages is $h = 2$. Moreover, from Eqn. 5.51 a the reduced set Σ of harmonic indexes corresponding to $h = 2$ was calculated as:

$$\begin{aligned}
\Sigma &= \Big(h \ \ (NZ-h) \ \ (NZ+h) \ \ (2\cdot NZ-h)\Big) = \\
&= \Big(2 \ \ (50-2) \ \ (50+2) \ \ (2\cdot 50-2)\Big) = \\
&= \Big(2 \ \ 48 \ \ 52 \ \ 98\Big)
\end{aligned} \tag{5.52}$$

Therefore, a third multi-stage ROM was created. Such ROM is here denoted by *III* and its reduced vector of generalized coordinates is given by:

$$\boldsymbol{x}_{III} = \begin{Bmatrix} \boldsymbol{a}_{i_1}^{\rho} - \boldsymbol{a}_{i_2}^{\rho} \\ \boldsymbol{a}_{i_2}^{\rho} \\ \boldsymbol{a}_{i_1}^{\theta} - \boldsymbol{a}_{i_2}^{\theta} \\ \boldsymbol{a}_{i_2}^{\theta} \\ \boldsymbol{a}_{i}^{z} \\ \boldsymbol{x}_{a_1} \\ \boldsymbol{x}_{a_2} \\ \eta_{k_1} \\ \eta_{k_2} \end{Bmatrix} \tag{5.53}$$

where:

$$\boldsymbol{a}_{i_j}^{d} = \left\{ \left(\boldsymbol{a}_{i_2}^{c,d}\right)^T \ \left(\boldsymbol{a}_{i_{48}}^{c,d}\right)^T \ \left(\boldsymbol{a}_{i_{52}}^{c,d}\right)^T \ \left(\boldsymbol{a}_{i_{98}}^{c,d}\right)^T \right. \\ \left. \left(\boldsymbol{a}_{i_{98}}^{s,d}\right)^T \ \left(\boldsymbol{a}_{i_{52}}^{s,d}\right)^T \ \left(\boldsymbol{a}_{i_{48}}^{s,d}\right)^T \ \left(\boldsymbol{a}_{i_2}^{s,d}\right)^T \right\}^T \tag{5.54}$$

The size of the multi-stage ROMs *I*, *II* and *III*, and the corresponding number of non-linear EQM are compared in Table 5.7

Table 5.7 Size of the multi-stage ROM *I*, *II III* and corresponding number of non-linear EQM.

Multi-stage ROM	# DoFs	# non-linear EQM
ROM_{I}	1900	600
ROM_{II}	1700	400
ROM_{III}	740	32

By assuming a modal damping ratio of $\zeta = 0.005$, the structural damping matrix $\boldsymbol{C}_{III}$ was obtained exactly as done for $\boldsymbol{C}_{I}$. Considering the same contact parameters and excitation amplitudes used in the previous case, new forced response calculation were performed and compared to those of Figure 5.11 and 5.12.

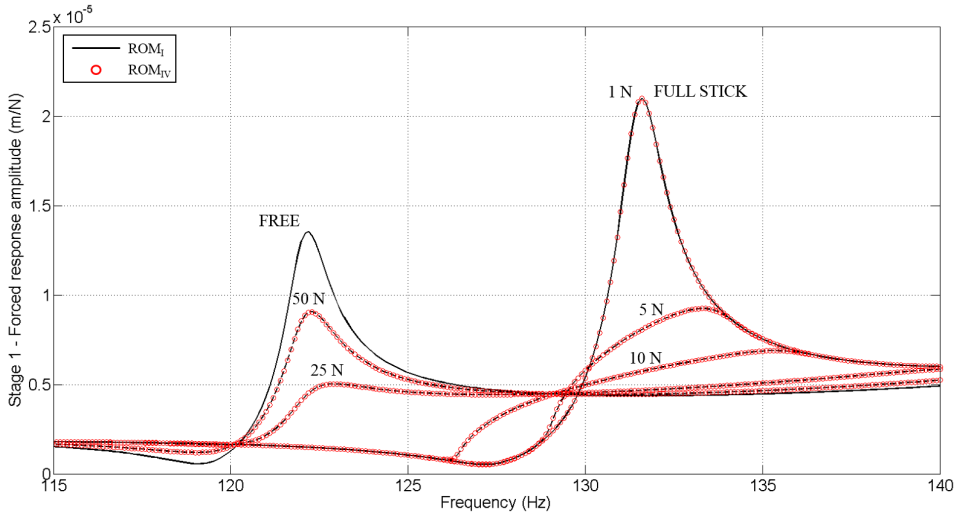

Fig. 5.15 Comparison of forced response calculation obtained from the ROM$_I$ and ROM$_{III}$. The plots refer to displacements detected at the blades of the stage 1.

Figure 5.15 and 5.16 show again a perfect match between the non-linear forced response calculations carried out with both ROMs. These results confirms the goodness of the multi-stage reduction technique for full stages developed in section 4.3. In fact, the selected set of harmonic basis functions used to approximate the interface displacement did not lead to any significant approximation of the solution. Therefore, performing non-linear forced response calculation on the multi-stage ROM$_{III}$ appears much more convenient than using the ROMs *I* and *II*. Besides the smaller number of DoFs involved in such calculations, the performance of the ROM$_{III}$ can be better appreciated if the time spent in the simulation is taken into account (Table 5.9).

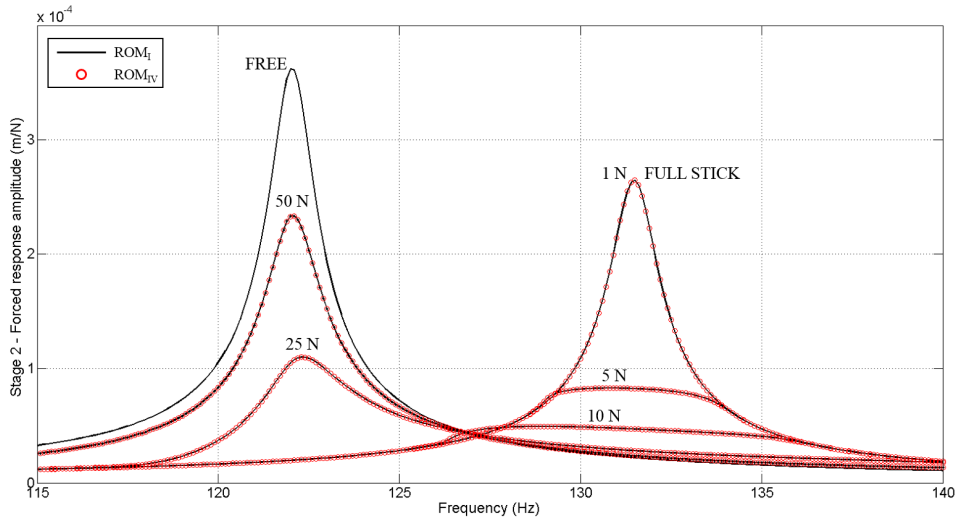

Fig. 5.16 Comparison of forced response calculation obtained from the ROM_I and ROM_{III}. The plots refer to displacements detected at the blades of the stage 2.

Table 5.8 Average time for the non-linear forced response calculation: comparison between the multi-stage ROM_I, ROM_{II} and ROM_{III}.

Multi-stage ROM	Time (s)
ROM_I	2700
ROM_{II}	890
ROM_{III}	60

5.7 Multi-Stage ROM for Cyclic Stages & Friction Contacts

In this section the reduced non-linear EQM of a multi-stage system with friction contacts at the flange joint are obtained starting from the fundamental sectors of two stages treated in cyclic symmetry conditions. The approach employed to reduce such sectors is exactly that of section 4.5, where the DoFs at the interface of each sector are reduced to those of the first radial line segment.

Let Σ be the set of harmonic indexes denoting the harmonics approximating the DoFs at the interface of both stages. As already stated, due to the hypothesis n.1 this set must contain at least the dominant harmonic index h, which is linked to the assumed EO by Eqn. 2.70. In general, if k_m is the m^{th} extra harmonics index included into the set Σ, the generalized coordinates vector for the j^{th} cyclic sector

can be written as:

$$\boldsymbol{x}_{CS_j} \approx \begin{Bmatrix} \boldsymbol{x}^h_{R_1,j} \\ \boldsymbol{x}^{k_1}_{R_1,j} \\ \vdots \\ \boldsymbol{x}^{k_m}_{R_1,j} \\ \boldsymbol{x}^h_{a_j} \\ \eta^h_{k_j} \end{Bmatrix} = \begin{Bmatrix} \boldsymbol{x}^{\Sigma}_{R_1,j} \\ \boldsymbol{x}^h_{a_j} \\ \eta^h_{k_j} \end{Bmatrix} \tag{5.55}$$

where $\boldsymbol{x}^{\Sigma}_{R_1,j}$ is the vector collecting the reduced DoFs at the interface of the j^{th} sector. By separating its ρ, θ and z components, $\boldsymbol{x}^{\Sigma}_{R_1,j}$ can be written as:

$$\boldsymbol{x}^{\Sigma}_{R_1,j} = \begin{Bmatrix} \boldsymbol{x}^{\Sigma,\rho}_{R_1,j} \\ \boldsymbol{x}^{\Sigma,\theta}_{R_1,j} \\ \boldsymbol{x}^{\Sigma,z}_{R_1,j} \end{Bmatrix} \tag{5.56}$$

Therefore, by enforcing the compatibility condition in the z direction between the interface DoFs of both cyclic sectors ($\boldsymbol{x}^{\Sigma,z}_{R_1,1} = \boldsymbol{x}^{\Sigma,z}_{R_1,2} = \boldsymbol{x}^{\Sigma,z}_{R_1}$), a new cyclic multi-stage ROM having the following generalized coordinate vector is obtained:

$$\boldsymbol{x}_{CS} = \begin{Bmatrix} \boldsymbol{x}^{\Sigma,\rho}_{R_1,1} \\ \boldsymbol{x}^{\Sigma,\rho}_{R_1,2} \\ \boldsymbol{x}^{\Sigma,\theta}_{R_1,1} \\ \boldsymbol{x}^{\Sigma,\theta}_{R_1,2} \\ \boldsymbol{x}^{\Sigma,z}_{R_1} \\ \boldsymbol{x}^h_{a_1} \\ \boldsymbol{x}^h_{a_2} \\ \eta^h_{k_1} \\ \eta^h_{k_2} \end{Bmatrix} \tag{5.57}$$

Hence, Eqn. 5.2 can in this case be expressed as:

$$\boldsymbol{M}_{CS}\ddot{\boldsymbol{x}}_{CS}(t) + \boldsymbol{C}_{CS}\dot{\boldsymbol{x}}_{CS}(t) + \boldsymbol{K}_{CS}\boldsymbol{x}_{CS}(t) = \boldsymbol{f}_{CS,e}(t) - \boldsymbol{f}_{CS,n}(\boldsymbol{x}_{CS}, t) \tag{5.58}$$

Under the hypothesis of SHBM, the former EQM can be turned into a set of non-linear algebraic complex equation:

$$\boldsymbol{D}^1_{CS}(\Omega) \cdot \boldsymbol{X}^1_{CS} = \boldsymbol{F}^1_{CS,e} - \boldsymbol{F}^1_{CS,n} \tag{5.59}$$

where the superscript "1" indicates the first harmonic component of the corresponding quantity. Hereafter this superscript will be omitted in order to simplify the notation.

According to the DoFs partition given in Eqn.5.57, the Fourier coefficients of the cyclic displacement and force vectors can be expressed as:

$$\boldsymbol{X}_{CS} = \begin{Bmatrix} \boldsymbol{X}_{i_1}^{\Sigma,\rho} \\ \boldsymbol{X}_{i_2}^{\Sigma,\rho} \\ \boldsymbol{X}_{i_1}^{\Sigma,\theta} \\ \boldsymbol{X}_{i_2}^{\Sigma,\theta} \\ \boldsymbol{X}_{i}^{z} \\ \boldsymbol{X}_{a_1}^{h} \\ \boldsymbol{X}_{a_2}^{h} \\ \boldsymbol{E}_{k_1}^{h} \\ \boldsymbol{E}_{k_1}^{h} \end{Bmatrix} \quad \boldsymbol{F}_{CS,e} = \begin{Bmatrix} \boldsymbol{0} \\ \boldsymbol{0} \\ \boldsymbol{0} \\ \boldsymbol{0} \\ \boldsymbol{0} \\ \boldsymbol{F}_{e_1} \\ \boldsymbol{F}_{e_2} \\ \boldsymbol{0} \\ \boldsymbol{0} \end{Bmatrix} \quad \boldsymbol{F}_{CS,n} = \begin{Bmatrix} \boldsymbol{F}_{n_1}^{\Sigma,\rho} \\ \boldsymbol{F}_{n_2}^{\Sigma,\rho} \\ \boldsymbol{F}_{n_1}^{\Sigma,\theta} \\ \boldsymbol{F}_{n_2}^{\Sigma,\theta} \\ \boldsymbol{0} \\ \boldsymbol{0} \\ \boldsymbol{0} \\ \boldsymbol{0} \\ \boldsymbol{0} \end{Bmatrix} \tag{5.60}$$

where:

- $\boldsymbol{X}_{i_j}^{\Sigma,d}$ and $\boldsymbol{X}_{a_j}^{h}$ are the 1^{st} order Fourier coefficients of the physical DoFs $\boldsymbol{x}_{i_j}^{\Sigma,d}$ and $\boldsymbol{x}_{a_j}^{h}$ respectively.
- $\boldsymbol{E}_{k_j}^{h}$ are the 1^{st} order Fourier coefficients of the *CB*-CMS modal coordinates $\eta_{k_j}^{h}$.
- $\boldsymbol{F}_{e_j}^{h}$ are the 1^{st} order Fourier coefficients of the harmonic force acting on the j^{th} cyclic sector.
- $\boldsymbol{F}_{n_j}^{\Sigma,d}$ are the 1^{st} order Fourier coefficients describing the distribution of the contact force at the interface of the j^{th} stage.

Since the non-linear contact forces depend on the relative displacements of equally collocated nodes (Figure 5.17), the 1^{st} order Fourier coefficients of the relative cyclic displacement at the inter-stage boundary can be calculated as:

$$\Delta\boldsymbol{X}_{R}^{\Sigma,d} = \boldsymbol{X}_{R_1,1}^{\Sigma,d} - \boldsymbol{X}_{R_1,2}^{\Sigma,d} \qquad d = \rho, \theta \tag{5.61}$$

Therefore, the coordinate transformation linking the absolute to the relative cyclic

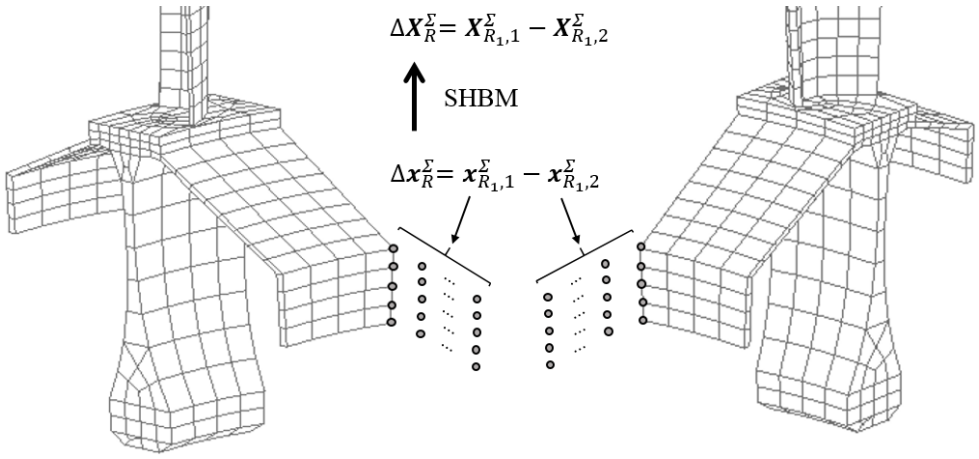

Fig. 5.17 Relative displacements from cyclic coordinates at the sectors' interfaces.

displacements is given by:

$$\boldsymbol{X}_{CS}^{h} = \begin{Bmatrix} \boldsymbol{X}_{R_1,1}^{\Sigma,\rho} \\ \boldsymbol{X}_{R_1,2}^{\Sigma,\rho} \\ \boldsymbol{X}_{R_1,1}^{\Sigma,\theta} \\ \boldsymbol{X}_{R_1,2}^{\Sigma,\theta} \\ \boldsymbol{X}_{i}^{\Sigma,z} \\ \boldsymbol{X}_{a_1}^{h} \\ \boldsymbol{X}_{a_2}^{h} \\ \boldsymbol{E}_{k_1}^{h} \\ \boldsymbol{E}_{k_1}^{h} \end{Bmatrix} = \begin{bmatrix} \boldsymbol{I} & \boldsymbol{I} & \boldsymbol{0} & \boldsymbol{0} & \boldsymbol{0} & \boldsymbol{0} & \boldsymbol{0} & \boldsymbol{0} & \boldsymbol{0} \\ \boldsymbol{0} & \boldsymbol{I} & \boldsymbol{0} & \boldsymbol{0} & \boldsymbol{0} & \boldsymbol{0} & \boldsymbol{0} & \boldsymbol{0} & \boldsymbol{0} \\ \boldsymbol{0} & \boldsymbol{0} & \boldsymbol{I} & \boldsymbol{I} & \boldsymbol{0} & \boldsymbol{0} & \boldsymbol{0} & \boldsymbol{0} & \boldsymbol{0} \\ \boldsymbol{0} & \boldsymbol{0} & \boldsymbol{0} & \boldsymbol{I} & \boldsymbol{0} & \boldsymbol{0} & \boldsymbol{0} & \boldsymbol{0} & \boldsymbol{0} \\ \boldsymbol{0} & \boldsymbol{0} & \boldsymbol{0} & \boldsymbol{0} & \boldsymbol{I} & \boldsymbol{0} & \boldsymbol{0} & \boldsymbol{0} & \boldsymbol{0} \\ \boldsymbol{0} & \boldsymbol{0} & \boldsymbol{0} & \boldsymbol{0} & \boldsymbol{0} & \boldsymbol{I} & \boldsymbol{0} & \boldsymbol{0} & \boldsymbol{0} \\ \boldsymbol{0} & \boldsymbol{0} & \boldsymbol{0} & \boldsymbol{0} & \boldsymbol{0} & \boldsymbol{0} & \boldsymbol{I} & \boldsymbol{0} & \boldsymbol{0} \\ \boldsymbol{0} & \boldsymbol{0} & \boldsymbol{0} & \boldsymbol{0} & \boldsymbol{0} & \boldsymbol{0} & \boldsymbol{0} & \boldsymbol{I} & \boldsymbol{0} \\ \boldsymbol{0} & \boldsymbol{0} & \boldsymbol{0} & \boldsymbol{0} & \boldsymbol{0} & \boldsymbol{0} & \boldsymbol{0} & \boldsymbol{0} & \boldsymbol{I} \end{bmatrix} \begin{Bmatrix} \Delta \boldsymbol{X}_{R_1}^{\Sigma,\rho} \\ \boldsymbol{X}_{R_1,2}^{\Sigma,\rho} \\ \Delta \boldsymbol{X}_{R_1}^{\Sigma,\theta} \\ \boldsymbol{X}_{R_1,2}^{\Sigma,\theta} \\ \boldsymbol{X}_{i}^{\Sigma,z} \\ \boldsymbol{X}_{a_1}^{h} \\ \boldsymbol{X}_{a_2}^{h} \\ \boldsymbol{E}_{k_1}^{h} \\ \boldsymbol{E}_{k_1}^{h} \end{Bmatrix} = \boldsymbol{T}_{rel} \boldsymbol{X}_{CS}^{h,rel} \quad (5.62)$$

where $\boldsymbol{T}_{rel}$ is the matrix transforming the interface displacement from absolute to relative. By substituting Eqn. and pre-multiplying both side by $\boldsymbol{T}_{rel}^{T}$, the following system of equation is obtained:

$$\boldsymbol{T}_{rel}^{T} \boldsymbol{D}_{CS} \boldsymbol{T}_{rel} \boldsymbol{X}_{CS}^{h,rel} - \boldsymbol{T}_{rel}^{T} \boldsymbol{F}_{CS,e} + \boldsymbol{T}_{rel}^{T} \boldsymbol{F}_{CS,n} \approx \boldsymbol{0} \quad (5.63)$$

Although the pre-multiplication by $\boldsymbol{T}_{rel}^T$ leaves $\mathbf{F}_{CS,e}$ unchanged, more attention has to be paid on $\boldsymbol{T}_{rel}^T\mathbf{F}_{CS,n}$:

$$\boldsymbol{T}_{rel}^T\mathbf{F}_{CS,n} = \begin{bmatrix} \boldsymbol{I} & \boldsymbol{0} & \boldsymbol{0} & \boldsymbol{0} & \boldsymbol{0} & \boldsymbol{0} & \boldsymbol{0} & \boldsymbol{0} & \boldsymbol{0} \\ \boldsymbol{I} & \boldsymbol{I} & \boldsymbol{0} & \boldsymbol{0} & \boldsymbol{0} & \boldsymbol{0} & \boldsymbol{0} & \boldsymbol{0} & \boldsymbol{0} \\ \boldsymbol{0} & \boldsymbol{0} & \boldsymbol{I} & \boldsymbol{0} & \boldsymbol{0} & \boldsymbol{0} & \boldsymbol{0} & \boldsymbol{0} & \boldsymbol{0} \\ \boldsymbol{0} & \boldsymbol{0} & \boldsymbol{0} & \boldsymbol{I} & \boldsymbol{0} & \boldsymbol{0} & \boldsymbol{0} & \boldsymbol{0} & \boldsymbol{0} \\ \boldsymbol{0} & \boldsymbol{0} & \boldsymbol{0} & \boldsymbol{0} & \boldsymbol{I} & \boldsymbol{0} & \boldsymbol{0} & \boldsymbol{0} & \boldsymbol{0} \\ \boldsymbol{0} & \boldsymbol{0} & \boldsymbol{0} & \boldsymbol{0} & \boldsymbol{0} & \boldsymbol{I} & \boldsymbol{0} & \boldsymbol{0} & \boldsymbol{0} \\ \boldsymbol{0} & \boldsymbol{0} & \boldsymbol{0} & \boldsymbol{0} & \boldsymbol{0} & \boldsymbol{0} & \boldsymbol{I} & \boldsymbol{0} & \boldsymbol{0} \\ \boldsymbol{0} & \boldsymbol{0} & \boldsymbol{0} & \boldsymbol{0} & \boldsymbol{0} & \boldsymbol{0} & \boldsymbol{0} & \boldsymbol{I} & \boldsymbol{0} \\ \boldsymbol{0} & \boldsymbol{0} & \boldsymbol{0} & \boldsymbol{0} & \boldsymbol{0} & \boldsymbol{0} & \boldsymbol{0} & \boldsymbol{0} & \boldsymbol{I} \end{bmatrix} \begin{Bmatrix} \boldsymbol{F}_{n_1}^{\Sigma,\rho} \\ \boldsymbol{F}_{n_2}^{\Sigma,\rho} \\ \boldsymbol{F}_{n_1}^{\Sigma,\theta} \\ \boldsymbol{F}_{n_2}^{\Sigma,\theta} \\ \boldsymbol{0} \\ \boldsymbol{0} \\ \boldsymbol{0} \\ \boldsymbol{0} \\ \boldsymbol{0} \end{Bmatrix} = \begin{Bmatrix} \boldsymbol{F}_{n_1}^{\Sigma,\rho} \\ \boldsymbol{F}_{n_1}^{\Sigma,\rho} + \boldsymbol{F}_{n_2}^{\Sigma,\rho} \\ \boldsymbol{F}_{n_1}^{\Sigma,\theta} \\ \boldsymbol{F}_{n_1}^{\Sigma,\theta} + \boldsymbol{F}_{n_2}^{\Sigma,\theta} \\ \boldsymbol{0} \\ \boldsymbol{0} \\ \boldsymbol{0} \\ \boldsymbol{0} \\ \boldsymbol{0} \end{Bmatrix} \tag{5.64}$$

The contact forces at the two contact interfaces are equal in amplitude but opposite in sign, meaning that the terms $\boldsymbol{F}_{n_1}^{\Sigma,\rho} + \boldsymbol{F}_{n_2}^{\Sigma,\rho}$ and $\boldsymbol{F}_{n_1}^{\Sigma,\theta} + \boldsymbol{F}_{n_2}^{\Sigma,\theta}$ are both null:

$$\boldsymbol{T}_{rel}^T\mathbf{F}_{MS,n} = \begin{Bmatrix} \boldsymbol{F}_{n_1}^{\Sigma,\rho} \\ \boldsymbol{0} \\ \boldsymbol{F}_{n_1}^{\Sigma,\theta} \\ \boldsymbol{0} \\ \boldsymbol{0} \\ \boldsymbol{0} \\ \boldsymbol{0} \\ \boldsymbol{0} \\ \boldsymbol{0} \end{Bmatrix} = \begin{Bmatrix} \boldsymbol{F}_{n}^{\Sigma,\rho} \\ \boldsymbol{0} \\ \boldsymbol{F}_{n}^{\Sigma,\theta} \\ \boldsymbol{0} \\ \boldsymbol{0} \\ \boldsymbol{0} \\ \boldsymbol{0} \\ \boldsymbol{0} \\ \boldsymbol{0} \end{Bmatrix} \tag{5.65}$$

In this way only the non-linear equations corresponding to the term $\boldsymbol{F}_n$ have to be iteratively solved. In must be pointed out that thanks to the coordinates transformation of Eqn. 5.62 the number of non-linear algebraic equations results halved with respect that of Eqn. (5.59).

The complex coefficients $\boldsymbol{F}_n^{\Sigma,d}$ correspond to the cyclic contact forces $\boldsymbol{f}_t^{\Sigma,d}$ that are applied to the condensed DoFs belonging to first radial line segment of a cyclic sector (Figure 5.18). In the following it will be shown how the term $\boldsymbol{f}_t^{\Sigma,d}$ has to be evaluated.

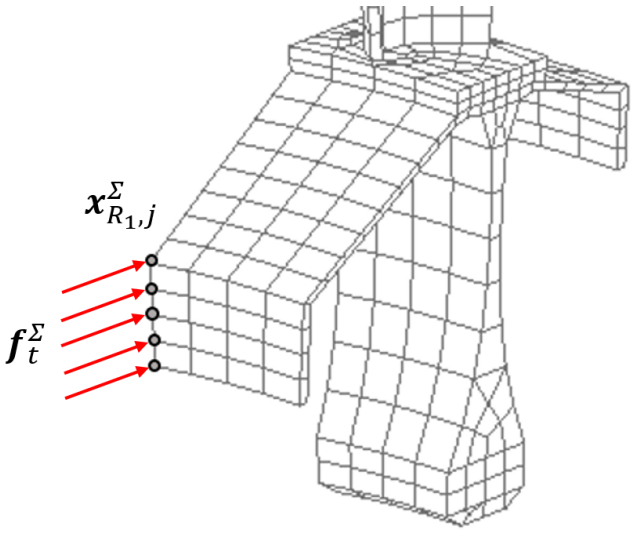

Fig. 5.18 Cyclic interface contact forces exciting the cyclic interface DoFs at the first radial line segment.

As explained in Chapter 4, $\boldsymbol{x}^{\Sigma,d}_{R_1,j}$ results from the condensation of all the sector's interface DoFs to the first radial line segment. Similarly, the cyclic contact forces $\boldsymbol{f}^{h,d}_{t,R_r}$ should be the result of a condensation process that reduces the contact forces acting on the whole sector's interface to the first radial line segment too.

Since the distribution of the contact forces at the stage's interface is harmonic with the same periodicity of the relative displacements generating it, assuming a spatial harmonics displacement of order h, the non-linear contact forces at the sector's interface can be expressed as (Figure 5.19):

$$\begin{Bmatrix} \boldsymbol{f}^{h}_{t,R_1} \\ \vdots \\ \boldsymbol{f}^{h}_{t,R_r} \\ \vdots \\ \boldsymbol{f}^{h}_{t,R_Z} \end{Bmatrix} = \begin{bmatrix} \boldsymbol{I} \\ \vdots \\ \boldsymbol{I}e^{\pm\imath(r-1)\varphi_{h_r}} \\ \vdots \\ \boldsymbol{I}e^{\pm\imath(Z-1)\varphi_{h_r}} \end{bmatrix} \boldsymbol{f}^{h}_{t,R_1} \tag{5.66}$$

where φ_{h_r} is the inter-line phase angle corresponding to the harmonic index h (see Chapter 4).

The physical contact forces $\boldsymbol{f}^{h,d}_{t}$ can then be obtained by reducing the force vector of Eqn. 5.66 to the first radial line segment exactly as done for the displacements. Hence, by using the interface reduction matrix Γ_h of Eqn. 4.51 the reduced contact

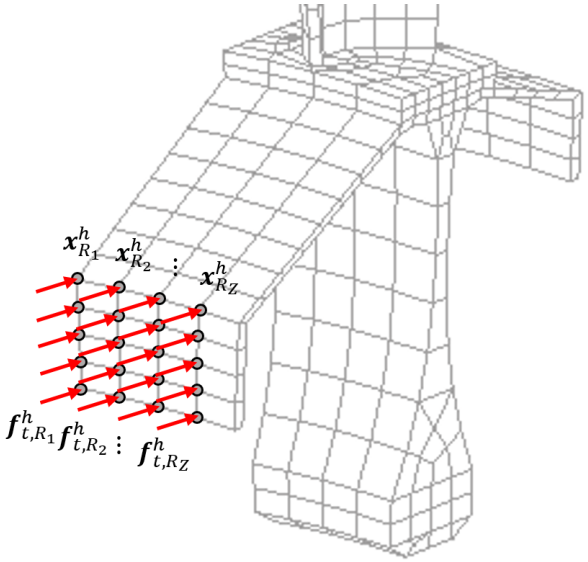

Fig. 5.19 Non-linear contact forces at the sector's interface before the condensation on the first radial line segment.

forces for the harmonic index h are given by:

$$f_t^{h,d} = \Gamma_h^T \begin{bmatrix} \boldsymbol{I} \\ \vdots \\ \boldsymbol{I}e^{\pm\imath(r-1)\varphi_{h_r}} \\ \vdots \\ \boldsymbol{I}e^{\pm\imath(Z-1)\varphi_{h_r}} \end{bmatrix} f^h_{t,R_1} =$$

$$= \begin{bmatrix} \boldsymbol{I} & \cdots & \boldsymbol{I}e^{\mp\imath(r-1)\varphi_{h_r}} & \cdots & \boldsymbol{I}e^{\mp\imath(Z-1)\varphi_{h_r}} \end{bmatrix} \begin{bmatrix} \boldsymbol{I} \\ \vdots \\ \boldsymbol{I}e^{\pm\imath(r-1)\varphi_{h_r}} \\ \vdots \\ \boldsymbol{I}e^{\pm\imath(Z-1)\varphi_{h_r}} \end{bmatrix} f^h_{t,R_1} =$$

$$= Z \cdot f^h_{t,R_1} \tag{5.67}$$

The complete set of reduced contact forces can be obtained by employing the described reduction procedure for each harmonic index collected into the set Σ.

Example

The application treated in the previous sections is now analyzed by using the multi-stage reduction technique involving cyclic sectors. In this case a preliminary *CB*-CMS reduction of the fundamental sectors was performed by retaining the interface DoFs at the medium radius of the flange, one active DoFs for the force application and 20 fixed-interface normal modes. Then, a further interface reduction of both cyclic sector was carried out for all the harmonic indexes of Eqn. 5.52. Figure 5.20 shows the position of the master DoFs at end of the complete reduction process.

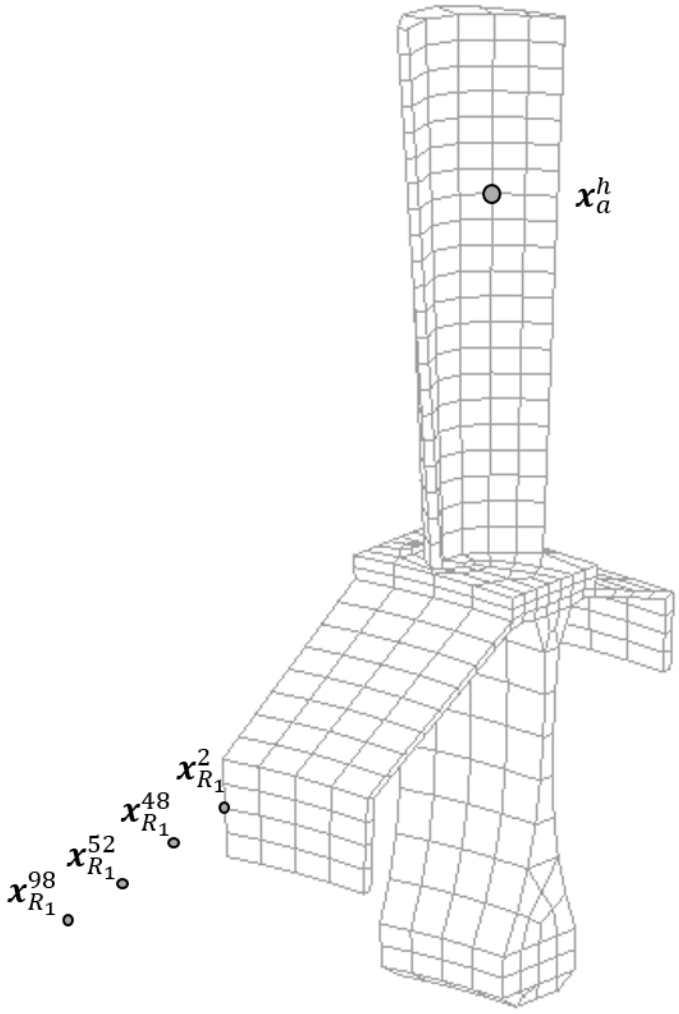

Fig. 5.20 Master DoFs location for the generic cyclic stage.

A fourth multi-stage ROM was created. Such ROM is here denoted by *IV* and its reduced vector of generalized DoFs can be expressed as:

$$\boldsymbol{x}_{CS} = \begin{Bmatrix} \Delta\boldsymbol{x}_{R_1}^{\Sigma,\rho} \\ \boldsymbol{x}_{R_1,2}^{\Sigma,\rho} \\ \Delta\boldsymbol{x}_{R_1}^{\Sigma,\theta} \\ \boldsymbol{x}_{R_1,2}^{\Sigma,\theta} \\ \boldsymbol{x}_{R_1}^{\Sigma,z} \\ \boldsymbol{x}_{a_1}^{h} \\ \boldsymbol{x}_{a_2}^{h} \\ \eta_{k_1}^{h} \\ \eta_{k_1}^{h} \end{Bmatrix} \tag{5.68}$$

where:

$$\boldsymbol{x}_{R_1,j}^{\Sigma,d} = \begin{Bmatrix} \boldsymbol{x}_{R_1,j}^{2,d} \\ \boldsymbol{x}_{R_1,j}^{48,d} \\ \boldsymbol{x}_{R_1,j}^{52,d} \\ \boldsymbol{x}_{R_1,j}^{98,d} \end{Bmatrix} \tag{5.69}$$

The size of the multi-stage ROM$_I$, ROM$_{II}$, ROM$_{III}$ and ROM$_{IV}$, and the corresponding number of non-linear EQM are compared in Table 5.9

Table 5.9 Size of the multi-stage ROM *I*, *II*, *III* and *IV*, and corresponding number of non-linear EQM.

Multi-stage ROM	# DoFs	# non-linear EQM
ROM$_I$	1900	600
ROM$_{II}$	1700	400
ROM$_{III}$	740	32
ROM$_{IV}$	66	8

By assuming a modal damping ratio of $\zeta = 0.005$, the structural damping matrix $\boldsymbol{C}_{IV}$ was obtained exactly as done for $\boldsymbol{C}_I$. Considering again the same contact parameters and excitation amplitudes adopted in the previous cases, new forced response calculation were performed and the results compared to those of Figure 5.11 and 5.12.

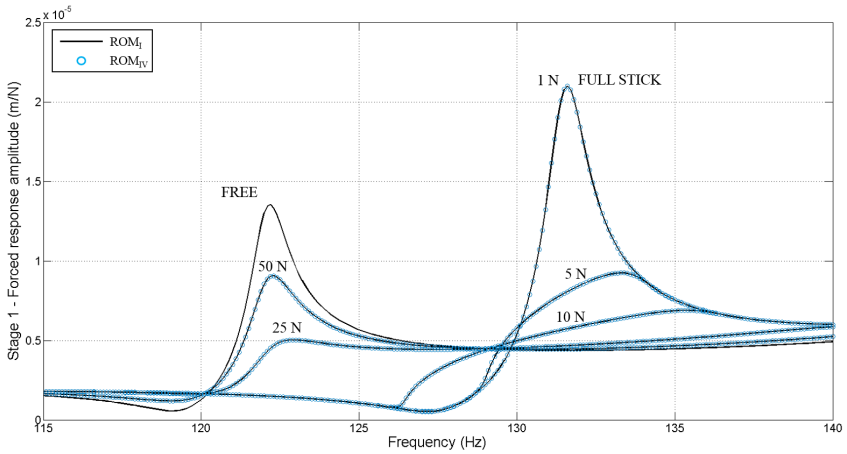

Fig. 5.21 Comparison of forced response calculation obtained from the ROM$_I$ and ROM$_{IV}$. The plots refer to displacements detected at the blades of the stage 1.

Figure 5.21 and 5.22 show a perfect match between the non-linear forced response calculations performed on both ROMs. Besides confirming the goodness of the multi-stage ROM technique applied to cyclic stages (see section 4.5), these results give further confidence in the approximation of the contact interface displacements by means of few harmonic basis functions.

Performing non-linear forced response calculation on the multi-stage ROM$_{IV}$ appears much more convenient than using all the previous ROMs. Besides the smaller number of DoFs involved in the calculations, the performance of the ROM$_{IV}$ can be better appreciated by comparing the computational times with the other ROMs (Table 5.10).

Table 5.10 Average time for the non-linear forced response calculation: comparison between the multi-stage ROM$_I$, ROM$_{II}$, ROM$_{III}$ and ROM$_{IV}$

Multi-stage ROM	Time (s)
ROM$_I$	2700
ROM$_{II}$	890
ROM$_{III}$	60
ROM$_{IV}$	8

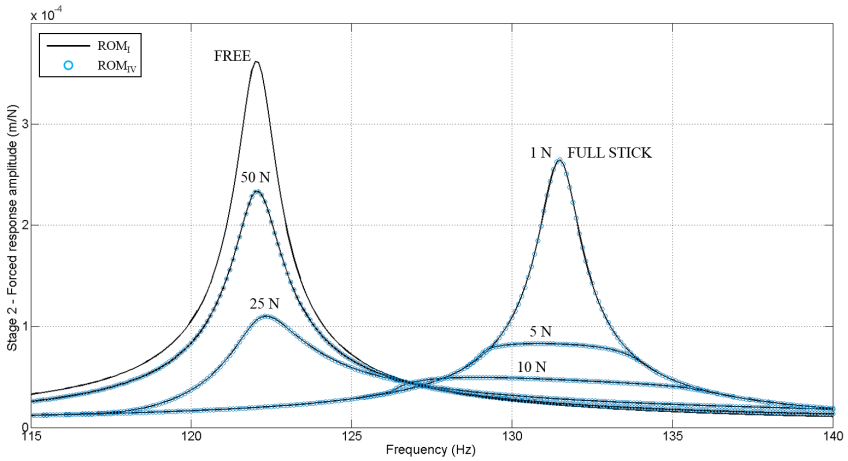

Fig. 5.22 Comparison of forced response calculation obtained from the ROM$_I$ and ROM$_{IV}$. The plots refer to displacements detected at the blades of the stage 2.

5.8 Discussion

In this Chapter the ROM techniques developed in Chapter 4 were combined with a macroslip contact model in order the efficiently predict the forced response of a multi-stage bladed disk with friction contact at the inter-stage boundary.

The approaches proposed were validated on a simplified model composed by two stages having the same number of sectors ($N = 50$) and compatible meshes at the interfaces. Although this second condition does not prevent the use of the multi-stage ROM techniques, it was necessary to calculate the benchmark forced responses by using the *CB*-CMS ROMs of the two stages. In fact, all the interface DoFs were retained as master in the reduction, so that classic node-to-node contact elements could be easily applied.

For all the cases analyzed the multi-stage non-linear dynamics was predicted under the following hypotheses:

1. The traveling waves exciting the stages have the same Engine Order;
2. The multi-stage ROM is obtained from the ROMs of the single-stages by enforcing the compatibility conditions just in the axial direction;
3. The steady state displacements and the non-linear contact forces are approximated with their 1^{st} order Fourier coefficients (SHMB).

Although some of them could be interpreted as restrictive of the current practice, they are based on practical considerations on the bladed disks dynamics and the bolted flange joints' working principle. However, the combination between the contact models introduced in section 5.3 and the multi-stage reduction techniques developed in Chapter 4, can be exploited also for the analysis of lap joints featuring circular geometry. In such cases the joint's non-linear dynamics may be more complex than that described for multi-stage bladed disks, since separation of the contact interfaces may occur. From a numerical point of view the prediction of such non-linear behavior requires to relax at least the hypotheses 2 and 3, without substantially modifying the reduction approach described in the sections 5.5, 5.6 and 5.7:

- Relaxing hypothesis 2 coincides to adopt the same approach used in the example of section 5.5, where the contact model with normal load variation was employed. In that case the compatibility condition between the stages' ROMs in the axial direction was not present and the non-linear contact forces were evaluated in the θ, ρ and z direction;
- When strong non-linearities are present, i.e. when lift-off occurs at the joint's contact interface, the steady-state displacements and non-linear contact forces cannot be satisfactorily approximated by their first order Fourier component. In such cases the *Multi-Harmonic Balance Method* has to be used, since the nature of the mentioned quantities requires a multi-harmonic description.

Relaxing both hypotheses has "just" the effect to increase the non-linear partition of the EQM and the computational costs associated to their numerical resolution.

Different is the case of hypothesis 1. As shown in the previous sections, the fast evaluation of the non-linear forced response of a bladed disk assembly requires at least using the *Single-Harmonic Balance Method*. According to this approach the set of non-linear differential EQM in time domain can be turned into a set of non-linear algebraic equations, by approximating the steady-state displacements and contact forces with their first order Fourier components. However, the contact forces are evaluated in the time domain, due to the fact that the contact models just requires as input the time history of the non-linear displacements. This means that an arbitrary time discretization of the non-linear displacements is needed before being processed by the contact model. But the number of time instants of such discretization is strictly

related to the duration of the oscillation period characterizing the response. In this regards two different scenarios may occurs:

1. *The traveling waves exciting the stages have the same Engine Order*: the nodes at the contact interfaces experience the same number of oscillations during the multi-stage rotation period T. In the simplest case this number coincides to EO, and the contact forces can be evaluated by just considering non-linear displacement into the period of the elementary oscillation $T_e = T/\mathrm{EO}$;

2. *The traveling waves exciting the stages have different Engine Orders*: the nodes at the contact interfaces experience a different number of oscillations during the system's rotation period T. In this case the contact forces have to be computed by considering the evolution of the non-linear displacement during the whole period T (the system's response repeats equal to itself after T).

By assuming the same period T for the two cases, especially for large EO excitations, the number of time instants used to satisfactorily discretize the non-linear displacement and contact forces in the second case is much larger than in the first one. For this reason the evaluation of the Fourier coefficients of the non-linear contact forces for each pair of nodes in contact becomes extremely expensive from a computational point of view, and numerical time integration may represent a valid alternative.

In this study the bolted flange joint was considered as a possible source of friction damping that appears beneficial in terms of attenuation of the blades' response. In this regard, the damping was supposed being generated by the relative displacements occurring at the inter-stage boundary, without explicitly considering the presence of the bolts. However, it is reasonable to considerate their non-linear behavior as one with that of the flange. In fact, possible friction phenomena may also occur at the interfaces bolt's head-flange and bolt's nut-flange.

By applying the mentioned contact models and assuming an uniform pressure distribution along the flange, the expected non-linear behavior of the joint come out. The same typical non-linear behavior was then obtained by employing different mathematical approaches without any significant differences in terms of predicted resonance frequency and blades' vibration amplitude. However, strong advantages can be found when the multi-stage ROM techniques are used. In those cases, the time spent for the prediction of a forced response of the system is much lower than that required by classic approaches.

The example developed throughout this Chapter shows identical non-linear forced responses for the both multi-stage reduction techniques. Such results do not exhibit any significant approximation with respect the benchmark forced responses obtained by using the Craig-Bampton model of each stage. However, it should be pointed out that the use of the multi-stage reduction technique working on fundamental sectors allowed non-linear forced response calculation almost 9 times faster than the other multi-stage reduction technique (8 s vs 60 s), and 340 times faster than the classic approach based on the Craig-Bampton method.

Chapter 6

Blade Tip Timing Measurements on Bladed Disks

6.1 Introduction

The main goal of the methods described in the previous Chapters concerns the fast prediction of the multi-stage bladed disk dynamics when friction phenomena at the inter-stage boundary occur. The results obtained actually confirm the accuracy of such methods that can be used as powerful tools helping in a robust and safety design. However, friction is just one of the several aspects that have to be considered in the design of a complex mechanical system. In fact, the causes leading to strong resonances of such structures are numerous and nowadays numerical codes dealing with all of them are either limited or not reliable. Therefore, the commonest approach used to study the dynamics of component even representing just a part of a complex turbomachinery requires the integration of numerical and experimental tests.

As already discussed in Chapter 1 turbomachinery blades undergo various types of vibrations during operation, which may reduce their fatigue life by increasing the risk of crack formation and the occurring of costly damages. As mentioned in [61], "High Cycle Fatigue (HCF) is a major cost, safety, and reliability issue for gas-turbine engines. For example, in 1998 it was estimated by the U.S. Air Force that about 55% of fighter jet engine safety Class A mishaps (over 1 million in damage or loss of aircraft) and 30% of all jet engine maintenance costs were due to HCF".

Due to the nature of rotating machinery, real-time monitoring of blades' vibration is an extremely hard task and innovative measurement systems to comply such challenge are still being developed. In this frame the *Blade Tip-Timing* (BTT) is presently the most promising measurement technique for blade health monitoring. The technique employs a set of non-intrusive sensors mounted on the casing that detect the passing time or *Time-of-Arrival* (ToA) of every single rotating blade [62, 63] (Figure 6.1).

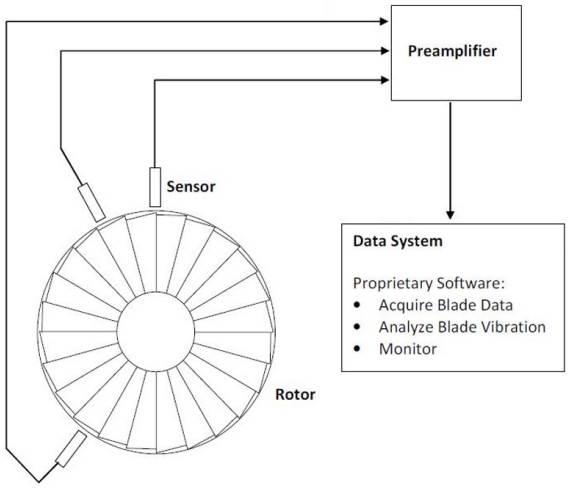

Fig. 6.1 Schematic setup of a Blade-Tip Timing measurement system.

The working principle of this method lie on the analysis of the differences between the actual and theoretical ToA. In particular, in absence of vibration and in case of constant rotation speed, a certain sensor would detect the blade passages with a constant time interval ΔT between them. Whereas, when the blade vibrates such intervals fluctuate since the actual ToA depends of the blade's vibration amplitude (Figure 6.2).
By knowing the radial position of the measurement point on the blade, the rotation speed of the rotor and the Δt between the actual and theoretical ToA, the blade vibration amplitude can be found.

Being a *non-intrusive* measurement system, the BTT has a lot of advantages over the standard method used for blade vibration monitoring:

- Blade vibrations are detected without any mechanical interaction with the sensors, which can be of optical, capacitive or eddy-current type. In particular, the sensors are located within the casing, around the disk without interfering

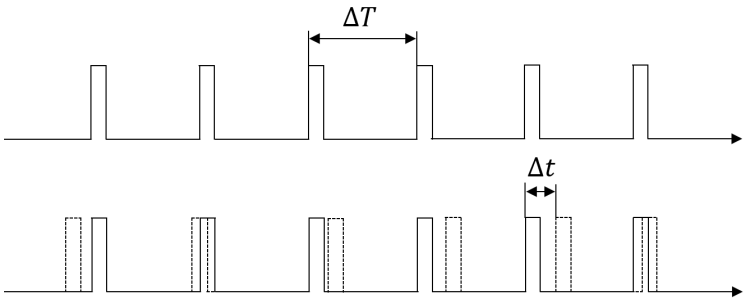

Fig. 6.2 Detection of the time interval Δt between the theoretical (upper plot) and actual (lower plot) ToA.

with the flow path. This means that neither the air flow nor the disk dynamics are effected during measurements. On the contrary, contact measurement systems like strain gauges have to be stuck on the blade's airfoil, a condition that unavoidably modifies the blade's dynamics.

- The other crucial advantage of using BTT is that every sensor is being used to detect vibrations on every blade. Since all the blades are monitored it can be possible to identify whether a blade is vibrating more than the others as in the case of typical mistuning problems. This particular feature does not hold when strain gauges are used. In fact, they are typically mounted on few blades since their application on a bladed disk with more than hundred blades is unfeasible for time and cost reasons. Therefore, only the (affected) dynamics of a few blade can be measured, while all the others are completely missed.

Although the BTT has recently become a typical industry equipment for bladed disks vibration surveys, the type of sensors, the way how they are positioned around the disk and the algorithm used for data post-processing are still non-standard. For this reasons, the reliability of such system has to be proved for different operation conditions by the comparison with other well-established measurement techniques like strain gauges.

Dynamic tests aimed at proving the accuracy of a latest generation BTT system were therefore carried out at the *LAQ Aermec* laboratory of the Politecnico di Torino in collaboration with *GE Avio Aero*. In this frame an extensive experimental campaign was performed on two dummy blisk. The first have the simple geometry of a flat plate and it is characterized by bending vibration modes of the blades in the disk axial direction. The second was designed in order to simulate a dynamic behavior

closer to that of a real turbine disk where the blades are connected to each other at the tips by an outer ring. The performance of the BTT technique was then tested not only for the evaluation of the maximum vibration amplitude and corresponding resonance frequency of each single blade, but also for the identification of the deformed shape of the measured mode.

Two key features are described throughout the Chapter. The first concerns the validation on both blisk of the BTT measurements performed by using a new sensors placement named as *beam shutter* configuration. This sensors arrangement is particularly suitable for measurements on shrouded bladed disks and requires only one set of optical laser sensors working both as senders and receivers of the reflected laser beam. The BTT measurements were then validated by comparison with those acquired by the strain gauges that were glued only to few blades. The second issue concerns the proposal of an original method to identify, from the response data of all the blades, the nodal diameter number characterizing the dominant response mode of the disk. The method does not work when the mistuning is so large to completely destroy the ideal cyclic symmetry of the disk, but appears reliable when a small mistuning is present. It is proved, in fact, that a small mistuning pattern induces a particular modulation of the blades response amplitude. It is shown in different cases, both experimental and simulated, that the number of wave-length (WLs) of this modulation is related to the number of the nodal diameter of the dominant response mode of the disk.

6.2 The Spinning Test Rig

The two dummy disks were tested in a laboratory spinning rig at room temperature under vacuum conditions [64]. As shown in Figure. 6.3 a) the test rig has a vertical axis with two cylindrical protective structures (1 and 2) coaxial to the rotating shaft that is positioned under the floor. At the top of the shaft a flange allows the disk accommodation 3). The cylinder 1 also supports two static rings (Figure 6.3 b)): the ring 1 keeps in a fixed position a set of permanent magnets that are used to excite the rotating disk, while the ring 2 holds the BTT laser sensors.

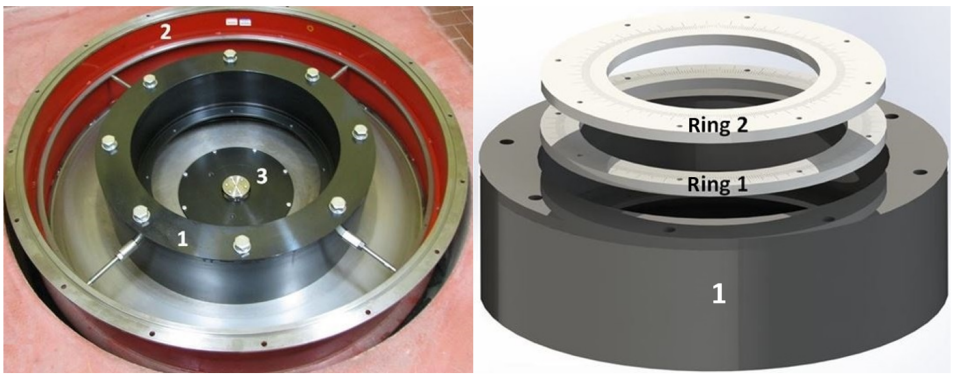

a) b)

Fig. 6.3 The spinning rig a) and the supporting rings for the magnets and laser sensors positioning b).

6.2.1 The Dummy Disks

The dummy disk 1 (Figure 6.4) is an aluminum disk with a simple geometry of a flat plate where each blade has the shape of a cantilever beam. The dummy disk 1 has 12 identical blades whose length and width are 150 mm and 25 mm respectively. The thickness and the outer diameter of the disk are 5 mm and 400 mm. A cylindrical magnet with a 5 mm diameter and 5 mm height is glued in a housing drilled at the tip of each blade.

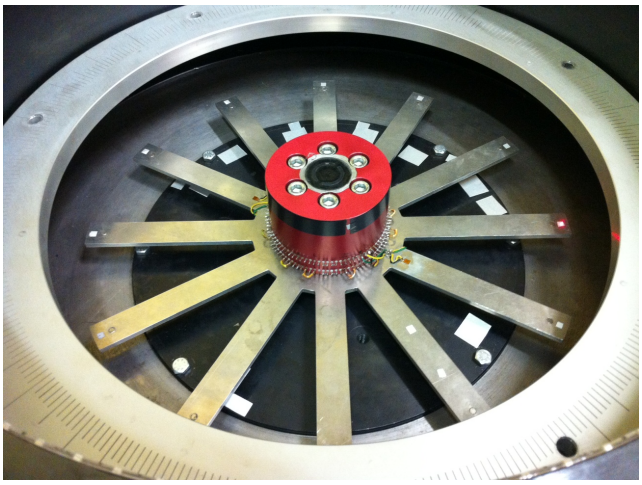

Fig. 6.4 The dummy disk 1 within the spinning test rig.

The dummy disk 2 (Figure 6.5) was designed to have a dynamic behavior closer to a real turbine disk. The blades are connected to each other at the tips by an

outer ring as in the case of shrouded bladed disks. It is a single piece made of the ferromagnetic steel AISI 460, in order to allow the magnetic interaction between the permanent magnets and the blade airfoils. It has 32 real profiled blades whose length and aspect ratio are respectively 100 mm and 7.31. Its disk outer diameter and axial height are 630 mm and 20 mm.

Fig. 6.5 The dummy disk 2 within the spinning test rig.

6.2.2 The Excitation System

The excitation system in the spinning test rig uses cylindrical permanent magnets (diameter 18 mm, height 10 mm, grade N52). The magnets are mounted in equally spaced positions on the static ring facing the rotating dummy disk (the Ring 1 in Figure 6.3 a)). A graduated scale impressed on the ring 1 upper surface is used to fix the magnets at the right angular positions [64].

Several supporting rings with different inner diameters are available in order to guarantee the correct radial positioning of the permanent magnets. Each magnet is glued on the tip of a screw that allows the regulation of the axial gap with respect to the disk blades (Figure 6.6).

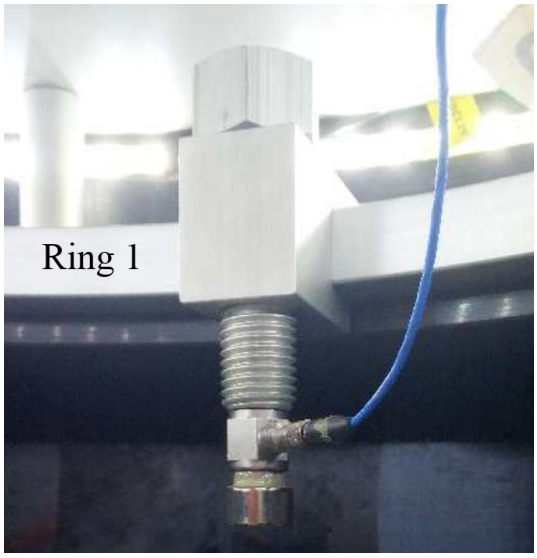

Fig. 6.6 Fixed magnet and load cell exciting the rotating disk.

Six of the magnets were instrumented with force transducers for the measurement of the axial force exerted on the blades during the tests [64].

The number of magnets used in a specific test must be equal to the main engine order (EO) characterizing the excitation force that should be simulated. The main engine order EO_m^1 can be defined as the fist not-null harmonic index resulting from the Fourier transform of the excitation force. In general for m equally spaced magnets, the EO pattern exciting the disk is defined as follows:

$$EO_m^i = i \cdot m, \qquad \forall\, i = 1,2,3,\ldots \tag{6.1}$$

For example, if 3 is the number of equally spaced magnets exciting the disk, the force profile acting on each blade is that of Figure 6.7 a). The harmonic content of such profile is shown in Figure 6.7 b), where some EO excitation are plotted. According to the previous description the main harmonic index is $EO_m^1 = 3$, while the less important harmonic contributes have EO defined Eqn. 6.1 for $i \neq 1$. As already explained in Chapter 2 each harmonic function may excite a mode shape having h nodal diameters when its EO satisfy Eqn. 2.70:

$$EO = z \cdot N \pm h, \qquad \forall\, z \in \mathbb{N}^* \tag{6.2}$$

where N_s is the number of blades and z is a positive integer.

The disk's excitation frequency f_{exc} can be calculated as:

$$f_{exc} = \frac{EO \cdot n}{60} \tag{6.3}$$

where the rotation speed n and f_{exc} are expressed respectively in rpm and Hz. From Eqn. 6.3 it can be noted that for increasing EO values the bladed disk can be excited at the same excitation frequency f_{exc} for lower values of the rotation speed n.

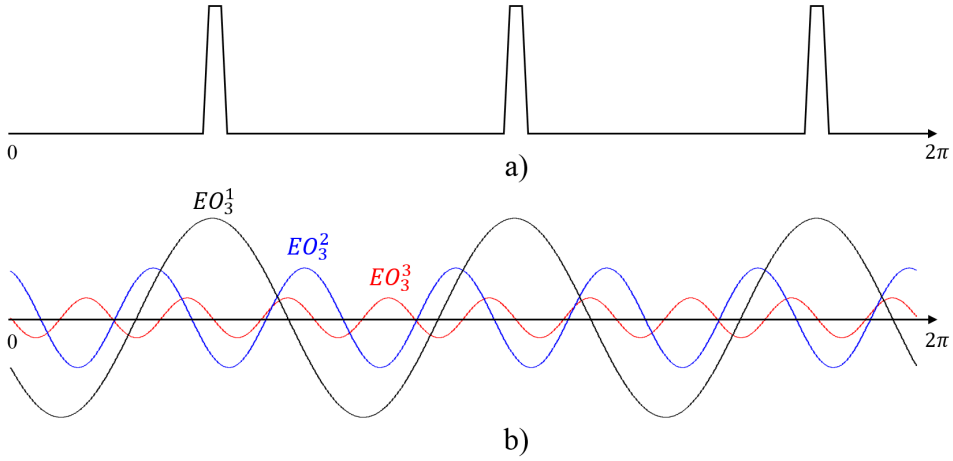

Fig. 6.7 Magnetic force profile acting on each blade a) and its harmonic content b).

6.2.3 The Strain Measurement System

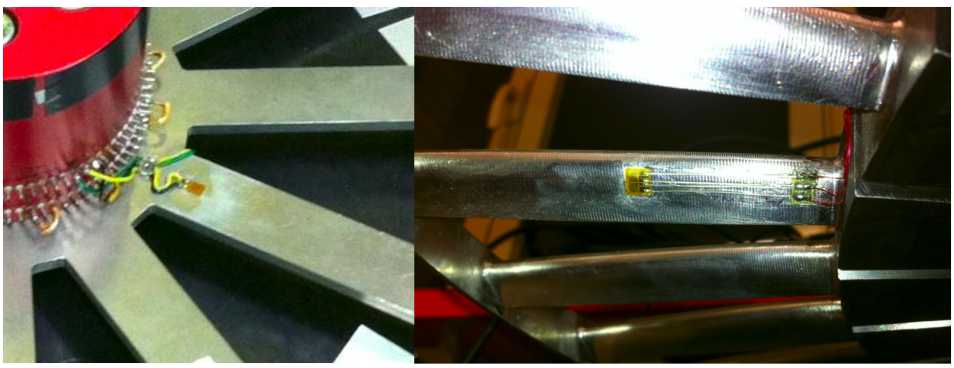

Fig. 6.8 Strain gauge at the blade root of the dummy disk 1 a), strain gauge at the back of the airfoil of a dummy disk 2 blade b).

The two dummy disks were instrumented by means of strain gauges. For both the disks the identification of the strain gauge positions came out from their FE modal analyses in cyclic symmetry conditions. Areas of high strains and low strain gradients were identified as the best locations for strain gauges. The strain gauges signals were acquired through a telemetry system. For the dummy disk 1 the strain gauges were attached at the two sides of the blade root (Figure 6.8 a)). This position was chosen in order to measure the Out-Of-Plane (OOP) bending mode (1F) belonging to its first modal family. The strain gauges adopted are composed by a single grid of dimension 1.52 mm $\times$ 3.05 mm, with a grid resistance of 350 Ω. The two grids at the two sides of the blade were connected together with a half bridge. For the dummy disk 2 the strain gauge was applied on the back of a blade airfoil (Figure 6.8 b)). The selected area was not affected by strain gradients for both the flap-restricted (1FR) and the torsional (1T) mode shapes belonging to its second and third modal family respectively (Figure 6.9).

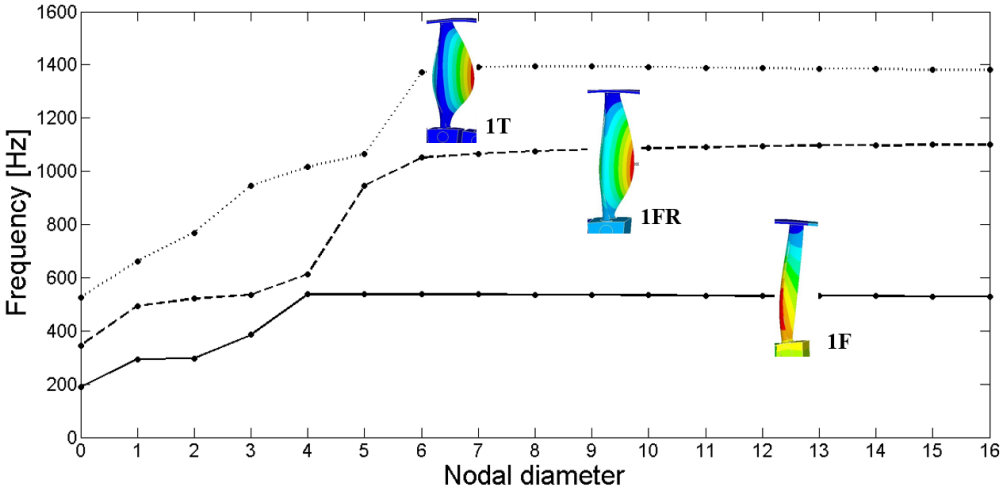

Fig. 6.9 FreND diagram for the dummy disk 2.

The strain gauges was a tee rosettes (grid resistance 350 Ω) composed by two separate grids (1.52 mm $\times$ 1.78 mm) with perpendicular axes that were connected together with a half bridge. During the dynamic tests the strain gauges signals were sampled with a sampling frequency of 8192 Hz and then post-processed using the following parameters (Figure 6.10):

- time width of each bin of samples for FFT analysis: 4 s.
- percentage of overlap between bins: 50 %.

- Ramp speed: 18.75 rpm/s.

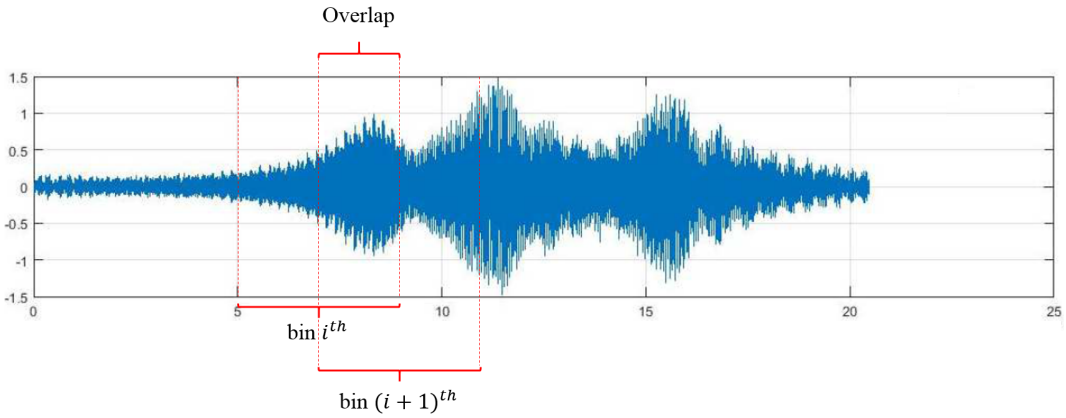

Fig. 6.10 Example of strain gauge signal and representation of the bins of samples.

The strain gauges measurement chain was verified by means of static tests on the dummy disk 1, which consisted in measuring the bending strains at the blade root due to a set of calibrated masses positioned on its free end. Three static tests were performed for three masses having different weights. The measured strains were compared to the corresponding numerical quantities determined by means of a static FE analysis. The results listed in Table 6.1 show the reliability of the strain gauges that can be used as a reference measurement system for the validation of the BTT technique.

Table 6.1 Experimental and numerical strains for the static tests on the dummy disk 1.

Mass	Experimental strain	Numerical strain
0.76	130.23	130.19
1	169.30	169.27
1.99	342.32	342.25

Although the static measurement was repeated, only negligible differences were found between the experimental strains since the test showed high repeatability.

6.3 The Blade Tip-Timing Measurement System

The BTT technique employs a set of non-contact sensors mounted on the casing and facing the blades of a rotating bladed disk[63, 65, 62]. This technique is based on the measurement and the subsequent analysis of the difference between the *Times-of-Arrival* (ToA) of each vibrating blade passing by the sensors and the theoretical ToA of the non-vibrating blade [63]. From the post-processing of the collected ToA the dynamic properties of each blade, i.e. the resonance frequencies, the vibration amplitudes and the modal damping can be identified. The BTT has two main advantages over the strain gauges:

- It is a non-contact measurement system that does not affect the dynamic behavior of the blades.
- It allows the measurement of all the blades of the disk, while the strain gauges are usually attached only to few blades.

The BTT system adopted in this study is a latest generation system that uses optical laser sensors. For the dummy disks 1 and 2 all the tests were performed by employing five sensors for the direct detection of the blades ToA and an additional sensor (*1/rev* sensor) measuring the rotational speed and representing the reference for all the others. The signal from the *1/rev* sensor was acquired by both the BTT and the strain gauges systems in order to synchronize the measured blade vibrations signals during the post-processing operations.

6.3.1 The Beam Shutter Method and the Sensor Positioning

The standard measurement approach for the BTT method is based on a set of sensors that are positioned along the radial direction in order to detect the ToA at the blade tip where the maximum vibration amplitude occurs. Although this sensor positioning is particularly suitable for disk with tip free blades, it is impracticable for shrouded bladed disks. In fact, due to the presence of shrouds the laser sensors are not able to capture the motion at the tips. For this reason a new sensor configuration called *beam shutter* was tested on the two dummy disks introduced in section 6.2.1. The sensors positioning adopted for the two cases are presented in Figure 6.11 and 6.12.

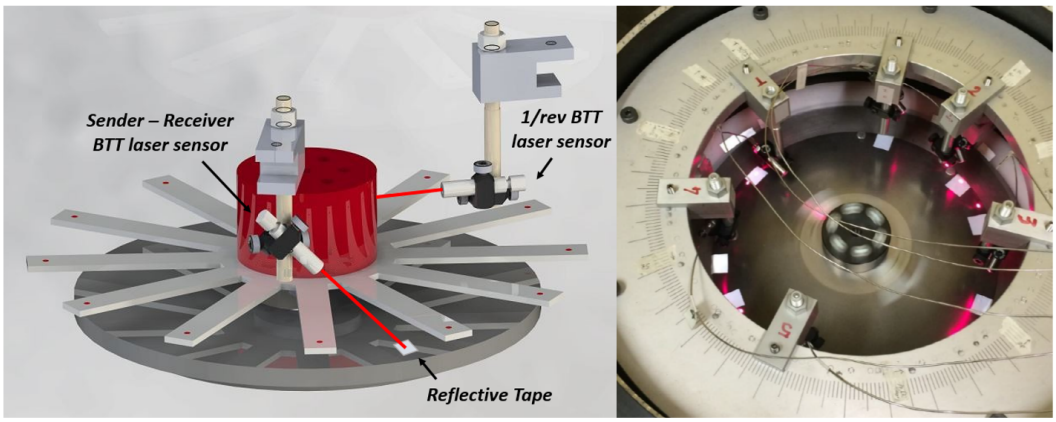

Fig. 6.11 Beam shutter configuration for the dummy disk 1.

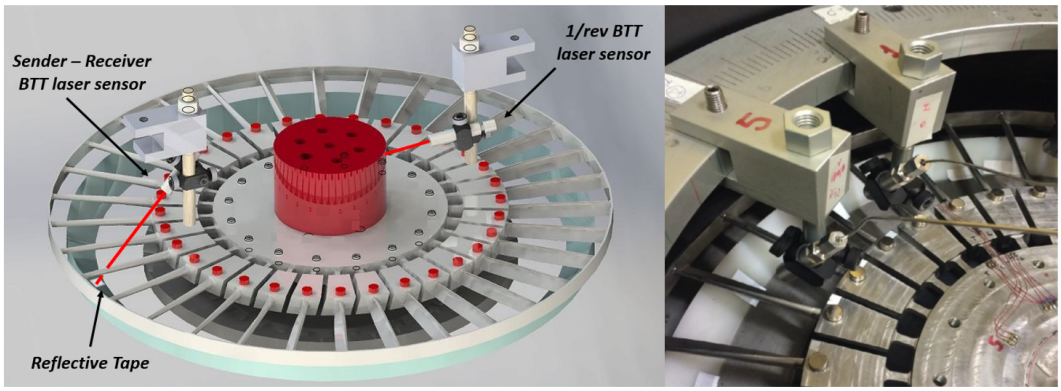

Fig. 6.12 Beam shutter configuration for the dummy disk 2.

While the application of Figure 6.11 tested the capabilities of the beam shutter configuration when the OOP vibration modes of the blades have to be detected (see section 6.4), the case of Figure 6.12 clearly shows the need of measuring the vibrations at the blade trailing and leading edges since a direct detection of the vibrations at the blade tips cannot take place.

One of the attempts of using the BTT method to measure the blade vibrations at the trailing and leading edges makes use of the *beam interrupt* configuration as shown in [66], where two sets of laser sensors, one acting as a sender of the laser beam and the other as a receiver , were employed within the flow path of a working engine. The configuration proposed in the present paper would overcome this inconvenient because in the case of real applications only one set of sender-receiver optical laser sensors are embedded in only one probe (Figures 6.11 and 6.12). Since a smaller

number of sensors is involved in the measurements, the beam shutter appears more robust and less invasive than the beam interrupt configuration.

For both the applications each sensor was mounted above the disk and produced a laser beam that was collimated through a lens on a reflective tape stuck on a fixed surface beneath the disk. During the disk rotation the passing blade acts as a shutter, blocking the returning light towards the sender-receiver sensor. The system was set up in order to direct the laser beam towards the leading and trailing edge locations where the blade experienced the maximum vibration amplitudes. The optical sensors and the reflective tape were employed in measurements performed without any significant temperature variation from the room temperature. The maximum temperature at which the laser probes can work is 315°C.

The sensors were installed at the same distance from the disk center and their relative circumferential position was chosen in both the cases by means of an optimization tool, which avoids the aliasing effect in the identification of the traveling wave mode shape characterizing the vibrating disk. The optimization tool requires as input the number of sensors, the expected engine orders and the number of blades.

6.3.2 The Blade Tip-Timing data Post-Processing

The data were post-processed by using a fitting method called *Circumferential Fourier Fit* (CFF)[1] [67, 68].

This method is particularly useful for cases where the resonance peaks of a bladed disk forced response are not well-separated (condition typical of mistuned phenomena). The method requires three or more sensors installed at the same chord-wise position. Assuming a certain response order, corresponding to the selected EO, for each averaged rpm a sinusoidal wave is fitted to the data [69–72], in other words, each blade is assumed to vibrate according to a sinusoidal wave. The equation of the blade motion seen by the k^{th} sensor is:

$$y_k(\omega) = c(\omega) + A(\omega) \cdot \sin\left[2\pi \cdot EO \cdot f \cdot t + \Phi(\omega)\right] = \tag{6.4}$$

[1] An exhaustive comparison between three different BTT algorithms for synchronous vibration analysis can be found in [67]. Here the Auto-Regressive, Circumferential Fourier Fit and Bayesian regression methods are compared on simulated BTT data in terms of accuracy in estimating blades' resonance frequency and response amplitude.

where $A(\omega)$, $\Phi(\omega)$ and $c(\omega)$ are the vibration amplitude, the phase and the blade's static position between the *1/rev* sensor and the generic k^{th} sensor at a certain frequency ω (Figure 6.13).

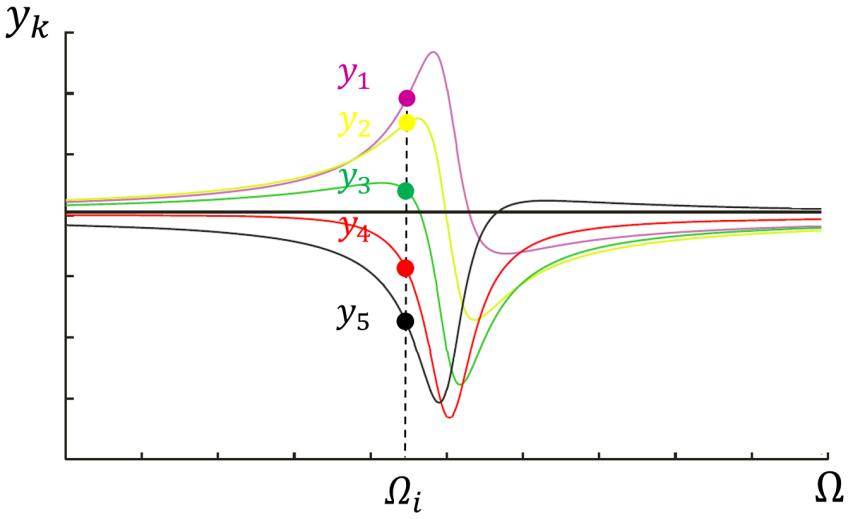

Fig. 6.13 Example of data collected by the sensors.

The k^{th} sensor sees the passing blade at the following time instant [62]:

$$t = \frac{\theta_k + 2\pi n_{rev}}{2\pi f_{shaft}} \tag{6.5}$$

where θ_k is the angular position of the k^{th} sensor, n_{rev} is the number of blade's revolution and f_{shaft} is the frequency associated to the shaft's rotation speed Ω_{shaft}. By substituting Eqn. 6.5 into Eqn. 6.4 $y_k(\omega)$ becomes:

$$y_k(\omega) = c(\omega) + A(\omega) \cdot \sin\left[EO \cdot \theta_k + \Phi(\omega)\right] \tag{6.6}$$

By assuming a number of sensors $K \geq 3$, for the i^{th} frequency ω_i, Eqn. 6.6 can be extended to all the sensors and written in matrix form as follows:

$$\begin{Bmatrix} y_1(\omega_i) \\ y_2(\omega_i) \\ \vdots \\ y_k(\omega_i) \\ \vdots \\ y_K(\omega_i) \end{Bmatrix} = \begin{bmatrix} 1 & \sin(EO \cdot \theta_1) & \cos(EO \cdot \theta_1) \\ 1 & \sin(EO \cdot \theta_2) & \cos(EO \cdot \theta_2) \\ \vdots & \vdots & \vdots \\ 1 & \sin(EO \cdot \theta_k) & \cos(EO \cdot \theta_k) \\ \vdots & \vdots & \vdots \\ 1 & \sin(EO \cdot \theta_K) & \cos(EO \cdot \theta_K) \end{bmatrix} \begin{Bmatrix} c(\omega_i) \\ A(\omega_i)\cos\left[\Phi(\omega_i)\right] \\ A(\omega_i)\sin\left[\Phi(\omega_i)\right] \end{Bmatrix} =$$

$$= \boldsymbol{y}(\omega_i) = \boldsymbol{M} \begin{Bmatrix} \chi(\omega_i) \\ \delta(\omega_i) \\ \gamma(\omega_i) \end{Bmatrix} \tag{6.7}$$

Eqn. 6.7 can be solved in a least square sense in order to minimize the error ε defined as:

$$\varepsilon = \boldsymbol{M} \begin{Bmatrix} \chi(\omega_i) \\ \delta(\omega_i) \\ \gamma(\omega_i) \end{Bmatrix} - \boldsymbol{y}(\omega_i) \tag{6.8}$$

where $\boldsymbol{y}(\omega_i)$ is the exact solution.

The amplitude and phase of the blade at the i^{th} frequency can be computed by using the following relationships:

$$\Phi(\omega_i) = \tan^{-1}\left[\frac{\gamma(\omega_i)}{\delta(\omega_i)}\right] \qquad A(\omega_i) = \frac{\delta(\omega_i)}{\cos\left[\Phi(\omega_i)\right]} \tag{6.9}$$

The amplitude $A(\omega)$ can then be plotted versus the rotation speed and the forced response of the blade be obtained for the assumed value of EO (Figure 6.10).

6.4 The Results Comparison Method

In order to verify the accuracy of the BTT method, the vibration parameters identified by the BTT were compared to those detected by the strain gauges in conjunction to the telemetry system. Simultaneous measurements with the BTT and the strain gauges systems were performed for a certain set of vibrating modes characterizing the dummy disks. While the comparison in terms of resonance frequencies is straightforward and requires a fast data processing, the comparison in terms of vibration amplitudes is a more demanding task. Indeed, it requires a preliminary FE modal analysis of the disks, since the strain gauges system measures strains (ε_{SG}), while the BTT measures displacements (u_{BTT}).

By the FE model the parameter $K_{mod} = u_{mod}/\varepsilon_{mod}$ can be calculated, where:

- u_{mod} is the modal displacement of the node corresponding to the laser position on the blade in the same direction of the displacement detected by the BTT.

- ε_{mod} is the modal strain in the area corresponding to the strain gauges position in the same direction of the strain detected by the strain gauges.

The same parameters can be defined for the physical measured quantities u (displacement of the blade at the BTT laser position) and ε (strain at the strain gauges position) $K_{phy} = u/\varepsilon$. Since the two disks can be considered linear and their responses give well separated modes, the following relationship should be satisfied:

$$K_{phy} = K_{mod} \quad \Rightarrow \quad \frac{u}{\varepsilon} = K_{mod} \tag{6.10}$$

The displacement of the blade corresponding to the strain measurement from Eqn. 6.10 can be determined as:

$$u_{SG} = K_{mod} \cdot \varepsilon_{SG} \tag{6.11}$$

Since the FE model was previously tuned by the strain gauge measurements (see Table 6.1) the parameter u_{SG} is considered as reference for the displacement value measured by the BTT system u_{BTT}.

6.5 Results on the Dummy Disk 1

In order to predict the natural frequencies and the mode shapes a FE dynamic calculation in cyclic symmetry conditions was performed. In Figure 6.14 a) the natural frequencies of the dummy disk 1 are plotted against the respective NDs (FreND diagram) resulting in the first modal family called 1F. Each black circle in Figure 6.14 a) refers to an OOP bending mode of the blade when the disk vibrates according to a certain ND. From the numerical Campbell diagram in Figure 6.14 b) the rotational speeds at which the resonances occur can be estimated. The modes corresponding to ND = 5 and ND = 6 were chosen to be tested since they represent the different cases of *rotating* and *standing* mode shapes respectively [10]. Furthermore, in order to avoid high operation speeds the mode with $h = 6$ was excited by a harmonic force with EO = 6 at 1951 rpm, while the mode with $h = 5$ was excited by a harmonic force with EO = 7 (Eqn. 6.2) at 1356 rpm instead of EO = 5 at 1910 rpm.

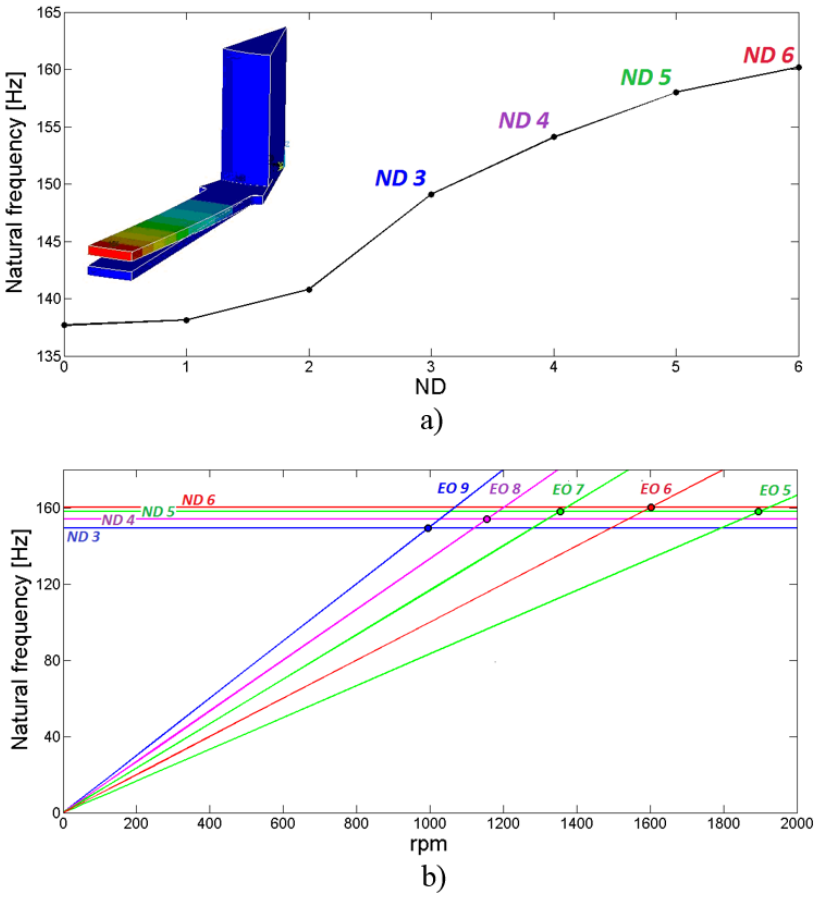

Fig. 6.14 Numerical FreND diagram for the dummy disk 1 a), numerical Campbell diagram for the dummy disk 1 b).

6.5.1 Displacement Measurement with the Blade Tip-Timing

The dummy disk 1 is excited in order to have OOP vibrations of the blades (the blade vibrates along the axial direction). In order to operate in the beam shutter configuration in case of an OOP vibration of the blades, the sensors cannot be positioned in order to have the laser beam pointing along the radial direction. Indeed, in this case there is no tangential displacement of the blade that can produce a different ToA with respect to the non-vibrating blade ToA. For this reason the sensors can be positioned as shown in Figure 6.11, where each sensor is tilted by an angle of 45° with respect to the plane containing the undeformed disk. This particular angle of the sensors allows the BTT system to detect a ToA of the blade under the sensor that is not zero as shown by the scheme of the blade interrupting the laser beam in Figure. 6.15. The time lag Δt between the detected ToA and the

theoretical ToA of the undeformed position (Δt in Figure 6.15) is proportional to a fictitious tangential displacement Δv of the blade that is equal to the actual axial displacement Δu. For this reason the ToA can be used to calculate the blade axial displacement Δu.

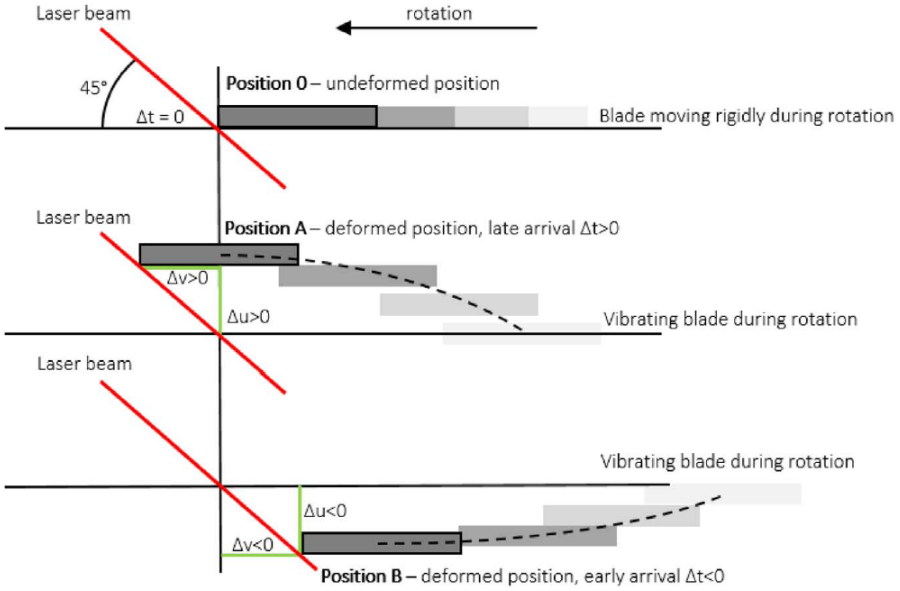

Fig. 6.15 Beam shutter working principle adopted for detecting the out of plane vibration modes for the dummy disk 1.

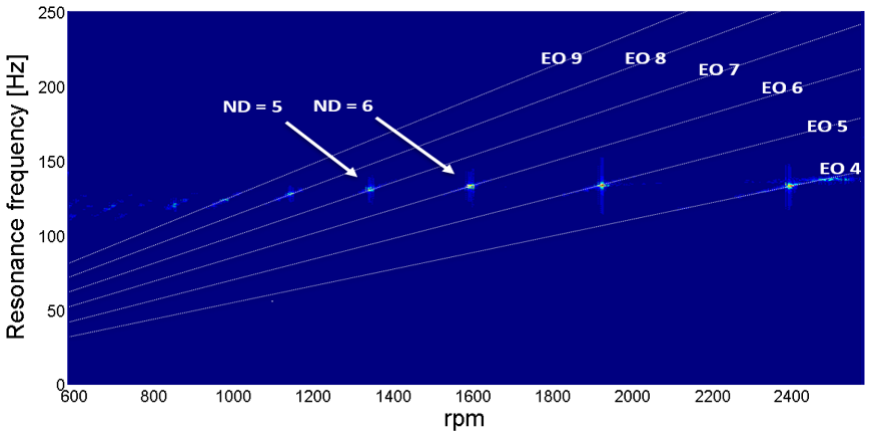

Fig. 6.16 Experimental Campbell diagram for the dummy disk 1.

6.5.2 Preliminary Test

A preliminary rotating test was performed to identify the actual resonance frequencies. A single magnet was mounted on the test rig so that the disk could be excited simultaneously by means of an infinite number of harmonic excitations ($EO_1 = 1,2,3,\ldots$). The test was planned in order to investigate the speed range 600 - 2600 rpm. From the strain gauges time signal the experimental Campbell diagram (Figure 6.16) was processed using Matlab. The natural frequencies for the modes corresponding to $h = 5$ and $h = 6$, which were determined by reading the y-axis values of the white points, are listed in Table 6.2.

Table 6.2 The dummy disk 1 resonance frequencies for the mode shapes with $h = 5$ and $h = 6$ (OOP bending modes).

EO	ND	n_{res}	f_{res}
7	5	1356	158.2
6	6	1591	159.1

6.5.3 Test Campaign on the Dummy Disk 1

The test campaign was performed for the modes that were excited by the EOs determined from Eqn. 6.2 for $z = 1$. A single permanent magnet was adopted for the excitation. A gap of 7 mm between the permanent magnet and those glued at the blades' tips was set for all the tests. Strain and ToA were acquired simultaneously for two speed ranges including the values of n_{res} at which the resonances occur. The main tests parameters are listed in Table 6.3.

Table 6.3 Test campaign for the dummy disk 1.

EO	h	n-range
7	5	1300 - 1400
6	6	1550 - 1650

The test campaign was repeated 3 times. For each test a linear sweep in speed with an acceleration of 18.75 rpm/s was performed.

6.5.4 The Comparison BTT - Strain Gauges on the Dummy Disk 1

The strain gauges and BTT data were post-processed for each of the studied modes by using the same procedure employed in the preliminary test. The detected and derived displacements (u_{BTT} and u_{SG}) and the corresponding resonance frequencies were averaged over the three acquisitions. The values of f_{SG}, f_{BTT}, u_{SG} and u_{BTT} for the three separate acquisitions are reported in the Table 6.4, where the high repeatability of the measurements can be noted.

Table 6.4 BTT and strain gauges measurements for the three tests on the dummy disk 1: the OOP vibration (1F) of the blades corresponding to $h = 5$ and $h = 6$ were detected.

Test	h	Mode	f_{SG}	f_{BTT}	u_{SG}	u_{BTT}
-	-	-	Hz	Hz	μm	μm
1	5	1F	158.10	159.80	1657.66	1651.50
2	5	1F	157.90	157.70	1669.50	1611.81
3	5	1F	158.00	156.50	1659.53	1631.13
1	6	1F	160.00	161.90	2314.57	2293.21
2	6	1F	160.00	159.80	2296.27	2289.21
3	6	1F	157.90	158.90	2285.41	2244.38

The mean values of the previous frequencies and displacements at resonance are listed in the Table 6.5 so that a direct comparison between the two measurement systems can be carried out using the following relationships:

$$\begin{aligned} e_f &= \frac{|\bar{f}_{BTT} - \bar{f}_{SG}|}{\bar{f}_{SG}} \cdot 100 \\ e_u &= \frac{|\bar{u}_{BTT} - \bar{u}_{SG}|}{\bar{u}_{SG}} \cdot 100 \end{aligned} \tag{6.12}$$

where e_f and e_u are the percentage differences between the resonance frequencies and vibration amplitudes detected by the strain gauges and the BTT respectively. From the Table 6.5 it can be noted that the difference in terms of resonance frequency is negligible ($e_f < 0.5\%$) while the difference in terms of resonance amplitude is less than 2% ($e_u < 2\%$).

Table 6.5 BTT - strain gauges measurements comparison on the dummy disk 1.

h	$\bar{f}_{SG}$	$\bar{f}_{BTT}$	e_f	$\bar{u}_{SG}$	$\bar{u}_{BTT}$	e_u
-	-	-	Hz	Hz	μm	μm
5	158.0	158.0	0	1662.23	1631.48	1.88
6	159.3	160.2	0.44	2298.75	2275.60	1.02

6.5.5 From a Single Blade Measurement to the Blobal Disk Response

One of the advantages of the BTT system over the strain gauges is that every blade can be measured while, if the strain gauges are used, only the response of the instrumented blades are detected. However, the measurement of the blades as independent structures having their own amplitude and resonance frequency does not allow to catch the global disk behavior when a mode shape with a certain number h of nodal diameters occurs. The estimation of the h number of a bladed disk vibrating in resonance condition can be carried out with aid of a numerical Campbell diagram (e.g. similar to that of Figure 6.14 (b)), obtained from the FE model of the bladed disk. In particular, when a resonance is detected by the measurements, the corresponding rotational speed is the input value for the Campbell diagram to verify the presence of a crossing h line - EO line that satisfies Eqn. 6.2. Instead of estimating the h number with the numerical Campbell diagram, it is here presented how it can be identified directly by the BTT measurements.

The forced responses of all the blades post-processed by the BTT for the studied mode shapes ($h = 5$ and $h = 6$) are plotted in Figure 6.17. If the dummy disk were a perfectly tuned disk, i.e. all the hypotheses for a cyclic symmetric body were satisfied in terms of geometry, material properties and constraints, the forced response of each blade would be the same. It can be observed that this holds for the standing *Operating Deflection Shape* (ODS) with $h = 6$ (Figure 6.17 a)), where the response peak of each blade occurs at the same rotational speed with the same amplitude. This is not the case of the traveling ODS with $h = 5$ (Figure. 6.17 b)), where the maxima amplitudes occur at slightly different rotational speed and their envelope appears as a spatial wave along the blade number. The same spatial wave can be observed along the blade number at a given rotational speed.

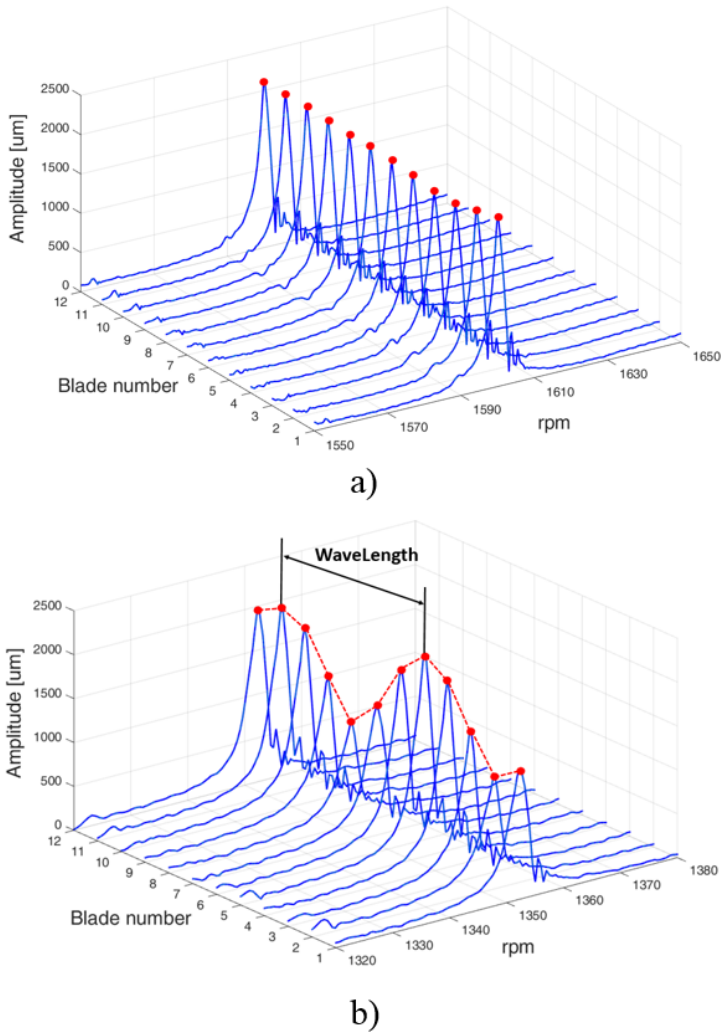

Fig. 6.17 Experimental forced responses for the twelve blades of the dummy disk 1 detected by the BTT in the case of $h = 6$ a) and $h = 5$ b) mode shape.

This phenomenon was already observed in [73] where a test campaign on a non-rotating blisk excited by a set electromagnets producing an EO traveling force was performed. In that case it was demonstrated that, due to the presence of small mistuning of the disk, the spatial wave resulting from the envelope of the blade peak amplitudes for a given excitation frequency had a number of Wavelengths (WLs, see Figure 6.17) equal to two times the number of the ODS nodal diameters. In detail, for a dummy bladed disk with 24 blades, four WLs were observed for an ODS with $h = 2$ and six WLs were observed for an ODS with $h = 3$. In the case of Figure 6.17 b), where the ODS with $h = 5$ is shown, ten WLs are expected. As it is shown in the same figure, the envelope of the maxima amplitudes clearly shows two WLs

instead of ten. This is due to the aliasing effect generated by the poor resolution of a spatial wave with ten WLs discretized by 12 blades only. In detail, assuming N as the number of blades, W_{exp} the number of WLs of the expected spatial wave and W_s the number of WLs of the spatial wave sampled by the blades, two cases can occur:

- if $W_{exp} \leq N/2$, the modulated spatial wave can be well recognized as a wave with W_{exp} wavelengths. In this case $W_{exp} = W_s$ and no aliasing occurs;
- if $W_{exp} > N/2$ (Figure 6.17 b)), the number of blades is not large enough to correctly discretize a spatial wave with W_{exp} wavelengths. In this case aliasing occurs and the observed spatial wave has a number of wavelengths W_s which satisfies the following relationship:

$$W_{exp} = z \cdot N \pm W_s, \qquad \forall\, z \in \mathbb{N}^* \tag{6.13}$$

In order to confirm the experimental observation in a simpler case where no aliasing occurs, the measurement was performed also in the range of the natural frequency corresponding to $h = 3$: the ODS, plotted in Figure 6.18, shows as expected a spatial wave with six WLs.

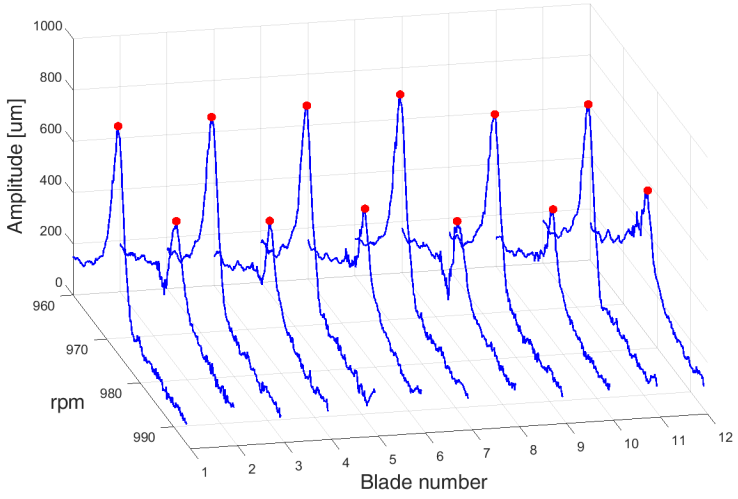

Fig. 6.18 Experimental forced responses for the 12 blades of the dummy disk 1 detected by the BTT in the case of the $h = 3$ mode shape.

In the next section a simplified lumped parameters system is used to explain the reason why the spatial wave is characterized by a number of WLs that is twice the number of h of the traveling response.

6.5.6 An Analytical Model to Explain the Blade Row Response

The relationship between the number of WLs and the number h is strictly associated to the existence of two repeated modes in the presence of small mistuning. Repeated modes occur for $1 < h < N/2$ if N is even. When $h = 0$ or $h = N/2$ (for an even number of blades) only one mode is present and the spatial wave does not appear. This is confirmed by the observation of the flat ODS corresponding to $h = N/2 = 6$ (Figure 6.17 a)).

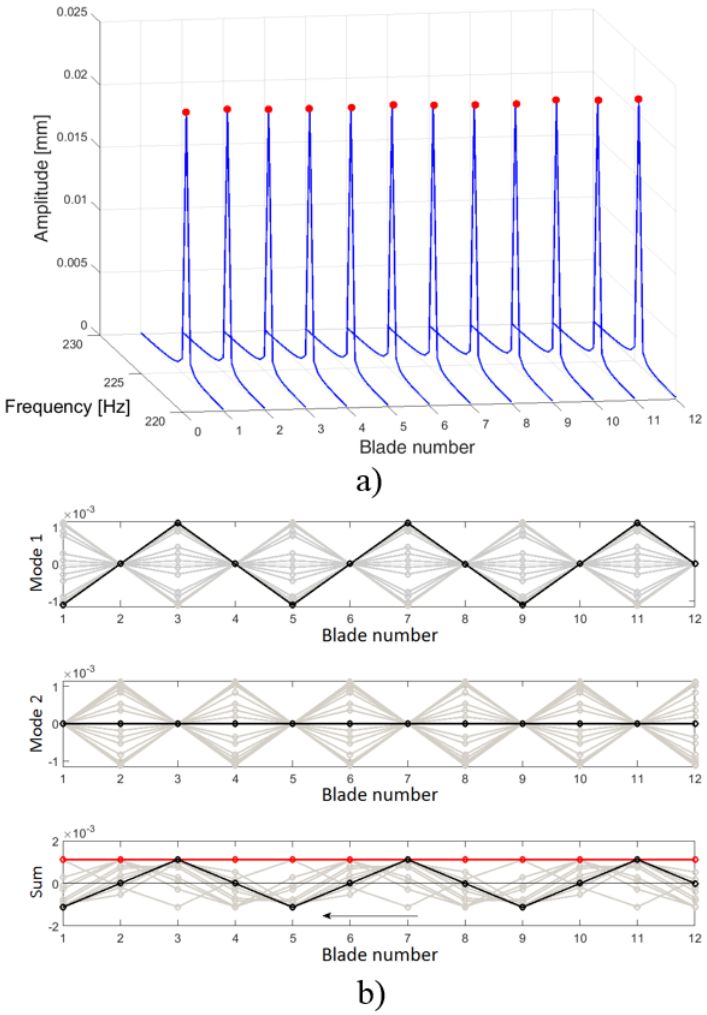

Fig. 6.19 Numerical forced responses a) and ODS b) for a cyclic symmetric mode shape with $h = 3$.

In order to explain the appearance of the spatial wave, a simple analytic model of a lumped parameter disk is used. The disk has 12 sectors, each one with one degree of

freedom coupled by means of springs to the neighbor sectors. The sectors are equal, therefore the disk is tuned and 12 identical forced response amplitudes are obtained as shown in Figure 6.19 a) when the mode shape with $h = 3$ is excited. In Figure 6.19 b) the two repeated mode shapes multiplied by their participation factors are plotted at resonance for different time instants. Under a traveling excitation the repeated mode shapes are orthogonal not only in space but also in time. The orthogonality along the blade number is clearly visible, while the orthogonality in time is indicated with the two black solid lines: when the first mode is at its maximum amplitude the second mode is at its neutral position. The linear combination of the two modes produces a traveling ODS (lowest subplot of Figure 6.19 b)). Since the disk is tuned, the peak envelope of the blade amplitudes is a straight spatial line (red).

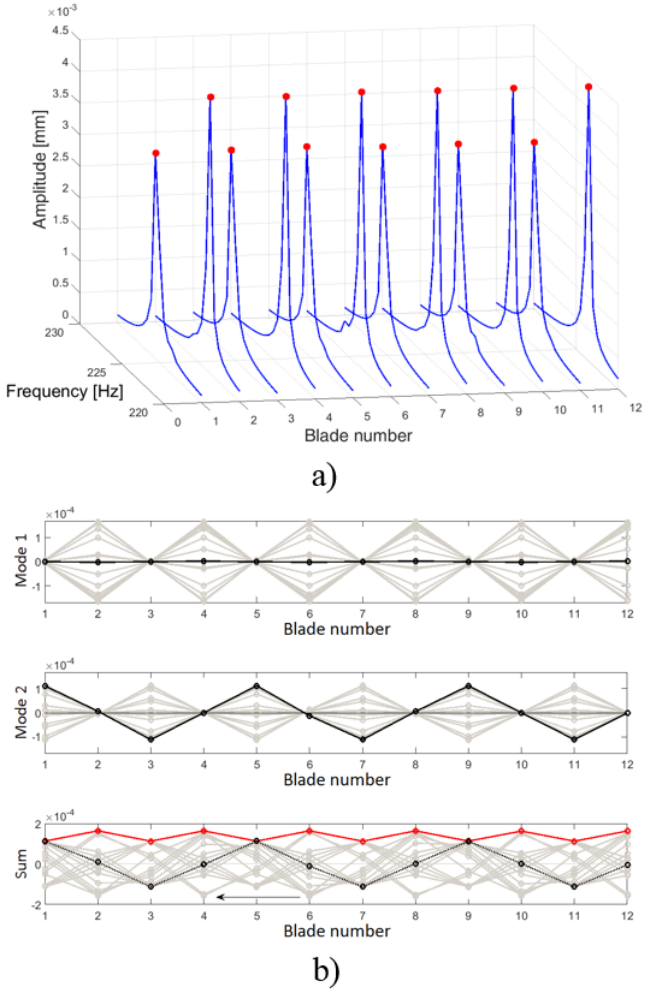

Fig. 6.20 Numerical forced responses a) and ODS b) for a mistuned mode shape with $h = 3$.

A random mistuning was then added to the disk model in terms of mass perturbation that causes a split of the repeated modes natural frequencies Δf of about 0.7 % of the tuned natural frequencies. As it can be seen in Figure 6.20 a), the consequence is that the sum of the two modes, having slightly different frequencies and amplitudes, gives an ODS where the peak envelope is a spatial wave with six WLs for a $h = 3$ response as they appear in Figure 6.18.

By using the same mistuned model the cases of Figure 6.17 a) and b) can also be simulated. Figure 6.21 a) shows the simulated forced responses corresponding to the experimental case of Figure 6.17 a), where a mode with $h = 6$ is excited. It can be seen in the simulation (Figure 6.21 b)) that the second mode does not exist since the mode is standing and then it can not give rise to a spatial wave.

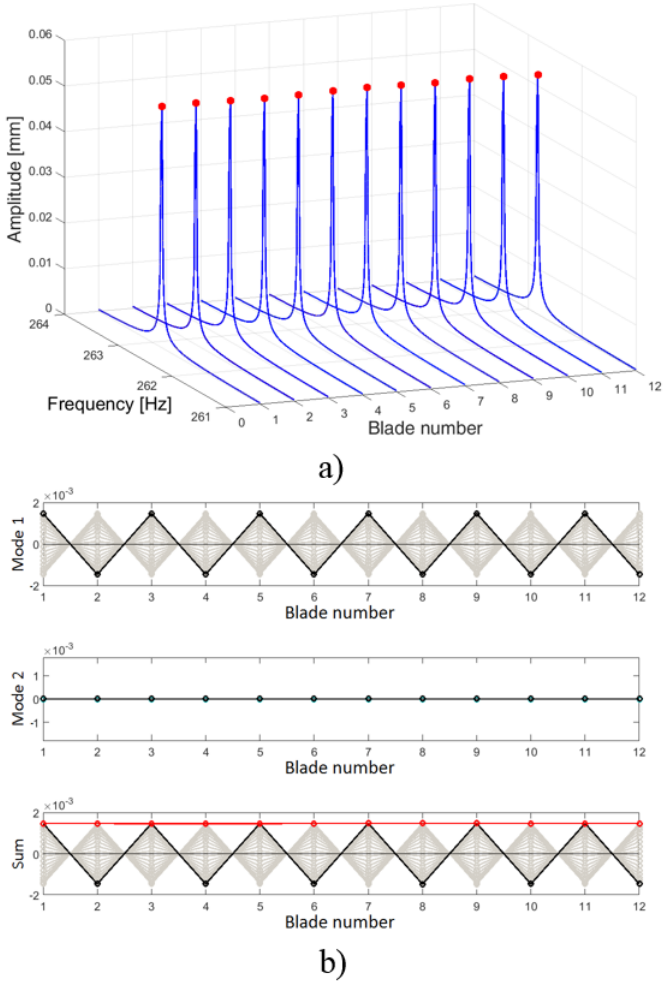

Fig. 6.21 Numerical forced responses a) and ODS b) for a mistuned mode shape with $h = 6$.

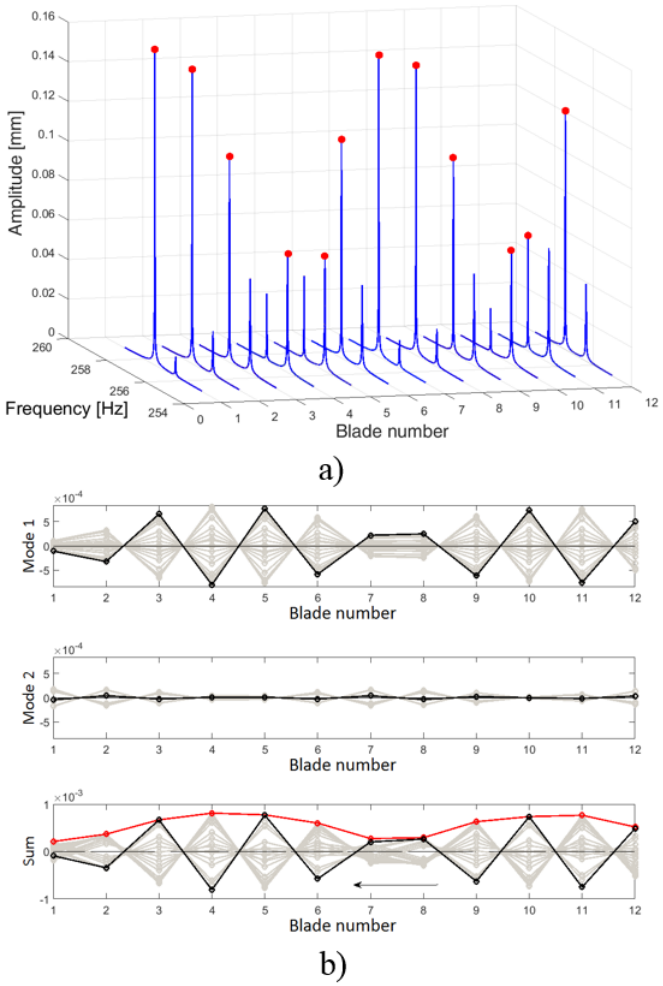

Fig. 6.22 Numerical forced responses a) and ODS b) for a mistuned mode shape with $h = 5$.

Figure 6.22 a) shows the result of the simulation for an ODS with $h = 5$. This example corresponds to the experimental case of Figure 6.17 b). It can be seen that the simulated forced responses shows a modulated spatial wave with two WLs due to aliasing as in the experiments. It can then be concluded that the presence of small mistuning, which is expected to be present in the real disks, can be useful to experimentally identified the nodal diameters number.

6.6 Results on the Dummy Disk 2

The dummy disk 2 was created to reproduce a bladed disk dynamics similar to that of a real turbine disk. The measurements on this disk allow testing the capability of the BTT system in the beam shutter configuration even on a disk with a more complex dynamics. The FE dynamic calculation on the dummy disk 2 showed that the modes belonging to the first three modal families are characterized by the flap (1F), flap restricted (1FR) and torsional (1T) mode shape of the blade. The FreND diagram corresponding to the 1^{st}, 2^{nd} and 3^{rd} modal family is shown in Fig. 6.23. From the FE analyses on the dummy disk 2 the high strain locations on the blade airfoil, both for the 1FR and 1T mode shape, were chosen for the strain gauges installation (Figure 6.8 b)).

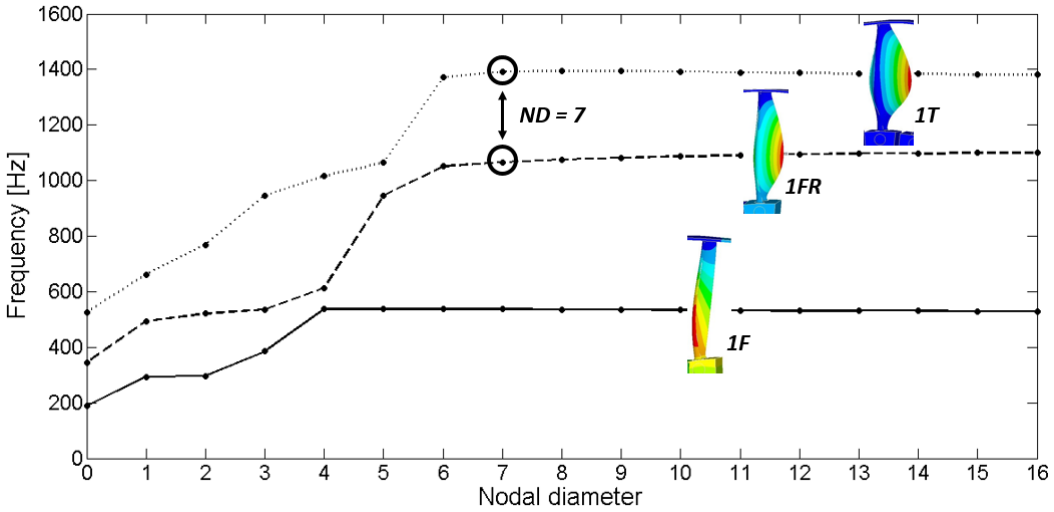

Fig. 6.23 Numerical FreND diagram for the dummy disk 2 and identification of the mode with $h = 7$ nodal diameters.

6.6.1 Preliminary Hammer Test

A preliminary hammer test was performed to detect the modal parameters of the disk in static conditions (not rotating). In order to have the same constraints with the shaft as during the rotation, the disk was kept mounted on the spinning rig during the hammer test. The response of each blade was measured by a laser scanner at the same location where the BTT laser sensors detect the blade vibrations.

It was observed that the cleanest disk responses for both the 1FR and 1T modes occurred for ND = 7 at 1029 Hz and 1402 Hz respectively. In Figure 6.24 an example of the response processed by the laser scanner is shown. Considering these preliminary results, it was chosen to compare the BTT and the strain gauges measurements when the disk was excited in rotating conditions to vibrate according the modal families 1FR and 1T for $h = 7$.

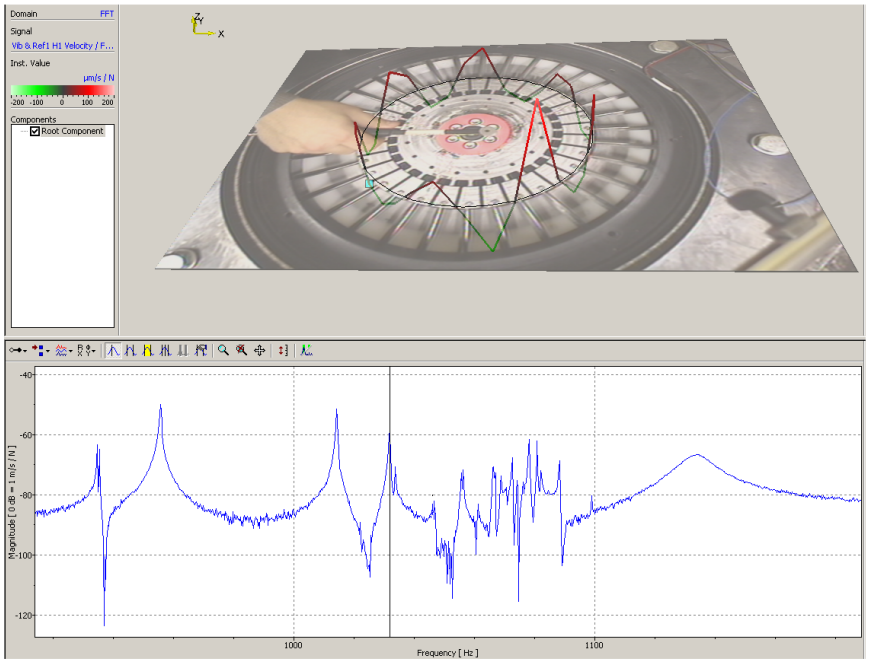

Fig. 6.24 Hammer test on dummy disk 2: 1FR mode identification.

6.6.2 Test Campaign on the Dummy Disk 2

According to Eqn. 6.2, considering that the number of blades is $N = 32$ and assuming $z = 2$, it can be deduced that the mode with $h = 7$ can be excited by an excitation with EO = 57. Moreover, assuming $i = 3$, from Eqn. 6.1 it can be derived that a number of 19 equally spaced magnets ($m = 19$) facing the rotating disk can produce an excitation with EO = 57. The test campaign was then performed with 19 permanent magnets (Figure 6.25) at a gap of 5 mm from the blade leading edges. This produces in the disk a travelling excitation with $EO^3_{19} = 57$ that into a suitable speed range excites the modes at $h = 7$.

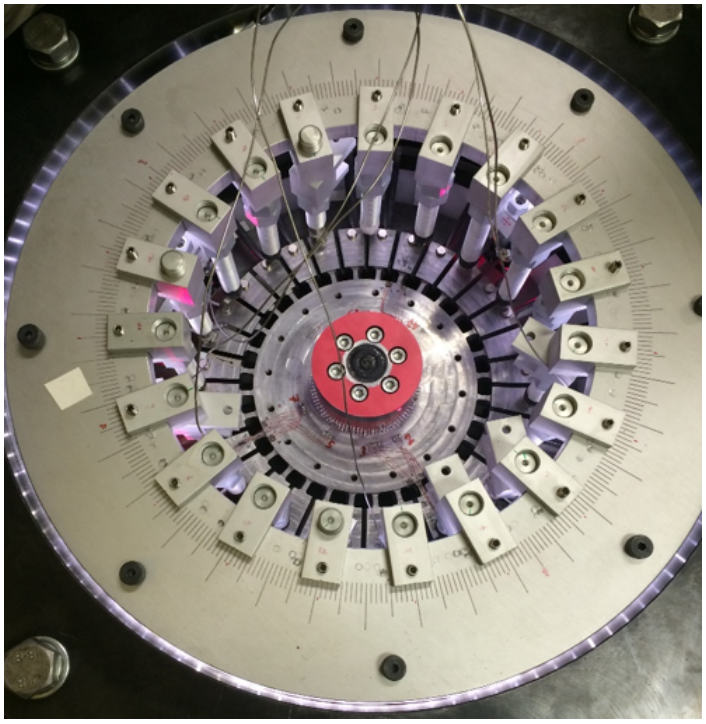

Fig. 6.25 Dummy disk 2 excited by 19 permanent magnets.

The main tests parameters are listed in Table 6.6. Strain and displacement were acquired simultaneously for 2 speed ranges (Table 6.6) including the values of n_{res} at which the resonances occur. For each test a linear speed sweep with an acceleration of 18.75 rpm/s was performed. As in the case of the dummy disk 1 the test campaign was repeated 3 times.

Table 6.6 Rotational speed ranges for the test campaign on the dummy disk 2.

Mode	*EO*	*ND*	n-range
-	-	-	rpm
1FR	57	7	1000 - 1150
1T	57	7	1350 - 1500

6.6.3 The Comparison BTT - Strain Gauges on the Dummy Disk 2

The strain gauges signals were post-processed using the same procedure adopted for the dummy disk 1. Also for the dummy disk 2 the detected and derived displacements (u_{BTT} and u_{SG}) and the corresponding resonance frequencies were averaged over three acquisitions. As shown in Table 6.7 the measured quantities show high repeatability.

Table 6.7 BTT and strain gauges measurements for the three acquisitions on the dummy disk 2.

Test	h	Mode	f_{SG}	f_{BTT}	u_{SG}	u_{BTT}
-	-	-	Hz	Hz	μm	μm
1	7	1FR	1025.60	1020.30	136.21	130.85
2	7	1FR	1032.20	1026.20	135.30	130.51
3	7	1FR	1030.40	1021.90	137.78	132.75
1	7	1T	1404.30	1371.40	153.62	161.33
2	7	1T	1403.60	1370.60	155.89	161.91
3	7	1T	1398.70	1362.30	156.93	164.38

The mean values of the resonance frequencies, amplitudes and the relative percentage differences e_f and e_u (Eqn. 6.12) are listed in Table 6.7.

Table 6.8 BTT-strain gauges comparison for the dummy disk 2 when the CFF method is adopted.

Mode	h	$\bar{f}_{SG}$	$\bar{f}_{BTT}$	e_f	$\bar{u}_{SG}$	$\bar{u}_{BTT}$	e_u
-	-	Hz	Hz	%	μm	μm	%
1FR	7	1029.40	1022.80	0.65	136.43	131.37	3.70
1T	7	1402.20	1368.10	2.43	155.48	162.54	4.54

It can be noted that the values of displacement (u_{BTT} or u_{SG}) are an order of magnitude lower than those detected for the dummy disk 1 (Table 6.5). Even in the case of small vibration amplitudes the comparison between the two measurement systems led to acceptable values of e_f and e_u (Table 6.8).

6.6.4 Nodal Diameter Identification on the Dummy Disk 2

The forced responses obtained for the mode 1T on each blade of the dummy disk 2 are plotted in Figure 6.26 a).

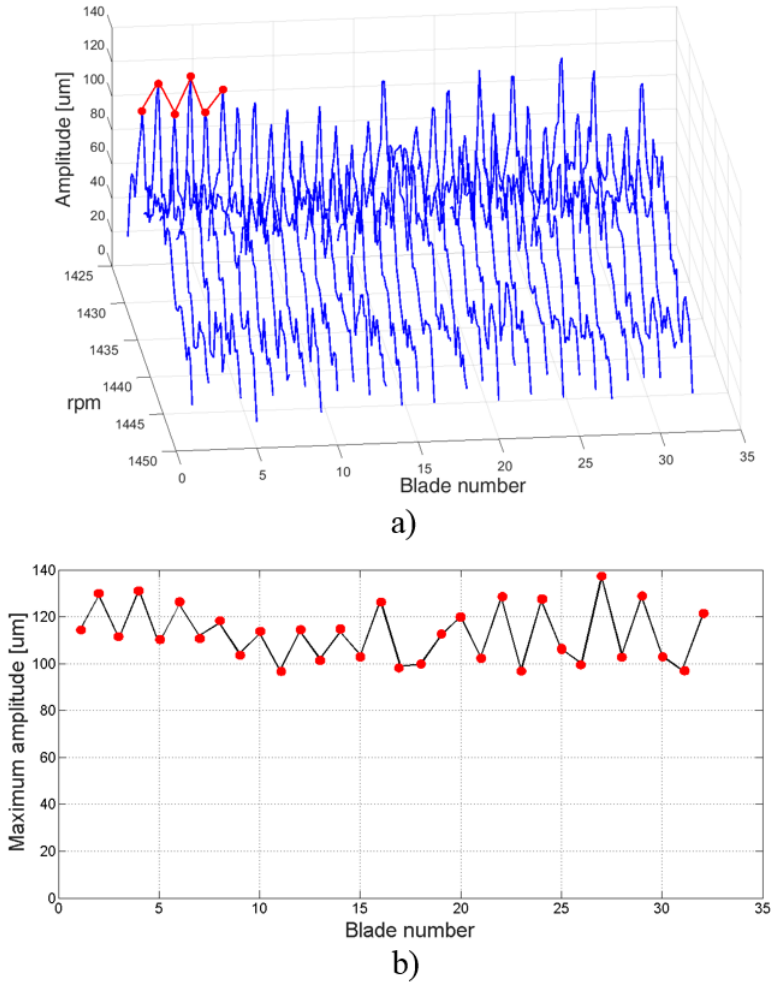

Fig. 6.26 Experimental measurements on the dummy disk 2 ($N = 32$) by the BTT, mode shape with $h = 7$ mode. a) Forced responses of all the blades, b) spatial wave.

Although the small vibration amplitudes led to a set of noisy data collected by the BTT sensors, it can however be observed that also in this case the phenomenon of the spatial wave can still be present as highlighted in Figure 6.26 b). The shape of the WLs is in this case quite irregular, but it is still possible to recognize a modulated spatial wave with 14 peaks. In this case 14 peaks are expected since the excited travelling response is characterized by a number of nodal diameter $h = 7$.

The observation of this phenomenon is confirmed by other tests. An excitation with EO = 19 is produced by 19 magnets. According to Eqn. 6.2, considering the number of blades ($N = 32$) and $z = 1$, the engine order EO = 19 excites the mode with $h = 13$. The envelope of the maxima amplitudes of the forced responses in this case is that of Figure 6.27 a) where six WLs are visible. In this case the presence of six WLs instead of the expected 26 can be justified by the Eqn. 6.13 since the aliasing occurs. In fact, the number 26 of the expected WLs of the spatial waves is higher than $N/2$. For the aliasing the visible number of WLs is six (32 - 26 = 6).

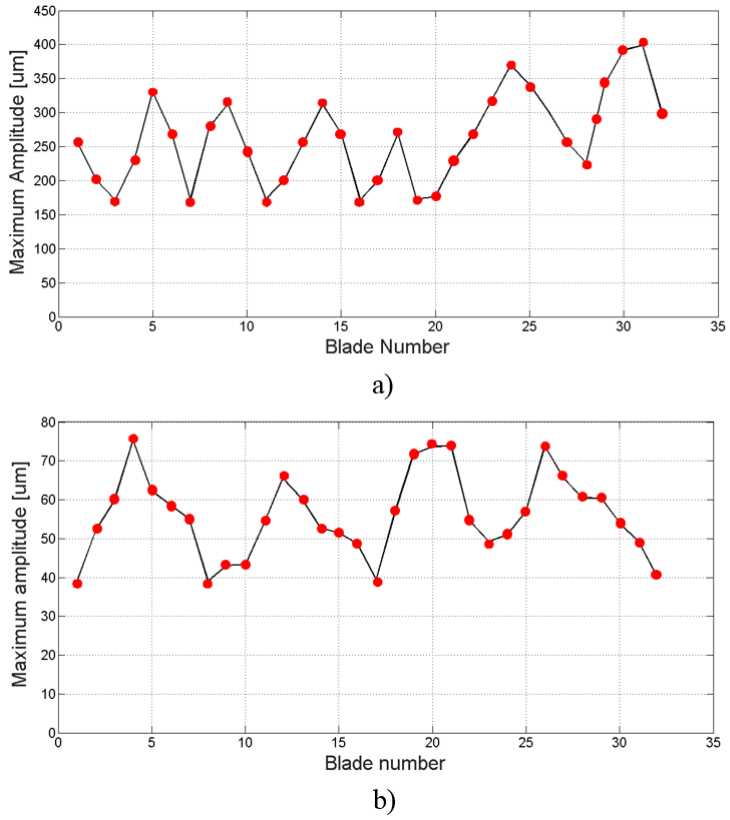

Fig. 6.27 Envelope of the maxima amplitudes of the experimental forced responses (spatial waves) for the dummy disk 2 ($N = 32$). Mode shape with $h = 13$ a) and $h = 2$ b).

In order to confirm the results in one case where the aliasing phenomenon is not present, the measurement was repeated with 5 magnets. According to the Eqn. 6.1 5 magnets produce on the blades a set of traveling forces characterized by $EO_{15} = 15, 30, 45, \ldots$. In particular, the measurement was performed considering an excitation corresponding to EO = 30 in order to excite, according to Eqn. 6.2,

the mode shape with $h = 2$. The envelope of the maxima amplitudes of the forced responses in this case is that of Figure 6.27 b) where four WLs, as expected, are visible since the aliasing is not present.

6.7 Discussion

In this paper a BTT system with a new concept of sensors positioning was tested on two dummy disks (dummy disk 1 and dummy disk 2). The dummy disk 1 has a simple flat geometry and its blades show in resonance high displacement amplitudes (1600 - 2300 μm). The dummy disk 2 is more similar to a real turbine disk and it is characterized by families of modes close to each others.

Two key features were here presented. First, a new measurement configuration for the optical probes of a BTT system, the *beam shutter* configuration, was tested by comparing the BTT with the strain gauges measurements. The beam shutter configuration proved to work properly since it gives the expected collection of measured data from the ToA of each blade under each sensor. In the case of the dummy disk 1, for the selected modes, high vibration amplitudes (1600 - 2300 μm) were found with an accuracy less than 2% with respect to the strain gauges measurements. For the dummy disk 2 the vibration amplitudes for the measured modes (130 - 150 μm) were smaller than in the case of the previous disk. Even if the small amplitude values led to a set of noisy BTT data, the accuracy with respect to the strain gauge measurements was still high (differences less than 5%). These results give confidence in this new way of positioning the optical probes. Second, a novel method to experimentally identified the nodal diameter number of the detected mode is proposed. The method takes advantage from the availability of the forced responses of all the blades that typical of the processed BTT measurements. The method works when the detected mode is quite isolated from the others and in presence of small mistuning. It does not work when the mistuning is large enough to completely decouple the blade row and destroy the ideal cyclic symmetry of the disk. It was proved that a small mistuning produces a spatial wave modulating the vibration amplitude of the blade row. It was then shown that the number of nodal diameter related to the dominant mode can be identified starting from the number of WLs of this modulation.

Chapter 7

Conclusions

7.1 Summary and Main Achievements

The bladed disks are known to suffer severe vibration problems owed to the non-stationary components of the gas flow pressure. Such condition is much more critical for turbines than compressors due the high temperatures of the exhaust gasses characterizing the environment in which they work. Dynamic stresses on turbine bladed disks generally depend on excitation causes that can be grouped into the following two main categories:

- *Mechanical excitations*: ascribable to the wrong rotor balance (whirl), blade tip-casing contacts and possible impacts between either rotating or non-rotating components with items sucked into the engine while working.
- *Aerodynamic excitations*: while bending stresses are caused by the stationary component of the gas flow pressure (mean value), vibration stresses are induced by its non-stationary components. These are attributable to the gas flow-structure interaction concerning the non-uniform circumferentially distributed pressure, stator-rotor interactions and self-excited aeroelastic phenomena (flutter).

Most of the mentioned excitation causes are the main responsible of high cycle fatigue damages, which represent the most important cause of failure for bladed disks. Hence, the prediction of the dynamic behavior of such structure in resonance condition

becomes of extraordinary importance when the amount of damping necessary to lower the blades' vibrations has to be evaluated.

Finite element models of industrial rotors may easily consist of thousands or even million of nodes. Performing dynamic analyses without reducing their model size is often prohibitive due to the large number of degrees of freedom (DoFs) involved in the simulations. For single-wheel bladed disks such analyses can be greatly simplified by exploiting their ideal *cyclic symmetry* so that a more compact model representation can be obtained. Chapter 2 of this thesis presents the commonest approaches found in literature used to predict the whole tuned bladed disk dynamics, starting from the finite element model of its fundamental sector. Such approaches, which are mainly based on studies concerning the waves propagation on periodic structures, were exploited to give an insight into the physical meaning of a generic bladed disk's mode shape. These modes feature particular harmonic distributions of the displacements over the structure that are commonly identified by their number of nodal diameters, i.e. nodal lines crossing the disk's center along which all the modal quantities are null. However, this description is valid only in the case the mode is discretized by homologous locations whose number equals the number of disk's sectors, but no information are provided on the shape of the mode within a single sector. By looking at the mode shapes at a disk's level, new small wavelength spatial harmonics can also be detected. These were referred to as *extra harmonics* and were presented for the first time in a recent paper concerning a reduced order model technique for multi-stage bladed disks [6, 7].

Interface Reduction Methods for Sub-Systems Coupling

Cyclic symmetric reductions of stand-alone fundamental sectors may be not sufficient when a significant compression of the number of DoFs is requested. For this reason *dynamic substructuring* methods in the class of *component mode synthesis* (CMS) are widely employed in the turbomachinery field, since they guarantee high fidelity in modeling the structure's dynamic behavior. In this regard Chapter 3 reports a literature survey on the most used methods utilized to reduce the finite element model size of a complex structure as a bladed disk is. Among these, particular emphasis has been given to the well-established *Craig-Bampton* method, which aims at defying a *superelement* by condensing most of the component's DoFs on a smaller set of boundary DoFs. However, although a dramatic reduction may be achieved

for the non-boundary DoFs, all the boundary ones are retained, a condition that is inconvenient for components having extended interfaces. In this frame Chapter 3 proposes an original interface reduction method that improves the pre-existing *Characteristic Constraint Modes* formulation [5]. The developed technique has been named as *Gram-Schmidt Interface* reduction method and allows performing the following two tasks:

1. Besides reducing the interface DoFs, the method allows the components coupling even in the case on non-conforming interface meshes between them. This task is carried out by writing the compatibility equations not in the domain of physical DoFs but in the space of the *Gram-Schmited Characteristic Constrait* modes.

2. It can be used as a valid alternative of the Tran's method for the reduction of cyclic symmetric structures. In particular, the independent frontier of a sector treated in cyclic symmetry conditions can be condensed without performing ulterior static condensations of the full FE model. In this way the offline reduction costs can be considerably lowered.

Multi-Stage Reduced Order Model Techniques

The idea of interface reduction and subsequent components coupling has been readily extended to multi-stage bladed disks assemblies. These structures consist of two or more bladed disks coupled together by means of bolted flange joints. The main challenge associated with modeling multi-stage assemblies is strictly related to the possible different cyclic symmetry of the stages, since a sectors representative of the whole system's geometry does not exist in general. Hence, when dealing with multi-stage systems the single-stage approach is no more valid and the effects of dynamic coupling between stages have to be taken into account. In this context Chapter 4 presents two novel reduction techniques for multi-stage systems based on the same theory background of cyclic symmetric structures, but different mathematical approaches:

1. The first method starts from the finite element models of isolated full stages. These are individually reduced and then assembled leading to a reduced order model of the complete multi-stage structure. The first reduction step for each

single-stage is the application of the well-known Craig-Bampton method, which requires that at least the DoFs at the inter-stage boundary are retained as master. Later, such physical DoFs are approximated by few spatial harmonic basis functions taking into account the presence of either dominant of extra harmonic patterns. Once the mentioned reduction is performed for both stages' interfaces, the multi-stage coupling procedure is performed by equaling the same order spatial Fourier coefficients (i.e. the generalized coordinates) of the functions adopted for the interfaces reduction. The main idea behind this coupling process can be summarized as follows: *the vibration energy can be transferred from one stage to the adjacent ones if their motion at the interface has the same spatial shape*.

It can be noted that the stages' coupling is performed for all the harmonic functions approximating the motion at the stage's interfaces. The assembled multi-stage ROM then allows the force response prediction for any traveling wave excitation applied to the stages. In the example of section 4.3, the application of this method led to an effective model size compression (1306 vs 260000) that guaranteed to lower the computational costs of almost 140 times.

2. The second method just requires the finite element models of stand-alone fundamental sectors representative of the stages' geometries. Each sector is reduced by applying a modified version of the *cyclic Craig-Bampton* method proposed by Bladh [9], which takes into account a further reduction of the interface DoFs considering the extra harmonic pattern related to the dominant harmonic index for which the starting cyclic reduction is performed. At the end of each stage's reduction the interface is modeled by few cyclic physical DoFs. The final multi-stage reduced order model is this time obtained by enforcing the compatibility conditions in the space of such cyclic DoFs.

   For this second case the model size compression was much more effective than that achieved with the first reduction method (53 vs 1306 vs 260000). However, the stages reduction is in this case valid just for one dominant harmonic function. This means that the forced response calculations can be performed for traveling wave excitations having engine order compatible with the order of the harmonic function used for the cyclic reduction of the sectors.

It has been proved that the application of both methods on a multi-stage bladed disks model allows an excellent prediction of its dynamics in terms of natural frequencies,

eigenvectors and forced response calculations. The choice of one method over the other depends on the objective of the dynamic calculations on a multi-stage ROM. If the complete system dynamics has to be modeled, the first method is preferred. Differently, if the behavior of the system for few nodal diameter patterns is of interest, the second method appears much more efficient.

Multi-Stage Bladed Disks with Friction Contacts at the Bolted Flange Joint

Due to the large operative speed ranges, bladed disks can not work outside of all the possible resonant zones. In fact, since their configuration is obtained from preliminary aerodynamic and efficiency calculations, it can not be easily modified. In this regard, some critical resonances can not be avoided and a way to provide additional damping to the system is necessary. The commonest approach to reduce vibration stresses and high cycle fatigue phenomena consists in producing energy dissipation by *dry friction* at the interfaces of the joints employed in bladed disk assemblies. Nowadays the mechanical arrangements used to perform such energy dissipation are mainly three: *blade root joints*, *blade shrouds* and *underplatform dampers*.

Although established, all these arrangements exploit as a sources of friction damping specific blade locations, being focused on the attenuation of the dynamic response of a single-stage bladed disk. However, the bolted flange joint connecting adjacent bladed disks may be considered as a further source of friction damping capable to attenuate mechanical vibrations at a system level. In Chapter 5 the non-linear behavior of the bolted flange joint is for the first time studied and its effect in damping blades' vibrations is evaluated. Here, the multi-stage reduction techniques of Chapter 4 are combined with the *macroslip Jenkins contact element*, in order to efficiently predict the forced response of a simplified multi-stage bladed disk assuming the following hypotheses:

1. The traveling waves forces exciting the stages have the same engine order.
2. The relative displacement generating the friction forces at the joint interface occur in the radial and circumferential directions.

3. The steady state displacements and the non-linear contact forces are approximated with their 1^{st} order Fourier coefficients (*Single Harmonic Balance Method*).

By applying the mentioned contact models and assuming an uniform pressure distribution along the flange, the non-linear behavior typical of friction joints come out. According to the second hypothesis, the damping was supposed being generated by the relative displacements occurring at the inter-stage boundary, without explicitly considering the presence of the bolts. However, it is reasonable to consider their non-linear behavior as one with that of the flange. In fact, possible friction phenomena may also occur at the interfaces bolt's head-flange and bolt's nut-flange.

The example developed throughout Chapter 5 shows that identical non-linear forced responses were obtained by employing both multi-stage reduction techniques. Such results do not exhibit any significant approximation with respect the benchmark forced responses obtained by using the Craig-Bampton model of each stage. However, it should be pointed out that the use of the multi-stage reduction technique involving the fundamental sectors allowed non-linear forced response calculation almost 9 times faster than the other multi-stage reduction technique (8 s vs 60 s) and almost 340 times faster than the classic approach based on the Craig-Bampton method.

Blade Tip-Timing Measurements

Accuracy and predictability of the numerical tools developed in this thesis should be checked again real structures preferably in realistic working conditions. However, the experimental validation of a numerical model on real gas turbines is an extremely difficult task for three main reasons:

1. Numerical tools generally simulate the system or component's dynamics by considering just few of the causes leading to critical resonance conditions. In reality the causes responsible of such resonances are several and in most of the cases the separation of the effect they involve is an extremely hard.

2. The high temperature characterizing the engine in working condition prevents the employment of well-established measurement systems that need to be in contact with the blades (e.g. the strain gauges).

3. From a practical point of view there is no enough room to install measurement systems that are able to monitor the blades response during operation.

For all these reasons it is a common practice to carefully design experimental setups that exhibit only the dynamic phenomena under investigation. Once the numerical models are demonstrated to be accurate representation of the experimental data, they can be used can be used as a optimization tools for real bladed disks design.

In this frame Chapter 6 reports an extensive experimental laboratory campaign aimed at proving the reliability of a latest generation *Blade Tip-Timing* (BTT) system on the measure of the forced response of rotating dummy disks. Two key features were here presented. First, a new sensor placement for the BTT optical sensors, i.e. the *beam shutter* configuration, was tested on two dummy blisk by comparing the BTT with the strain gauges measurements. For both disks the BTT measurements were consistent to those obtained by the strain gauges (differences $< 5\%$) . These results give confidence in the proposed sensors' arrangement and in the method used for comparing the displacements and strains detected by the two measurements systems. Second, a novel method to experimentally identify the nodal diameter number of the detected mode is proposed. The method takes advantage from the availability of the forced responses of all the blades that is typical of the processed BTT measurements. The method works when the detected mode is quite isolated from the others and in presence of small mistuning. It does not work when the mistuning is large enough to completely decouple the blade row and destroy the ideal cyclic symmetry of the disk. It was proved that a small mistuning produces a spatial wave modulating the vibration amplitude of the blade row. It was then shown that the number of nodal diameter related to the dominant mode can be identified starting from the number of *wavelengths* of this modulation.

7.2 Outlook & Future Directions

The value of a model order reduction technique lays on the remarkable speed up one can obtain in solving the reduced governing equations as opposed to solving the full system. However, also the offline costs associated to the construction of the reduced order models needs to be taken into account. Although acceptable when an unique reduced order model is used for several and repeatable analyses, the offline reduction costs may become significantly high when the model's parameters have to be investigated. In fact, for a broad class of problems the equations representing the system dynamics depend on a set of parameters. These parameters may enter in the models in many ways, representing, for example, material properties, system geometry, system configuration, initial conditions and boundary conditions. This parametric dependence represents a challenge for model reduction, since one cannot afford to create a new reduced model for every change in the parameter values.

In this frame the reduction methods proposed in this thesis would be no exceptions, and future developments aiming to extend their applicability to parametric studies have to be taken into account. However, one should consider that both *GSI* and multi-stage methods basically perform secondary reductions on pre-condensed ROMs. For this reason such methods may be combined with parametric reduction techniques that preserve physical interface DoFs as a master.

Being developed mainly for turbomachinary applications, where no significant changes of the model's parameters are allowed, the reduction techniques here developed are sufficiently mature to be used for dynamic analyses of bladed disks involving friction joints. In this regards, although the techniques developed as such can be used to predict non-linear contact phenomena, their applicability still remain valid as long the external forces guarantee the linear behavior of the structures (i.e. no geometric non-linearities occur).

Further possible extensions of both *GSI* and multi-stage methods may concern the development of a reduction strategy taking into account the thermomechanical behavior of the structure under investigation; an aspect that is crucial when analyzing turbomachinery components.

The experimental activity presented in Chapter 6 had as a main objective the definition of a strong know-how on a non-intrusive measurement system featuring a lot of advantages with respect the classic strain-gauges. In this way most of the future validations of numerical models predicting the forced response of rotating bladed disks can be better performed by looking at global response of system. Although predictability and accuracy of the reduction techniques were already checked against linear analyses on full finite element models, their application on problems involving non-linearities due to friction has still to be tested. In this regards, BTT test campaigns on ad-hoc designed rotating test cases may help in validating the predictability of the developed numerical techniques.

References

[1] R.R. Craig and A.J. Kurdila. *Fundamental of Structural Dynamics - Second Edition*. John Wiley & Sons, New Jersey, 2006.

[2] S.N. Voormeeren. *Dynamic Substructuring Methodologies for Integrated Dynamic Analysis of Wind Turbines*. PhD thesis, TU Delft, 2012.

[3] A. Sternchüss, E. Balmès, P. Jean, and J.-P. Lombard. Reduction of multi-stage disk models: Application to an industrial rotor. *Journal of Engineering for Gas Turbines and Power, American Society of Mechanical Engineers*, 131(1):012506, 2009.

[4] G. Battiato, C.M. Firrone, T.M. Berruti, and B.I. Epureanu. A General Method for Sub-Systems Coupling for the Dynamic Analysis. *Proceedings of ISMA Conference*, 2016. Leuven, Belgium.

[5] M.P. Castanier, Yung-Chang Tan, and C. Pierre. Characteristic Constraint Modes for Component Mode Synthesis. *AIAA Journal*, 36(6):1182–1187, 2001.

[6] G. Battiato, C.M. Firrone, T.M. Berruti, and B.I. Epureanu. Reduced Order Modeling for Multi-Stage Coupling of Cyclic Symmetric Structures. *Proceedings of ISMA Conference*, 2016. Leuven, Belgium.

[7] G. Battiato, C.M. Firrone, and B.I. Epureanu. Modeling the Microslip in the Flange Joint and its Effect on the Dynamics of a Multi-Stage Bladed Disk Assembly. *Proceedings of ASME Turbo Expo, Turbomacinery Technical Conference and Exposition*, 2016. Seoul, South Korea.

[8] G. Battiato, C.M. Firrone, and T.M. Berruti. Forced response of rotating bladed disks: Blade Tip-Timing measurements. *Mechanical Systems and Signal Processing*, 85:912–926, 2017.

[9] R. Bladh, M.P. Castanier, and C. Pierre. Component-mode-based reduced order modeling techniques for mistuned bladed disks. Part I: theoretical models. *Journal of Engineering for Gas Turbines and Power*, 123:89–99, 2001.

[10] D.L. Thomas. Standing Waves in Rotationally Periodic Structures. *Journal of Sound and Vibration*, 37:288–290, 1974.

[11] D.L. Thomas. Dynamics of Rotationally Periodic Structures. *International Journal for Numerical Methods in Engineering*, 14:81–102, 1979.

[12] M.P. Castanier, G. Ottarsson, and C. Pierre. A reduced order modeling technique for mistuned bladed disks. *Journal of Vibration and Acoustics*, 119(3):439–447, 1995.

[13] D.J. Mead. Wave Propagation and Natural Modes in Periodic Systems: I. Mono-Coupled Systems. *Journal of Sound and Vibration*, 40:1–18, 1975.

[14] D.J. Mead. Wave Propagation and Natural Modes in Periodic Systems: II. Multi-Coupled Systems. *Journal of Sound and Vibration*, 40:19–39, 1975.

[15] G.S. Óttarson. *Dynamic Modeling and Vibration Analysis of Mistuned Bladed Disks*. PhD thesis, University of Michigan, 1994.

[16] Gilbert Strang. *Introduction to linear algebra*. Wellesley, MA: Wellesley-Cambridge Press, 1993.

[17] C. Pierre. Mode Localization and Eigenvalue Loci Veering Phenomena in Disordered Structures. *Journal of Sound and Vibration*, 126:485–502, 1988.

[18] W.C. Hurty. Vibrations of Structural Systems by Component Mode Synthesis. *Journal of Engineering Mechanics, Division American Society of Civil Engineers*, 86:51–69, 1960.

[19] W.C. Hurty. Dynamic Analysis of Structural Systems Using Component Modes. *AIAA Journal*, 3.4:678–685, 1965.

[20] R. Guyan. Reduction of Stiffness and Mass Matrices. *AIAA Journal*, 3:380, 1965.

[21] R. Craig and M. Bampton. Coupling of Substructures for Dynamic Analysis. *AIAA Journal*, 6:1313–1319, 1968.

[22] S. Rubin. Improved Component-Mode Representation for Structural Dynamic Analysis. *AIAA Journal*, 13:995–1006, 1975.

[23] R. MacNeal. A Hybrid Method of Component Mode Synthesis. *Computers & Structures*, 1:581–601, 1971.

[24] D.-M. Tran. Hybrid Methods of Component Mode Synthesis. *ONERA TP*, 1993.

[25] B. Irons. Free-Interface Methods of Substructures Coupling for Dynamic Analysis. *International Journal of Numerical Methods in Engineering*, 1:5–32, 1970.

[26] R. Craig and C. Chang. Substructure Coupling for Dynamic Analysis and Testing. *Tech. Rep. CR-2781, NASA*, 1977.

[27] D.-M. Tran. Component Mode Synthesis Methods Using Interface Modes: Application to Structures with Cyclic Symmetry. *Computer & Structure*, 79:209–222, 2001.

[28] D.-M. Tran. Component Mode Synthesis Methods Using Partial Interface Modes: Application to Tuned and Mistuned Structures with Cyclic Symmetry. *Computer & Structure*, 787:1141–1153, 2009.

[29] D.J. Rixen. *Substructuring and Dual Methods in Structural Analysis*. PhD thesis, Université de Liège, 1997.

[30] R. Bladh, M.P. Castanier, and C. Pierre. Effects of Multistage Coupling and DiskFlexibility on Mistuned BladedDisk Dynamics. *Journal of Engineering for Gas Turbines and Power*, 125:121–130, 2003.

[31] R. Bladh. *Efficient Prediction of the Vibratory Response of Mistuned Bladed Disks by Reduced Order Modeling*. PhD thesis, University of Michigan,, 2001.

[32] S.H. Song, M.P. Castanier, and C. Pierre. Multi-stage Modeling of Turbine Engine Rotor Vibration. *Proceedings of the IDETC/CIE 2005, ASME Paper DETC2005-85740*, 2005. Long Beach, CA, USA.

[33] S.H. Song. *Vibration Analysis and System Identification of Mistuned Multistage Turbine Engine Rotors*. PhD thesis, University of Michigan,, 2007.

[34] D. Laxalde, F. Thouverez, and J.-P. Lombard. Dynamical Analysis of Multi-stage Cyclic Structures. *Mechanics Research Communications*, 34:379–384, 2007.

[35] D. Laxalde, J.-P. Lombard, and F. Thouverez. Dynamics of Multistage Bladed Disks Systems. *Journal of Engineering for Gas Turbines and Power*, 129:1058–1064, 2007.

[36] A. Sternchüss and E. Balmès. Reduction of multistage rotor models using cyclic mode shapes. *Proceedings of GT2007, ASME Turbo Expo, ASME Paper GT2007-27974*, 2007. Montreal, Canada.

[37] K.X. D'Souza and B.I. Epureanu. A statistical characterization of the effects of mistuning in multistage bladed disks. *Journal of Engineering for Gas Turbines and Power*, 134(1), 2011.

[38] C.M. Firrone, S. Zucca, and M.M. Gola. Effect of static/dynamic coupling on the forced response of turbine bladed disks with underplatform dampers. *Proceedings of the ASME Turbo Expo, Power for Land, Sea and Air*, 2009. Orlando, South Korea.

[39] C.M. Firrone and S. Zucca. Underplatform dampers for turbine blades: the effect of damper static balance on the blade dynamics. *Mechanics Research Communications*, 36:515–522, 2009.

[40] C.M. Firrone. Measurement of the kinematics of two underplatform dampers with different geometry and comparison with numerical simulation. *Journal of Sound and Vibration*, 323:313–333, 2009.

[41] C.W. Schwingshackl, E.P. Petrov, and D.J. Ewins. Effects of contact interface parameters on vibration of turbine bladed disks with underplatform dampers. *Journal of Engineering for Gas Turbines and Power*, 134, 2012.

[42] S. Zucca, C.M. Firrone, and M.M. Gola. Numerical assessment of friction damping at turbine blade root joints by simultaneous calculation of the static and dynamic contact loads. *Nonlinear Dynamics*, 67(3):1943–1955, 2012.

[43] M. Krack, L. Panning-Von Scheidt, J. Wallaschek, C. Siewert, and A. Hartung. Reduced order modeling based on complex nonlinear modal analysis and its application to bladed disks with shroud contact. *Journal of Engineering for Gas Turbines and Power*, 135, 2013.

[44] J.J. Chen and C.H. Menq. Prediction of periodic response of blades having 3d nonlinear shroud constraints. *Proceedings of the ASME International Gas Turbine and Aeroengine Congress and Exhibition*, 1999.

[45] L. Gaul and J. Lenz. Nonlinear Dynamics of Structures Assembled by Bolted Joints. *Acta Mechanica*, 125:169–181, 1997.

[46] L. Gaul and R. Nietsche. *Nonlinear Dynamics of Structures with Joint Connections*. Structural Dynamics 2000, edited by D.J. Ewins, D.J. Inman. Series Engineering Dynamics, 1999.

[47] M.J. Oldfield, H. Ouyang, and J.E. Mottershead. Simplified Models of Bolted Joints Under Harmonic Loading. *Computers & Structures*, 84:25–33, 2005.

[48] C.W. Schwingshackl, , and E.P. Petrov. Modeling of flange joints for the nonlinear dynamic analysis of gas turbine engine casings. *Journal of Engineering for Gas Turbines and Power*, 134, 2012.

[49] C.W. Schwingshackl, D. Di Maio, I. Sever, and J.S. Green. Modeling and Validation of the Nonlinear Dynamic Behavior of Bolted Flange Joints. *Journal of Engineering for Gas Turbines and Power*, 135, 2013.

[50] D. Di Maio, C.W. Schwingshackl, D., and I. Sever. Development of a test planning methodology for performing experimental model validation of bolted flanges. *Nonlinear Dynamics*, 83:983–1002.

[51] DJ Ewins, B Weekes, and A delli Carri. Modal testing for model validation of structures with discrete nonlinearities. *Phil. Trans. R. Soc. A*, 373(2051):20140410, 2015.

[52] Arnaldo delli Carri, B Weekes, Dario Di Maio, and DJ Ewins. Extending modal testing technology for model validation of engineering structures with sparse nonlinearities: A first case study. *Mechanical Systems and Signal Processing*, 84:97–115, 2017.

[53] A. Cardona, A. Lerusse, and M. Geradin. Fast Fourier Nonlinear Vibration Analysis. *Computational Mechanics*, 22:128–142.

[54] J.H. Griffin. Friction damping of resonant stresses in gas turbine engine airfoils. *Journal of Engineering for Power*, 102:329–333.

[55] E.P. Petrov and D.J. Ewins. Analytical formulation of friction interface elements for analysis of nonlinear multiharmonic vibrations of bladed discs. *Transactions of ASME Journal of Turbomachinery*, 125:364–371.

[56] T.M. Cameron and J.H. Griffin. An Alternating Frequency/Time Domain Method for Calculating the Steady-State Response of Nonlinear Systems. *Journal of Applied Mechanics*, 56:149–154.

[57] O. Poudou and C. Pierre. Hybrid Frequency-Time Domain Methods for the Analysis of Complex Structural Systems with Friction Damping. *Collection of Technical Papers - AIAA / ASME / ASCE / AHS / ASC Structural Dynamics and Materials Conference*, 1:111–124.

[58] B.D. Yang, M.L. Chu, and C.H. Menq. Stick–Slip–Separation Analysis and Non-Linear Stiffness and Damping Characterization of Friction Contacts Having Variable Normal Load. *Journal of Sound and Vibrations*, 210:461–481.

[59] Christian Maria Firrone and Stefano Zucca. *Modelling friction contacts in structural dynamics and its application to turbine bladed disks*. InTech, 2011.

[60] G. Battiato, C.M. Firrone, T.M. Berruti, and Epureanu B.I. Reduced order modeling for multistage coupling of cyclic symmetric structures with friction at the flange joint. *Nonlinearities in Reduced Order Modeling Workshop, ETH Zurich*, 2016.

[61] M.P. Castanier and C. Pierre. Modeling and Analysis of Mistuned Bladed Disk Vibration: Status and Emerging Directions. *Journal of Propulsion and Power*, 210:384–396.

[62] Y.I. Zablotskiy and Y. A. Korostelev. Measurement of resonance vibrations of turbine blades with the elura device. *Energomashinostroneniye (USSR)*, 2:36–39.

[63] M. Zielinski and G. Ziller. Noncontact vibration measurements on compressor rotor blades. *Meas. Sci. Technol.*, 11, 2000.

[64] T. Berruti, V. Maschio, and P. Calza. Experimental investigation on the forced response of a dummy counter-rotating turbine stage with friction damping. *Journal of Engineering for Gas Turbines and Power*, 134, 2012.

[65] M. Zielinski and G. Ziller. Noncontact blade vibration measurement system for aero engine application. *17th International Symposium on Airbreathing Engines*, 11, 2005.

[66] M. Zielinski. Vibration Measurements on Compressor Blades and Shrouded Turbine Blades. 14^{th} Blade Mechanics Seminar, 2009.

[67] DH Diamond, PS Heyns, and AJ Oberholster. A comparison between three blade tip timing algorithms for estimating synchronous turbomachine blade vibration. In *9th WCEAM Research Papers*, pages 215–225. Springer, 2015.

[68] Analyze blade vibration user manual (ver 7.5). Hood Technology, 2014.

[69] I.B. Carrington, J.R. Wright, J.E. Cooper, and G. Dimitriadis. A comparison of blade tip timing data analysis methods. *Proceedings of the Institution of Mechanical Engineers, Part G: Journal of Aerospace Engineering*, 215:301–312, 2001.

[70] G. Dimitriadis, I.B. Carrington, J.R. Wright, , and J.E. Cooper. Blade-Tip Timing Measurement of Synchronous Vibrations of Rotating Bladed Assemblies. *Mechanical Systems and Signal Processing*, 16:599–622, 2002.

[71] J. Gallego-Garrido, G. Dimitriadis, , and J.R. Wright. A class of methods for the analysis of blade tip timing data from bladed assemblies undergoing simultaneous resonances-part i: Theoretical development. *International Journal of Rotating Machinery*, 2007.

[72] J. Gallego-Garrido, G. Dimitriadis, , and J.R. Wright. A class of methods for the analysis of blade tip timing data from bladed assemblies undergoing simultaneous resonances- Part II: Experimental validation. *International Journal of Rotating Machinery*, 2007.

[73] Firrone C.M. and T.M. Berruti. An electromagnetic system for the non-contact excitation of bladed disks. *Experimental Mechanics*, 52:447–459, 2012.

Appendix A

Appendix to Chapter 2

A.1 Matrices Derivation of a Lumped Parameters Cyclic Symmetric Structure

In this section the mass and stiffness matrices of a lumped parameters cyclic symmetric structure will be obtained by adopting the DoFs partitioning of Eqn. 2.3. The cyclic symmetric structure consists of 4 sectors each of which is composed by two lumped masses (i.e. m_n and m_{s_n}, $n = 1,2,3,4$) connected to each other with a spring having stiffness k_{s_n}.

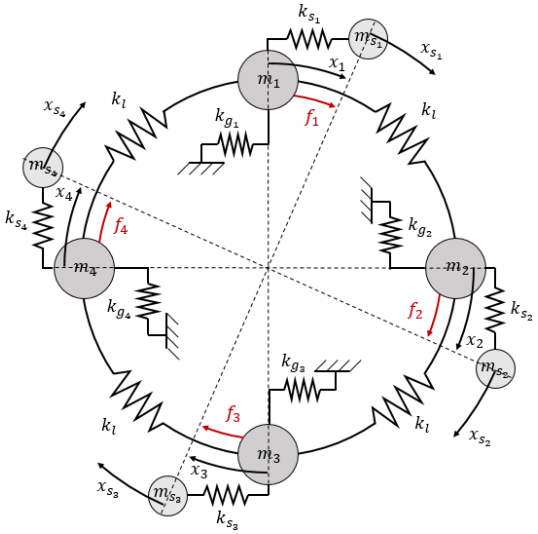

Fig. A.1 Example of a lumped parameters cyclic symmetric structure with 4 sectors.

The masses m_n are mutually linked by means of equal springs having stiffness k_l and their connection to the ground is guaranteed by the springs with stiffness k_{g_n} (Figure A.1).

The corresponding system of EQM can be obtained by resorting to the *free body diagram* (FBD) of each mass. As an example, Figure A.2 shows the FBDs of the mass m_1 and m_{s_1} belonging to the first sector.

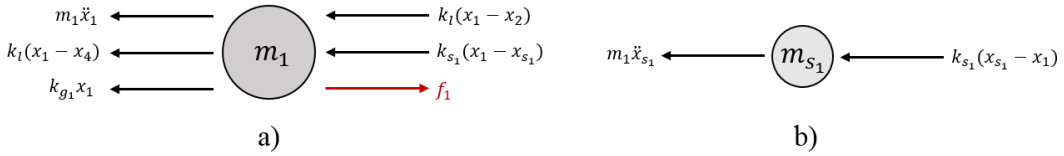

Fig. A.2 a) FBD of the mass m_1, b) FBD of the mass m_{s_1}.

According to the previous FBDs the equilibrium equations for m_1 and m_{s_1} can thus be written as:

$$\begin{cases} m_1\ddot{x}_1 + k_l(x_1-x_4) + k_{g_1}x_1 + k_l(x_1-x_2) + k_{s_1}(x_1-x_{s_1}) - f_1 = 0 \\ m_{s_1}\ddot{x}_{s_1} + k_{s_1}(x_{s_1}-x_1) = 0 \end{cases} \tag{A.1}$$

By repeating the same procedure for all the other sectors and grouping all the terms referring the same DoF (i.e. either x_n or x_{s_n}, $n = 1,2,3,4$), the following system of EQM is obtained:

$$\begin{cases} m_1\ddot{x}_1 + (2k_l + k_{s_1} + k_{g_1})x_1 - k_{s_1}x_{s_1} - k_l x_2 - k_l x_4 = f_1 \\ m_{s_1}\ddot{x}_{s_1} - k_{s_1}x_1 + k_{s_1}x_{s_1} = 0 \\ m_2\ddot{x}_2 - k_l x_1 + (2k_l + k_{s_2} + k_{g_2})x_2 - k_{s_2}x_{s_2} - k_l x_3 = f_2 \\ m_{s_2}\ddot{x}_{s_2} - k_{s_2}x_2 + k_{s_2}x_{s_2} = 0 \\ m_3\ddot{x}_3 - k_l x_2 + (2k_l + k_{s_2} + k_{g_2})x_3 - k_{s_3}x_{s_3} - k_l x_4 = f_3 \\ m_{s_3}\ddot{x}_{s_3} - k_{s_3}x_3 + k_{s_3}x_{s_3} = 0 \\ m_4\ddot{x}_4 - k_l x_1 - k_l x_3 + (2k_l + k_{s_2} + k_{g_2})x_4 - k_{s_4}x_{s_4} = f_4 \\ m_{s_4}\ddot{x}_{s_4} - k_{s_4}x_4 + k_{s_4}x_{s_4} = 0 \end{cases} \tag{A.2}$$

Under the assumption of cyclic symmetry the parameters shown in Figure A.1 must satisfy the following relationships:

$$\begin{cases} m_n = m & \forall\, n \\ m_{s_n} = m_s & \forall\, n \\ k_{g_n} = k_g & \forall\, n \\ k_{s_n} = k_s & \forall\, n \end{cases} \tag{A.3}$$

Therefore, Eqn. A.2 can thus be expressed as:

$$\begin{cases} m_1\ddot{x}_1 + k_{tot}x_1 - k_s x_{s_1} - k_l x_2 - k_l x_4 = f_1 \\ m_{s_1}\ddot{x}_{s_1} - k_s x_1 + k_s x_{s_1} = 0 \\ m_2\ddot{x}_2 - k_l x_1 + k_{tot}x_2 - k_s x_{s_2} - k_l x_3 = f_2 \\ m_{s_2}\ddot{x}_{s_2} - k_s x_2 + k_s x_{s_2} = 0 \\ m_3\ddot{x}_3 - k_l x_2 + k_{tot}x_3 - k_s x_{s_3} - k_l x_4 = f_3 \\ m_{s_3}\ddot{x}_{s_3} - k_s x_3 + k_s x_{s_3} = 0 \\ m_4\ddot{x}_4 - k_l x_1 - k_l x_3 + k_{tot}x_4 - k_s x_{s_4} = f_4 \\ m_{s_4}\ddot{x}_{s_4} - k_s x_4 + k_s x_{s_4} = 0 \end{cases} \tag{A.4}$$

where $k_{tot} = 2k_l + k_s + k_g$.

The system of EQM of Eqn. A.4 can be written in matrix form as:

$$\boldsymbol{M}\ddot{\boldsymbol{x}} + \boldsymbol{K}\boldsymbol{x} = \boldsymbol{0} \tag{A.5}$$

where:

$$\boldsymbol{M} = \begin{bmatrix} m & 0 & 0 & 0 & 0 & 0 & 0 & 0 \\ 0 & m_s & 0 & 0 & 0 & 0 & 0 & 0 \\ 0 & 0 & m & 0 & 0 & 0 & 0 & 0 \\ 0 & 0 & 0 & m_s & 0 & 0 & 0 & 0 \\ 0 & 0 & 0 & 0 & m & 0 & 0 & 0 \\ 0 & 0 & 0 & 0 & 0 & m_s & 0 & 0 \\ 0 & 0 & 0 & 0 & 0 & 0 & m & 0 \\ 0 & 0 & 0 & 0 & 0 & 0 & 0 & m_s \end{bmatrix}$$

$$\boldsymbol{K} = \begin{bmatrix} k_{tot} & -k_s & -k_l & 0 & 0 & 0 & -k_l & 0 \\ -k_s & k_s & 0 & 0 & 0 & 0 & 0 & 0 \\ -k_l & 0 & k_{tot} & -k_s & -k_l & 0 & 0 & 0 \\ 0 & 0 & -k_s & k_s & 0 & 0 & 0 & 0 \\ 0 & 0 & -k_l & 0 & k_{tot} & -k_s & -k_l & 0 \\ 0 & 0 & 0 & 0 & -k_s & k_s & 0 & 0 \\ -k_l & 0 & 0 & 0 & -k_l & 0 & k_{tot} & -k_s \\ 0 & 0 & 0 & 0 & 0 & 0 & -k_s & k_s \end{bmatrix} \tag{A.6}$$

are the mass and stiffness matrices of the cyclic symmetric structure and:

$$\boldsymbol{x} = \begin{Bmatrix} x_1 \\ x_{s_1} \\ x_2 \\ x_{s_2} \\ x_3 \\ x_{s_3} \\ x_4 \\ x_{s_4} \end{Bmatrix} \qquad \boldsymbol{f} = \begin{Bmatrix} f_1 \\ 0 \\ f_2 \\ 0 \\ f_3 \\ 0 \\ f_4 \\ 0 \end{Bmatrix} \tag{A.7}$$

are the corresponding DoFs and force vectors.

According to Eqn. A.6 $\boldsymbol{M}$ and $\boldsymbol{K}$ have a block circulant symmetric structure, since they can be finally expressed as in the case of Eqn. 2.3:

$$\boldsymbol{M} = \begin{bmatrix} \boldsymbol{M}_0 & \boldsymbol{M}_1 & \boldsymbol{M}_2 & \boldsymbol{M}_1 \\ \boldsymbol{M}_1 & \boldsymbol{M}_0 & \boldsymbol{M}_1 & \boldsymbol{M}_2 \\ \boldsymbol{M}_2 & \boldsymbol{M}_1 & \boldsymbol{M}_0 & \boldsymbol{M}_1 \\ \boldsymbol{M}_1 & \boldsymbol{M}_2 & \boldsymbol{M}_1 & \boldsymbol{M}_0 \end{bmatrix} \qquad \boldsymbol{K} = \begin{bmatrix} \boldsymbol{K}_0 & \boldsymbol{K}_1 & \boldsymbol{K}_2 & \boldsymbol{K}_1 \\ \boldsymbol{K}_1 & \boldsymbol{K}_0 & \boldsymbol{K}_1 & \boldsymbol{K}_2 \\ \boldsymbol{K}_2 & \boldsymbol{K}_1 & \boldsymbol{K}_0 & \boldsymbol{K}_1 \\ \boldsymbol{K}_1 & \boldsymbol{K}_2 & \boldsymbol{K}_1 & \boldsymbol{K}_0 \end{bmatrix} \tag{A.8}$$

where:

$$\boldsymbol{M}_0 = \begin{bmatrix} m & 0 \\ 0 & m_s \end{bmatrix} \qquad \boldsymbol{M}_1 = \boldsymbol{M}_2 = \begin{bmatrix} 0 & 0 \\ 0 & 0 \end{bmatrix}$$

$$\boldsymbol{K}_0 = \begin{bmatrix} k_{tot} & -k_s \\ -k_s & k_s \end{bmatrix} \qquad \boldsymbol{K}_1 = \begin{bmatrix} -k_l & 0 \\ 0 & 0 \end{bmatrix} \qquad \boldsymbol{K}_2 = \begin{bmatrix} 0 & 0 \\ 0 & 0 \end{bmatrix} \tag{A.9}$$